

University of Windsor

## Scholarship at UWindor

---

Electronic Theses and Dissertations

Theses, Dissertations, and Major Papers

---

6-24-2022

# Plastic Deformation and Fracture Behaviour of AA5182-O Aluminum Alloy at Sub-Zero Temperatures

Taryn Coutts  
*University of Windsor*

Follow this and additional works at: <https://scholar.uwindsor.ca/etd>

---

### Recommended Citation

Coutts, Taryn, "Plastic Deformation and Fracture Behaviour of AA5182-O Aluminum Alloy at Sub-Zero Temperatures" (2022). *Electronic Theses and Dissertations*. 9594.  
<https://scholar.uwindsor.ca/etd/9594>

This online database contains the full-text of PhD dissertations and Masters' theses of University of Windsor students from 1954 forward. These documents are made available for personal study and research purposes only, in accordance with the Canadian Copyright Act and the Creative Commons license—CC BY-NC-ND (Attribution, Non-Commercial, No Derivative Works). Under this license, works must always be attributed to the copyright holder (original author), cannot be used for any commercial purposes, and may not be altered. Any other use would require the permission of the copyright holder. Students may inquire about withdrawing their dissertation and/or thesis from this database. For additional inquiries, please contact the repository administrator via email ([scholarship@uwindsor.ca](mailto:scholarship@uwindsor.ca)) or by telephone at 519-253-3000ext. 3208.

**Plastic Deformation and Fracture Behaviour of AA5182-O Aluminum Alloy at Sub-Zero Temperatures**

By

**Taryn Coutts**

A Thesis

Submitted to the Faculty of Graduate Studies  
through the Department of Mechanical, Automotive & Materials Engineering  
in Partial Fulfillment of the Requirements for  
the Degree of Master of Applied Science at the  
University of Windsor

Windsor, Ontario, Canada

2022

© 2022 Taryn Coutts

**Plastic Deformation and Fracture Behaviour of AA5182-O Aluminum Alloy at Sub-Zero Temperatures**

By

**Taryn Coutts**

APPROVED BY:

---

J. Stagner

Department of Mechanical, Automotive & Materials Engineering

---

D. Green

Department of Mechanical, Automotive & Materials Engineering

---

A. Alpas, Advisor

Department of Mechanical, Automotive & Materials Engineering

May 24<sup>th</sup>, 2022

# Declaration of Originality

I hereby certify that I am the sole author of this thesis and that no part of this thesis has been published or submitted for publication.

I certify that, to the best of my knowledge, my thesis does not infringe upon anyone's copyright nor violate any proprietary rights and that any ideas, techniques, quotations, or any other material from the work of other people included in my thesis, published or otherwise, are fully acknowledged in accordance with the standard referencing practices. Furthermore, to the extent that I have included copyrighted material that surpasses the bounds of fair dealing within the meaning of the Canada Copyright Act, I certify that I have obtained a written permission from the copyright owner(s) to include such material(s) in my thesis and have included copies of such copyright clearances to my appendix.

I declare that this is a true copy of my thesis, including any final revisions, as approved by my thesis committee and the Graduate Studies office, and that this thesis has not been submitted for a higher degree to any other University or Institution.

# Abstract

Commercial aluminum alloy AA5182 is being increasingly used as a predominant material for aircraft and automotive industries in an effort to light-weight these applications. Previous work indicates that the ductility/formability of aluminum alloys increases with decreasing temperature, however, the subject of the mechanisms behind this improvement is still up for debate. In this study, deformation and fracture behaviour of AA5182-O aluminum sheets are investigated. Tensile tests are conducted at temperatures ranging from 25 to -196°C, and a strain rate of  $1.9 \times 10^{-3} \text{ s}^{-1}$ , in an environmental chamber cooled with liquid nitrogen. The mechanical properties are mapped as a function of temperature. It was observed that the fracture elongation increased from 0.26 to 0.5 mm/mm from 25°C to -196°C, and that the dynamic strain aging effect was not visible at temperatures below -80°C. Cottrell-Stokes tests (temperature jump and strain-rate jump tensile tests) were conducted to evaluate the dynamic changes of mechanical properties at constant microstructure at different temperatures and strain rates. These tests provided insight on the flow dependency of AA5182-O on both temperature and strain rate. Microscopic investigation of ductile fracture at different temperatures using SEM and EDS analysis was conducted. Quantitative fractography was used to measure void sphericity, percentage, and size as function of temperature to show a transition in plastic shear deformation at 25°C to more ductile tearing deformation at -196°C.

# Dedication

*To my family and friends, whose endless love and support has guided me  
through this adventure to the end.*

# Acknowledgements

I would like to begin by expressing my sincerest gratitude to my advisor Dr. Ahmet Alpas for offering me an opportunity to learn, experience, and work alongside such a gifted and caring mentor. Dr. Alpas' ambition and support inspired each day of my research to create and work towards something we could both be proud of.

I am truly thankful to my committee members, Dr. Daniel Green and Dr. Jacqueline Stagner, for their endless patience and encouragement. I would like to thank them for their time, discussion, and invaluable feedback that has helped develop this work to what it is today. Special thanks to Bill Middleton, Matt St. Louis, and Mark Gryn for their tireless efforts and meticulous work during the many labs and trials developed throughout this research. I am extremely thankful to Ms. Sharon Lackie for sharing her expertise in scanning electron microscopy at the Great Lakes Institute for Environmental Research and always going above and beyond to help.

Thank you to the many friendly faces I have met along the way. To name a few, thank you Dillon, Mingxiao, Xi, Mike, Jen, Alexandra, and many others. Thank you for not only helping me through my graduate years, but also for your kindness and friendship.

Finally, thank you to my family. Thank you to my sister Alexa, for being my best friend and my biggest supporter. Thank you, Jeff, you have given me so much love and support over the years, and you are always there to remind me to step back and breathe when things get tough. Thank you, Austyn, for always making me push myself one page at a time and for teaching me how to celebrate the small victories. Thank you to my dad, sisters, and entire family for your unconditional love and encouragement.

Thank you to my mom. Thank you for your love, your patience, and your sacrifices. You have given me more than I can ever put into words. All I can say is that you are my whole world and everything I do, I dedicate to you.

# Table of Content

<b>Declaration of Originality</b>	<b>iii</b>
<b>Abstract</b>	<b>iv</b>
<b>Dedication</b>	<b>v</b>
<b>Acknowledgements</b>	<b>vi</b>
<b>List of Tables</b>	<b>x</b>
<b>List of Figures</b>	<b>xii</b>
<b>Nomenclature</b>	<b>xxiv</b>
<b>Abbreviations</b>	<b>xxvi</b>
<b>1 Introduction</b>	<b>1</b>
1.1 Motivation.....	1
1.2 Objectives of Research.....	4
1.3 Structure of Subsequent Chapters.....	5
<b>2 Literature Review</b>	<b>6</b>
2.1 5xxx-Series Aluminum Alloys.....	6
2.1.1 Alloying Elements, Chemical Composition, and Mechanical Properties.....	6
2.1.2 Second Phase Particles.....	18
2.1.3 Damage Mechanisms.....	21
2.2 The Portevin Le-Chatelier Effect.....	28
2.2.1 Strain Rate Sensitivity.....	28
2.2.2 Dynamic Strain Aging.....	32
2.2.3 Deformation Instability.....	37
2.3 Cottrell-Stokes Testing.....	42
2.3.1 Temperature Change Tensile Testing.....	42
2.3.2 Strain Rate Change Tensile Testing.....	45
2.4 Sub-Zero Temperature Tensile Testing.....	49

Bibliography.....	56
<b>3 Methodology</b>	<b>67</b>
3.1 Material Characterization.....	67
3.1.1 Grinding, Polishing, and Etching.....	67
3.1.2 Hardness Testing.....	71
3.1.3 OM, SEM, and EDS.....	74
3.2 Grid Application.....	76
3.3 Tensile Testing.....	79
3.3.1 Tensile Samples and Testing Equipment.....	79
3.3.2 Room Temperature Tensile Testing.....	82
3.3.3 Sub-Zero Temperature Tensile Testing.....	83
3.3.4 Cottrell-Stokes Tensile Testing.....	86
3.3.5 Strain Rate Change Tensile Testing.....	87
3.4 Formability Testing.....	88
3.4.1 Testing Equipment.....	91
3.4.2 Specimen Geometries.....	93
Bibliography.....	<b>95</b>
<b>4 Experimental Results</b>	<b>97</b>
4.1 Material Characterization.....	97
4.1.1 Hardness Testing.....	97
4.1.2 OM, SEM, and EDS.....	98
4.2 Mechanical Properties.....	106
4.2.1 Room Temperature Tensile Testing.....	106
4.2.2 Sub-Zero Temperature Tensile Testing.....	108
4.3 Fractography.....	119
4.4 Cottrell-Stokes Testing.....	135
4.4.1 Temperature Change Tensile Testing.....	135
4.4.2 Strain Rate Change Tensile Testing.....	140
<b>5 Discussion</b>	<b>144</b>
5.1 Microstructure.....	144
5.2 Mechanical Properties.....	145

5.2.1	Room Temperature Tensile Testing.....	145
5.2.2	Sub-Zero Temperature Tensile Testing.....	145
5.2.3	Fractography.....	147
5.3	Cottrell-Stokes Testing.....	149
	Bibliography.....	151
<b>6</b>	<b>Conclusions and Future Work</b>	<b>153</b>
6.1	Conclusions.....	153
6.2	Future Work.....	154
6.2.1	Sub-Zero Temperature Tensile Testing.....	154
6.2.2	Sub-Zero Formability Testing.....	155
6.2.3	Fractography.....	155
	<b>Appendices</b>	<b>157</b>
	<b>Vita Auctoris</b>	<b>214</b>

# List of Tables

<b>Table 2.1</b> Aluminum Association (AA) numbers and nominal compositions of common 5xxx-series aluminum alloys.....	7
<b>Table 2.2</b> Yield stress of 5xxx-series (Al-Mg) alloys with respective (wt% Mg).....	12
<b>Table 2.3</b> Chemical composition of various AA5182-O alloying elements in weight percent (The hyphen –O for an alloy refers to an alloy that has been annealed)....	13
<b>Table 2.4</b> Mechanical property values for AA5182 aluminum from literature.....	15
<b>Table 3.1</b> Metallographic Abrasive Grinding Procedure.....	70
<b>Table 3.2</b> Revised Keller’s Etchant for Aluminum-Magnesium Alloys.....	71
<b>Table 3.3</b> Table used for data collection of FMTI grid analysis.....	94
<b>Table 4.1</b> Average grain values calculated from initial material characterization of AA5182-O aluminum alloy.....	99
<b>Table 4.2</b> Settings for the EDAX SiLi Detector for EDS analysis.....	103
<b>Table 4.3</b> Chemical composition of the as-received AA5182-O aluminum alloy...	104
<b>Table 4.4</b> Average mechanical properties obtained from the engineering stress strain curve for aluminum alloy AA5182 obtained at ambient temperature; respective strain rate $1.9 \times 10^{-3} \text{ s}^{-1}$ .....	105
<b>Table 4.5</b> Internal Data for Cottrell-Stokes $\Delta 20^\circ\text{C}$ temperature jump tests.....	136
<b>Table A.1</b> AA5182-O average surface hardness measurements and calculations..	153
<b>Table A.2</b> AA5182-O longitudinal direction hardness measurements and calculations.....	154
<b>Table A.3</b> AA5182-O transverse direction surface hardness measurements and calculations.....	154

<b>Table A.4</b> AA5182-O average length measurements from <i>Figure A.3</i> SEM images.....	157
<b>Table A.5</b> AA5182-O average length measurements from <i>Figure A.8</i> SEM images.....	160
<b>Table A.6</b> AA5182-O reference measurements from <i>Figure A.8</i> SEM images...	161
<b>Table A.7</b> AA5182-O reference measurements from <i>Figure A.26</i> SEM images...	173
<b>Table A.8</b> AA5182-O conversion reference measurements from <i>Figure A.26</i> SEM images.....	174
<b>Table A.9</b> AA5182-O reference measurements from <i>Figure A.27</i> SEM images... 176	
<b>Table A.10</b> AA5182-O conversion reference measurements from <i>Figure A.27</i> SEM images.....	177
<b>Table A.11</b> AA5182-O reference measurements from <i>Figure A.28</i> SEM images. 180	
<b>Table A.12</b> AA5182-O conversion reference measurements from <i>Figure A.28</i> SEM images.....	180
<b>Table A.13</b> AA5182-O reference measurements from <i>Figure A.29</i> SEM images... 181	
<b>Table A.14</b> AA5182-O conversion reference measurements from <i>Figure A.29</i> SEM images.....	181
<b>Table A.15</b> AA5182-O reference measurements from <i>Figure A.30</i> SEM images... 183	
<b>Table A.16</b> AA5182-O reference measurements from <i>Figure A.30</i> SEM images... 184	
<b>Table A.17</b> AA5182-O reference measurements from <i>Figure A.31</i> SEM images... 186	
<b>Table A.18</b> AA5182-O conversion reference measurements from <i>Figure A.31</i> SEM images.....	187
<b>Table A.19</b> Mechanical property values obtained from <i>Figure 32</i> . (Anisotropy data).....	188

# List of Figures

<b>Figure 1.1</b> Fracture elongation versus yield stress for aluminum magnesium alloys compared to modern steels in automotive applications.....	2
<b>Figure 1.2</b> Flow stresses measured from true stress-strain curves at plastic strains of 0.1 and 0.2 mapped as a function of temperature for AA5182 aluminum alloy.....	3
<b>Figure 2.1</b> Correlation between tensile yield stress and elongation as a function of magnesium content for some commercial aluminum-magnesium alloys in annealed condition.....	8
<b>Figure 2.2.</b> Comparison of a model for grain size and solution strengthening and experimental yield stress values for AA5052, AA5754, and AA5182 aluminum alloys.....	10
<b>Figure 2.3</b> Aluminum side of the Al-Mg binary phase diagram.....	11
<b>Figure 2.4</b> TTT diagram for the precipitation of $Mg_5Al_8$ from the Al-5.5 wt% Mg solid.....	12
<b>Figure 2.5</b> Work hardening plots for various Al alloys, where the flow stress is expressed as $(\sigma - \sigma_Y)$ to normalize the values with respect to diverse yield stress.....	17
<b>Figure 2.6</b> Aluminum magnesium binary phase diagram.....	19
<b>Figure 2.7</b> Micro mechanisms for ductile fracture with accompanying SEM.....	22
<b>Figure 2.8</b> Mechanisms of void nucleation around inclusions through (a) decohesion between particle and the matrix, (b) particle cracking, and (c) shear deformation.....	23
<b>Figure 2.9</b> Five mechanisms for ductile fracture in polycrystalline materials including failure by (a) localized plastic flow, (b) localized plastic flow prior to damage, (c) damage softening, (d) void coalescence, and (e) ductile tearing.....	24
<b>Figure 2.10</b> Schematics and SEM micrographs showing (a) ductile (uniaxial) fracture under tensile load and (b) fracture surface with spherical dimples and (c) lateral load causing tearing with (d) parabolic dimples that are characteristic of ductile tears or shear loading.....	26

<b>Figure 2.11</b> (a) Cross-sectional reduction of 5xxx-series aluminum alloy specimen illustrating localized necking at an angle of $55^\circ$ and (b) Schematic cross-sectional reduction in thickness occurring alongside shear deformation in multiple planes.....	27
<b>Figure 2.12</b> (a) True stress versus true strain curves for aluminum alloy 5182 over a range of strain rates with (b) enlarged views of the curves.....	28
<b>Figure 2.13</b> Strain rate sensitivity parameter with two strain rates as a function of temperature for aluminum alloy AA5182-O. The strain rate differential for this data is 1:100, a base rate of $\dot{\epsilon}_1 = 10^{-3} \text{ s}^{-1}$ , and plastic strains of 10 and 20% respectively.....	30
<b>Figure 2.14</b> Variation of the total elongation at failure with temperature for a temperature range for AA 5182-O aluminum alloy from -120 to $150^\circ\text{C}$ .....	31
<b>Figure 2.15</b> A schematic of (a) mobile dislocations (b) mobile dislocations meeting and being arrested by obstacles such as a Cottrell-atmosphere and (c) subsequent lattice and pipe diffusion.....	33
<b>Figure 2.16</b> A solute atom inside a crystal structure resulting in a Cottrell atmosphere demonstrating: (a) a dislocation in the crystal structure, (b) solute atoms congregate underneath the dislocations to form Cottrell atmospheres, and (c) dislocation arrested by the solute atoms and unable to move.....	35
<b>Figure 2.17</b> Serrated flow range of the aluminum alloy AA5083 dependent on log strain rate ( $\text{s}^{-1}$ ) and $1/T$ ( $\text{K}^{-1}$ ).....	38
<b>Figure 2.18</b> Experimental and numerical simulation (developed using a one-dimensional phenomenological model) observations of three PLC types in tensile test at different applied strain rates: (a) type A, $5 \times 10^{-3} \text{ s}^{-1}$ with (b) enlarged view, (c) type B, $5 \times 10^{-4} \text{ s}^{-1}$ with (d) enlarged view, and (e) type C, $5 \times 10^{-5} \text{ s}^{-1}$ with (f) enlarged view.....	39
<b>Figure 2.19</b> Schematics of motion, orientation, spatio temporal appearances and strain controlled tensile curve characteristics for (a) Type A, (b) Type B, and (c) Type C serrations.....	40
<b>Figure 2.20.</b> Schematic of Cottrell-Stokes method of investigating the temperature dependence of the flow stress (reversible change in flow stress with temperature.....	43
<b>Figure 2.21</b> Stress-strain curves (schematic) showing the form of yield drop developed at room temperature after straining an aluminum specimen in liquid air ( $-196^\circ\text{C}$ )...	44
<b>Figure 2.22</b> Stress-strain curves using the method of (a) testing two samples at different strain rates and (b) testing with one sample and a strain rate jump.....	47

<b>Figure 2.23.</b> Schematic of the Haasen plot with an intercept of thermal components, athermal components, and forest dislocation components as three types of components that can dominate flow stress.....	48
<b>Figure 2.24</b> True stress versus true strain curve for AA5182 aluminum alloy at temperatures of RT to -196°C (78 K) and strain rates of 0.001 s <sup>-1</sup> and 0.05 s <sup>-1</sup> ....	49
<b>Figure 2.25.</b> a) Experimental and b) numerical temperature-dependent forming limit curves for AA5182.....	50
<b>Figure 2.26</b> Microstructures of the RT rolled and LN <sub>2</sub> rolled 7050 Al alloys (a) as quenched, (b) 40% RTR, (c) 56% RTR, (d) 63% RTR, (e) 76% LN <sub>2</sub> R (f,g) 91% LN <sub>2</sub> R with different magnifications.....	52
<b>Figure 2.27</b> Work hardening rate of strip cast AA5754 sheet under 298 K and 223 K temperature conditions.....	53
<b>Figure 2.28</b> Work hardening rate as a function of reduced flow stress, both normalized by temperature dependent shear modulus. SC and Al denote AA5754 aluminum alloy and pure aluminum, respectively. NA and AQ denote natural aged and as-quenched Al-Zn-Mg alloys, respectively.....	53
<b>Figure 2.29.</b> Schematic of the instability point from Considère criterion showing the interception of a stress-strain curve with a strain hardening curve.....	54
<b>Figure 3.1</b> AA5182-O as received samples mounted in one part Epoxy Hardener and two parts Epoxy Resin exposing the (a) face of the metal, (b) rolling direction, and (c) parallel to the rolling direction.....	68
<b>Figure 3.2</b> Image of the (a) sheet metal shearing machine and (b) low speed diamond saw cutter used to AA5182-O aluminum alloy samples for grinding and polishing....	69
<b>Figure 3.3</b> Buehler EcoMet metallographic polishing machine.....	69
<b>Figure 3.4</b> A schematic of a Vickers hardness test using a square based pyramid diamond indenter and showing relevant nomenclature.....	72
<b>Figure 3.5</b> Buehler Micromet II model MHT-1B Micro Hardness Tester.....	72
<b>Figure 3.6</b> Omano OM159T (40x-1,000x ) Trinocular Compound Microscope.....	75
<b>Figure 3.7</b> FEI Quantra 200 FEG scanning electron microscope equipped with an energy-dispersive X-ray EDAX (SiLi Detector) spectrometer.....	75
<b>Figure 3.8</b> Grid pattern circles prior to and after deformation where (a) the strain causes the circles to deform into an ellipse and (b) there is a case of pure biaxial stretching.....	76

<b>Figure 3.9</b> A schematic of the apparatus used for grid pattern etching with (a) the grid marking machine and (b) the electrolyte solution and felt pad.....	77
<b>Figure 3.10(a)</b> An image of the schematic and grid pattern stencil that was used and <b>(b)</b> an image of the stencil etched onto a specimen.....	78
<b>Figure 3.11</b> ASTM Standard E8/E8M-16 schematic of sample.....	80
<b>Figure 3.12</b> Anisotropy directions.....	80
<b>Figure 3.13</b> MTS Model Universal Tensile Testing Machine (Model E45).....	81
<b>Figure 3.14</b> Epsilon extensometer 3542-050M-050-LT.....	81
<b>Figure 3.15</b> Setup/schematic of tensile testing machine with environmental chamber, specimen, and thermocouple.....	84
<b>Figure 3.16</b> Temperature control unit attached to the MTS tensile machine.....	84
<b>Figure 3.17</b> Set-up for samples tested at -196°C tensile testing temperature.....	85
<b>Figure 3.18</b> Erichsen sheet metal testing machine model 102.....	89
<b>Figure 3.19</b> Schematic of Erichsen cupping test (cross-section).....	89
<b>Figure 3.20</b> Process for cooling samples for low temperature formability testing using a thermocouple, cryogenic dewar of liquid nitrogen, and cooling container.....	90
<b>Figure 3.21</b> FMTI Systems grid analyzer hardware (grid analysis gun).....	91
<b>Figure 3.22.</b> FMTI Systems grid analysis software screen example.....	92
<b>Figure 3.23</b> Grid Analysis Area Criterion example (Failed, Neck, Acceptable)...	93
<b>Figure 3.24</b> Formability curve with modes of strain.....	94
<b>Figure 4.1</b> Schematic showing nomenclature for directions.....	95
<b>Figure 4.2</b> Average hardness calculations and respective standard deviations for AA5182-O calculated for the rolling surface, rolling direction, and transverse direction of the sample.....	96
<b>Figure 4.3</b> Optical microscopic images of AA5182-O after metallographic grinding and polishing procedures at a magnification of 1000x magnification.....	97
<b>Figure 4.4</b> SEM image of the etched surface of aluminum alloy AA5182-O showing the grain boundaries under 1000x magnification.....	98
<b>Figure 4.5</b> EDS image captured using energy-dispersive X-ray EDAX (SiLi Detector) of AA5182 fractured specimen.....	100

<b>Figure 4.6</b> Element distribution graph obtained from EDS analysis of spot 1....	101
<b>Figure 4.7</b> Element distribution graph obtained from EDS analysis of spot 2....	101
<b>Figure 4.8</b> Element distribution graph obtained from EDS analysis of spot 3.....	102
<b>Figure 4.9</b> Element distribution graph obtained from EDS analysis of spot 4.....	102
<b>Figure 4.10</b> Engineering Stress Strain Curve for aluminum alloy AA5182 obtained at ambient temperature and 0.002 offset of elastic region; respective strain rate $1.9 \times 10^{-3} \text{ s}^{-1}$ .....	104
<b>Figure 4.11</b> Engineering Stress Strain Curves for aluminum alloy AA5182 obtained at -40°C; respective strain rate $1.9 \times 10^{-3} \text{ s}^{-1}$ .....	106
<b>Figure 4.12</b> Engineering Stress Strain Curves for aluminum alloy AA5182 obtained at -80°C; respective strain rate $1.9 \times 10^{-3} \text{ s}^{-1}$ .....	107
<b>Figure 4.13</b> Engineering Stress Strain Curves for aluminum alloy AA5182 obtained at -120°C; respective strain rate $1.9 \times 10^{-3} \text{ s}^{-1}$ .....	108
<b>Figure 4.14</b> Engineering Stress Strain Curves for aluminum alloy AA5182 obtained at -160°C; respective strain rate $1.9 \times 10^{-3} \text{ s}^{-1}$ .....	109
<b>Figure 4.15</b> Engineering Stress Strain Curves for aluminum alloy AA5182 obtained at -196 °C; respective strain rate $1.9 \times 10^{-3} \text{ s}^{-1}$ .....	110
<b>Figure 4.16</b> Engineering Stress Strain Curves for aluminum alloy AA5182 obtained at temperature points of from 25, -40, -80, -120, -160. and -196 °C; respective strain rate $1.9 \times 10^{-3} \text{ s}^{-1}$ .....	111
<b>Figure 4.17</b> Yield stress and ultimate tensile stress values from 25, -40, -80, -120, -160, and -196°C tensile tests.....	112
<b>Figure 4.18</b> Strain at necking average values from 25, -40, -80, -120, -160, and -196 °C.....	112
<b>Figure 4.19</b> Strain at fracture average values from 25, -40, -80, -120, -160, and -196 °C.....	113
<b>Figure 4.20</b> Strain hardening exponent mapped as a function of uniform elongation of aluminum alloy AA5182 obtained at temperature points of 25, -40, -80, -120, -160. and -196 °C.....	113
<b>Figure 4.21</b> Work hardening rate mapped as a function of true stress for aluminum alloy AA5182 obtained at temperature points of 25 and -196°C.....	114

<b>Figure 4.22</b> Engineering Stress Strain Curves for aluminum alloy AA5182 obtained at temperature points of from 25, -40, -80, -120, -160, -196, and 120°C; respective strain rate $1.9 \times 10^{-3} \text{ s}^{-1}$ .....	115
<b>Figure 4.23</b> Engineering Stress Strain Curves for aluminum alloy AA5182 obtained at temperature points of from 25, -40, -80, -120, -160, and -196 °C; respective strain rate $1.9 \times 10^{-3} \text{ s}^{-1}$ .....	116
<b>Figure 4.24</b> Tensile samples fractured at temperature of a-25, b-40, c-80, d-120, e -160, and f-196°C respectively, and a crosshead velocity of 0.084 mm/s.....	117
<b>Figure 4.25</b> Average measured angle of fracture mapped as a function of temperature at 25, -40, -80, -120, -160, and -196°C.....	118
<b>Figure 4.26</b> shows the BSE SEM image of AA5182-O after experiencing a ductile fracture from tensile testing at a temperature of -160°C and a crosshead velocity of 0.084 mm/s.....	119
<b>Figure 4.27</b> Average dimple radius/length values for aluminum alloy AA5182 obtained at temperature points of from 25, -40, -80, -120, -160, and -196 °C.....	120
<b>Figure 4.28</b> The average aspect ratio of dimples for aluminum alloy AA5182 obtained at temperature points of from 25, -40, -80, -120, -160, and -196 °C.....	121
<b>Figure 4.29</b> The average aspect ratio of dimples with standard deviation for aluminum alloy AA5182 obtained at temperature points of from 25, -40, -80, -120, -160, and -196 °C.....	122
<b>Figure 4.30</b> The average dimple area ( $\pi \times \text{radius}^2$ ) measured for aluminum alloy AA5182 obtained at temperature points of from 25, -40, -80, -120, -160, and -196 °C.....	123
<b>Figure 4.31</b> The average dimple area ( $\pi \times \text{radius}^2$ ) measured with standard deviation for aluminum alloy AA5182 obtained at temperature points of from 25, -40, -80, -120, -160, and -196 °C.....	123
<b>Figure 4.32</b> BSE SEM image of ductile fracture of AA5182 at X800 magnification at 25°C.....	124
<b>Figure 4.33</b> BSE SEM image of ductile fracture of AA5182 at X2000 magnification at 25°C.....	125
<b>Figure 4.34</b> BSE SEM image of ductile fracture of AA5182 at X2000 magnification at -160°C.....	126
<b>Figure 4.35</b> BSE SEM image of ductile fracture of AA5182 at X800 magnification at -160°C.....	127

<b>Figure 4.36</b> BSE SEM image of ductile fracture of AA5182 at X800 magnification at - 40°C.....	128
<b>Figure 4.37</b> BSE SEM image of ductile fracture of AA5182 at X800 magnification at - 80°C.....	129
<b>Figure 4.38</b> BSE SEM image of ductile fracture of AA5182 at X800 magnification at - 120°C.....	130
<b>Figure 4.39</b> BSE SEM image of ductile fracture of AA5182 at X800 magnification at - 160°C.....	131
<b>Figure 4.40</b> BSE SEM image of ductile fracture of AA5182 at X800 magnification at - 196°C.....	132
<b>Figure 4.41</b> Engineering Stress Strain Curve for aluminum alloy AA5182 obtained at 120°C and crosshead velocity of 0.084 mm/s.....	134
<b>Figure 4.42</b> Cottrell-Stokes Engineering Stress Strain curve for temperature change tests from 120°C to 34°C.....	135
<b>Figure 4.43</b> Cottrell-Stokes Engineering Stress Strain curve for $\Delta 20^\circ\text{C}$ temperature jump tests.....	136
<b>Figure 4.44</b> Interval plot of the change in stress as a function of temperature for $\Delta 20^\circ\text{C}$ temperature jump tests.....	137
<b>Figure 4.45</b> Initial load-displacement curve obtained at 1 mm/min and 25°C.....	138
<b>Figure 4.46</b> Section 1 of Cottrell-Stokes load-displacement curve for strain rate jump tests of 1 mm/min to 5 mm/min at 1 mm extensometer displacement.....	139
<b>Figure 4.47</b> Section 2 of Cottrell-Stokes load-displacement curve for strain rate jump tests of 5 mm/min to 10 mm/min at 2 mm extensometer displacement.....	139
<b>Figure 4.48</b> Section 3 of Cottrell-Stokes load-displacement curve for strain rate jump tests of 10 mm/min to fracture.....	140
<b>Figure 4.49</b> Segment of the load-displacement curve for aluminum alloy AA5182 obtained at 25°C and a strain rate change of 1mm/min to 100 mm/min.....	141
<b>Figure A.1</b> Optical microscopy image of AA5182-O after metallographic grinding and polishing procedures at a magnification of 1000x magnification.....	155
<b>Figure A.2</b> Optical microscopy images of AA5182-O after metallographic grinding and polishing and etching procedures at a magnification of 1000x magnification.....	156

<b>Figure A.3</b> SEM images of as-received (a) Etched 5182_SE_1000x_001 (b) Etched 5182_SE_1000x_002 and (c) Etched 5182_SE_1000x_004 (Method 1).....	157
<b>Figure A.4</b> Optical microscopy images of AA5182-O after metallographic grinding and polishing and etching procedures at a magnification of 1000x magnification....	158
<b>Figure A.5</b> Optical microscopy images of AA5182-O after metallographic grinding and polishing and etching procedures at a magnification of 1000x magnification....	158
<b>Figure A.6</b> Optical microscopy images of AA5182-O after metallographic grinding and polishing and etching procedures at a magnification of 1000x magnification....	159
<b>Figure A.7</b> Optical microscopy images of AA5182-O after metallographic grinding and polishing and etching procedures at a magnification of 1000x magnification.....	159
<b>Figure A.8</b> SEM images of as-received (a) Etched 5182_SE_1000x_001 (b) Etched 5182_SE_1000x_002 and (c) Etched 5182_SE_1000x_004 (Method 2).....	160
<b>Figure A.9</b> Tensile sample fractured at temperature of 120°C.....	165
<b>Figure A.10</b> Tensile sample fractured at temperature of 25°C.....	165
<b>Figure A.11</b> Tensile sample fractured at temperature of -40°C.....	166
<b>Figure A.12</b> Tensile sample fractured at temperature of -80°C.....	166
<b>Figure A.13</b> Tensile sample fractured at temperature of -120°C.....	167
<b>Figure A.14</b> Tensile sample fractured at temperature of -160°C.....	167
<b>Figure A.15</b> Tensile sample fractured at temperature of -196°C.....	167
<b>Figure A.16</b> BSE SEM image of AA5182-O after experiencing a ductile fracture from tensile testing at a temperature of 25°C and a crosshead velocity of 0.084 mm/s .....	168
<b>Figure A.17</b> BSE SEM image of AA5182-O after experiencing a ductile fracture from tensile testing at a temperature of -40°C and a crosshead velocity of 0.084 mm/s .....	168
<b>Figure A.18</b> BSE SEM image of AA5182-O after experiencing a ductile fracture from tensile testing at a temperature of -80°C and a crosshead velocity of 0.084 mm/s.....	168
<b>Figure A.19</b> BSE SEM image of AA5182-O after experiencing a ductile fracture from tensile testing at a temperature of -120°C and a crosshead velocity of 0.084 mm/s.....	169

**Figure A.20** BSE SEM image of AA5182-O after experiencing a ductile fracture from tensile testing at a temperature of -196°C and a crosshead velocity of 0.084 mm/s..... 169

**Figure A.21** BSE SEM image of AA5182-O after experiencing a ductile fracture from tensile testing at a temperature of -40°C and a crosshead velocity of 0.084 mm/s..... 169

**Figure A.22** BSE SEM image of AA5182-O after experiencing a ductile fracture from tensile testing at a temperature of -40°C and a crosshead velocity of 0.084 mm/s..... 170

**Figure A.23** BSE SEM image of AA5182-O after experiencing a ductile fracture from tensile testing at a temperature of -80°C and a crosshead velocity of 0.084 mm/s..... 170

**Figure A.24** BSE SEM image of AA5182-O after experiencing a ductile fracture from tensile testing at a temperature of -80°C and a crosshead velocity of 0.084 mm/s..... 171

**Figure A.25** BSE SEM image of AA5182-O after experiencing a ductile fracture from tensile testing at a temperature of -80°C and a crosshead velocity of 0.084 mm/s..... 171

**Figure A.26** Mixed-signal SEM image of AA5182-O after experiencing a ductile fracture from tensile testing at a temperature of 25°C and a crosshead velocity of 0.084 mm/s with overlaid square grid for dimple measurements..... 172

**Figure A.27** Mixed-signal SEM image of AA5182-O after experiencing a ductile fracture from tensile testing at a temperature of -40°C and a crosshead velocity of 0.084 mm/s with overlaid square grid for dimple measurements..... 175

**Figure A.28** BSE SEM image of AA5182-O after experiencing a ductile fracture from tensile testing at a temperature of -80°C and a crosshead velocity of 0.084 mm/s with overlaid square grid for dimple measurements..... 178

**Figure A.29** shows the BSE SEM image of AA5182-O after experiencing a ductile fracture from tensile testing at a temperature of -120°C and a crosshead velocity of 0.084 mm/s with overlaid square grid for dimple measurements..... 179

**Figure A.30** BSE SEM image of AA5182-O after experiencing a ductile fracture from tensile testing at a temperature of -160°C and a crosshead velocity of 0.084 mm/s with overlaid square grid for dimple measurements..... 182

<b>Figure A.31</b> BSE SEM image of AA5182-O after experiencing a ductile fracture from tensile testing at a temperature of -196°C and a crosshead velocity of 0.084 mm/s with overlaid square grid for dimple measurements.....	185
<b>Figure A.32</b> Engineering stress-strain curves for AA5182-O at strain rate average of 0.0005 s <sup>-1</sup> and temperature 25°C with samples cut in the rolling direct (0°), perpendicular (90°) to the rolling direction, and 45° from the rolling direction.....	188
<b>Figure A.33</b> Engineering stress-strain curve for AA5182-O at strain rate average of 0.0005 s <sup>-1</sup> and temperature 25°C.....	189
<b>Figure A.34</b> True stress-strain curve for AA5182-O at strain rate average of 0.0005 s <sup>-1</sup> and temperature 25°C.....	189
<b>Figure A.35</b> Log of true stress-true strain to determine average strain hardening exponent (n-slope displayed on the plot).....	190
<b>Figure A.36</b> Engineering stress-strain curve for AA5182-O at strain rate average of 0.0005 s <sup>-1</sup> and temperature 25°C with 0.002 offset (for yield stress determination).....	190
<b>Figure A.37</b> Strain mapped as a function of time to determine average strain rate (slope) of the test for AA5182-O at strain rate average of 0.0005 s <sup>-1</sup> and temperature 25°C.....	191
<b>Figure A.38</b> Magnified engineering stress-strain curve for AA5182-O at strain rate average of 0.0005 s <sup>-1</sup> and temperature 25°C with 0.002 offset (elastic modulus=slope, intersection=yield strength) with equation displayed on the graph.....	191
<b>Figure A.39</b> Engineering stress-strain curve for AA5182-O at strain rate average of 0.001 s <sup>-1</sup> and temperature 25°C with 0.002 offset (for yield stress determination).....	192
<b>Figure A.40</b> True stress-strain curve for AA5182-O at strain rate average of 0.001 s <sup>-1</sup> and temperature 25°C.....	192
<b>Figure A.41</b> Engineering stress-strain curve for AA5182-O at strain rate average of 0.0019 s <sup>-1</sup> and temperature 25°C with 0.002 offset (for yield stress determination).....	193
<b>Figure A.42</b> True stress-strain curve for AA5182-O at strain rate average of 0.0019 s <sup>-1</sup> and temperature 25°C.....	193
<b>Figure A.43</b> Engineering stress-strain curve for AA5182-O at strain rate average of 0.0031 s <sup>-1</sup> and temperature 25°C with 0.002 offset (for yield stress determination).....	194
<b>Figure A.44</b> True stress-strain curve for AA5182-O at strain rate average of 0.0031 s <sup>-1</sup> and temperature 25°C.....	194

<b>Figure A.45</b> Strain mapped as a function of time to determine average strain rate (slope) of the test for AA6061 at strain rate average of $0.0031 \text{ s}^{-1}$ and temperature $25^\circ\text{C}$ ..	195
<b>Figure A.46</b> Engineering stress-strain curve for AA5182-O at strain rate average of $0.0019 \text{ s}^{-1}$ and temperature $25^\circ\text{C}$ (0.084 mm/s).....	195
<b>Figure A.47</b> Strain mapped as a function of time to determine average strain rate (slope) of the test for AA5182-O at strain rate average of $0.0019 \text{ s}^{-1}$ and temperature $25^\circ\text{C}$ .....	196
<b>Figure A.48</b> Engineering stress-strain curve for AA6061 at strain rate average of $0.0013 \text{ s}^{-1}$ and temperature $25^\circ\text{C}$ with 0.002 offset (for yield stress determination).....	196
<b>Figure A.49</b> True stress-strain curve for AA6061 at strain rate average of $0.0013 \text{ s}^{-1}$ and temperature $25^\circ\text{C}$ .....	197
<b>Figure A.50</b> Strain mapped as a function of time to determine average strain rate (slope) of the test for AA6061 at strain rate average of $0.0013 \text{ s}^{-1}$ and temperature $25^\circ\text{C}$ ..	197
<b>Figure A.51</b> Temperature Time Gradient of AA5182-O from $25^\circ\text{C}$ to $-160^\circ\text{C}$ in the MTS Tensile Testing Machine Environmental Chamber.....	198
<b>Figure A.52</b> Plot of (a) $ds/de$ as a function of strain and (b) $ds/de$ as a function of Stress from tensile testing data at $25^\circ\text{C}$ and initial cross-head velocity of 0.084 mm/s.....	199
<b>Figure A.53</b> Plot of (a) $ds/de$ as a function of strain and (b) $ds/de$ as a function of Stress from tensile testing data at $-40^\circ\text{C}$ and initial cross-head velocity of 0.084 mm/s.....	200
<b>Figure A.54</b> Plot of (a) $ds/de$ as a function of strain and (b) $ds/de$ as a function of Stress from tensile testing data at $-80^\circ\text{C}$ and initial cross-head velocity of 0.084 mm/s.....	201
<b>Figure A.55</b> Plot of (a) $ds/de$ as a function of strain and (b) $ds/de$ as a function of Stress from tensile testing data at $-120^\circ\text{C}$ and initial cross-head velocity of 0.084 mm/s..	202
<b>Figure A.56</b> Plot of (a) $ds/de$ as a function of strain and (b) $ds/de$ as a function of Stress from tensile testing data at $-160^\circ\text{C}$ and initial cross-head velocity of 0.084 mm/s..	203
<b>Figure A.57</b> Plot of (a) $ds/de$ as a function of strain and (b) $ds/de$ as a function of Stress from tensile testing data at $-196^\circ\text{C}$ and initial cross-head velocity of 0.084 mm/s..	204
<b>Figure A.58</b> True Stress Strain Curve for aluminum alloy AA5182 obtained at $120^\circ\text{C}$ and 0.002 offset of elastic region; respective strain rate $1.9 \times 10^{-3} \text{ s}^{-1}$ .....	205
<b>Figure A.59</b> True Stress Strain Curve for aluminum alloy AA5182 obtained at $120^\circ\text{C}$ and 0.002 offset of elastic region; respective strain rate $1.9 \times 10^{-3} \text{ s}^{-1}$ .....	206
<b>Figure A.60</b> True Stress Strain Curve for aluminum alloy AA5182 obtained at $120^\circ\text{C}$ and 0.002 offset of elastic region; respective strain rate $1.9 \times 10^{-3} \text{ s}^{-1}$ .....	207

<b>Figure A.61</b>	Drawing of specimen #1 for sheet metal formability testing.....	209
<b>Figure A.62</b>	Drawing of specimen #2 for sheet metal formability testing.....	209
<b>Figure A.63</b>	Drawing of specimen #3 for sheet metal formability testing.....	210
<b>Figure A.64</b>	Drawing of specimen #4 for sheet metal formability testing.....	210
<b>Figure A.65</b>	Drawing of specimen #5 for sheet metal formability testing.....	211
<b>Figure A.66</b>	Drawing of specimen #6 for sheet metal formability testing.....	211

# Nomenclature

<i>AA5182-O</i>	Aluminum alloy containing 5% magnesium, annealed (O) selected for this study
$\Delta T$	Temperature difference (K)
<i>LN<sub>2</sub></i>	Liquid nitrogen
<i>r</i>	Radius (mm)
<i>L</i>	Length (mm)
$\sigma_y$	Predicted yield strength of the material (MN m <sup>-2</sup> )
$\alpha$	Linear coefficient of thermal expansion (MK <sup>-1</sup> )
$\varepsilon_s$	Mismatch parameter
<i>C</i>	Solute concentration
$\sigma_o$	Frictional stress (MPa)
<i>k</i>	Petch slope (MNm <sup>-3/2</sup> )
<i>d</i>	Grain size ( $\mu\text{m}$ )
$\sigma_{YS}$	Yield stress
$\sigma_{UTS}$	Ultimate tensile stress
<i>E</i>	Young's modulus
<i>F</i>	Force (N)
<i>A<sub>0</sub></i>	Area (mm <sup>2</sup> )
<i>R</i>	Lankford coefficient
$\varepsilon_y^p$	In-plane plastic strain
$\varepsilon_z^p$	Through-thickness plastic strain
$\sigma$	Stress in the plastic region (MPa)
<i>K</i>	Strength coefficient

$\epsilon$	True strain
$m$	Strain rate sensitivity
$\dot{\epsilon}$	Strain rate ( $s^{-1}$ )
$\sigma_t$	Thermal stress
$\sigma_a$	Athermal stress
$n$	Strain hardening exponent
wt%	Weight percent

# Abbreviations

<i>AA</i>	Aluminum Association
<i>BCC</i>	Body-centered cubic
<i>CGA</i>	Circle grid analysis
<i>DSA</i>	Dynamic strain ageing
<i>EDS</i>	Energy-dispersive x-ray spectroscopy
<i>FCC</i>	Face-centered cubic
<i>FLC</i>	Forming limit curve
<i>FLD</i>	Forming limit diagram
<i>LYP</i>	Lower yield point
<i>nSRS</i>	Negative strain rate sensitivity
<i>OM</i>	Optical microscopy
<i>PLC</i>	Portevin Le Chatelier
<i>RD</i>	Rolling direction
<i>RT</i>	Room temperature (25°C)
<i>SEM</i>	Scanning electron microscopy
<i>SRS</i>	Strain rate sensitivity
<i>TTT</i>	Time temperature transformation
<i>UTS</i>	Ultimate tensile stress
<i>UE</i>	Uniform elongation
<i>UYP</i>	Upper yield point

# 1 Introduction

## 1.1 Motivation

Modern automotive and aircraft industries are strongly advocating for the usage of advanced lightweight alloys for structural components. The application of high strength-to-weight ratio metal alloys offers emission reductions without having to compromise on safety or performance. Aluminum alloys are widely used in the automotive and aircraft industry due to their strength, weldability, and corrosion resistance [1]. The benefits of using aluminum alloys also include the reduction of body weight and, as a result, an improvement to a component's fuel economy and reduction of greenhouse gas emissions [2]. Specifically, AA5xxx-series aluminum alloys, which are aluminum alloys that contain magnesium as the primary alloying element, have been known to improve the strength-to-weight ratio when compared to mild steel on the order of 3:1 [3]. Al-Mg alloys, such as AA5182-O aluminum alloys, are extensively used for the inner body panels of vehicles. However, compared to most modern steels, aluminum alloys have very low formability [4]. In **Figure 1.1**, it can be seen that aluminum alloys typically exhibit fracture elongation values that fall well below the fracture elongation of modern steels, such as dual-phase steels and bake-hardening steels, at comparable yield strength values [5].

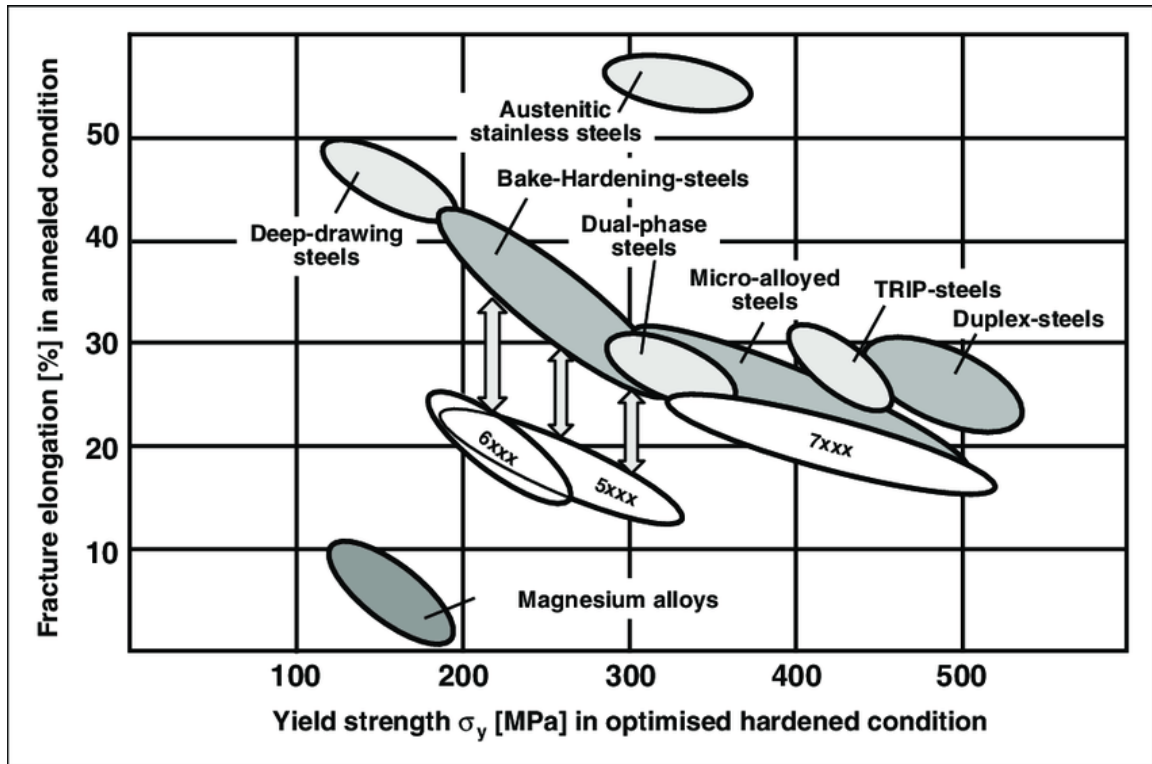


**Figure 1.1** Fracture elongation versus yield strength for aluminum magnesium alloys compared to modern steels in automotive applications [5].

There are many ways to improve the low formability of aluminum. Past methods have included incremental forming [6-8], electromagnetic forming [9, 10], and hydro forming [11]. Each of these methods are often evaluated with their own specific set of process parameters and tested under different process conditions. Some methods of forming aluminum include testing at different temperature conditions, such as cold (room temperature) forming [12, 13], warm forming [14, 15] or hot forming [16, 17]. However, each method comes with its drawbacks. When forming aluminum at room temperature, visual bands caused by discontinuous deformation can cause a serious cosmetic issue for manufactured products [18]. During warm [19, 20, 21] and hot [22, 23] conditions, aluminum will gain the necessary formability properties that are required to prevent these visual bands, but it will also result in an undesirable loss of strength for forming and subsequent use. This loss of strength is a result of induced recrystallization and recovery mechanisms. Kim et al. [24] performed warm U-draw bending tests on a AA5182

aluminum alloy with strain rates varying from  $5 \times 10^{-4} \text{ s}^{-1}$  to  $10^{-1} \text{ s}^{-1}$  and at temperatures ranging from  $25^\circ\text{C}$  to  $450^\circ\text{C}$ . **Figure 1.2** shows the true stress versus temperature curves at two plastic strains of 0.1 and 0.2. It is observed that as temperature increases, the flow stress of the material decreases. For a strain rate of  $5 \times 10^{-4} \text{ s}^{-1}$ , and comparing a testing temperature of  $25^\circ\text{C}$  to  $250^\circ\text{C}$ , the true stress of the material is reduced by almost 60% [24].

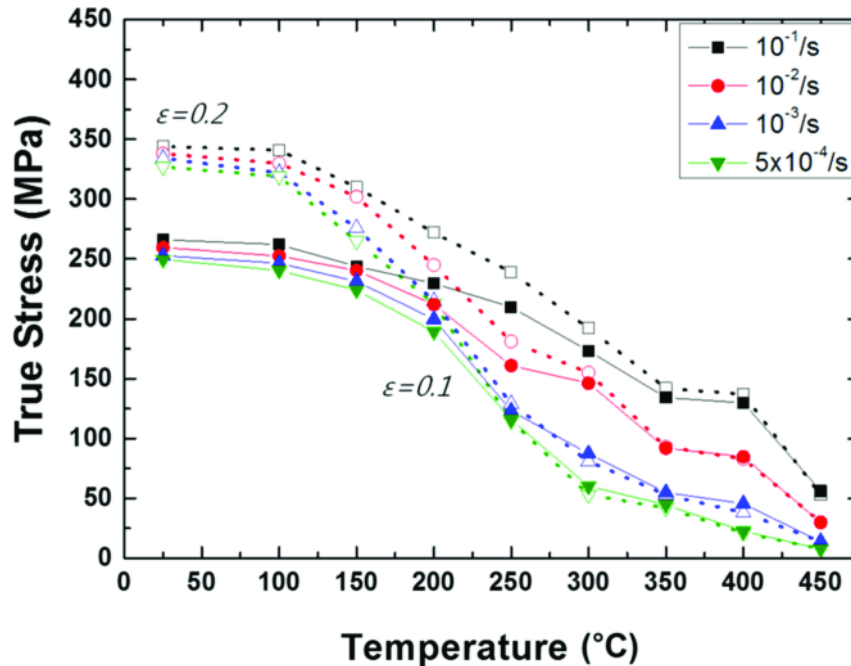


**Figure 1.2** Flow stresses measured from true stress-strain curves at plastic strains of 0.1 and 0.2 mapped as a function of temperature for AA5182 aluminum alloy [24].

During hot forming, there can also be difficulties related to transferred material, such as adhesion and galling [25], which cause major drawbacks due to the reduction in tool life that can be caused by this adhesive wear [26]. There are also difficulties associated with high temperature lubricants, as high temperatures are a main influence towards the degradation of lubricants and the resultant reduction in anti-wear properties [27]. Difficulties related to hot forming of aluminum alloys can also include failure of dies, such as cracks, thermal fatigue or plastic deformation caused by hot working dies [28, 29].

To avoid issues such as tooling degradation and damage, caused by warm and hot forming, new research has involved low temperature forming of aluminum alloys. In these papers, aluminum alloys are tested at temperatures that drop to 77 K (-196°C) and tensile elongation values are observed to increase by approximately 100% percent, as well as an increase in the ultimate tensile stress of approximately 100% at 77 K (-196°C) [30]. Although there are numerous papers that show the enhancement of strength and ductility for aluminum alloys at low temperatures [30, 31, 32, 33] there is little known as to why this enhancement transpires and the micro-mechanisms that are occurring during this process.

## 1.2 Objectives of Research

The primary objective of this study is to demonstrate the enhanced mechanical behaviour of aluminum alloy AA5182 at subzero temperatures. This objective involves the quantitative analysis of the plastic deformation of AA5182 sheets subjected to tensile testing at temperatures of 25 to -196°C to determine the magnitude of ductility and strength improvement. Secondary objectives of this research include:

1. Interpretation of the mechanical properties (such as work hardening) at sub-zero temperatures to understand the mechanisms behind the change in fracture behaviour.
2. Interpretation of the fracture surfaces and investigation into the failure mechanisms of AA5182 sheets subjected to tensile testing at subzero temperatures.
3. Investigation of the effect of temperature on the crystal structure using Cottrell-Stokes's method of examining flow stress at two different temperatures for the same dislocation distribution.

## 1.3 Structure of Subsequent Chapters

Chapter 2 of this thesis introduces the background and motivation for this research. This involves the discussion of 5xxx-series wrought aluminum alloys, the chemical composition of the aluminum alloy that is being studied, and details regarding second phase particles and damage mechanisms for these alloys. The Portevin Le-Chatelier (PLC) effect is then reviewed, with discussions on strain rate sensitivity, dynamic strain aging, and the deformation instability for Al-Mg alloys. The next section of Chapter 2 presents details on Cottrell-Stokes's testing methods, including both temperature change and strain rate change tensile testing. The final section of this chapter details sub-zero temperature tensile testing from 25 to -196°C. Chapter 3 outlines the necessary procedures to complete the preparation and testing of the study, such as initial material characterization, methods for room temperature and sub-zero temperature strain measurements with a low temperature extensometer, and methods for Cottrell-Stokes's testing. The results are then provided in Chapter 4 and thoroughly discussed in Chapter 5. Chapter 6 concludes on the study and provides some new insights and interprets the results of the study. The research concludes that forming aluminum alloy AA5182 at subzero temperatures enhances the formability and some mechanical behaviors and suggests some reasons for changes in the fracture behaviour. At the end of this chapter, suggestions are made for future research. The appendix provides further data and calculations to support the results (such as more stress-strain curves and measurements from dimple characterization).

## 2 Literature Review

### 2.1 5xxx-Series Aluminum Alloys

#### 2.1.1 Alloying Elements, Chemical Composition, and Mechanical Properties

Aluminum alloys where magnesium is used as the primary alloying element are classified as 5xxx-series aluminum alloys. Magnesium is one of the most widely used alloying elements for aluminum, ranging from 0.8 wt% to over 5 wt% magnesium content [34]. **Table 2.1** shows a list of common 5xxx-series aluminum alloys with respect to their magnesium content.

**Table 2.1** Aluminum Association (AA) numbers and nominal compositions of common 5xxx-series aluminum alloys [35].

AA number	Composition, %							
	Al	Si	Cu	Mn	Mg	Cr	Zn	Others
5005	99.2	...	...	...	0.8	...	...	...
5050	98.6	...	...	...	1.4	...	...	...
5052	97.2	...	...	...	2.5	0.25	...	...
5056	95.0	...	...	0.12	5.0	0.12	...	...
5083	94.7	...	...	0.7	4.4	0.15	...	...
5086	95.4	...	...	0.4	4.0	0.15	...	...
5154	96.2	...	...	...	3.5	0.25	...	...
<b>5182</b>	<b>95.2</b>	...	...	<b>0.35</b>	<b>4.5</b>	...	...	...
5252	97.5	...	...	...	2.5	...	...	...
5254	96.2	...	...	...	3.5	0.25	...	...
5356	94.6	...	...	0.12	5.0	0.12	...	0.13 Ti
5454	96.3	...	...	0.8	2.7	0.12	...	...
5456	93.9	...	...	0.8	5.1	0.12	...	...
5457	98.7	...	...	0.3	1.0	...	...	...
5652	97.2	...	...	...	2.5	0.25	...	...
5657	99.2	...	...	...	...	...	...	...

The addition of magnesium as a primary alloying agent for aluminum provides considerable solid solution strengthening and an improvement to the strain hardening ability [36]. Solid solution hardening is the process of dissolving soluble elements in a metal matrix for the purpose of improving the matrix strength. The misfit of atomic radius in comparison to the original polycrystalline matrix results in an inhibition of dislocation movement and a subsequent increase in strength that is attained through the distortion of the atomic lattice. **Figure 2.1** shows the tensile yield stress and elongation of some commercial aluminum-magnesium alloys as a function of their magnesium content [37].

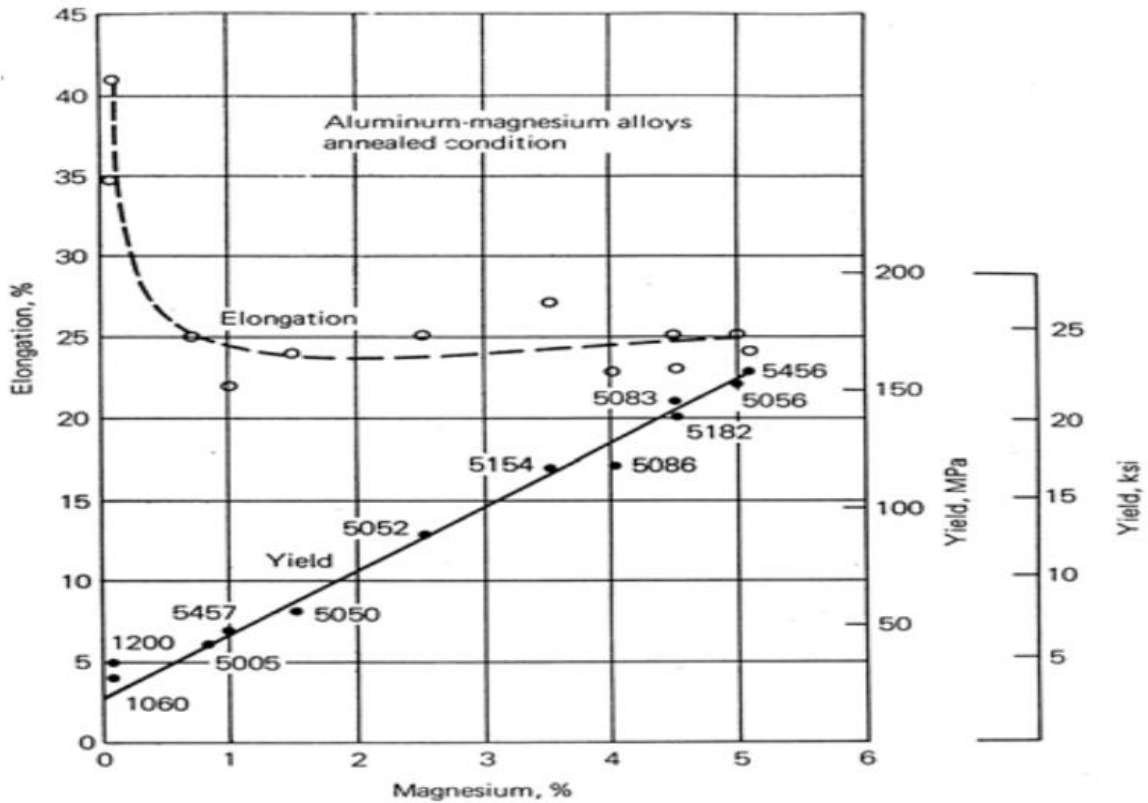


**Figure 2.1** Correlation between tensile yield stress and elongation as a function of magnesium content for some commercial aluminum-magnesium alloys in annealed condition [37].

As shown in the plot, the yield stress of 5xxx-series aluminum alloys increases linearly with magnesium content, as a result of solid solution hardening. In this process, the difference in size, stiffness, and charge between the solute atoms and the solvent atoms can cause resistance when the dislocations interact with the non-uniform lattice. Although the model of solid solution hardening is complex, Ashby et al. [38], predicts the yield stress through the following relation,

$$\sigma_y = \alpha \varepsilon_s^{\frac{3}{2}} C^{\frac{1}{2}} \quad (1)$$

where  $\sigma_y$  is the predicted yield stress of the material ( $\text{MN m}^{-2}$ ),  $\alpha$  is the linear coefficient of thermal expansion ( $\text{MK}^{-1}$ ),  $\varepsilon_s$  is the mismatch parameter, and  $C$  is the solute concentration. In this equation, it can be seen that the yield stress is proportional to the

concentration of solute atoms and is also dependent on the mismatch of the original metal atoms and primary alloying element atoms. If the solute and solvent atoms are badly matched, the dislocations will experience a higher resistance of motion. As well, if the concentration of solutes is increased, the obstruction to dislocation motion will also increase. This relationship can be further developed through combining solute concentration along with the grain size.

The primary factor controlling the strength of fully annealed 5xxx-series aluminum alloys is the grain size and solution hardening [39]. The following relationship can be broken down from equation (1),

$$\sigma_y \propto (C)^{1/2} \quad (2)$$

Although the yield stress sees a stronger increase when supersaturated Mg compositions (above 1.8%) are used, the stress in 5xxx-series aluminum alloys can also be fairly characterized by the linear relationship between yield stress and the Mg content [39],

$$\sigma_y \propto B \text{ (wt\% Mg)} \quad (3)$$

where  $B$  is approximately equal to 15 MPa. The Hall-Petch equation [40], which gives the quantitative description of the inverse relationship between the yield stress and grain size is given by,

$$\sigma_y = \sigma_o + kd^{-1/2} \quad (4)$$

where  $\sigma_o$  gives the frictional stress, inclusive of any solution hardening,  $d$  represents the grain size and  $k$  is the Petch slope; a constant showing the strength of the barrier to dislocation motion [41, 42]. The combination of Hall-Petch law along with the linear relationship of the Mg content, gives the strength for fully annealed 5xxx-series aluminum alloys as,

$$\sigma_y = \sigma_o + B \text{ (wt\% Mg)} + kd^{1/2} \quad (5)$$

and can be used to further describe the relationship between the strength of Al-Mg alloys, solutes, and grain size hardening.

Due to variable processing conditions, some of these values can fluctuate, but can be approximated as  $\sigma_o = 5\text{-}10\text{MPa}$ ,  $B = 15\text{MPa}$ , and  $k = 0.1\text{-}0.3\text{MNm}^{-3/2}$ , dependent on Mg content.

Lloyd [39] predicted the yield stress of three 5xxx-series aluminum alloys in the following plot, **Figure 2.2**. In this plot, experimental yield stress values are compared to values obtained using the predictive model developed in equation (5).

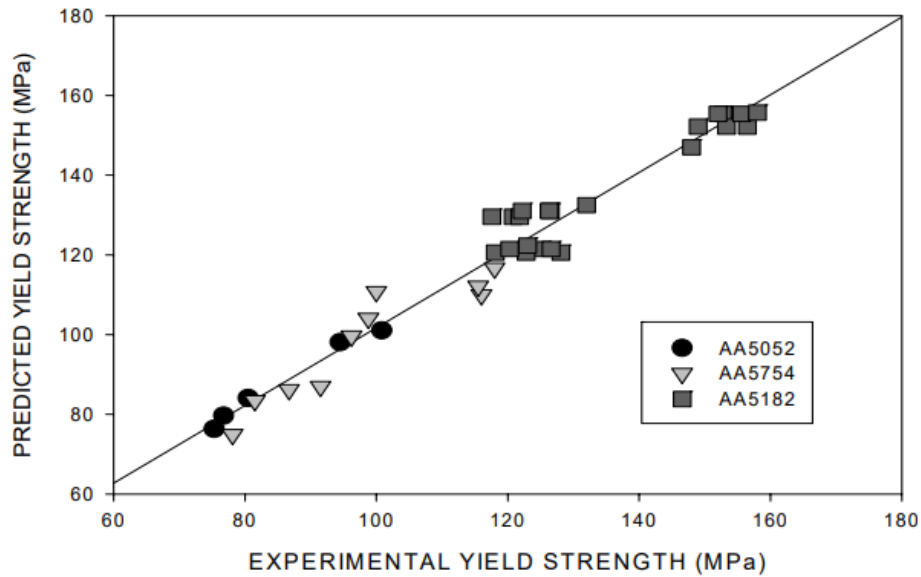


**Figure 2.2.** Comparison of a model for grain size and solution strengthening and experimental yield stress values for AA5052, AA5754, and AA5182 aluminum alloys [39].

The binary Al-Mg phase diagram can also be used to understand the process of solution hardening. **Figure 2.3** shows the aluminum end of the Al-Mg phase diagram [43]. At room temperature and equilibrium, aluminum is capable of dissolving up to 1.8 wt% of Mg. If the aluminum alloy contains more than 1.8 wt% Mg in solid solution at room temperature, the alloy is said to be in a state of supersaturation. In this diagram, the supersaturation of a 5.5 wt% of Mg in solid solution at room temperature can be calculated as followed,

$$5.5 - 1.8 = 3.7 \text{ wt\% supersaturation}$$

As previously shown in **Figure 2.1**, the supersaturation of Mg in Al gives a significant increase to the material's yield stress, this can also be seen in **Table 2.2**, which gives the yield stress of 5xxx-series (Al-Mg) alloys along with the respective wt% of Mg [44]. The heat treatment required to obtain this amount of supersaturation can be observed in **Figure 2.4**, which gives the time-temperature-transformation (TTT) diagram for the precipitation of  $Mg_5Al_8$  from an Al-Mg alloy with 5.5 wt% Mg solid solution treatment [45]. First, the solution is held at a temperature of 450°C. This step allows the Mg to dissolve in the Al, as shown by the single phase ( $\alpha$ ) field in the diagram. The solution treatment line shows that if the solution is allowed to cool moderately quickly, the nose of the C-curve will be avoided, and the solution will remain supersaturated. The Al-Mg phase diagram is further reviewed and discussed in **Section 2.1.2**.

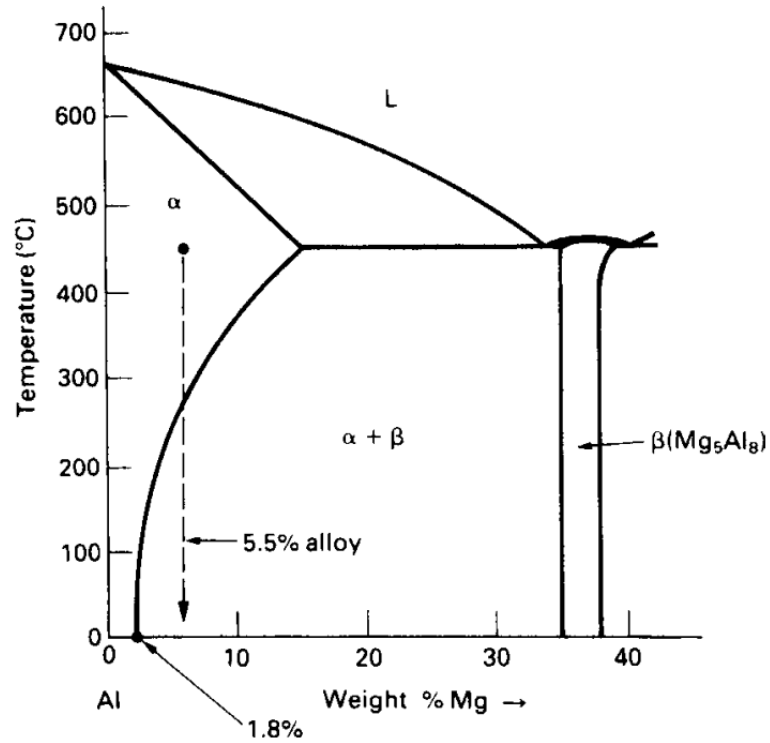


**Figure 2.3** Aluminum side of the Al-Mg binary phase diagram [43].

**Table 2.2** Yield stress of 5xxx-series (Al-Mg) alloys with respective (wt% Mg) [44].

Alloy	(wt% Mg)	$\sigma_y$ (MPa) (annealed condition)
5005	0.8	40
5050	1.5	55
5052	2.5	90
5454	2.7	120
5083	4.5	145
5456	5.1	160

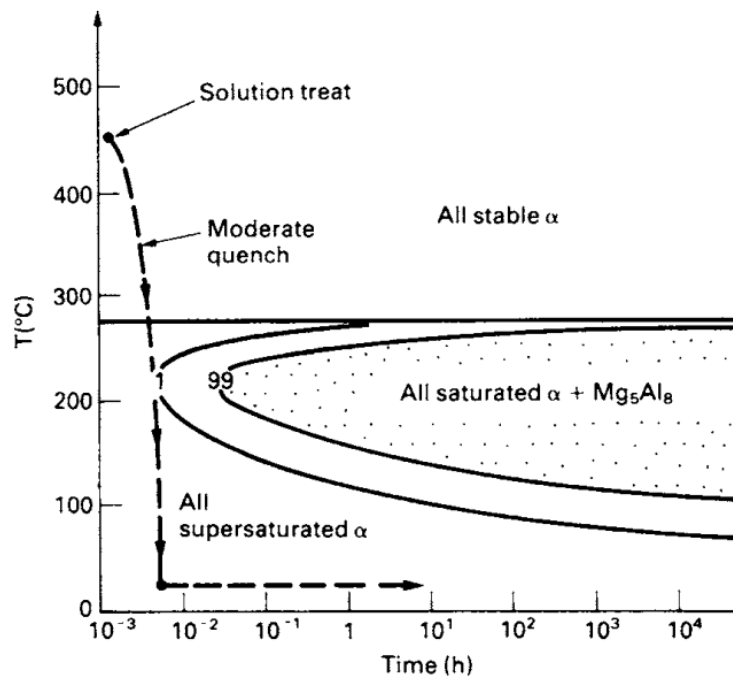


**Figure 2.4** TTT diagram for the precipitation of  $Mg_5Al_8$  from the Al-5.5 wt% Mg solid solution [45].

Although 5xxx-series alloys are not typically heat-treatable, they still exhibit high strength to density ratios, high young's modulus to density ratios, and corrosion resistance in many environments. These mechanical properties result in their widespread use in automotive, aerospace, and shipbuilding applications [46]. There are other alloying elements as well, such as manganese, iron, and silicon which are typically added to 5xxx-series aluminum alloys. **Table 2.3** shows the range of chemical composition of AA5182 from literature from a more detailed perspective than given in **Table 2.1**. Some of these alloys are added for specific properties as discussed further in this chapter.

**Table 2.3** Range of chemical composition of various AA5182-O alloying elements in weight percent (The hyphen –O for an alloy refers to an alloy that has been annealed) [47].

Mg	Fe	Mn	Si	Zn	Cu	Cr	Ti	Al
4.0-5.0	0.35	0.2-0.5	0.2	0.25	0.15	0.1	0.1	Bal.

A summary of the mechanical properties, as well as some other characteristics of AA5182 aluminum alloys from published literature, are provided in **Table 2.4**. These values are used to compare the tested values for the as-received AA5182-O sheet material.

The first mechanical property that is listed for the material is yield stress. The yield stress is denoted by  $\sigma_{YS}$ , and describes the stress that a material can endure before experiencing permanent damage. For aluminum alloys, the method for calculating this value is often referred to as the 0.2% offset yield stress, or the 0.2% proof stress. This method involves creating a line parallel to the initial section of the stress-strain curve (prior to the occurrence of permanent damage), but offset by 0.002 mm/mm (0.2%) from the origin and provides the value of stress that will result in a plastic strain of 0.2%.

The second type of stress in the table is the tensile stress and is denoted by  $\sigma_{UTS}$ . This is the value of stress that is required to change from a state of uniform plastic deformation, into a state of concentrated local deformation (necking). This value will be the highest point of the stress-strain curve and is calculated by taking the maximum applied force over the cross-sectional area of the tested specimen,

$$\sigma_{UTS} = \frac{F}{A_0} \quad (6)$$

The young's modulus, also referred to as modulus of elasticity or elastic modulus, relates to the stiffness of a material. The young's modulus is denoted by  $E$  and can be calculated by taking the slope of the initial section of the curve, prior to the yield stress being reached. The young's modulus equation is as follows,

$$E = \frac{\text{tensile stress}}{\text{tensile strain}} = \frac{FL}{A\Delta L} \quad (7)$$

Anisotropy describes a material's directional dependence of its mechanical properties. The Lankford coefficient, also referred to as the R-value, Lankford value, or the plastic strain ratio [48], is a value used to indicate the mechanical anisotropy of rolled sheet metal. The Lankford coefficient is given by,

$$R = \frac{\epsilon_y^p}{\epsilon_z^p} \quad (8)$$

where  $\epsilon_y^p$  is the in-plane plastic strain, perpendicular to the loading direction. The through-thickness plastic strain is given by  $\epsilon_z^p$ . For sheet metals, the Lankford coefficient is typically found in three directions of in-plane loading:  $0^\circ$  (parallel to the loading direction,  $45^\circ$ , and  $90^\circ$  (perpendicular to the loading direction). In tensile testing experiments, the Lankford coefficient is commonly measured at 20% elongation of the tested specimen [49].

Strain at maximum load, or uniform strain/elongation, is defined as the value of strain at which the material reaches the ultimate tensile stress during tensile testing. The fracture elongation, or fracture strain, is the value of strain at which the tested material fails or fractures.

The formula used to find the strength coefficient of a material is given by,

$$\sigma = K\epsilon^n \quad (9)$$

where  $\sigma$  gives the stress in the plastic region (MPa),  $K$  represents the strength coefficient equal to the true stress at a true strain value that is equal to 1,  $\epsilon$  is the true strain, equal to  $\ln(1+e)$ , and  $n$  gives the strain hardening exponent.

**Table 2.4** Mechanical property values for AA5182-O aluminum from literature at 25°C.

<b>Property</b>	<b>Nomenclature</b>	<b>Unit</b>	<b>Value</b>	<b>Reference</b>
Yield stress	$\sigma_{YS}$	MPa	130	[30, 50]
Tensile stress	$\sigma_{UTS}$	MPa	275	[30, 50]
Young's modulus	$E$	GPa	69	[30, 50]
Lankford coefficient	$R$	--	0.836	[49]
Uniform elongation	$e_u$	%	23.7	[30, 50]
Fracture elongation	$e_f$	%	26.5	[30, 50]
Strength coefficient	$K$	--	560	[51]
Strain hardening exponent	$n$	--	0.317	[51]

Like magnesium, manganese is added to aluminum alloys to provide an increase in strength through solid solution hardening without noticeably reducing the passivity of the aluminum or the ductility [52]. Manganese also provides an improvement to the strain hardening ability [53]. Mn, Fe, Cr, and Si alloying elements often improve material production and product weldability [54]. The addition of Mn and Cr also act as grain growth stabilizers [55, 56]. Other alloying elements, such as Fe and Si, can also help to somewhat strengthen the alloy, but can also significantly influence the damage mechanisms and fracture behavior [57]. In most aluminum alloys, Fe is found as an impurity [58]. In investigations involving quasi-static tension tests of Al-Mg alloys, Fe has been shown to negatively contribute to the formability of these alloys as both the fracture strain and ductility is significantly reduced [59].

The formability of a material can be considered in terms of limitations from both the initiation of localized strain and the fracture strain. The localized strain is defined as

the strain at which the ultimate tensile stress is reached, also referred to as the uniform strain. This is the strain at which necking will begin to initiate. In terms of formability, the tensile strain, or tensile elongation, is often denoting the total elongation of the material, inclusive of both the uniform strain and the strain from the point of necking to the point of final failure. The uniform strain is primarily influenced by material properties whereas the growth from necking to final failure, and as a result, the total elongation, is influenced by the specimen design. This influence is a direct result of the sensitivity of necking to the development of triaxiality stresses [60].

Another topic of importance in relation to formability, is the Considère criterion. The Considère criterion specifies that when the work hardening rate ( $d\sigma/d\varepsilon$ ) reaches the value of the flow stress,  $\sigma$ , the necking process can initiate and continue until final fracture [61]. The Considère criterion states,

$$\frac{d\sigma}{d\varepsilon} = \sigma \quad (10)$$

Aluminum alloys' uniform strain will typically exhibit a behavior that is in agreeance with the Considère criterion [62]. This criterion is further discussed in **Section 2.4**. **Figure 2.5** shows the work hardening plots for various aluminum alloys where the flow stress is expressed as  $(\sigma - \sigma_Y)$  to normalize the values with respect to diverse yield stress.

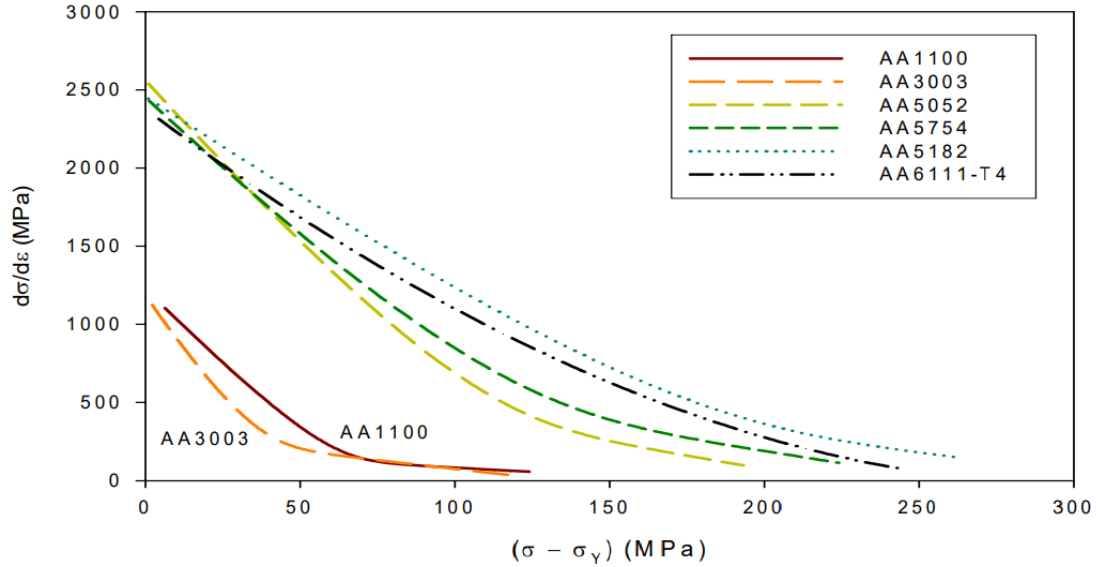


**Figure 2.5** Work hardening plots for various Al alloys, where the flow stress is expressed as  $(\sigma - \sigma_Y)$  to normalize the values with respect to diverse yield stress [60].

The above plot is referred to as Kocks-Mecking plot, where the strain hardening rate  $\theta = \frac{d\sigma}{d\varepsilon}$  is mapped as a function of flow stress [63]. This plot is often used to analyze the effect of solid solution strengthening in different Al alloys on the strain hardening behaviour of those alloys [64]. Solid solution additions to these Al alloys have been observed to influence the rate of dislocation storage by means of slowing down the rate of dynamic recovery (the gradual re-ordering and annihilation of stored dislocations) [65]. In the Kocks-Mecking plot this is demonstrated as a decrease in the slope, illustrating the relationship of the strain hardening coefficient on the flow stress (typically normalized with yield stress and expressed as  $(\sigma - \sigma_Y)$ ) [63].

Work hardening rate at the onset of necking is different for different Al alloys. In **Figure 2.5**, it can be observed that as the content of Mg in Al is increased, the rate of dynamic recovery decreases. Looking at Al-Mg alloy AA5182 in this plot, which has the highest amount of Mg content, the strain hardening rate  $\theta$  is typically higher at comparable flow stress values. It is not only the value of work hardening at high stresses that is notable in this plot, but also the rate at which the work hardening decreases as  $(\sigma - \sigma_Y)$  increases. For AA5182, it can be observed that the work hardening at high stresses is retained for

longer than some other alloys such as AA5754 or AA5052 which contain lower amounts of Mg addition [60].

5xxx-series aluminum alloys are alloys containing higher amounts of solutes when compared to AA1100 and AA3003, which are low solute alloys. The 5xxx-series alloys also display a higher work hardening rate, as the rate of dynamic recovery will decrease with increasing solute concentration [60]. This phenomenon is attributed to Mg solute drag and the interaction of pinning dislocations. The pinning of these dislocations inhibits their ability to rearrange and annihilate each other. The growth rate of the necking process is also associated with the strain rate sensitivity of the material. The influence of the strain rate sensitivity is further discussed in **Section 2.2.1**.

## 2.1.2 Second Phase Particles

The binary phase diagram of Al-Mg describes the different phases that are formed when mixing Al and Mg over a range of temperatures. In the Al-Mg phase diagram, as shown in **Figure 2.6**, up to approximately 5% of Mg can be completely dissolved in the aluminum matrix at a temperature over 190°C. At room temperature, aluminum has a face-centered-cubic crystal (FCC) structure and as indicated in **Figure 2.6**, a melting temperature of 660°C [66].

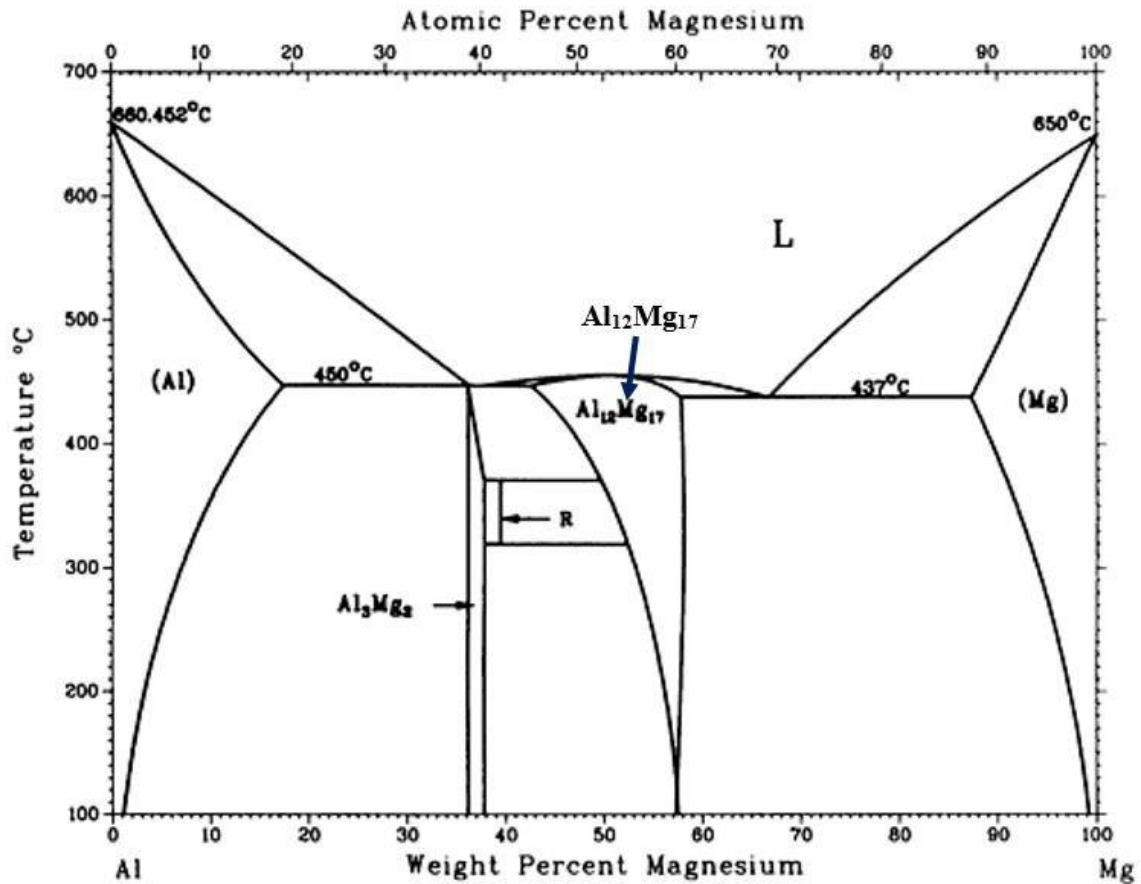


Figure 2.6 Aluminum magnesium binary phase diagram [66].

Aluminum will combine with transition metals such as manganese, chromium, or iron, which possess valence electrons that can readily form chemical bonds in two shells as opposed to only one. The combination of these metals forms intermetallic phases that exhibit little to no solubility in the aluminum matrix [67]. As a result, intermetallic phases can increase the strength of the matrix in two ways. These chemical compounds consisting of two or more metals work to enhance work hardening and refine the grain structure of the material [68]. Intermetallic phases, as incoherent structures within the matrix, increase work-hardening by acting as obstacles to the movement of dislocations. These compounds are usually nondeformable and dislocations are required to loop or bypass them. Subsequently, this process works to increase dislocation density as well as impedes dynamic recovery [67].

The equilibrium phases present in the Al-Mg phase diagram at 25°C include the Al solid solution, the  $\text{Al}_3\text{Mg}_2$ , also referred to as the  $\beta$  phase, at around 37 wt% Mg, compound R (rhombohedral structure present at 42 wt% Mg), compound  $\text{Al}_{12}\text{Mg}_{17}$ , and Mg solid solution [66]. At room temperature, the magnesium added to the aluminum alloy is frozen in solid solution. In equilibrium cooling, the rate of cooling is gradual enough to keep the phase composition uniform. This is typically the desired process of cooling as it keeps the microstructure consistent [69]. Below 190°C, the added magnesium forms a coherent beta prime phase,  $\beta'$ , with the aluminum. This  $\beta'$  prime phase appears in a fine dispersion in the aluminum matrix and is considered to be relatively stable [70]. The thermodynamically stable phase,  $\text{Al}_3\text{Mg}_2$ , as seen in the Al-Mg phase diagram in **Figure 2.6**, precipitates after considerable annealing at temperatures directly below 200°C [71].

As mentioned, the mechanical properties of the alloy are predominantly controlled by the Mg atoms in solid solution. At room temperature, these Al-Mg alloys exhibit non-uniform dislocation motion which manifests as serrations in stress-strain curves. The movement of these dislocations involve becoming temporarily arrested by forest obstacles and breaking away from these obstacles following thermal activation. Dislocations move fast between these obstacles [42]. If the dislocation diffusion time is equal to the dislocation arrest time, the dynamic strain ageing effect is shown to be at its maximum [71]. The interactions between these particles and dislocations are further discussed in **Section 2.2.2**.

However, there are also second phase particles that exist in aluminum alloy 5182 because of the addition of Si, Mn, Cr, and Fe elements [71]. Specifically, the addition of Si and Mg to aluminum produces a magnesium silicide,  $\text{Mg}_2\text{Si}$ , which is a well-known intermetallic particle found in AA5182 alloys [43]. The addition of Mn, Fe, and Cr to aluminum-magnesium alloys forms  $(\text{Mn,Fe})\text{Al}_6$ ,  $\text{Cr}_2\text{Mg}_3\text{Al}_{18}$  and  $\text{FeCrAl}_3$  precipitates [72]. The characterization of second phase particles and their effects on aluminum alloys is significant as they often provide damage nucleation sites that can limit the formability of aluminum alloys [73].

### 2.1.3 Damage Mechanisms

The plastic deformation and failure mechanisms of 5xxx-series aluminum alloys can be influenced by the chemical composition, second phase particles and overall microstructure of the alloy, as well as the applied strain rate and temperature conditions [74]. As mentioned, the addition of Fe to aluminum alloys can reduce both the ductility and the fracture strain during quasi-static tension tests. The presence of Fe as an impurity, results in a decrease in the amount of manganese that can dissolve in aluminum. This reduction in solubility then causes an increase in the formation of large  $\text{Al}_6\text{Mn}$  particles which, due to its size, can provide potential crack initiation sites and subsequently lead to a decrease in ductility [58, 75].

The existence of second phase particles can also contribute to an effect on the failure mechanisms of aluminum alloys. Pilkey, et al. [76] studied particle contributions in aluminum alloy systems and showed that distribution of second phase particles in these alloys are appreciably inhomogeneous in both size and spacing. When there are no pre-existing defects that can cause failure in the material, the fracture process for metals that are subjected to uniaxial tension will initiate by the nucleation of voids in regions of higher triaxial stress [77]. This nucleation of voids, or nucleation of internal cavities, will most often propagate at microstructural heterogeneities [59]. It is well established that these intermetallic particles and precipitates will provide damage nucleation sites during material loading, as the interface between particle and matrix can often be weak [78-80]. The failure of aluminum alloys is predominantly a result of ductile fracture caused by the existence of second phase particles and their promotion of coalescence of voids, or their ability to act as obstacles in front of shear zones [81].

Ductile fracture describes a failure of a material that is characterized by necking or by extensive plastic deformation. It involves a slow rate of propagation and the absorption

of large amounts of energy before fracture occurs [82]. These types of failures are often not as catastrophic as brittle fracture but are still significant and can occur in a range of applications from forming sheet metal for automotive bodies to the rupture of oil and gas pipelines [83].

Ductile fracture is often viewed as occurring in three main stages, as shown in **Figure 2.7**. As a metal is stretched, plastic flow in the material will result in necking and the initiation of voids around weak regions inside the structure. Subsequently, these voids will then grow and join together through void coalescence. The coalescence of voids will catalyze a ductile crack through the material and lead to fracture [84].

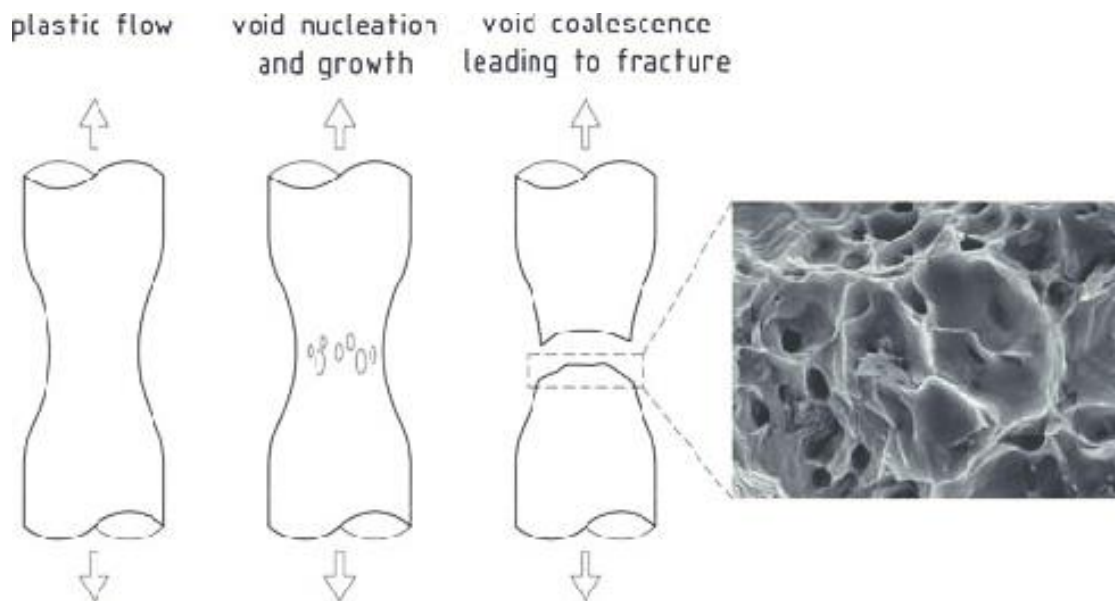


**Figure 2.7** Micro mechanisms for ductile fracture with accompanying SEM image [85].

The nucleation of voids at second phase particles can occur through the process of particle cracking, decohesion between the matrix and particles, and shear deformation. **Figure 2.8(a)** shows the decohesion of the particle-matrix interface and **2.8(b)** shows the fracture of a brittle particle. In both mechanisms, the fracture surface will contain dimples with spherical and elliptical shapes. **Figure 2.8(c)** shows another possible mechanism for void nucleation, where decohesion is caused by shear deformation or by sliding grain

boundaries. Unlike the first two mechanisms, shear deformation will result in a fracture surface that contains parabolic shaped dimples [59].

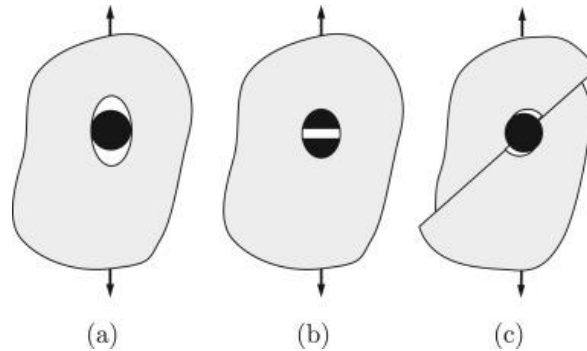


**Figure 2.8** Mechanisms of void nucleation around inclusions through (a) decohesion between particle and the matrix, (b) particle cracking, and (c) shear deformation [59].

Ductile failure can also be categorized by the severity of ductility, the mechanisms of void coalescence, and the type of loading on the material. Tekoglu et. al. [86] investigated void coalescence and localization as a precursor to ductile fracture and describes 5 main mechanisms. A material that exhibits ductile fracture can be classified as highly ductile or moderately ductile. In cases for very pure metals, the mechanism of failure is sometimes described as highly ductile, where the evidence of a ductile fracture is clear both macroscopically and microscopically. As a result of the lack of void nucleation sites, these pure metals fail by localized plastic flow. In this case, the mechanism falls into the first category where the plastic flow can either localize through a large extent of necking on the tensile specimen, also called diffuse necking, or in a shear band. **Figure 2.9(a)** illustrates both types of failure by localized plastic flow.

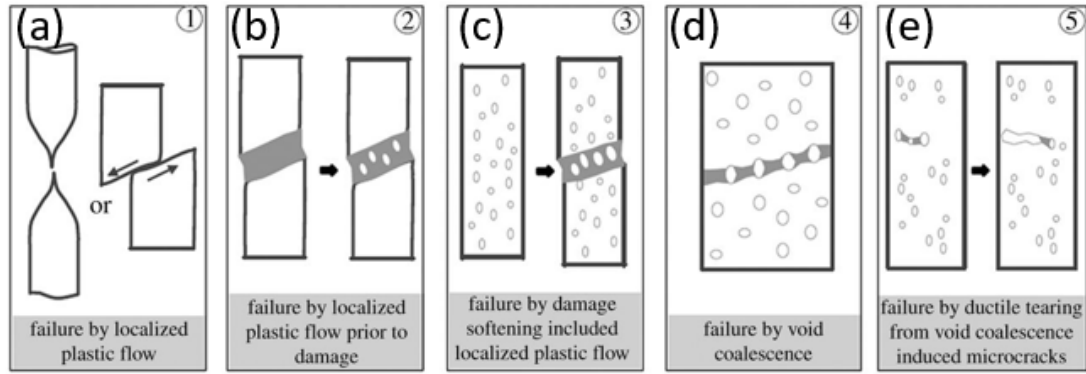


**Figure 2.9** Five mechanisms for ductile fracture in polycrystalline materials including failure by (a) localized plastic flow, (b) localized plastic flow prior to damage, (c) damage softening, (d) void coalescence, and (e) ductile tearing [86].

The second mechanism, **Figure 2.9(b)**, also involves localized plastic flow. In this scenario, plastic strain is localized into shear bands, which can result from several softening, or recovery, mechanisms [87]. In this case, voids can nucleate and coalesce until fracture of the material, but the localized plastic flow will occur prior to any void nucleation [88].

The third mechanism for failure, as shown in **Figure 2.9(c)**, is also dominated by macroscopic plastic localization. This type of failure involves nucleation of damage in the material, softening of the material because of damage porosity, and the formation of plastic localization as a narrow band. Macroscopically, this type of mechanism typically shows dimples because of enlarged voids, and disconnections between the voids as a result of large shear distortions [86].

The last two mechanisms are dominated by void coalescence failure and share similar characteristics. Mechanism 4, **Figure 2.9(d)**, is a typical failure by void coalescence. In this case, coalescence occurs simultaneously with plastic-flow localization and dictates the onset of the macroscopic localization. Mechanism 5, **Figure 2.9(e)**, involves clusters of void growth and coalescence of voids, microcrack propagation, and final failure by ductile tearing of the material [86].

Aluminum alloys can experience a ductile tensile, shear fracture, or combination of the two. Shear fracture, also referred to as a slip surface, is characterized as plastic

deformation that is concentrated in a cross-diagonal localized necking zone [89]. This necking quickly develops into a shear fracture [90]. For 5xxx-series aluminum alloys, studies have shown that shear deformation will often occur alongside of localized through-thickness bands, also called Portevin Le-Chatelier (PLC) bands [91, 92]. This localized plastic strain is macroscopically observed in the form of bands moving along the specimen. These PLC bands and their mechanisms are discussed further in **Section 2.2**.

**Figure 2.10** [93] shows the characteristics typical of uniaxial tensile loads, where **(a)** shows a schematic of failure by void growth and coalescence due to applied uniform stress, and **(b)** shows a scanning electron fractograph of spherical dimples. These fractographs typically involve flat dimple ruptures, where the mechanism for the final failure is necking and fracture of the intervoid ligaments [94]. **Figure 2.10(c)** and **(d)** show a case ductile fracture resulting from shear loading, where the scanning electron fractograph exhibits parabolic-shaped dimples. In these scenarios, shear deformation occurs at a  $45^\circ$  angle at the outer perimeter of the necking region. Other characteristics of a ductile fracture can include the central region of the fractured surface appearing as irregular or fibrous as a result of plastic deformation, and spherical dimples in the center with c-shaped elongated dimples in the outer perimeter [95].

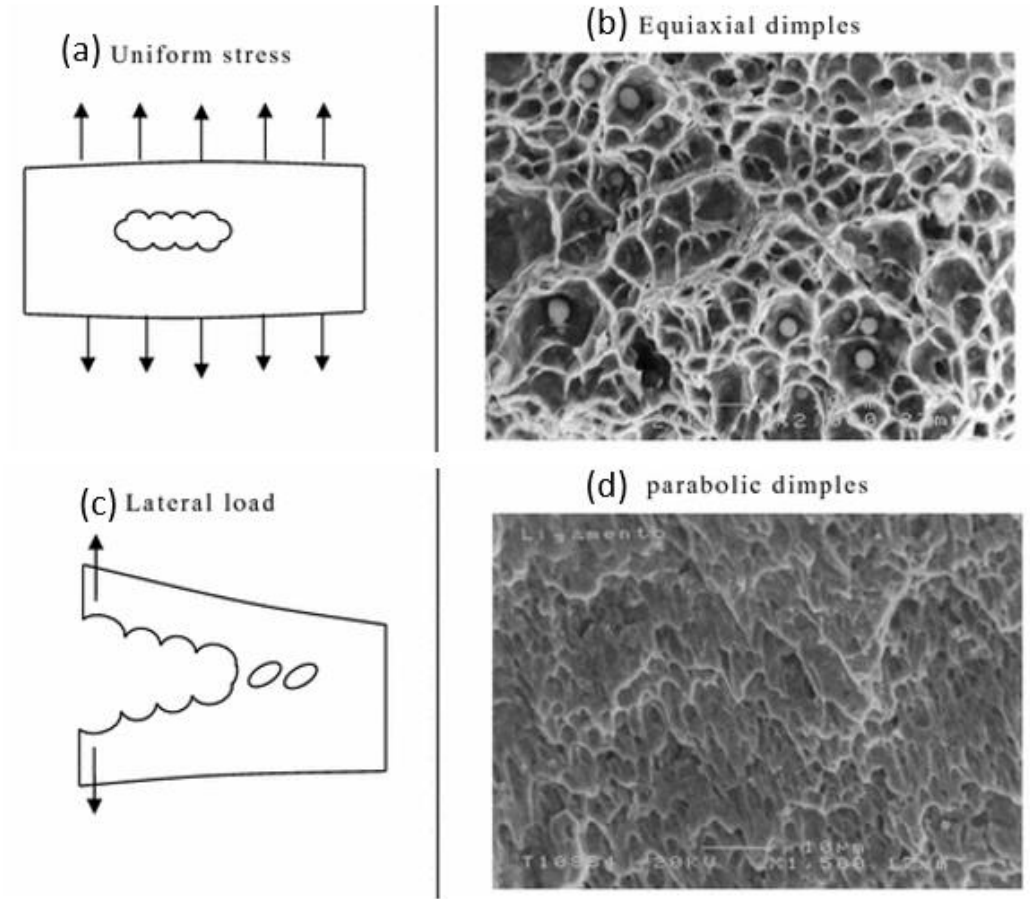


**Figure 2.10** Schematics and SEM micrographs showing (a) ductile (uniaxial) fracture under tensile load and (b) fracture surface with spherical dimples and (c) lateral load causing tearing with (d) parabolic dimples that are characteristic of ductile tears or shear loading [93].

**Figure 2.11(a)** and **2.11(b)** show cross-sectional reduction of a 5xxx-series aluminum alloy specimen and a schematic of cross-sectional reduction co-occurring with shear deformation respectively [5]. In these schematics, these bands are typically orientated around a  $\pm 55^\circ$  direction to the principal normal stress. The PLC effect, along with these subsequent bands, are further discussed in **Section 2.2**.

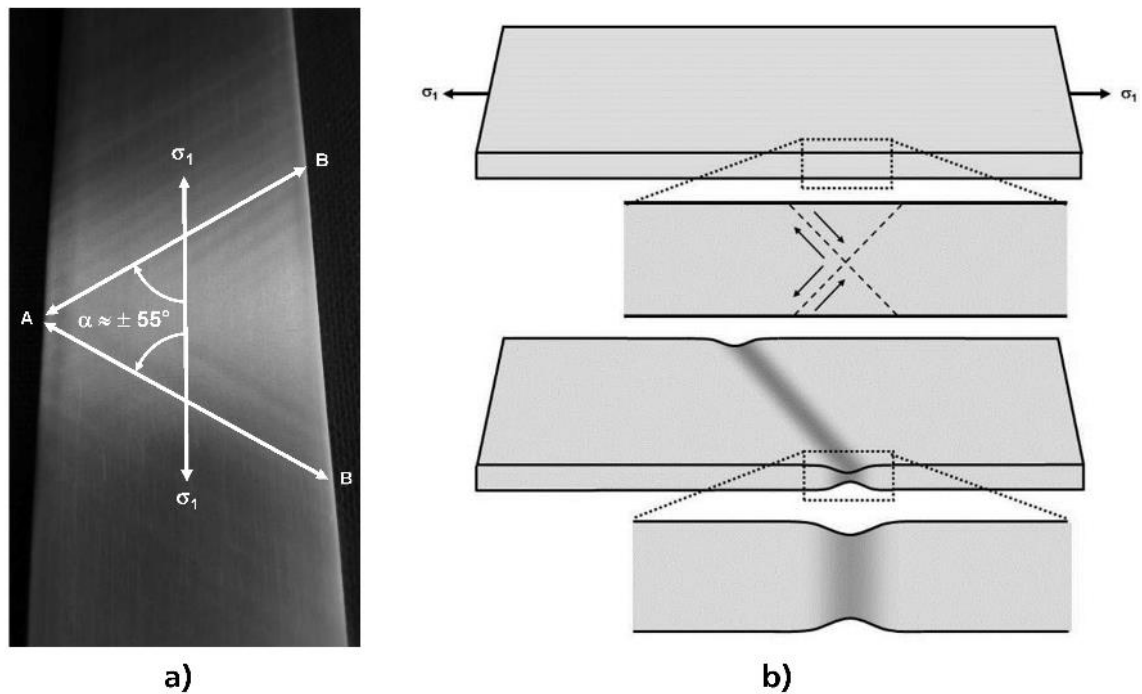


**Figure 2.11** (a) Cross-sectional reduction of 5xxx-series aluminum alloy specimen illustrating localized necking at an angle of  $55^\circ$  and (b) Schematic cross-sectional reduction in thickness occurring alongside shear deformation in multiple planes [5].

As well as chemical composition and second phase particles, the strain rate and temperature can also affect the damage mechanisms of aluminum alloys. These parameters are further discussed in detail regarding the influence of strain rate sensitivity of aluminum alloys, the Portevin Le-Chatelier effect, and the consequence of changing the testing temperature and loading rate, with regard to the damage mechanisms and mechanical properties.

## 2.2 The Portevin Le-Chatelier Effect

### 2.2.1 Strain Rate Sensitivity

Strain rate sensitivity describes the dependency of stress and strain of a material on the rate of loading. The phenomena of strain rate sensitivity can be demonstrated in **Figure 2.12**, where tensile tests were conducted at room temperature on AA5182 aluminum at a range of strain rates from  $1.0 \times 10^{-4}$  to  $1.0 \times 10^3 \text{ s}^{-1}$  [96].

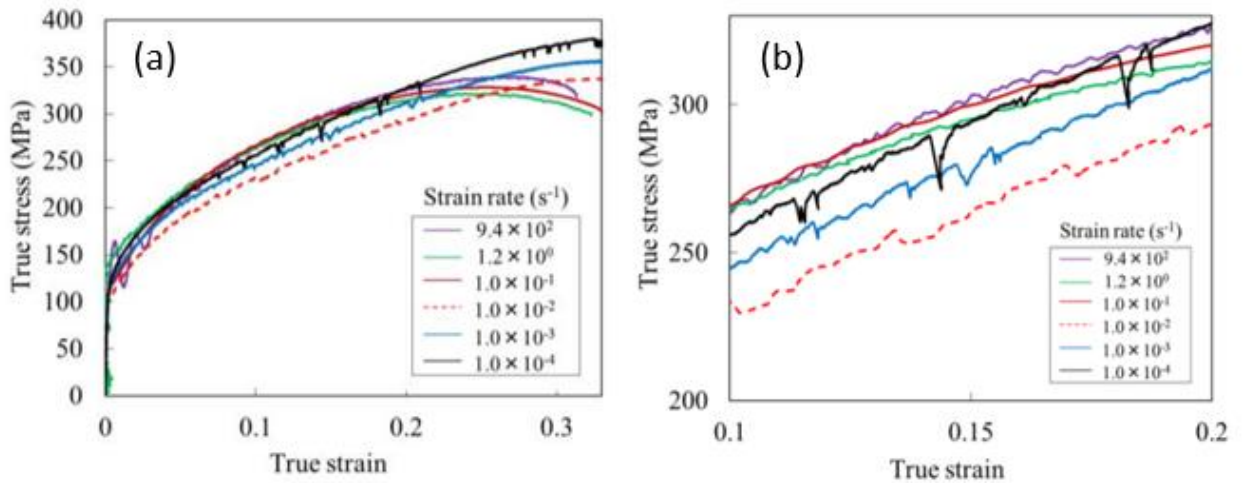


**Figure 2.12** (a) True stress versus true strain curves for aluminum alloy 5182 over a range of strain rates with (b) enlarged views of the curves at RT [96].

The strain rate sensitivity parameter,  $m$ , also called the strain rate sensitivity exponent, is calculated using the following equation,

$$m = \frac{\log [\sigma_1 / \sigma_2]}{\log [\dot{\epsilon}_1 / \dot{\epsilon}_2]} \quad (11)$$

where the computation requires conducting separate tensile tests at different constant strain rates.  $\sigma_1$  and  $\sigma_2$  denote the flow stress at the present strain measured from the conducting the tensile tests at strain rates of  $\dot{\epsilon}_1$  and  $\dot{\epsilon}_2$ , respectively [96]. Dieter discusses another method of obtaining the strain rate sensitivity parameter through conducting a tensile test and increasing the strain rate suddenly after reaching a certain point in plastic strain [97].

In **Figure 2.12**, it can be observed that as the strain rate is increased from  $1.0 \times 10^{-4}$  to  $9.4 \times 10^2 \text{ s}^{-1}$ , not only does the flow stress increase, but a smoother stress-strain curve is obtained [96]. In previous studies on serration theory, it was proposed that negative strain rate sensitivity, and corresponding serrations in the stress-strain curve, are both strongly dependent on temperature and strain rate [97]. In these studies, it is suggested that during dislocation motion, obstacles including solute atoms and forest dislocations, are capable of temporarily arresting these dislocations. Eventually, these dislocations can overcome the obstacles and continue their motion until meeting another obstacle and becoming briefly arrested again. This is the proposed mechanism for the macroscopic serrations observed in stress-strain curves attributing to the discontinuous dislocation motion that is occurring microscopically [98]. This increase in flow stress, as well as the disappearance of serrations in the stress-strain curve, are further discussed in association with these theories in **Section 2.2.2**.

**Figure 2.13** shows the strain rate sensitivity parameter with two strain rates as a function of temperature for aluminum alloy AA5182-O [71].

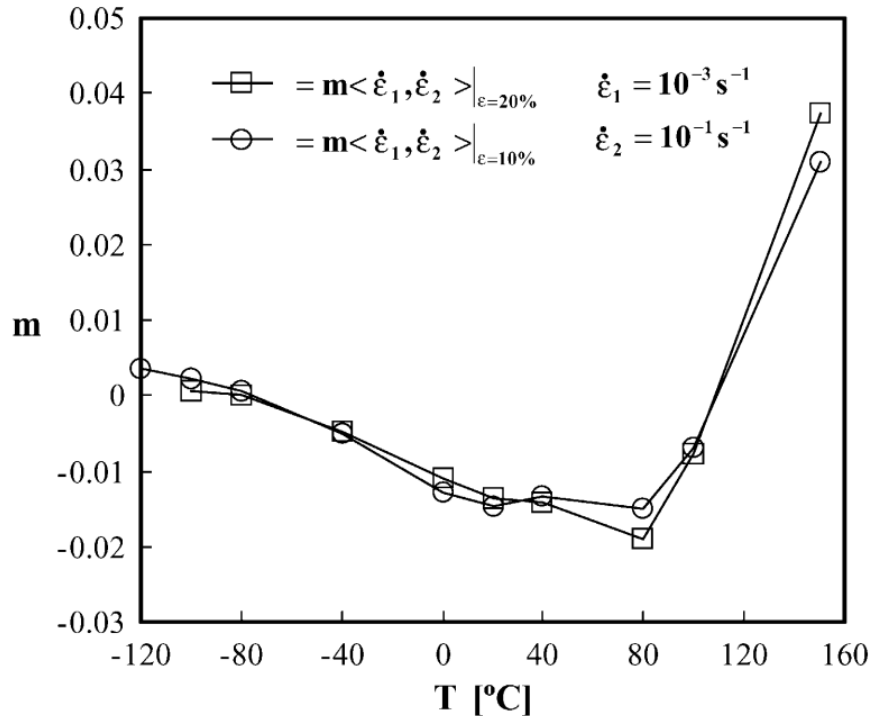


**Figure 2.13** Strain rate sensitivity parameter with two strain rates as a function of temperature for aluminum alloy AA5182-O. The strain rate differential for this data is 1:100, a base rate of  $\dot{\epsilon}_1 = 10^{-3} \text{ s}^{-1}$ , and plastic strains of 10 and 20% respectively [71].

In this plot,  $m$  is observed to be relatively independent of the strain rate and shows a stronger dependency on the test temperature. It is also important to note that as the strain rate sensitivity parameter decreases with strain, this sensitivity will show as more pronounced for the flow stress when compared to the sensitivity of the yield stress. As the temperature moves from room temperature to  $-120^\circ\text{C}$ , the strain rate changes from negative to positive. The other important aspect of this plot to note, is the rate at which  $m$  changes with temperature. In this study, it is noted that at temperatures of approximately  $-120^\circ\text{C}$  the strain rate sensitivity parameter is negative at small plastic strains and then positive as deformation proceeds. In the range of strains between room temperature and approximately  $50^\circ\text{C}$ , this parameter is negative.

In the lower temperature range, between  $-80$  and  $-120^\circ\text{C}$ , the strain rate sensitivity parameter is positive and slightly decreases with the plastic strain. The rate of increase is visually apparent to be higher at a higher temperature range compared to the lower

temperature range, outside of the PLC range. Thereby, the variation of the strain rate sensitivity of the material regarding the temperature is indicative of the activation energy for PLC occurrence being different at these two ranges. This performance suggests that there are two different mechanisms dominating the DSA response. The mechanisms that are proposed by Picu [71], suggest that there is a dissolution that occurs at the clusters of solutes formed on forest dislocations at higher temperatures attributing to this difference in behaviour.

With a similar trend to **Figure 2.13**, **Figure 2.14** maps the variation of the fracture strain with temperature for a temperature range from -120 to 150°C. It is noted that the minimum ductility can be observed to occur at room temperature for aluminum alloy AA5182-O. This observation is the primary motivating factor for improving the development process for this material. In this study, it is also observed that the ductility variance with temperature can be correlated to the variance of the transient and steady state strain rate sensitivity parameter. This observation, along with **Figure 2.14**, provides a picture of the influence of DSA on the reduction in ductility.

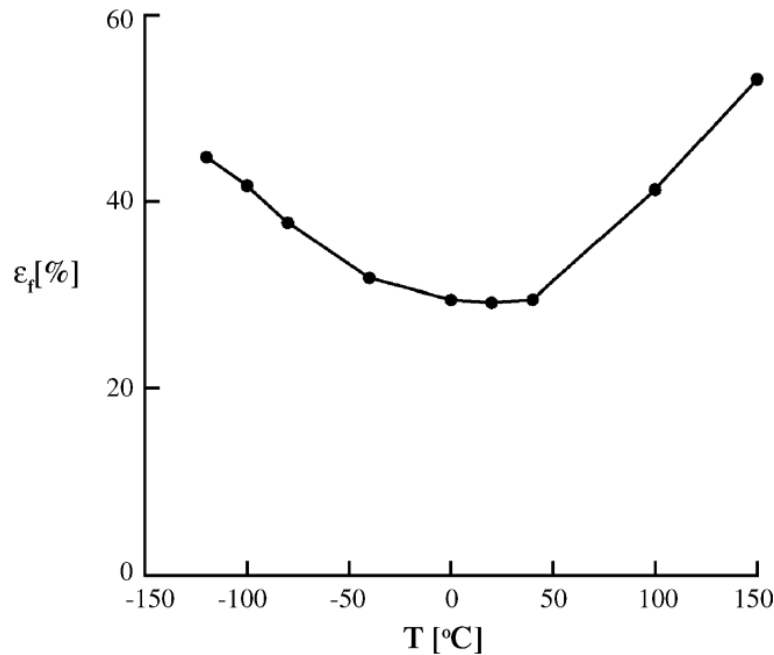


**Figure 2.14** Variation of the fracture strain with temperature for a temperature range for AA 5182-O aluminum alloy from -120 to 150°C [71].

Negative strain rate sensitivity (nSRS) often manifests as serrations in the stress-strain curve of a tensile test [71]. The 5xxx-series aluminum alloys, or more specifically, Al-Mg alloys, are observed to have a negative strain rate dependence at room temperature and quasi-static strain rate conditions [96]. It has also been observed that this value should be negative for Al alloys that exhibit higher flow stress and strain hardening at lower strain rates when compared to higher strain rates [99]. The mechanisms that are proposed for these serrations include the interaction between dislocations and obstacles such as solute atoms and forest dislocations [96]. Eliminating the PLC effect corresponds to increasing strain rate sensitivity (SRS), or  $m$ , to positive values. These mechanisms and their effect on the serration behavior are discussed further in the **Section 2.2.2**.

## 2.2.2 Dynamic Strain Aging

The PLC effect is often considered to be a macroscopic manifestation of dynamic strain aging (DSA) [100]. DSA refers to a process that involves instability in the plastic flow of a material. This instability is usually associated with the interaction between diffusing solute atoms and mobile dislocations [101]. In this interaction, the mobile dislocations will meet obstacles, such as Cottrell atmospheres, and become temporarily stopped. These atmospheres are caused by interstitial atoms surrounding dislocations in the crystal structure. The mechanisms and formation of these Cottrell atmospheres are further discussed in **Section 2.2.4**. The arresting obstacles may also include forest dislocations themselves, grain boundaries, and precipitates. During this temporary arrest, solute atoms

will diffuse around dislocations, strengthen the obstacles, and increase the difficulty of movement for the dislocations. After sufficient stress is applied to the material, the dislocations will gain the strength necessary to overcome the obstacles and move freely until meeting the next obstacle. The repetition of this process leads to the discontinuous flow stress, which appears as strain bursts and arrests in the stress-strain curve.

It is largely accepted that the mechanism behind dynamic strain ageing and the subsequent PLC effect is a result of interactions between mobile dislocations and obstacles, but the models for this process are often debated. **Figure 2.15** gives a schematic of one of the proposed models of this process, where (a) shows the movement of dislocations towards a Cottrell atmosphere in the crystal structure. Figure 2.15(b) shows the arrest of the mobile dislocation at an obstacle, such as the Cottrell atmosphere generated by a forest dislocation [102].

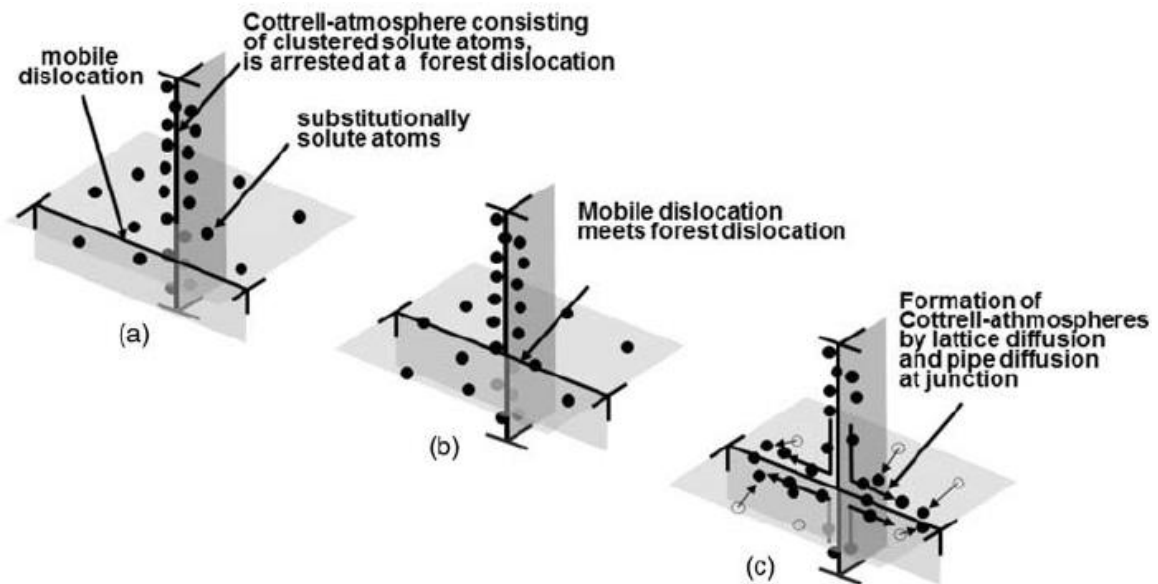


**Figure 2.15** A schematic of (a) mobile dislocations (b) mobile dislocations meeting and being arrested by obstacles such as a Cottrell-atmosphere and (c) subsequent lattice and pipe diffusion [102].

Picu et al. [98] developed a relatively new model that proposes that the interaction between forest dislocations that are surrounded by Cottrell-atmospheres, and moving

dislocations, is dependent on the strength of dislocation junctions. In this model, higher strain rates and subsequent faster deformation reveal less clustering of solute atoms, resulting in lower junction strength. On a second paper researching the strain rate sensitivity of AA5182-O, Picu et al. [71] demonstrated that the solute clusters formed at these forest dislocations will increase the strength of these dislocation junctions. Picu et al. concluded that the thermally activated component of the flow stress appears to be unaffected by the presence of clusters, and that the increased strength of junctions that results from the cluster formation at forest dislocations leads to an increase in the athermal component of the flow stress [71]. The thermal and athermal components of flow stress are further discussed in **Section 2.3**.

The PLC effect in aluminum-magnesium alloys has been largely attributed to Cottrell atmospheres and subsequent DSA [30]. Cottrell atmospheres occur in both body-centered cubic (BCC) and face-centered cubic (FCC) materials [103]. These materials often contain small impurity atoms, which are also referred to as substitutional or interstitial solutes. Cottrell atmospheres describe the solutes that surround a dislocation. Below a dislocation, atoms are more spread out, as shown in **Figure 2.16** [104]. In this space, it is more likely for solute atoms to congregate underneath the dislocation and cause these Cottrell atmospheres. These atmospheres restrict dislocation motion, pinning them in place until enough stress is applied to overcome the obstacle. These dislocations are then free to move until meeting other Cottrell atmospheres. The interaction between these interstitial atoms and mobile dislocations produces a continuing arrest-and-release effect, leading to microscopic dynamic strain ageing of the material, as well as the macroscopic PLC effect.

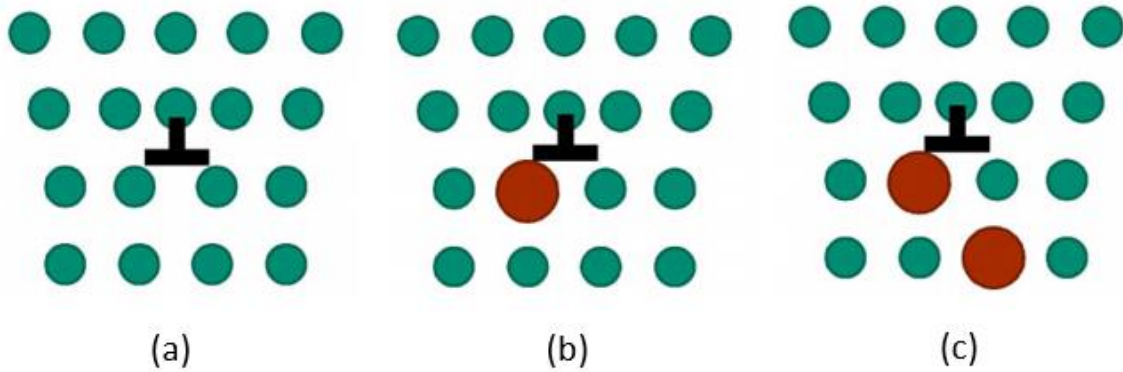


**Figure 2.16** A solute atom inside a crystal structure resulting in a Cottrell atmosphere demonstrating: (a) a dislocation in the crystal structure, (b) solute atoms congregate underneath the dislocations to form Cottrell atmospheres, and (c) dislocation arrested by the solute atoms and unable to move [104].

Although it is still a debated topic, the current understanding of DSA is that if sufficient mobility exists for a solute, it is possible for clustering to occur during the period that an obstacle has arrested a mobile dislocation [5]. There are two current ideas for clustering. The first interpretation involves clustering that occurs through lattice diffusion, from the lattice to the mobile dislocations that have been temporarily arrested. The second scenario is pipe diffusion, where the clustering is then assumed to occur from the solute clusters on the forest dislocations to the core of the mobile dislocations [71].

Picu et al. have proposed a new mechanism which suggests that the strength of the dislocation junctions is influenced by the existence of clusters in forest dislocations. In this study, it is also explained that these dislocation junctions control the athermal component of flow stress, which is further discussed in **Section 2.3**. This study proposes that there is a chain of influence which follows that junction strength is dependent on the cluster size in forest dislocations. Subsequently, the cluster size is dependent on the residence (or ageing) time of forests, which is, in turn, dependent on the strain rate. It is shown that an increase in the strain rate for these experiments will reduce the residence time of forests, result in smaller clusters, reduce the strength of junctions, and consequently lead to a negative SRS value [71].

This theory can be summarized and expounded using the following equation,

$$t_w = \frac{\rho b L}{\dot{\epsilon}} \quad (12)$$

In this formula,  $t_w$  is the waiting time, or the time that the dislocations are temporarily arrested,  $\rho$  is dislocation density,  $b$  is the Burgers vector, and  $L$  is the average distance between obstacles [105, 106]. The model suggests that mobile dislocations are first arrested at forest dislocations or solute atoms. These solute atoms then diffuse and pin these dislocations for some time, defined as  $t_a$ . If the time that the dislocations are temporarily arrested at these obstacles is greater or equal to the time that it takes for the solute atoms to effectively pin the dislocations, the condition for nSRS exists [107]. Subsequently, nSRS will result in the manifestation of PLC effect and serrations in the stress-strain curve [71].

During high strain rate deformation, cluster sizes are smaller and result in a lower junction strength. At lower strain rates, the cluster sizes are larger and cause an increase in junction strength, producing a negative strain rate sensitivity for the material [71]. The overall mechanism that is proposed in this study which is discussed in further detail within subsequent chapters, is that at low strain rates and a temperature range between -80 and 50°C, mobile dislocations are temporarily arrested at forest dislocations. During this interaction, solute atoms diffuse and pin these mobile dislocations and lead to negative strain rate sensitivity, and serrations in the flow stress of the material.

### 2.2.3 Deformation Instability

Traditionally, plastic deformation of crystalline materials was viewed as a smooth and uniform process. Recent experimental studies of solution hardened materials, such as 5xxx-series aluminum alloys, have observed plastic flow on smaller scales and have indicated that contrary to traditional views of plasticity as homogenous deformation, it can instead be characterized by strain bursts [108-110].

Another way to look at plastic deformation, is through the mechanisms of dislocations. As stress is applied to a solid material, the nucleation and movement of dislocations occurs. At the nanoscale, the mobility of these dislocations is not a smooth transition but involves bursts of motion [110]. At the macroscopic scale, these load-displacement curves appear as a smooth process. H. Li studied a range of crystalline and amorphous metals, including an Al-Mg alloy, and found that at the nanometer scale, this deformation involves a series of continuous strain bursts [111].

The Portevin-Le Chatelier (PLC) effect manifests itself as unstable plastic flow, appearing as serrations of a stress-strain curve during tensile testing (due to DSA). Both substitutional alloys, (e.g. Al-Mg) and interstitial alloys (e.g. low carbon steel) are susceptible to this unstable plastic flow [112, 113]. The PLC effect can cause both visual and structural complications in aluminum alloys in a regime of strain rates (typically lower than  $10^{-1} \text{ s}^{-1}$ ) and temperatures (approximately -80 to 120°C) [71, 107]. Serajzadeh [114] investigated the occurrence of DSA, or the instability of plastic flow, in the commercial aluminum alloy AA5083. As shown in **Figure 2.17**, Serajzadeh was able to develop a strain rate and temperature range for the serrated flow of AA5083 aluminum alloy, with log strain rate ( $\text{s}^{-1}$ ) on one axis and temperature ( $\text{K}^{-1}$ ) on the other [114]. The typical range of temperatures where DSA has been observed includes 193 K to 393 K (-80 to 120°C) and

at strain rates lower than  $10^{-1} \text{ s}^{-1}$  [71, 107, 114]. In this range,  $m$  is negative and PLC bands are present [71].

The unstable plastic flow can also affect a range of material properties as well. Brindley [115] and Robinson [116] reviewed yield-point and dynamic strain aging phenomena in substitutional alloys and observed an increase in the ultimate tensile stress and work hardening rate, as well as a decrease in the ductility, strain rate sensitivity coefficient, and fracture toughness.

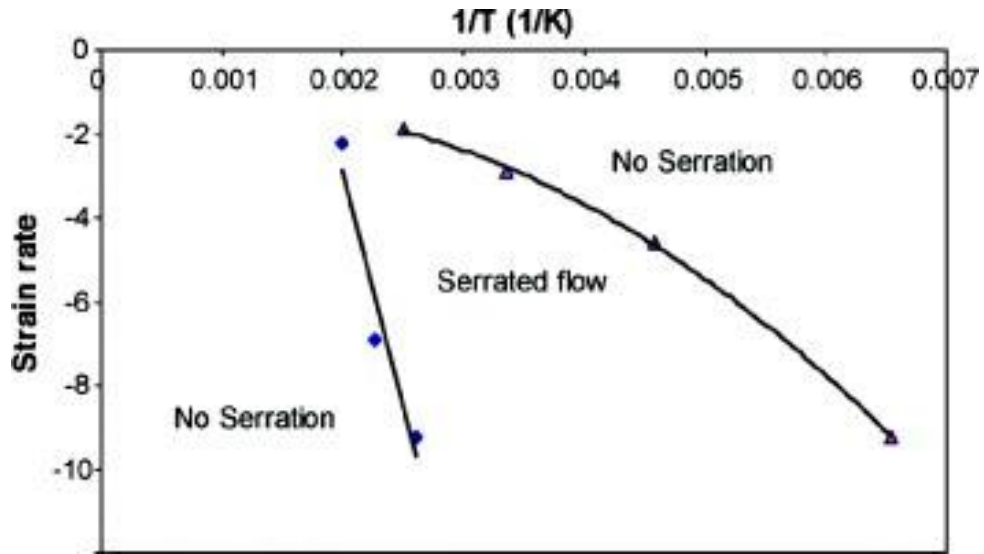


**Figure 2.17** Serrated flow range of the aluminum alloy AA5083 dependent on log strain rate ( $\text{s}^{-1}$ ) and  $1/T$  ( $\text{K}^{-1}$ ) [114].

There are three types of deformation bands produced by the PLC effect and are recognized as type A, B, or C bands. Jiang used dynamic digital speckle pattern interferometry (DSPI) techniques, tensile tests, and numerical simulation to investigate these three PLC effects in aluminum alloys [117, 118]. **Figure 2.18** shows the observation of each band type using both experimental and simulated data of the PLC effect in tensile tests for an Al-Mg alloy at different strain rates. Type A serrations typically occur in a periodic manner, where the curve spikes above the average value of stress before exhibiting a sharp decrease. The second type of serration, Type B, fluctuates above the average stress values with a higher frequency. Type C serrations are recognized by yield drops that occur below the average stress value, observed by sharp decreases on the curve [117]. The

schematics of band type, location, and attributed stress-strain tensile curves are provided in **Figure 2.19**.

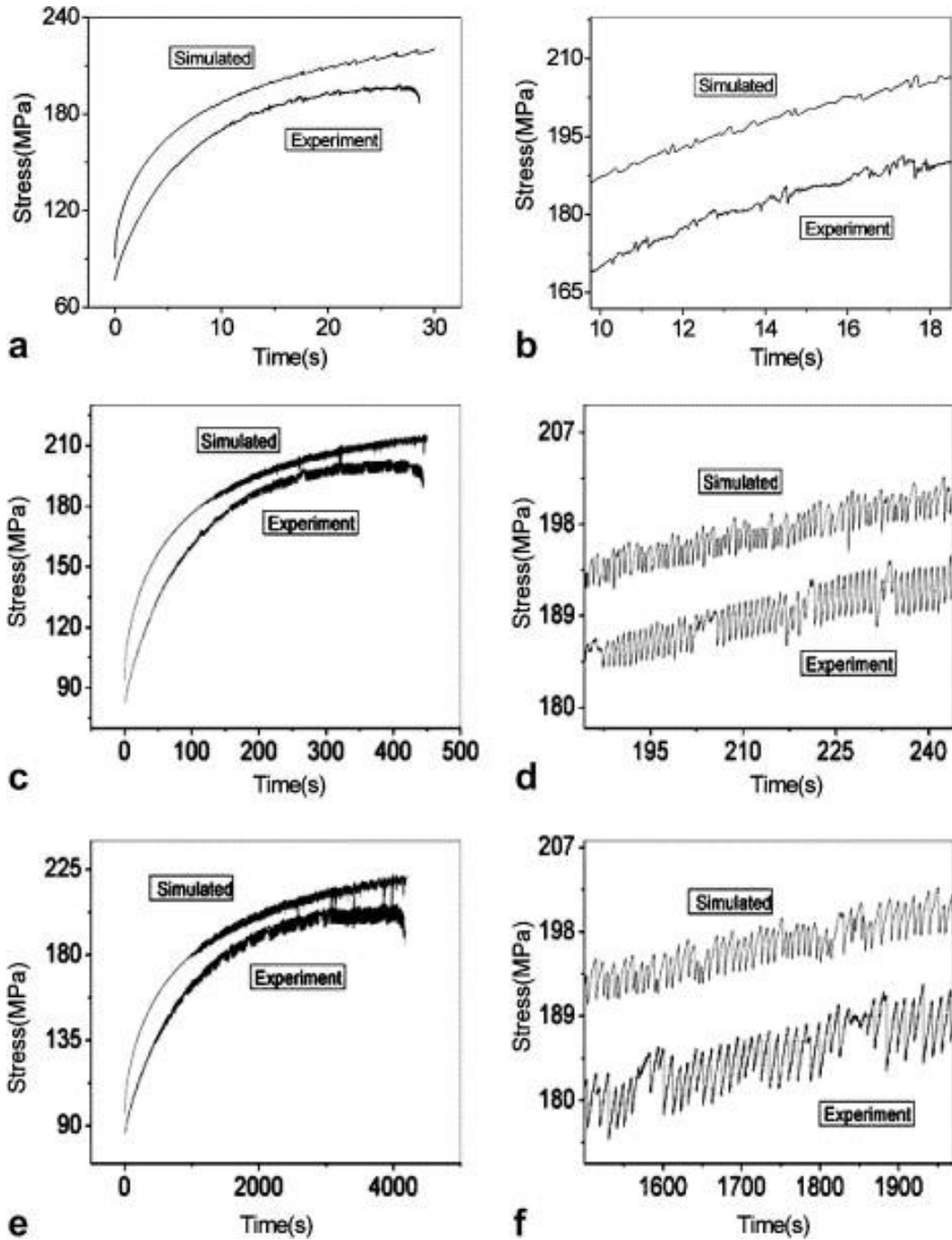


**Figure 2.18** Experimental and numerical simulation (developed using a one-dimensional phenomenological model) observations of three PLC types in tensile test at different applied strain rates: (a) type A,  $5 \times 10^{-3} \text{ s}^{-1}$  with (b) enlarged view, (c) type B,  $5 \times 10^{-4} \text{ s}^{-1}$  with (d) enlarged view, and (e) type C,  $5 \times 10^{-5} \text{ s}^{-1}$  with (f) enlarged view [117, 118].

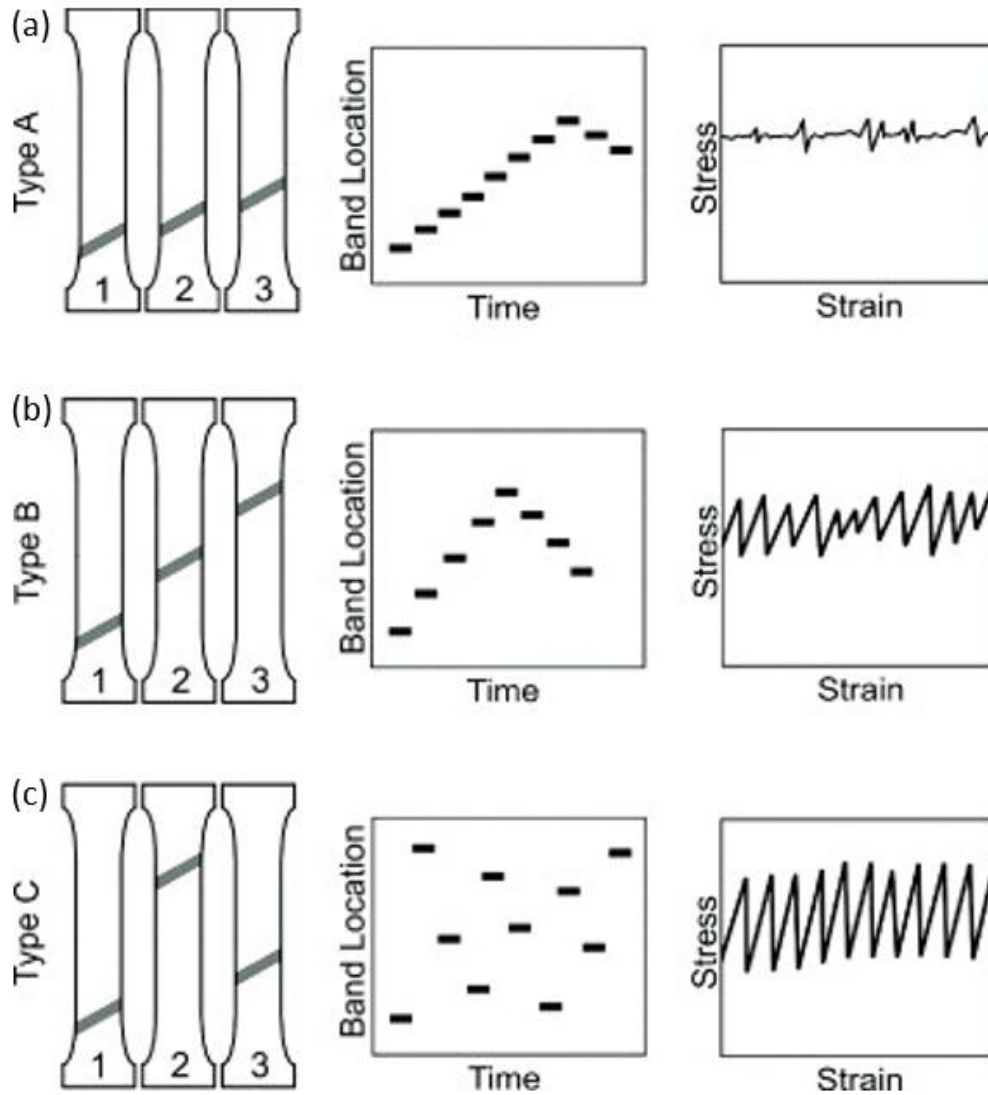


**Figure 2.19** Schematics of motion, orientation, spatio temporal appearances and strain controlled tensile curve characteristics for (a) Type A, (b) Type B, and (c) Type C serrations [100].

Aside from the serrations of the stress-strain curve, there are two other distinguishing characteristics of the PLC effect. These characteristics, as shown in **Figure 2.19**, include localized strain in sections of the samples under stress, as well as the motion of these localized strain sections as the stress is increased. The localized strain sections are revealed by bands that are often a few millimeters in thickness and orientated at approximately  $55^\circ$  to the axis of applied stress [100].

From **Figure 2.18** and **Figure 2.19**, Type A serrations can be characterized by small, sharp increases and then decreases in the stress embedded in the average flow of the curve, and the bands are often propagated in a continuous manner along the gauge length of the specimen, similar to a longitudinal wave [119]. Stress-strain data for Type B serrations is typically observed as small and irregular frequencies and amplitudes in the flow stress, typically smaller than amplitudes of Type C serrations. Type B bands often occur intermittently across the gauge length of the sample with approximately identical intervals. Type C serrations are characterized by serrations in the stress-strain curve that manifest as relatively consistent amplitudes and frequencies with bands that appear randomly across the gauge length [100].

These band types are dependent on both strain rate and temperature. Aik-Amokhtar conducted tensile tests for an Al-3.2%Mg alloy at room temperature over a strain rate range of  $4 \times 10^{-5}$  to  $5 \times 10^{-2} \text{ s}^{-1}$ , where band type was varied, and observed type A bands at higher strain rates, type B bands for intermediate levels of strain rates, and type C bands for lower strain rates [120]. An inverse effect to the band type is caused by temperature [100]. At low temperatures, type A bands were observed, type B bands at intermediate temperatures, and type C bands appearing at higher temperatures. Although there are some cases, in critical regimes of temperatures and strain rates [121, 122], generally only one type of deformation band appears at a time [123]. Applying laser scanning extensometry, Neuhauser tested Al-Mg and Al-Cu alloys and demonstrated PLC bands forming in single or several locations along the effective gauge length [124].

## 2.3 Cottrell-Stokes Testing

### 2.3.1 Temperature Change Tensile Testing

In an effort to study the differences between reversible and irreversible changes of flow stress with temperature, Cottrell and Stokes developed a testing procedure that involved changing the deformation temperature during tensile experiments at a given strain value [125]. Prior to this method, investigating the temperature dependence of flow stress often involved taking similar crystals and conducting stress-strain tests at different temperatures. However, irreversible changes can occur to dislocation distributions because of temperature (and these dislocation distributions would be different for different crystals). The Cottrell-Stokes method benefits from investigating the temperature dependence of flow stress of the same crystal, and therefore, the same dislocation distribution. The process for this method involves taking a crystal, deforming it to strain,  $\epsilon_T$ , at temperature  $T_1$ . The crystal is then unloaded, the temperature is changed to the new temperature,  $T_2$ . The flow stress is measured at the strain  $\epsilon_T$  and  $T_1$ , and then measured at  $\epsilon_T$  and the new temperature  $T_2$  (as shown in **Figure 2.20**). This difference in flow stress that is measured is termed the *reversible* change in flow stress (this is done to differentiate between the irreversible changes observed from deforming multiple crystal samples, with varying dislocation distributions, at different temperatures) [126].

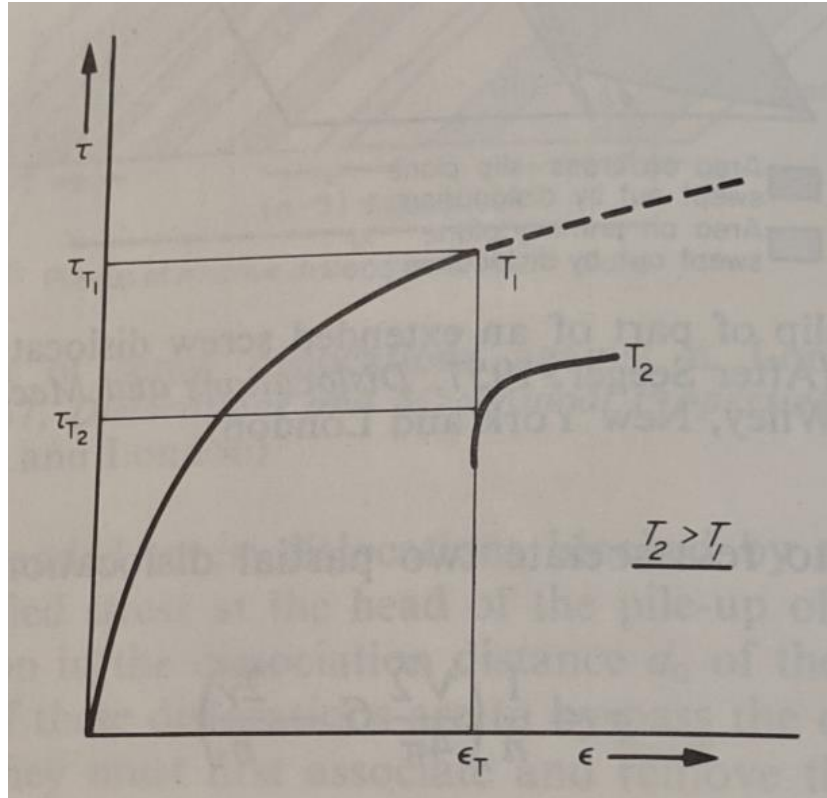


**Figure 2.20.** Schematic of Cottrell-Stokes method of investigating the temperature dependence of the flow stress (reversible change in flow stress with temperature) [126].

These experiments were applied to single crystals of aluminum and the method involved applying a tensile load at a specific temperature, interrupting the test by unloading and reloading the sample at a different temperature, and then resuming the tensile load. **Figure 2.21** shows a schematic of the stress-strain curve obtained from testing an aluminum crystal under tensile load that has been initially tested in liquid air, unloaded, and then reloaded and tested at room temperature.

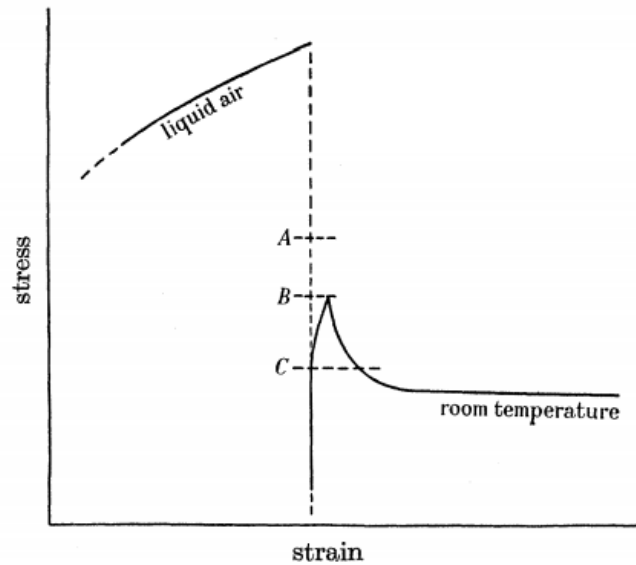


**Figure 2.21** Stress-strain curves (schematic) showing the form of yield drop developed at room temperature after straining an aluminum specimen in liquid air ( $-196^{\circ}\text{C}$ ) [125].

In this schematic, the differences between the A, B, and C values are interpreted. The point A on the dotted line, marks the expected yield stress of the material. The actual yield stress of the material during testing is marked by B. C denotes the value of the applied stress to the material if held constant, similar to other stress relaxation experiments [125]. Using these tests, Cottrell and Stokes made two important observations,

- i. the structure of the material is a function of the test temperatures and is independent of strain
- ii. the ratio of flow stress at the second temperature,  $T$ , and initial test temperature,  $T_0$ , is a function of the two testing temperatures and independent of the strain.

The ratio of the flow stress,  $\sigma(T)/\sigma(T_0)$ , is known as the Cottrell-Stokes (CS) ratio. The strain independence of the material structure and the ratio of flow stress is known as the CS law [122].

These studies, initiated by Cottrell and Stokes in 1955, were able to provide considerable insight into the thermally activated nature of plastic flow [125]. As plastic deformation in metals involves the creation, movement and buildup of dislocations, the

plasticity of most metals is dependent on strain rate and temperature [127]. When looking at flow stress as a function of dislocation creation and motion, it is not sufficient to study only the observed stress of the material. When using the Cottrell-Stokes testing method, as well as other temperature and strain-rate changing techniques, flow stress can be divided into two components. These components are thermal stress,  $\sigma_t$ , and athermal stress,  $\sigma_a$ . The flow stress of the material is then expressed as a sum of these contributions,

$$\sigma = \sigma_t + \sigma_a \quad (13)$$

The thermal stress component, which is more sensitive to temperature and strain rate, is also sometimes referred to as the effective stress [128, 129]. The thermal stress is attributed to dislocation mobility as it overcomes localized energy barriers such as solutes, impurities, and forest dislocations [130]. For the process of applied stress to a crystalline material, this term describes dislocation motion aided by thermal activation. The athermal stress component is considered the internal stress of the material and is attributed to athermal obstacles (such as dislocation networks) [131-133]. This internal stress is caused by existing dislocations to the lattice structure (dislocation substructure) in the deformed material, or long-range barriers to the motion of dislocations [128, 130].

## 2.3.2 Strain Rate Change Tensile Testing

Due to the difficulties attributed with temperature changes during tensile testing, another methodology of investigating the thermal activated nature of plastic flow was developed. This method is used to determine the strain rate sensitivity of a material by using a series of strain rate changes during testing. In these experiments, the temperature is held constant, and the strain rate is typically changed by a strain rate differential of 1:100 [71]. In strain rate change tests, there are two types of strain rate sensitivities to consider

[134]. Instead of using equation (11) to calculate the steady state strain sensitivity parameter,  $m$ , can be determined by,

$$m = m_i + m_t \quad (14)$$

The steady state strain is calculated from the change in instantaneous stress associated with the values of the strain rate jump from  $\dot{\epsilon}_1$  to  $\dot{\epsilon}_2$  and by extending the flow curve through extrapolation at the moment of the jump, to the transient following the strain rate jump. The instantaneous strain rate sensitivity,  $m_i$ , always a positive value as it increases with strain [135]. The transient strain rate sensitivity parameter,  $m_t$ , describes a latent effect, which is negative in the DSA regime observed for that material [98]. In strain rate change tests, there are effects that are observed immediately (captured by the instantaneous strain rate sensitivity parameter) and there are effects that can not be observed immediately upon imposing a change to the strain rate. The change in obstacle, or junction, strength is not observed instantaneously but described by the transient following the strain rate change [136]. When the strain rate sensitivity, summing both the instantaneous ( $m_i$ ) and latent  $m_t$  constituents, is a negative value, the condition for the PLC effect is present.

In **Section 2.2.1**, equation (11) can also be expressed as follows,

$$m = \left( \frac{\partial \ln \sigma}{\partial \ln \dot{\epsilon}} \right)_{\Sigma, T} \quad (15)$$

where, if the temperature (T) and the structure ( $\Sigma$ ) remains constant, the strain rate sensitivity is typically calculated by testing two samples at different strain rates and calculating  $m$  based on the stress at the same strain or changing the strain rate while conducting the test and calculating based on the stress before and after the strain rate jump [137]. An illustration of the stress-strain curves obtained using each of the testing methods is given in **Figure 2.22**.

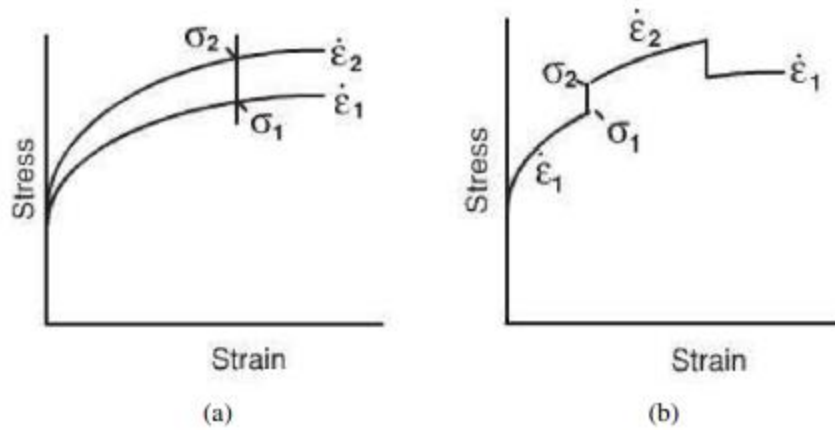


**Figure 2.22** Stress-strain curves using the method of (a) testing two samples at different strain rates and (b) testing with one sample and a strain rate jump [137].

As previously discussed, the second method of using the same material is a preferred method for maintaining the same structure with testing as the dislocation substructure should theoretically be the same when compared to using a new material with different dislocation networks. The strain rate sensitivity coefficient is given by,

$$S = \frac{\partial \sigma}{\partial \log \dot{\epsilon}} \quad (16)$$

which should be proportional to the stress, and the strain rate sensitivity parameter,  $m$ , should be strain independent for the CS law to be valid for that material [121]. The method of showing the validity for CS law by plotting  $S$  versus the flow stress, or the offset (effective) flow stress  $\sigma - \sigma_0$ , where  $\sigma_0$  is the material yield stress. This plot is called the Haasen plot, as shown in **Figure 2.23** [137].

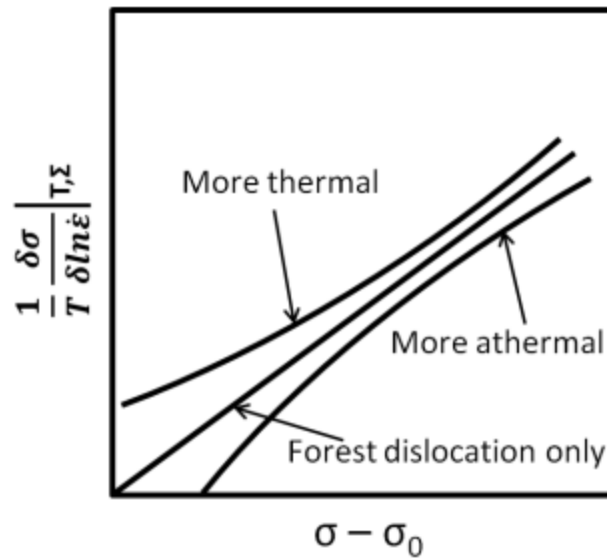


**Figure 2.23.** Schematic of the Haasen plot with an intercept of thermal components, athermal components, and forest dislocation components as three types of components that can dominate flow stress [137].

A positive intercept represents the existence of thermally activated components (attributed to dislocation mobility from effective stress overcoming localized energy barriers such as solutes and impurities). More athermal components exist when a Haasen plot achieves a negative intercept (athermal components are often attributed to internal stress caused by existing dislocations in the dislocation substructure or long-range barriers). When the slope intercepts zero on the Haasen plot, forest dislocations or dislocation-dislocation interactions are the only components that dominate the flow stress (typical for pure metals where dislocations are the only obstacles present [121]).

### 3.4 Sub-Zero Temperature Tensile Testing

Recent studies have revealed that deforming aluminum alloys at low temperatures can result in the improvement of certain mechanical properties [5, 30, 31, 49]. Sotirov et al. [49] studied the forming behavior of aluminum alloy sheets at cryogenic temperatures and found that strength, elongation, and forming limits increase with decreasing temperature. Using tensile tests and subsequent stress-strain curves, as shown in **Figure 2.24**, the elongation of AA5182 aluminum sheets were observed to increase by a factor of 1.1 to 2.0 from RT to 78 K (25°C to -195.15°C) respectively. With experimental and numerical testing (using Nakajima forming processes and Finite Element Models respectively), Sotirov et al. demonstrated an increase in the forming limits, as shown in **Figure 2.25**, through an increase in the low major strain at RT from 0.19 at the lowest point in the curve to a major strain of 0.27 at -100°C experimentally. Numerical simulation showed an even further increase of formability to an approximate major strain of 0.32 at -195°C.

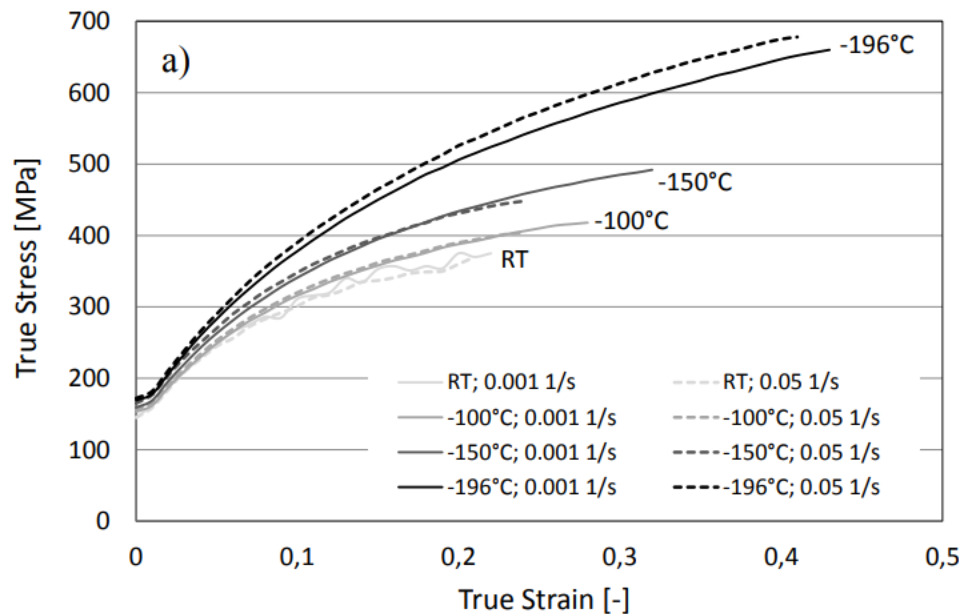


**Figure 2.24** True stress versus true strain curve for AA5182 aluminum alloy at temperatures of RT to -196°C (78 K) and strain rates of 0.001 s<sup>-1</sup> and 0.05 s<sup>-1</sup> [49].

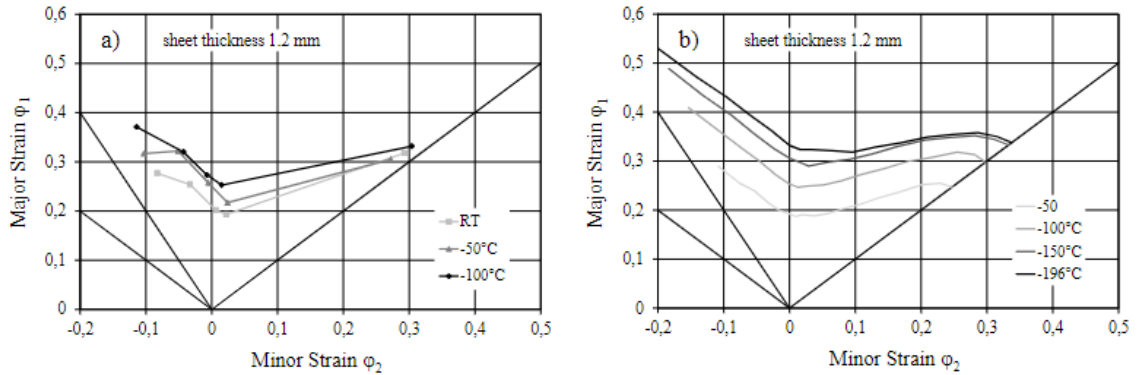


**Figure 2.25.** a) Experimental and b) numerical temperature-dependent forming limit curves for AA5182 [49].

Schneider et al. [30] investigated the mechanical behavior of aluminum alloys EN AW-5182, EN AW-6016 and EN AW-7021 at temperatures ranging from 298 to 77 K and mapped the resulting strain hardening behavior with experimentally determined elongation values. It was observed that the strain hardening of these alloys improved and resulted in an enhanced uniform elongation during tensile testing.

Jobba et al. [138] examined the flow stress and mechanical behavior of Al-Mg binary alloys at temperatures from 298, 78, and 4.2 K and demonstrated an increase in the yield stress, ductility, and work hardening rate as the temperature was decreased. This increase in the work hardening rate in tandem with a decrease in the temperature can also be observed in Hou et al.'s [139] study of cryogenic processing of 7050 aluminum alloys. **Figure 2.26** shows micrographs obtained from cryogenic rolling of hardened 7050 aluminum alloy sheets with RTR (room temperature rolling) and LN2R (liquid nitrogen rolling). **Figures 2.26(a)** through **(d)** show coarse grains (length  $<300\ \mu\text{m}$ , width  $<100\ \mu\text{m}$ ) of the 7050 aluminum alloy increased and elongated in the rolling direction. The RTR up to 63% led to severe cracking of the plate. **Figures 2.26(e)**, **(f)**, and **(g)** reveal the LN2R microstructure with significantly elongated grains. Cryogenic rolling was observed to produce grain structure refinement and increased dislocation density, leading to an increase in the strength of the material and the elongation.

Inhomogeneous deformation of strip cast AA5754 aluminum alloy was observed by Kang et al. [140] under tensile testing conditions at temperatures of 298 K (RT) and 223

K. In these experiments, the work hardening rate was mapped as a function of the true stress, as shown in **Figure 2.27**. The work hardening rates evolve similarly in both cases, until reaching the Considère Criterion. For room temperature, this maximum point is reached around 280 MPa flow stress, corresponding to a necking strain of 0.21 (notably lower than the strain hardening exponent of 0.30). When the same material is tested at a temperature of 223 K, diffuse necking begins where the work hardening rate is equal to the corresponding flow stress and the necking strain is almost equal to the strain hardening exponent. The paper suggests that there is an early onset of necking in the RT tested sample that is caused by DSA and the reduction of uniform elongation.

Plastic deformation and work-hardening behaviour of high-purity Al and AA5754 aluminum alloy was investigated between 4.2 K and 295 K by Park et al. [141]. The work-hardening rate was mapped as a function of the effective flow stress, normalized with the temperature dependent shear modulus, as shown in **Figure 2.28**. The work-hardening rate is observed to increase significantly as temperature is decreased for all three samples.

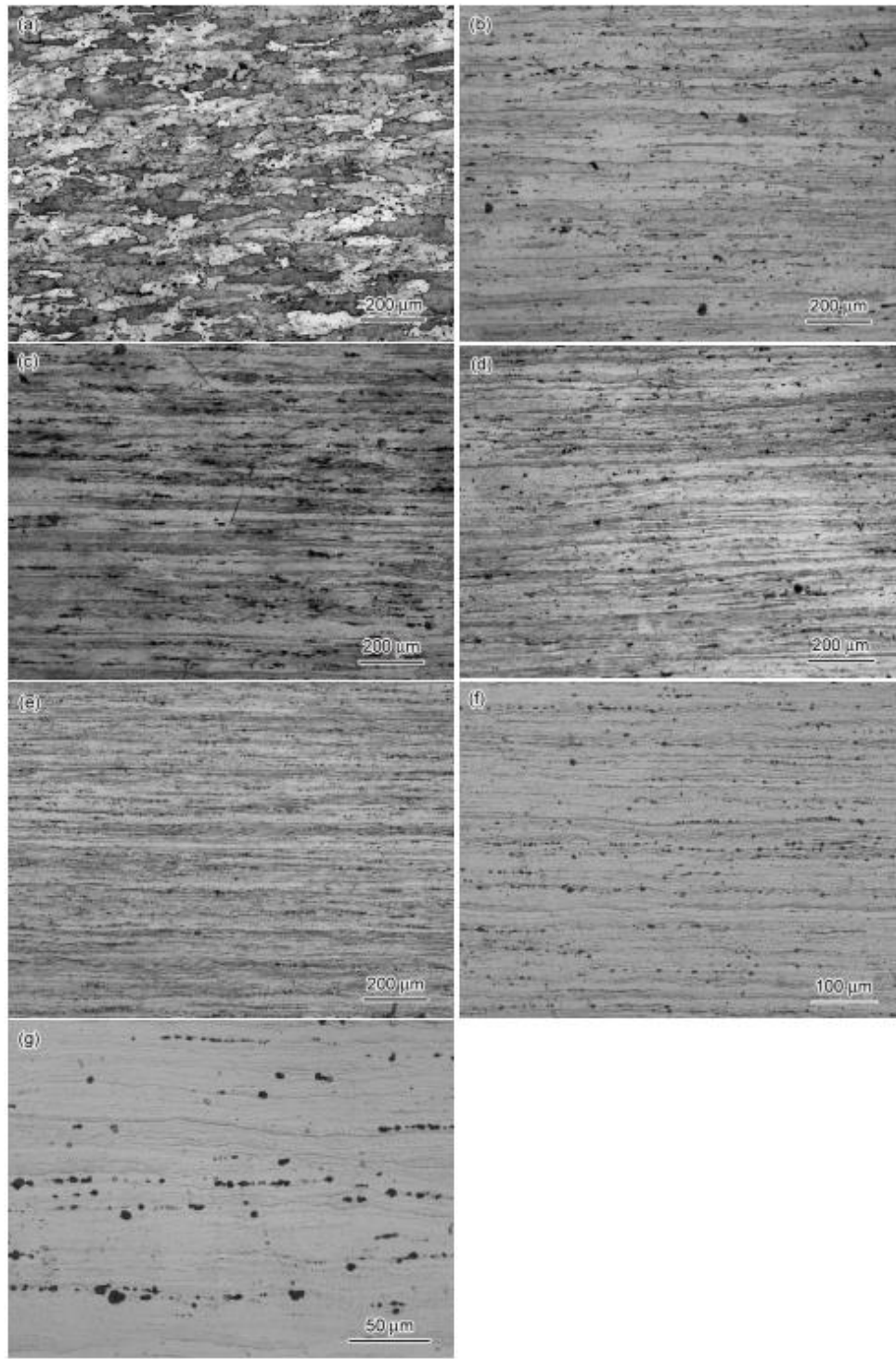


**Figure 2.26** Microstructures of the RT rolled and LN<sub>2</sub> rolled 7050 Al alloys (a) as quenched, (b) 40% RTR, (c) 56% RTR, (d) 63% RTR, (e) 76% LN<sub>2</sub>R (f,g) 91% LN<sub>2</sub>R with different magnifications [123].

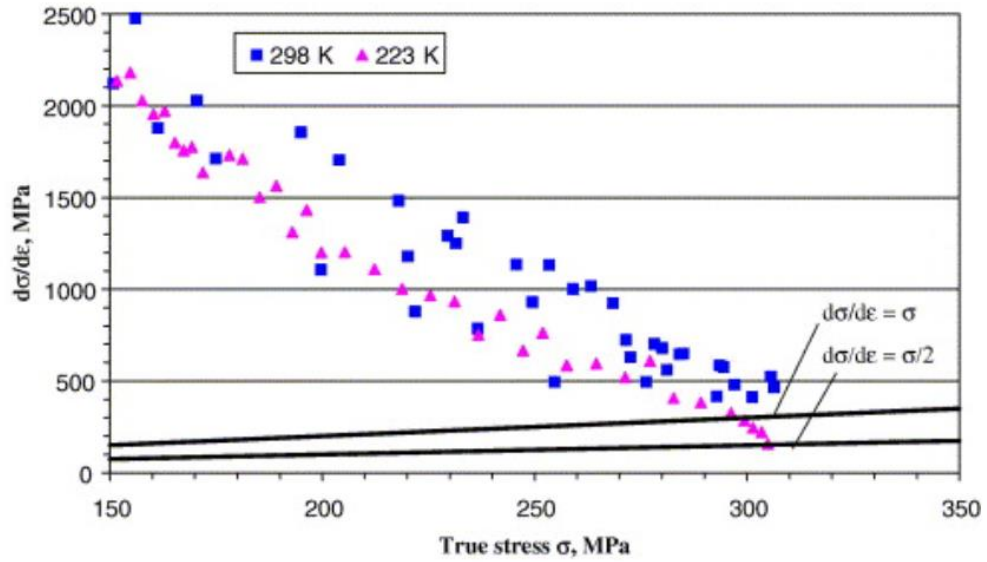


**Figure 2.27** Work hardening rate of strip cast AA5754 sheet under 298 K and 223 K temperature conditions [140].

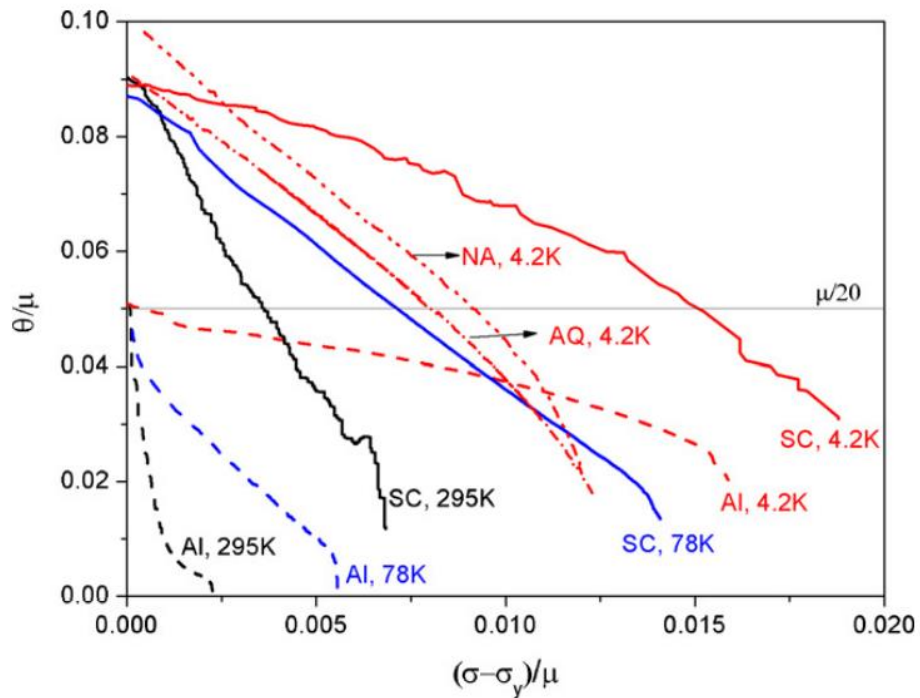


**Figure 2.28** Work hardening rate as a function of reduced flow stress, both normalized by temperature dependent shear modulus. SC and Al denote AA5754 aluminum alloy and pure aluminum, respectively. NA and AQ denote natural aged and as-quenched Al-Zn-Mg alloys, respectively [141].

**Figure 2.27**, the work hardening rate plotted against the true stress, shows two straight lines through the plot related to Considère's criterion. Considère's criterion is based off of a publication from Considère in 1885 [142] which introduced three basic concepts to better understand the formation of necking in materials. These concepts include

1. Prior to any deformation occurring, real materials have differences in dimensions and composition that cause local variations to both stress and strain.
2. During (tensile) deformation, the cross-sectional area of a material decreases.
3. During (tensile) deformation, strain hardening of the material occurs; varying with the extent of deformation that occurs.

Based on the last two points, there is a way to relate the strain hardening rate to the true stress-strain curve by the necking, or instability point. The instability point in a material is shown in the following stress-strain curve and explained by the Considère criterion in **Figure 2.29** [142].

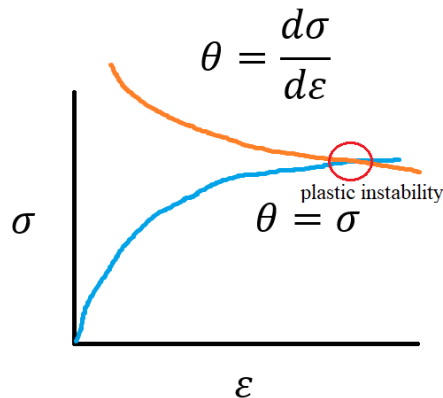


**Figure 2.29.** Schematic of the instability point from Considère criterion showing the interception of a stress-strain curve with a strain hardening curve [142].

The blue line in this figure is a representation of the true stress-strain curve, and the orange line is the respective strain hardening rate. The second point from Considère explains that as a sample is deformed in a tensile test, it is becoming thinner with elongation. The measure of stress, which is defined as load per unit area, is then known to be increasing in value. As the material is both strain hardening, as well as supporting increasing stress (due to reduction in area), the situation arises where the increase in stress

will become equal to the increase in load carrying capacity (resulting from strain hardening). This is represented on the graph by the instability point (circled in red) where,

$$\frac{d\sigma}{d\varepsilon} = \theta = \sigma \quad (17)$$

The strain hardening rate and the true stress-strain curve are represented by  $\theta$ , which is the derivative of the stress with respect to strain. This criterion shows the plastic instability at the necking point by demonstrating that the material is strengthened gradually as it is plastically deformed. Then, due to cross-sectional area decreasing at this point, the necking point increases significantly. The stress becomes greater than the hardening rate and this balance creates the necking.

There is little data available that gives comprehensive insight into the fracture behavior of these alloys. More work is required to understand the mechanisms behind the modes of fracture. Although there are experiments that demonstrate the increased properties at low temperatures, there are few studies that suggest the mechanisms behind this improvement. As well, most studies that have been conducted on the formability and mechanical behavior of aluminum alloys at low temperatures have concluded that the results need agreement with further investigations. Supplemental research data allows for more reliable execution into industry applications and productions.

The objective of this study is to identify the microstructural causes of formability enhancement of AA5182 aluminum during the subzero temperature conditions so as to facilitate the implementation of this forming technique into industrial application and production. AA5182 aluminum alloys produce the Portevin Le Chatelier effect at room temperature, but appear to lose this deformation instability at sub-zero temperatures. As a result, the effect of temperature on the deformation and fracture mechanisms was investigated. More specifically, the damage mechanisms of AA5182 aluminum were investigated by analyzing the microstructure of damage surfaces under OM and SEM. Finally, differences in mechanical properties during tensile testing under different strain rates and temperature conditions were analyzed in order to understand the effect of these changes against the microstructure of AA5182 aluminum.

# Bibliography

- [1] E. A. Starke Jr., J.T. Staley, “24 – Application of modern aluminum alloys to aircraft,” *Fundamentals of Aluminum Metallurgy*, pp. 747-783, 2011.
- [2] S. Kleinbaum, C. Jiang, S. Logan, “Enabling sustainable transportation through joining of dissimilar lightweight materials,” *MRS Bulletin* 44, pp. 608-612, 2019.
- [3] J. E. Gould, “Joining aluminum sheet in the automotive industry – A 30 year history,” *AWS Welding Journal*, Vol. 91, No. 2, pp. 23s-34s, 2012.
- [4] V. Smil, “Chapter 10 – Looking Ahead: The Future of Iron and Steel,” *Still the Iron Age: Iron and Steel in the Modern World*, pp. 203-228, 2016.
- [5] R. Schneider, B. Heine, R. J. Grant, Z. Zouaoui, “Mechanical behaviour of aircraft relevant aluminum wrought alloys at low temperatures,” *IMechE Part L: J Materials*, 2013.
- [6] M. Murugesan, M. Sajjad, D. W. Jung, “Experimental Investigations on Incremental Sheet Forming of Commercial Aluminum Alloys for Maximum Production Quality,” *International Journal of Mechanical Engineering and Robotics Research*, Vol. 9, No. 9, 2020.
- [7] G. Hussain, M. Ilyas, B.B. Isidore, W. A. Khan, “Mechanical properties and microstructure evolution in incremental forming of AA5754 and AA6061 aluminum alloys,” *Transactions of Nonferrous Metals Society of China*, Volume 30, Issue 1, pp. 51-64, 2020.
- [8] J. Jeswiet, E. Hagan, A. Szekeres, “Forming parameters for incremental forming of aluminum alloy sheet metal,” *Proc. Instn. Mech. Engrs. Vol. 216, Part B: J Engineering Manufacture*, pp.1367-1371, 2020.
- [9] S. Ouyang, C. Li, L. Du, Z. Li, Z. Lai, T. Peng, X. Han, Q. Cao, L. Li, “Electromagnetic forming of aluminum alloy sheet metal utilizing a low-frequency discharge: A new method for attractive forming,” *Journal of Materials Processing Technology*, Vol. 291, 171001, 2021.

- [10] P. Arumugam, K. ShanmugaSundaram, N. KamalaKannan, “Experimental Study of Electromagnetic Sheet Metal Forming Process,” *Procedia Engineering*, vol. 97, pp. 277-290, 2014.
- [11] X. Liu, Y. Xu, S. Yuan, “Hydro-forming of aluminum alloy complex-shaped components,” *Transactions of Nonferrous Metals Society of China*, Vol. 21, Sup. 2, pp. 417-422, 2011.
- [12] E. Argandona, L. Galdos, R. Ortubay, J. Mendiguren, X. Agirretxe, “Room temperature Forming of AA7075 Aluminum Alloys: W-Temper Process,” *Key Engineering Materials*, vol. 651, pp. 199-204.
- [13] J.R. Davis, *Alloying: Understanding the Basics: Aluminum and Aluminum Alloys*, *ASM International*, pp. 351-416, 2001.
- [14] P. Tebbe, G. Kridli, “Warm forming of aluminum alloys: an overview and future directions,” *International Journal of Materials and Product Technology*, vol. 21, 2004.
- [15] K. Zheng, D. J. Politis, L.W. Wang, J. Lin, “A review on forming techniques for manufacturing lightweight complex-shaped aluminum panel components,” *International Journal of Lightweight Materials and Manufacture*, Vol. 1, No. 2, pp. 55-80, 2018.
- [16] N. Abedrabbo, F. Pourboghrat, J. Carsley, “Forming of AA5182-O and AA5754-O at elevated temperatures using coupled thermo-mechanical finite element models,” *International Journal of Plasticity*, pp. 841-875, 2007.
- [17] S. Kim, C. Butcher, K. Omer, “Elevated temperature forming of aluminum and magnesium alloys: Hot forming of high strength Aluminum Alloy Sheet,” *University of Waterloo*, 2017.
- [18] R. Nogueira de Codes, O. S. Hopperstad, O. Engler, O.G. Lademo, “Spatial and Temporal Characteristics of Propagating Deformation Bands in AA5182 Alloy at Room Temperature,” *Metallurgical and Materials Transactions A*. 42., pp. 3358-3369, 2011.
- [19] F. Shehata, M.J. Painter, R. Pearce, *Journal of Mechanical Working Technology*, Volume 2, Issue 3, pp. 279-290, 1978
- [20] P. J. Bolt, N. A. P. M. Lamboo, P. J. C. M. Rozier, *Journal of Materials Processing Technology*, 115, pp. 118–121, 2001.
- [21] S. Kurukuri, A.H. van den Boogaard, A. Miroux, B. Holmedal, *Journal of Materials Processing Technology*, Volume 209, Issues 15–16, pp. 5636-5645, 2009.

- [22] X. Fan, Z. He, S. Yuan, P. Lin, *Materials Science and Engineering: A* Volume 587, pp. 221–227, 2013.
- [23] M. Kumar, N. Sotirov, C. Chimani, *Materials Science Forum*, Vols. 794-796, pp. 796-801, 2014.
- [24] H.K Kim, W.J. Kim, “A Springback Prediction Model for Warm Forming of Aluminum Alloy Sheets Using Tangential Stresses on a Cross-Section of Sheet,” *Metals – Open Access Metallurgy Journal*, 2018.
- [25] M Hanson, *On Adhesion and Galling in Metal Forming*, PhD Dissertation, Uppsala University, pp. 8-9, 2008.
- [26] L. Pelcastre, *Hot Forming Tribology: Galling of Tools and Associated Problems*, MAsc. Thesis, Lulea University of Technology, 2011.
- [27] K. Dohda, C. Boher, F. Rezai-Aria, N. Mahayotsanun, “Tribology in metal forming at elevated temperatures,” *Friction*, vol. 3, no. 1, pp. 1-27, 2015.
- [28] S. Jhavar, C. Paul, N. Jain, “Causes of Failure and Repairing Options for Dies and Molds: A review,” *Engineering Failure Analysis*, vol. 34, pp. 519-535, 2013.
- [29] R. Ebara, K. Kubota, “Failure analysis of hot forging dies for automotive components,” *Engineering Failure Analysis*, vol. 15, no. 7, pp. 881-893, 2008.
- [30] R. Schneider, B. Heine, R.J. Grant, R. Kelsch, F. Gertsner, T. Hagele, “Low Temperature Mechanical Properties of Wrought Aluminum Alloys Applicable to the Automotive Sector, Magazine WOMag, 2013.
- [31] S. Fritsch, M. Scholze, M.F.-X. Wagner, “Cryogenic forming of AA7075 by Equal-Channel Angular Pressing,” *Materials Science & Engineering Technology*, Volume 43, Issue 7, 2012.
- [32] F. Ostermann, *Application of Aluminum Technology*, Springer Verlag 2007, ISBN: 978-3-540-71196-4.
- [33] J.G. Kaufman, *Properties of Aluminum Alloys: Tensile, Creep, and Fatigue Data at High and Low Temperature*, ASM International, 1999, ISB: 978-0-87170-632-4.
- [34] A. Poznek, *Automotive Wrought Aluminum Alloys, Fundamentals of Aluminum Metallurgy*, 2018.
- [35] J.R. David, *Aluminum and Aluminum Alloys: Light Metals and Alloys, Alloying: Understanding the Basics*, pp. 356, 2001.

- [36] E.L. Huskins, B. Cao, K.T. Ramesh, "Strengthening mechanisms in an Al-Mg alloy," *Materials Science and Engineering A*, 527, pp. 1292-1298, 2010.
- [37] J.E. Hatch, *Aluminum: Properties and Physical Metallurgy*, American Society for Metals, Metals Park, On, 1984.
- [38] M. F. Ashby, D. R. H. Jones, "Light Alloys," *Engineering Materials 2: An Introduction to Microstructures and Processing*, 4th ed., pp. 190-191, 2013.
- [39] D.J. Lloyd and S.A. Court, *Mater. Sci. and Tech.*, 19, 1349-1354, 2003.
- [40] Y. Li, A. J. Bushby, and D.J. Dunstan, "The Hall-Petch effect as a manifestation of the general size effect," *Proceedings of the Royal Society A*, vol. 472, issue 2190, 2016.
- [41] Y. Song, J. Yeon, and B. Na, "Numerical Simulations of the Hall-Petch Relationship in Aluminum Using Gradient-Enhanced Plasticity Model," *Advances in Civil Engineering*, 2019.
- [42] J.R. Davis, "Aluminum and Aluminum Alloys," *Alloying: Understanding the Basics*, ASM International, p. 351-416, 2013.
- [43] M. F. Ashby, D. R. H. Jones, "Light Alloys," *Engineering Materials 2: An Introduction to Microstructures and Processing*, 4th ed., pp. 110, 2013.
- [44] M. F. Ashby, D. R. H. Jones, "Light Alloys," *Engineering Materials 2: An Introduction to Microstructures and Processing*, 4th ed., pp. 192, 2013.
- [45] M. F. Ashby, D. R. H. Jones, "Light Alloys," *Engineering Materials 2: An Introduction to Microstructures and Processing*, 4th ed., pp. 111, 2013.
- [46] C.N. Panagopoulos, E.P. Georgiou, "Cold rolling and lubricated wear of 5083 aluminum alloy," *Materials and Design*, vol. 31, no. 3, pp. 1050-1055, 2010.
- [47] N. Abedrabbo, F. Pourboghra, J. Carsley, "Forming of AA5182-O and AA5754-O at elevated temperatures using coupled thermos-mechanical finite element models," *International Journal of Plasticity*, Volume 23, Issue 5, pp. 841-875, 2007.
- [48] W. Shenghua, et.al, "The variation of the Lankford coefficient in magnesium alloy," *Conference: International Deep Drawing Research Group*, 2014.
- [49] N. Sotirov, G. Falkinger, F. Grabner, G. Schmid, R. Schneider, R.J. Grant, R. Kelsch, K. Radlmayr, M. Scheerer, C. Reichl, H. Sehrscho, M. Loipetsberger, "Improved Formability of AA5182 Aluminum Alloy Sheet at Cryogenic Temperatures," *Materialstoday: Proceedings*, Volume 2, Supplement 1, pp. S113-S118, 2015.

- [50] J. Li, Characterization of Post-Annealing Mechanical Behavior of Performed Aluminum Alloy 5182-O, PhD Dissertation, University of Michigan, 2011.
- [51] D. Banabic, K. Siegert, "Anisotropy and formability of AA5182-O aluminum alloy sheets," CIRP, Volume 53, Issue 1, pp. 219-222, 2004.
- [52] O.S.I. Fayomi, A.P.I. Popoola, N.E. Udoye, "Effect of Alloying Element on the Integrity and Functionality of Aluminum-Based Alloy," Aluminum Alloys – Recent Trends in Processing, Characterization, Mechanical Behavior and Applications, 2017.
- [53] S.W. Nam, D. H. Lee, "The effect of Mn on the mechanical behavior of Al alloys," Metals and Materials 6, 13, 2000.
- [54] W. Miller, L. Zhuang, J. Bottema, A. Wittebrood, P. De Smet, A. Haszler, and A. Vieregge, "Recent development in aluminum alloys for the automotive industry," Materials Science and Engineering: A, vol. 280, pp. 37-49, 2000.
- [55] S.M. de la Puente, B. Verlinden, L. Delaey, Journal of Material Science 29, 6167, 1994.
- [56] P. Ratchev, B. Verlinden, P. van Houtte, P. de Smet, Material Science Engineering A 222, 189, 1997.
- [57] W. S. Ebhota, T.C. Jen, "Intermetallics Formation and Their Effect on Mechanical Properties of Al-Si-X Alloys," Intermetallic Compounds – Formation and Applications, 2018. ISBN: 978-1-78923-179-3
- [58] E. A. Starke Jr., Encyclopedia of Materials: Science and Technology, Aluminum: Alloying, 2001
- [59] A. Jenab, D. E. Green, A. T. Alpas, "Microscopic investigated of failure mechanisms in AA5182-O sheets subjected to electro-hydraulic forming," Materials Science and Engineering A, Volume 691, pp. 31-41, 2017.
- [60] D. J. Llyod, "Some Aspects of the Metallurgy of Automotive Al Alloys," Materials Forum, vol. 28, pp. 107-117, 2004.
- [61] A. Pineau, T. Pardoen, "Fundamental Theories and Mechanisms of Failure: Fracture Strain of Metals," Comprehensive Structural Integrity, vol. 2, pp.684-797, 2007.
- [62] R.O. Smerd, "Constitutive Behavior of Aluminum Alloy Sheet at High Strain Rates," MAsc. Thesis, University of Waterloo, 2005.

- [63] M. Bambach, I. Sizova, S. Bolz, and S. Weib, "Devising Strain Hardening Models Using Kocks-Mecking Plots—A Comparison of Model Development for Titanium Aluminides and Case Hardening Steel," *Metals*, vol. 6, issue 204, 2016.
- [64] Z. Peng, et. al, "Solute cluster evolution during deformation and high strain hardening capability in naturally aged Al-Zn-Mg alloy," *Acta Materialia*, 2021.
- [65] J. Teixeira, et. al. "The Strain Hardening Behaviour of Supersaturated Al-Cu Alloys," *Proceedings of the 12<sup>th</sup> International Conference on Aluminum Alloys*, pp. 536-541, 2010.
- [66] A. Mishra, "Friction Stir Welding of Dissimilar Metal: A Review," *International Journal for Research in Applied Science & Engineering Technology*, vol. 6, no. 1, 2018.
- [67] J.W. Martin, "Aluminum: Alloying," *Concise Encyclopedia of the Structure of Materials*, 2007. ISBN: 978-0-08-045127-5.
- [68] P. Schempp, C.E. Cross, R. Hacker, A. Pittner, "Influence of grain size on mechanical properties of aluminum GTA weld metal," *The International Journal of Materials Joining: Welding in the World*, vol. 57, no. 3, pp. 294-304, 2013.
- [69] M. F. Ashby, "Phase Diagrams and Phase Transformations," Cambridge: Teach Yourself, ed. 5, 2009.
- [70] D.S. D'Antuono,  $\beta$  Phase Growth and Precipitation in the 5xxx-Series Aluminum Alloy System, MASc. Thesis, Drexel University, 2017.
- [71] R.C. Picu, G. Vincze, F. Ozturk, J.J. Gracio, F. Barlat, A.M. Maniatty, "Strain rate sensitivity of the commercial aluminum alloy AA5182-O," *Materials Science and Engineering A*, volume 390, issues 1-2, pp. 334-343, 2005.
- [72] P. Ratchev, B. Verlinden, P. van Houtte, "Effect of preheat temperature on the orientation relationship of (Mn,Fe)Al<sub>6</sub> precipitates in an AA 5182 Aluminum-Magnesium alloy," volume 43, issues 2, pp. 621-629, 1995.
- [73] Z. Chen, "Second phase particle distribution and its effect on the formability of aluminum alloys," *Computational Methods and Experiments in Materials Characterization II*, vol. 51, pp. 53-62, 2005.
- [74] M.J. Hadianfard, R. Smerd, S. Winkler, M. Worswick, "Effects of strain rate on mechanical properties and failure mechanism of structural Al-Mg alloys," *Materials Science and Engineering A*, volume 40, issues 10, pp. 283-292, 2008.

- [75] M.S. Remoe, The Effect of Alloying Elements on the Ductility of Al-Mg-Si Alloys, M.A.Sc. Thesis, Norwegian University of Science and Technology, 2014.
- [76] A.K. Pilkey, J.P. Fowler., M.J. Worswick, G. Burger, and D.J. Lloyd, "Characterizing particle contributions in model aluminum alloy systems," *Microstructural Science*, Vol. 22, ASM, 1995.
- [77] P. Noell, J. Carroll, K. Hattar, B. Clark, B. Boyce, "Do voids nucleate at grain boundaries during ductile rupture?" *Acta Materialia*, Vol. 137, pp. 103-114, 2017.
- [78] J.J. Williams, G. Piotrowski, R. Saha, N. Chawla, "Effect of overaging and particle size on tensile deformation and fracture of particle-reinforced aluminum matrix composites," *Metallurgical and Materials Transactions A*, vol. 33, pp. 3861-3869, 2002.
- [79] H. Li, M. Fu, "Tension-Induced Void Initiation, Growth, and Coalescence," *Deformation-Based Processing of Materials*, 2019. ISBN: 978-0-12-814381-0
- [80] R.E. Smallman, "Strengthening and toughening: Ductile failure," *Modern Physical Metallurgy and Materials Engineering*, ed. 6, 1999.
- [81] D. Hull, "Fractography Observing, Measuring and Interpreting Fracture Surface Topography," Cambridge University Press, 1999.
- [82] R. Singh, "Introduction to Basic Metallurgy: Fracture," *Applied Welding Engineering: Processes, Codes, and Standards*, ed. 2, pp. 100, 2016.
- [83] P.J. Noell, J. E.C. Sabisch, D. L. Medlin, B.L. Boyce, "Nanoscale conditions for ductile void nucleation in copper: vacancy condensation and the growth-limited microstructural state," *Acta Materialia*, vol. 184, pp. 211-224, 2020.
- [84] A. A. Benzerga, J.B. Leblond, "Ductile Fracture by Void Growth to Coalescence," *Advances in Applied Mechanics*, vol. 44, pp. 169-305, 2010.
- [85] P. Kossakowski, "Influence of Initial Porosity on Strength Properties of S235JR Steel at Low Stress Triaxiality," *Archives of Civil Engineering*, Volume 58, Issue 3, pp. 293-308, 2012.
- [86] C. Tekoglu, J.W. Hutchinson, T. Pardoen, "On localization and void coalescence as a precursor to ductile fracture," *Philosophical Transactions of the Royal Society A Mathematical Physical and Engineering Sciences*, vol. 373, 2015.
- [87] B. Verlinden, J. Driver, I. Samajdar, R.D. Doherty, "Chapter 5: Softening mechanisms," *Pergamon Materials Series*, vol. 11, pp. 83-108. 2007.

- [88] T.F. Morgeneuer, L. Helfen, H. Mubara, F. Hild, "3D Digital Volume Correlation of Synchrotron Radiation Laminography Images of Ductile Crack Initiation: An Initial Feasibility Study," *Experimental Mechanics*, vol. 53, pp. 543-556, 2013.
- [89] C.R. Brooks, A. Choudhury, *Failure Analysis of Engineering Materials. Glossary.* McGraw-Hill Education, 2002.
- [90] K.B. Broberg, "The Process Region," *Cracks and Fracture*, pp. 5-26, 1999.
- [91] E. Pink, A. Grinberg, *Praktische aspekte des Portevin-LeChatelier-effektes (1).* *Aluminum* 1984; 60; pp. 687-691.
- [92] E. Pink, A. Grinberg, *Praktische aspekte des Portevin-LeChatelier-effektes (1).* *Aluminum* 1984; 60; pp. 764-768.
- [93] J. L. Gonzalez-Velazques, "Fractography and Failure Analysis," *Brittle and Ductile Fracture*, vol. 3, pp. 49-69, 2018.
- [94] I. Barsoum, "Ductile Failure and Rupture Mechanisms in Combined Tension and Shear," a Licentiate Thesis, Department of Solid Mechanics of Royal Institute of Technology (KTH), 2002-2006.
- [95] R.W. Hertzberg, "Ductile Fracture," *Deformation and Fracture Mechanics of Engineering Materials*, ed. 3, pp. 191-193, 1989.
- [96] H. Yamada, T. Kami, R. Mori, T. Kudo, M. Okada, "Strain Rate Dependence of Material Strength in AA5xxx Series Aluminum Alloys and Evaluation of Their Constitutive Equation," *Metals* 8, 576, 2018.
- [97] G. E. Dieter, "Effect of Strain Rate on Tensile Properties," *Mechanical Metallurgy*, McGraw Hill Book Company, pp. 1961.
- [98] R.C. Picu, "A mechanism for the negative strain-rate sensitivity of dilute solid solutions," *Acta Materialia*, Volume 52, Issue 12, pp. 3447-3458, 2004.
- [99] S. Gupta, A. J. Beaudoin Jr., J. Chevy, "Strain rate jump induced negative strain rate sensitivity (NSRS) in aluminum alloy 2024: Experiments and constitutive modeling," *Materials Science and Engineering: A*, vol. 683, pp. 143-152, 2017.
- [100] A. Yilmaz, "The Portevin-Le Chatelier effect: a review of experimental findings," *Science and Technology of Advanced Materials*, Volume 12, Issue 6, 2011.
- [101] P. Hahner, "Modelling the spatiotemporal aspects of the Portevin-Le Chatelier effect," *Fundamental Aspects of Dislocation Interactions*, 1993.

- [102] R.A. Mulford, U.F. Kocks, "New observations on the mechanisms of dynamic strain ageing and of jerky flow," *Acta Metall*, Volume 27, pp. 1125-1134, 1979.
- [103] O. Waseda, R. Veiga, M. Julien, P. Chantrenne, "Formation of carbon Cottrell atmospheres and their effect on the stress field around an edge dislocation," *Scripta Materialia*, Vol. 129, Issue 16-19, 2017.
- [104] E. Epperly, R. Sills, "Dynamics of Cottrell Atmospheres and Dislocations," Sandia National Laboratories, 2018.
- [105] P.G. McCormick, *Acta Metall.* 20, 3, pp.351–354, 1972.
- [106] L.P. Kubin, Y. Estrin, *Acta Metall. Mater.* 38, 5, pp.697–708, 1990.
- [107] T. Kami, H. Yamada, and N. Ogasawara, "Dynamic behaviour of Al-Mg alloy at a wide range of strain rates," *DYMAT: EPJ Web of Conferences*, vol. 183, 2018.
- [108] R. Maass, *Micro-plasticity and recent insights from intermittent and small-scale plasticity*, *Acta Materialia*, vol. 143, pp. 338-363, 2018.
- [109] M. Zaiser, "Scale invariance in plastic flow of crystalline solids," *Advances in Physics*, 2007.
- [110] S. Papanikolaou, *Avalanches and plastic flow in crystal plasticity: an overview*, 2017.
- [111] H. Li, *Continuous strain bursts in crystalline and amorphous metals during plastic deformation by nanoindentation*, 2011.
- [112] M. Sakamoto, *Mater. Trans. JIM.* 1989; 30:337.
- [113] E. Pink, *Scr. Met. Mater.* 1994; 30:767. Doi: 10.1016/0956-716X(94)90196-1.
- [114] S. Serajzadeh, H. Sheikh, *Investigation into occurring dynamic strain aging in hot rolling of AA5083 using finite elements and stream function method*, 2008.
- [115] B.J. Brindley, P.J. Worthington, *Yield-point phenomena in substitutional alloys*, 2013.
- [116] J.M. Robinson, M.P. Shaw, *Microstructural and mechanical influences on dynamic strain aging phenomena*, 2013.
- [117] D. Gruyter, *Modelling the Portevin-Le Chatelier effects in aluminum alloys: a review*, *Journal of the Mechanical Behavior of Materials*, Volume 24, Issue 3-4, 2015.

- [118] H. Jiang, Q. Zhang, X. Chen, Z. Chen, Z. Jiang, Z. Wu, J. Fan, Three types of Portevin-Le Chatelier effects: Experiment and modelling, *Acta Materialia*, Volume 55, Issue 7, pp. 2219-2228, 2006.
- [119] L. Casarotto, R. Tutsch, R. Ritter, H. Dierke, F. Klose, and H. Neuhauser, "Investigation of PLC bands with optical techniques," *Comput. Mat. Sci.*, Volume 32, Issue 3-4, pp. 316-322, 2005.
- [120] H. Ait-Amokhtar, C. Fressengeas, Crossover from continuous to discontinuous propagation in the Portevin-Le Chatelier effect, *Acta Materialia*, Volume 58, Issue 4, pp. 1342-1349, 2010.
- [121] R. C. Picu, R. Li, On the relationship between the Cottrell-Stokes law and the Haasen plot, 2010.
- [122] R.C. Picu, G.T. Vincze, J.J. Gracio, Deformation and microstructure-independent Cottrell-Stokes ratio in commercial Al alloys, 2011.
- [123] G. Ananthakrishna, F. R. B. Nabarro, J. P Hirth, *Dislocations in Solids*, New York: Elsevier, pp. 81, 2007.
- [124] H. Neuhauser, F.B. Klose, F. Hagermann, J. Weidenmuller, H. Dierke, P. Hahner, On the PLC effect in strain-rate and stress-rate controlled tests-studies by laser scanning extensometry, *Journal of Alloys and Compounds*, Volume 378, Issues 1-2, pp. 13-18, 2004.
- [125] A. H. Cottrell, R. J. Stokes, *Effects of Temperature on the Plastic Properties of Aluminum Crystals*, 1955.
- [126] R. W. K. Honeycombe "Deformation of Metal Crystals," *The Plastic Deformation of Metals*, ed. 2, pp. 104-105, 1984.
- [127] G. Testa, N. Bonora, A. Ruggiero, G. Iannitti, Flow stress of bcc metals over a wide range of temperature and strain rates, 2019.
- [128] Z. Trojanova, K. Mathis, P. Lukac, G. Nemeth, F. Chmelik, Internal stress and thermally activated dislocation motion in an AZ63 magnesium alloy, *Materials Chemistry and Physics*, 2011.
- [129] H. Conrad, The athermal component of the flow stress in crystalline solids. *Mater. Sc. Eng.* 1970, 6, 265-273, doi:10.1016/0025-5416(70)90054-6.
- [130] D. Caillard, J.L. Martin, *Thermally Activated Mechanisms in Crystal Plasticity*, in Pergamon Materials Series, vol 8, pages 13-53, 2003.

- [131] S. Bruschi, T. Altan, D. Banabic, P.F. Bariani, A. Brosius, J. Cao, A. Ghiotti, M. Khraisheh, M. Merklein, 2014.
- [132] M. Piao, H. Huh, I. Lee, Characterization of flow stress at ultra-high strain rates by proper extrapolation with Taylor impact tests, 2016.
- [133] M. Mirmomeni, A. Heidarpour, X. Zhao, Fracture behaviour and microstructural evolution of structural mild steel under the multi-hazard loading of high-strain-rate load followed by elevated temperature.
- [134] C.P Ling, P.G. McCormick, *Acta Met. Mater.*, Volume 41, pp. 3127, 1993.
- [135] C.P Ling, P.G. McCormick, *Acta Met. Mater.*, Volume 38, pp. 2631, 1990.
- [136] P. Wycliffe, U.F. Kocks, and J.D. Embury, "On dynamic and static strain ageing in substitutional and interstitial alloys," *Scripta Metallurgica*, vol. 14, pp. 1349-1354, 1980.
- [137] X. Jia, "Solid Solution Strengthening and Texture Evolution in Mg-Y alloys," M.A.Sc. Thesis, McMaster University, pp. 17-19, 2013.
- [138] M. Jobba, R. K. Mishra, M. Niewczas, "Flow stress and work hardening behavior of Al-Mg binary alloys," *International Journal of Plasticity*, Volume 65, 2014.
- [139] L. Hou, M. Liu, X. Wang, L. Zhuang, J. Zhang, "Cryogenic Processing High-Strength 7050 Aluminum Alloy and Controlling of the Microstructures and Mechanical Properties," *Acta Metallurgica Sinica*, Vol. 53, No. 9, 2017.
- [140] J. Kang, D.S. Wilkinson, M. Jain, J.D. Embury, A.J. Beaudoin, S. Kim, R. Mishra, A.K. Sachdev, "On the sequence of inhomogeneous deformation processes occurring during tensile deformation of strip cast AA5754," Volume 54, Issue 1, pp. 209-218, 2006.
- [141] D.Y. Park, M. Niewczas, "Plastic deformation of Al and AA5754 between 4.2 K and 295 K," *Materials Science and Engineering A*, vol. 491, pp. 88-102, 2008.
- [142] I. Yasnikov, A. Vinogradov, Y. Estrin, "Revisiting the Considère criterion from the viewpoint of dislocation theory fundamentals," *Scripta Materialia*, vol. 76, pp. 37-40, 2014.

# 3 Methodology

## 3.1 Material Characterization

### 3.1.1 Grinding, Polishing, and Etching

Initial material characterization of the AA5182-O aluminum alloy involved preparing samples for grinding, polishing, and subsequent etching to obtain images of the material's microstructure. Large sheets of as-received AA5182 aluminum, with a thickness of 1.5 mm, were cut down using a sheet metal shearing machine and a low-speed diamond saw cutter (shown in **Figure 3.1(a)** and **(b)** respectively).



**Figure 3.1** Image of the (a) sheet metal shearing machine [1] and (b) low speed diamond saw cutter used to AA5182-O aluminum alloy samples for grinding and polishing.

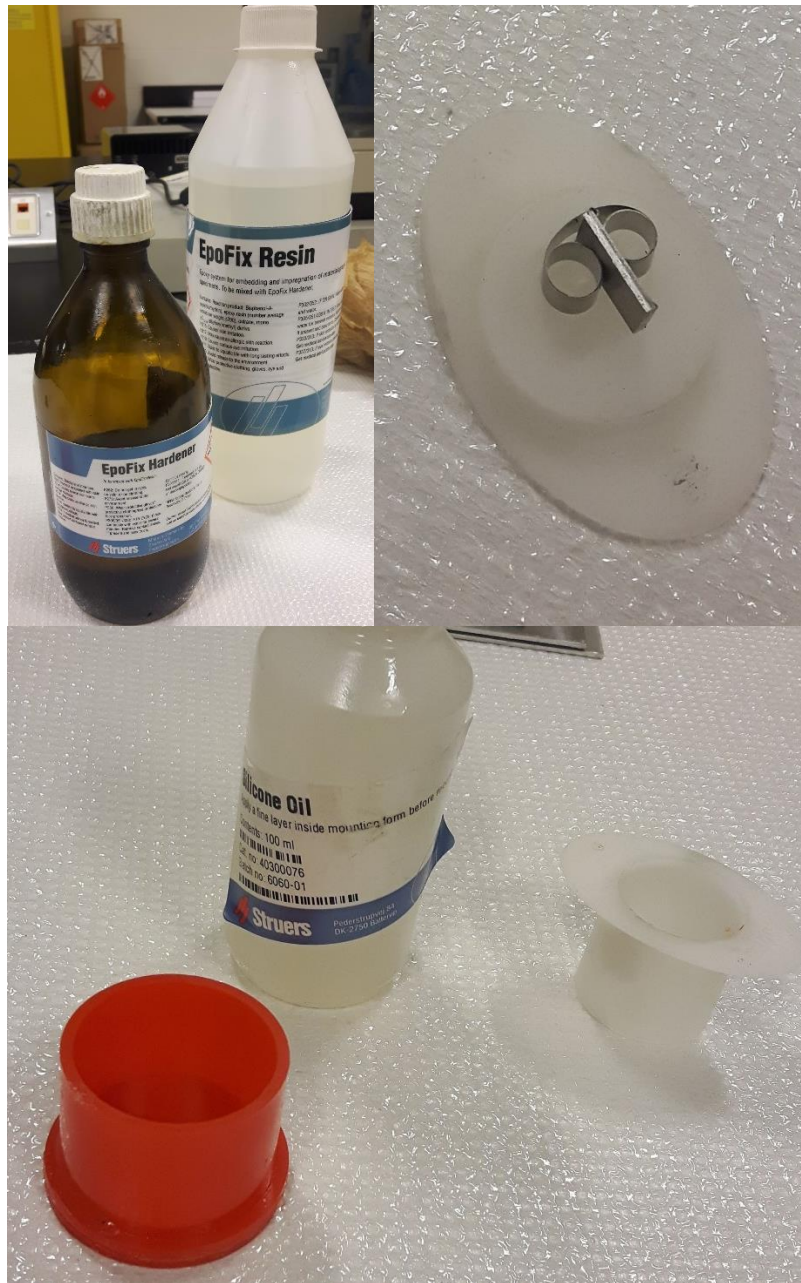


**Figure 3.1** AA5182-O as received samples mounted in one part Epoxy Hardener and two parts Epoxy Resin (used to expose the face of the metal, rolling direction, and parallel to the rolling direction).

These samples were cut to a size of 25 mm by 25 mm and then mounted in the as-received condition using one-part Epoxy Hardener and two-parts Epoxy Resin. The samples were mounted with the face of the sheet metal, the rolling direction, and parallel to the rolling direction exposed. Samples were set onto a plastic holder and held up using a metallic clip, as shown in **Figure 3.2**, and left for approximately 24 hours to fully set. This step was done to provide a more controllable specimen for the subsequent grinding and polishing steps. Silicone oil was brushed onto the plastic holders and used to reduce the amount of sticking of the hardened resin and hardener mixture to the plastic casing.

Manual grinding was completed using a series of increasing grit SiC abrasive paper, water as lubrication, and a lapping/polishing machine (as shown in **Figure 3.3**).



**Figure 3.3** Buehler EcoMet metallographic polishing machine.

The purpose of grinding the samples was to remove any damage to the surface of the material. Metallographic abrasive grinding is required to capture proper images during optical microscopy, OM, and scanning electron microscopy, SEM, analysis. For soft, non-ferrous materials, it is important to minimize embedded abrasives or surface deformation. It is important to note that aluminum is a material that oxidizes very quickly and should be carefully rinsed with ethanol during each step to prevent oxidation of the surface. Washing

the surface with ethanol has an additional purpose of removing any leftover SiC particles from the previous grit paper. **Table 3.1** outlines the grinding procedure and the series of abrasive papers used.

**Table 3.1** Metallographic Abrasive Grinding Procedure

<b>Abrasive Grit Paper</b>	<b>Lubrication</b>
P120 grit ALO paper	Water as lubrication and washed with ethanol
P220 grit ALO paper	Water as lubrication and washed with ethanol
P500 grit ALO paper	Water as lubrication and washed with ethanol
P1200 grit ALO paper	Water as lubrication and washed with ethanol

Sufficient pressure was given to press the specimen against the surface of the grit paper, attempting to keep the contact between both as even and flat as possible. After approximately 1-2 minutes of grinding, the sample was rotated at a 90° angle to ensure that any previous grinding damage was removed. This step was repeated a second time until any scratches caused by the previous grinding direction were visibly removed.

After grinding, samples were polished using 3 micro-m diamond suspension and a polishing cloth and 1 micro-m diamond suspension with a polishing cloth. Water was used during this step as an in-process grinding fluid, and ethanol was used between each step to ensure the removal of any previous particles and to prevent oxidation of the surface.

Samples were etched using a concentrated Keller’s reagent. The acid solution is used to reveal the grain structure in order to calculate the grain size of the alloy as well as second phases of the material. Concentrated Keller’s reagent is often recommended for pure aluminum, aluminum-magnesium, and aluminum-magnesium-silicon alloys [2]. The microstructure of samples was revealed using this etchant and optical microscopy. All samples were stored in a low oxygen tank to reduce any oxidation to the etched faces and maintain a visible surface for further microscopy analysis.

**Table 3.2** Revised Keller's Etchant for Aluminum-Magnesium Alloys [2]

<b>Etchant</b>	<b>Concentration</b>	<b>Conditions</b>
Methanol	25 ml	10-60 second immersion
Hydrochloric Acid	25 ml	
Nitric Acid	25 ml	
Hydrofluoric Acid	1 drop	

### 3.1.2 Hardness Testing

The hardness of a material can often be measured by pressing an indenter of specific shape, size, and load and calculating the value with the relevant formula. As a result of the thin geometry of the sheet metal used (approximately 1.5 mm thickness), a Vickers Hardness test, also referred to as a micro hardness test, was used. A Vickers Hardness test typically involves using a pyramid diamond shape to press a predetermined load into the surface of the specimen. Hardness tests were conducted using a Buehler Micromet II Model MHT-1B Micro Hardness Tester. This machine uses a square based pyramid diamond indenter, as shown in **Figure 3.4**. A schematic of the machine is given in **Figure 3.5**.

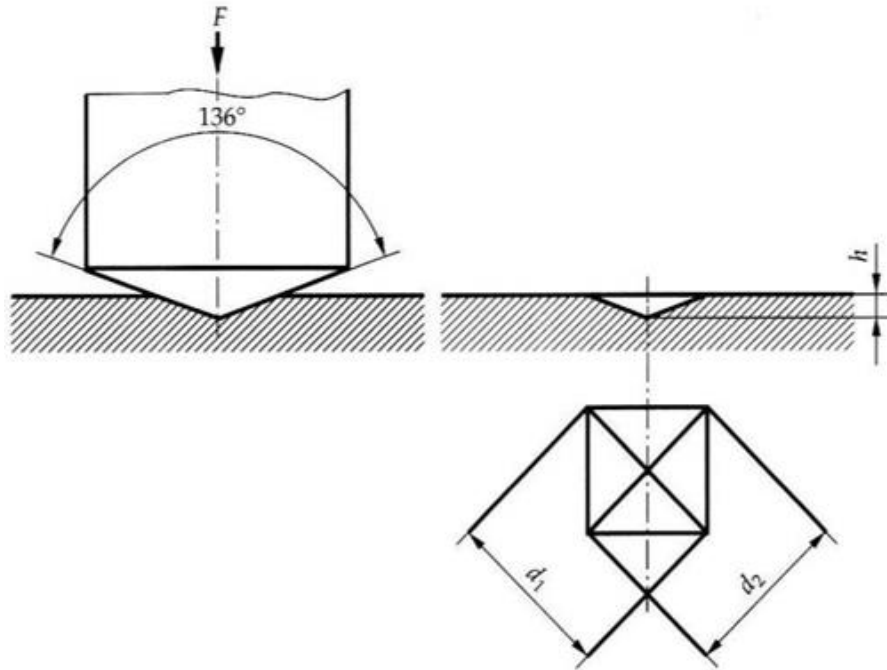


**Figure 3.4.** A schematic of a Vickers hardness test using a square based pyramid diamond indenter and showing relevant nomenclature [3].



**Figure 3.5** Buehler Micromet II model MHT-1B Micro Hardness Tester [4].

To obtain dependable results, samples were prepared using a similar method in the grinding and polishing section of the methodology. Three square shaped specimens with thickness 1.5mm and length and width 25mm by 25mm respectively were cut from AA5182 as-received sheets using both the sheet metal shearing machine and the diamond saw cutter. These samples were then mounted as described in 3.1.1, with the face of the sheet metal exposed, the rolling direction, and parallel to the rolling direction and left for approximately 24 hours to fully set.

The indenter was pressed into the surface of the sample using a load of 25 *gf* and a dwell time of 12 *s* as outlined in the ASTM E384 guidelines for standard test methods for microindentation hardness of materials [5]. The diagonals of the square based pyramid indenter were measured to the nearest 0.5  $\mu\text{m}$  using the optical microscope attached to the micro hardness tester. Tests were performed at 8 separate locations along the specimen surface to determine the overall average hardness value of the surface, rolling direction, and transverse direction of the material.

To determine the HV Vickers hardness number the following formula [3] is used,

$$HV = \frac{F}{A_s} = \frac{2P \sin\left(\frac{a}{2}\right)}{d^2} = 1854.4 \frac{F}{d^2} \quad (18)$$

Where *HV* is the Vickers hardness number, *F* is the test load, with units *gf*, and *A<sub>s</sub>* is the surface area of the indent, with units *mm<sup>2</sup>*. In the third part of the equation, *a* is the face angle of the indent, 136°, and *d* is the mean of the indent diagonals, in  $\mu\text{m}$ .

### 3.1.3 OM, SEM, and EDS

Optical Microscopy, OM, was performed using a Keyence optical microscope, as shown in **Figure 3.6**. OM was used to observe the distribution of alloying elements and check the surfaces for scratches prior to hardness testing and scanning electron microscopy, or SEM, analysis. Spectroscopy techniques were used to investigate the fracture behaviour of different samples after tensile testing, as well as a detailed chemical analysis of the size and distribution of second phase particles.

SEM analysis was conducted using an FEI Quanta 200 FEG scanning electron microscope equipped with an energy-dispersive X-ray EDAX (SiLi Detector) spectrometer, as shown in **Figure 3.7**. Prior to SEM, samples were placed inside an ultrasonic ethanol bath for two minutes to properly clean the surface to prevent any misinformation from analysis and protect the inside of the testing equipment. Conductive copper SEM tape was carefully applied to ground the sample surface to the sample holder prior to testing. The SEM analysis involved capturing images using high vacuum (HV) 15kV settings. Images of the fractured surface were taken at 50x, 100x, 200x, 800x, 1000x, and 2000x magnification for each test temperature sample. Autopano Pro software was used to stitch the SEM images of the entire fracture surface into a single image. During the SEM procedure, EDS analysis was used to determine the chemical composition of the matrix as well as intermetallic particles.



**Figure 3.6** Omano OM159T (40x-1,000x ) Trinocular Compound Microscope [6]

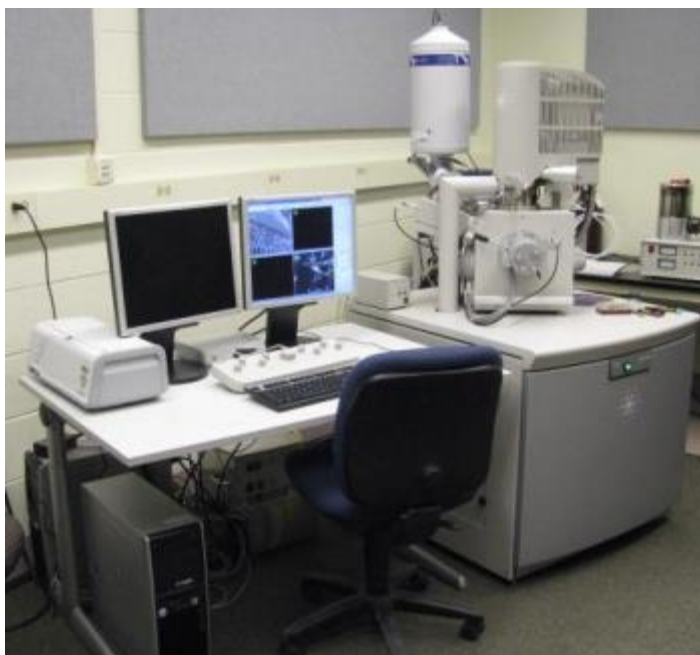


**Figure 3.7** FEI Quanta 200 FEG scanning electron microscope equipped with an energy-dispersive X-ray EDAX (SiLi Detector) spectrometer

## 3.2 Grid Application

The method of grid marking and measurement for sheet metals involves applying a pre-measured grid pattern to the surface of the specimen and measuring the changes to the grids after deformation of the specimen. Patterns are deformed by an amount that is dependent on the deformation experienced by the sheet metal. When circle grid patterns are used, this deformation can result in ellipsoidal deformation or circular deformation in the case of pure biaxial stretching, as illustrated in **Figure 3.8**. The longest measurement of the ellipse is called the major axis and the measurement that is perpendicular to the major axis is referred to as the minor axis.

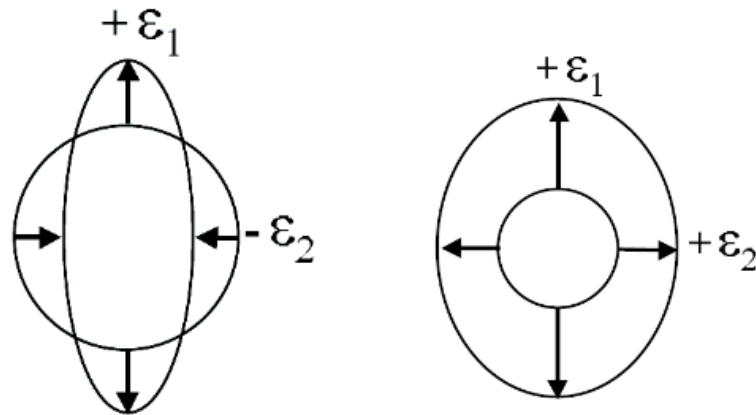


**Figure 3.8** Grid pattern circles prior to and after deformation where (a) the strain causes the circles to deform into an ellipse and (b) there is a case of pure biaxial stretching. [7]

Grid patterns were etched onto the surface of the samples using an electrochemical etching method. Electrochemical etching is one of the most commonly used methods for grid application for the evaluation of sheet metal formability. The popularity of this method of grid-marking is a result of its ease of application, the absence of any distortions to the

sheet metal, and the durability of the markings during the forming process [7]. Grid-marking was carried out using 1-mm-diameter circle grid stencils. The stencils were cut to size and placed flat against the surface of the metal. A felt pad was soaked in a solution of electrolyte 2A for a few seconds before squeezing out any excess solution. The felt pad was used to completely cover the aluminum sample and stencil and acts as a buffer between the metal alloy and the metal of the etching roller. A schematic of this setup is shown in **Figure 3.9**.

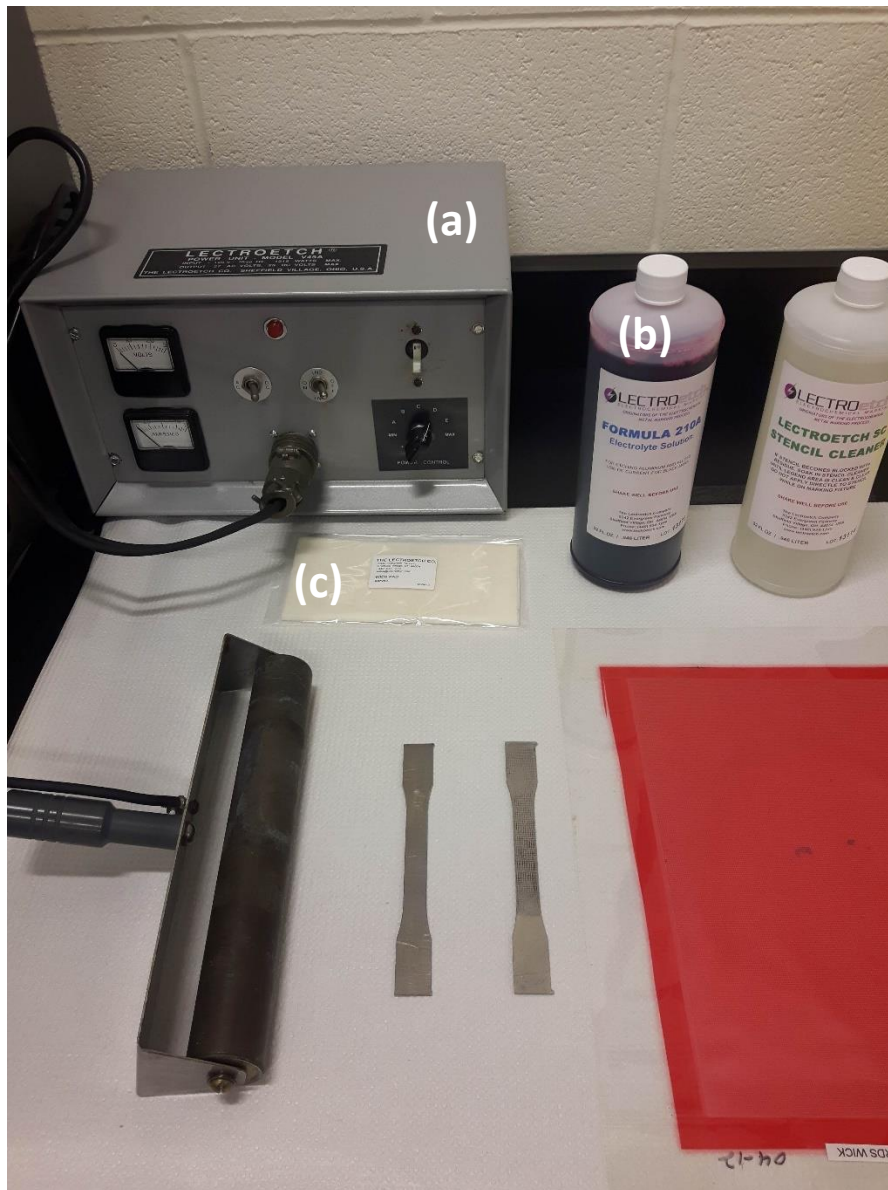


**Figure 3.9** A schematic of the apparatus used for grid pattern etching with (a) the grid marking machine and (b) the electrolyte solution and (c) felt pad.

Using the model V45A Lectroetch power unit and a DC voltage of 25 V, a metal roller was slowly rolled across the electrolyte soaked felt pad to ensure an evenly distributed grid pattern. A lint-free cloth and the formula 3 Lectroetch non-ferrous cleaning solution was used to carefully wipe the sample and remove any electrolyte build-up on the metal. This was done to avoid any corrosion and subsequent flaws on the metal. **Figure 3.10(a)** shows an image of the grid pattern stencil that was used and **(b)** shows an image of the stencil etched onto a specimen.

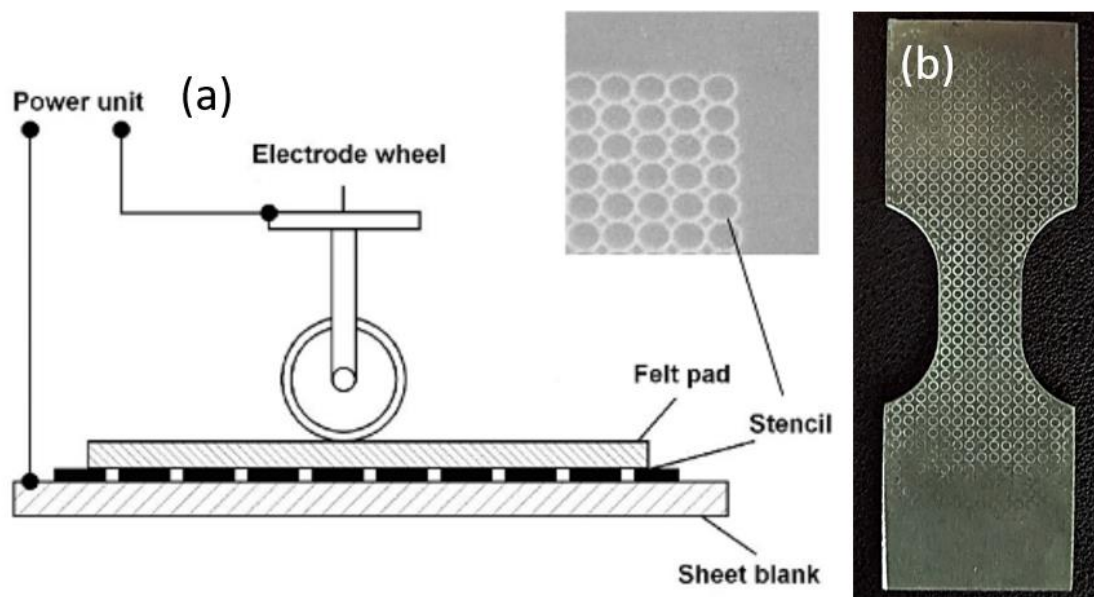


**Figure 3.10(a)** An image of the schematic and grid pattern stencil that was used [7] and **(b)** an image of the stencil etched onto an Erichsen specimen.

## 3.3 Tensile Testing

### 3.3.1 Tensile samples and testing equipment

Samples were designed using ASTM E8/E8M-16 [8] designation standards for 1.5 mm thickness sheet metal and drafted using CAD software. **Figure 3.11** shows the tensile specimen as per the E8/E8M standard. The specimen tensile length was cut in different orientations relative to the rolling direction of the sheet to investigate the effect of anisotropy of the material, as shown in **Figure 3.12**. The tensile specimen drafts were then input into a waterjet cutting machine and, once cut and removed from the machine, a hand-tool was used to remove any existing burrs that could initiate a fracture point. Tensile tests were conducted using a 300 kN MTS Universal Testing Machine model E45 (shown in **Figure 3.13**). Wedge grips were used along with diamond cut plates to account for the thinness of the samples. An MTS TestSuite TW Elite graphing software was used to create a template with inputs such as sample thickness, gauge length, and strain rate.

Measurements were taken before and after deformation. Using a digital caliper, a marker was used to indicate 50 mm gauge length on the samples. An Epsilon axial extensometer (shown in **Figure 3.14**) was attached at the gauge length of the sample during testing and feeding measurements into the MTS TestSuite TW Elite program to produce a proper load versus extension curve. The axial extensometer used was a model 3542-050M-050-LT for 50.00 mm gauge length specimens and suited for +50% to -10% travel, or 25.00mm to -5.00 mm respectively. The extensometer was also built to withstand temperature testing conditions of -270°C to 100°C.

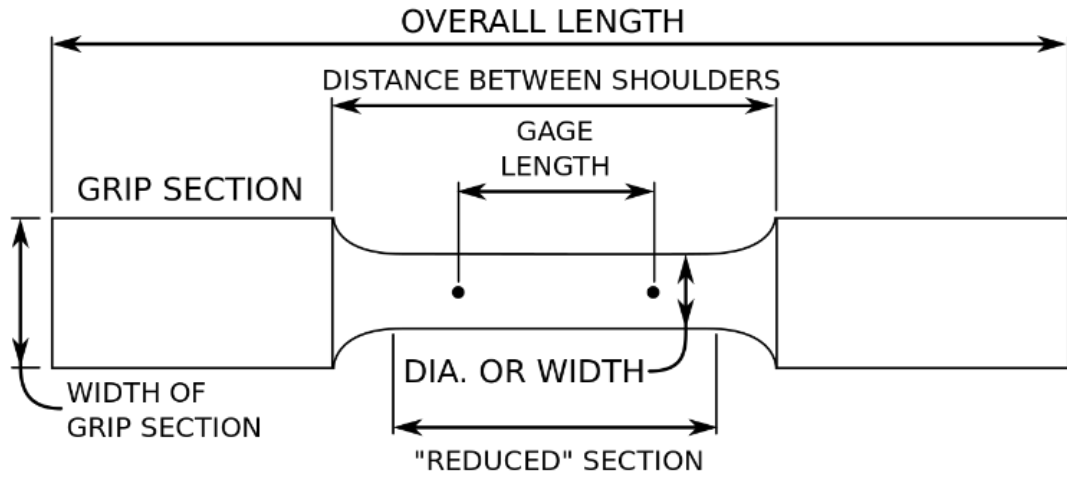


**Figure 3.11** ASTM Standard E8/E8M-16 schematic of sample [8]

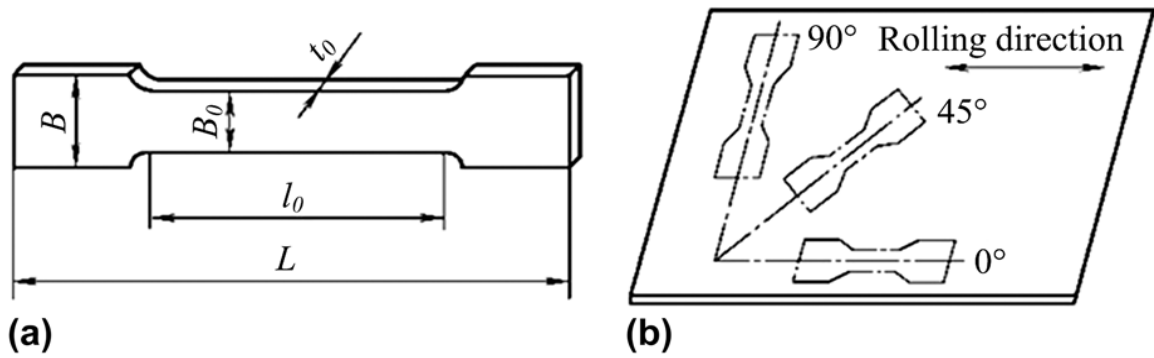


**Figure 3.12** Anisotropy directions [9]

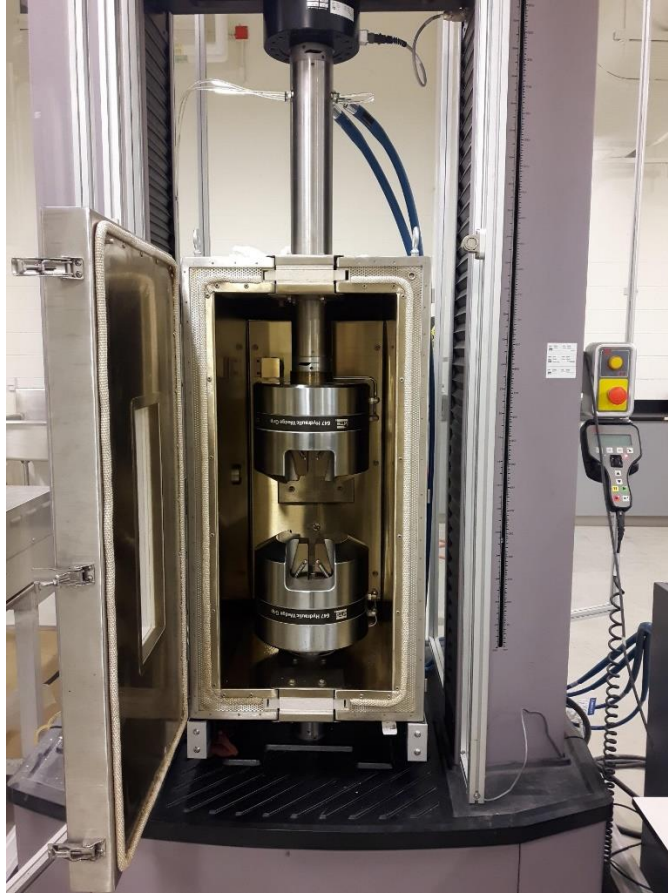


**Figure 3.13** MTS Model Universal Tensile Testing Machine (Model E45)



**Figure 3.14** Epsilon extensometer 3542-050M-050-LT [10]

### 3.3.2 Room Temperature Tensile Testing

Room temperature tensile tests were conducted using the process as described in **Section 3.3.1** Initial tensile testing in the as-received condition included a set of samples tested at a cross-head velocity of 0.084 mm/s, room temperature, and different directions, in order to verify certain material properties and behaviour. For these initial tensile tests, each of the samples were pulled to fracture and data was collected using the MTS TW elite program. Using these data, mechanical properties were calculated using Formulas 6 through 9 as outlined in **Section 2.1.1**.

5 samples were cut in a direction parallel to, 5 perpendicular to, and 5 45° out from the rolling direction as shown in **Figure 3.12**. These samples were tested at a cross-head velocity of 0.084 mm/s and used to determine the anisotropy of the as-received material at room temperature. Another 10 samples were cut with the gauge length of the samples parallel to the rolling direction and tested in room temperature tensile tests at different strain rates. 5 of the 10 samples were tested at a cross-head velocity of 0.084 mm/s and the other half were tested at 0.042 mm/s. These tests were conducted to compare the strain rate sensitivity of the material at room temperature. After the samples were pulled to fracture, measurements of the new sample thickness, width, and length were collected manually using a digital caliper and recorded to be compared with values calculated from the MTS TW Elite automatic calculations in the software and the data collected from the axial extensometer.

### 3.3.3 Sub-Zero Temperature Tensile Testing

The samples were cut to ASTM standards as described in **Section 3.3**. 3 samples (at each temperature) were deformed using an MTS tensile testing machine at temperatures of -40, -80, -120, and -160°C and at a constant cross-head velocity of 0.084 mm/s. First, the samples were loaded into the MTS tensile testing machine and a low temperature, axial, model 3542-050M-050-LT epsilon extensometer was attached to the gauge length. Two thermocouples were used to monitor the sample temperature,  $T_{AI}$ , and the surrounding temperature inside the tensile testing machine,  $T_{sur}$ . A third thermocouple was also attached to the specimen to verify accuracy of the sample temperature and produced measurements with an error of  $\pm 2.20^\circ\text{C}$ . A schematic of this setup is given in **Figure 3.15**. Liquid nitrogen was flowed into the environmental chamber using solenoids attached to the machine to ensure a steady flow rate. The sample was given 5 minutes to reach thermal equilibrium once the outside temperature reached the required testing temperature. A temperature control unit, as shown in **Figure 3.16**, was attached to the thermocouples and used to read and change the temperature inside the environmental chamber. The specimens were tested until fracture. Measurements were collected using the MTS TW elite program.

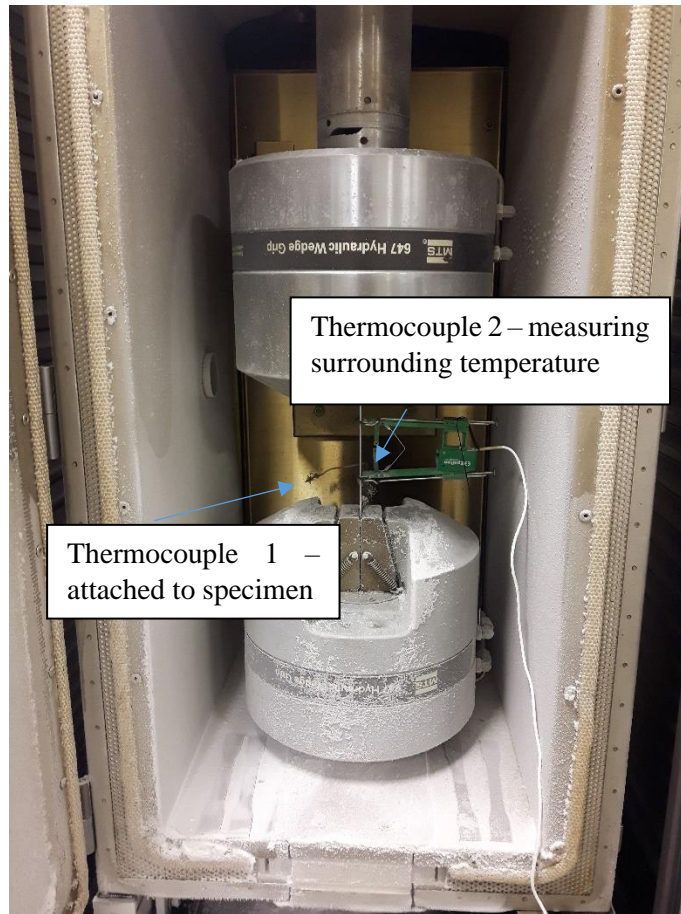


**Figure 3.15** Setup/schematic of tensile testing machine with environmental chamber, specimen, and thermocouple as indicated.



**Figure 3.16** Temperature control unit attached to the MTS tensile machine.

The samples that were tested at  $-196^{\circ}\text{C}$  temperatures used the same ASTM standards as previous samples. The same MTS tensile machine was used to pull the samples to fracture, however, a variation of the set-up was required for these very low temperature testing conditions. For this testing condition, a Styrofoam cup was used to submerge the sample in liquid nitrogen while the test was being completed. It was ensured that the entire gauge length of the sample remained submerged during the entire duration of the test. Before initiating the test, the sample was given 5 minutes to reach thermal equilibrium once the outside temperature reached the required testing temperature. This set-up is shown in **Figure 3.17**.



**Figure 3.17** Set-up for samples tested at  $-196^{\circ}\text{C}$  tensile testing temperature.

### 3.3.4 Cottrell-Stokes Tensile Testing

For the Cottrell-Stokes tensile testing, specimens were prepared using the ASTM standards as detailed in **Section 3.3.1**. These tests used the same process throughout, including pre-measurements, extensometers, and graphing software as described. Initial tensile tests were conducted to obtain stress-strain curves for each interval temperature to identify the regions of flow stress and points of interest at specific strain values, such as yield + 0.1 mm/mm strain. Two sets of tests were conducted. The first set was a preliminary trial for developing a Cottrell-Stokes procedure and involved developing stress-strain curves at room temperature and 120°C. The secondary set of tests involved testing at low temperature. For these tests, stress-strain curves were developed at room temperature and -40, -80, -120, and -160°C. Similar to the low temperature tensile testing procedures, thermocouples were used to measure the temperature of the sample,  $T_{Al}$ , and the surrounding temperature inside the tensile testing machine,  $T_{sur}$ . The same temperature control unit, as shown in **Figure 3.16**, was attached to the thermocouples and used to read and change the temperature inside the environmental chamber. For the test with a higher testing temperature, an axial extensometer was used with model number 3542-050M-050-HT1.

In these tests, the initial cross-head velocity was set to 0.084 mm/s and the initial testing temperature was set on the control unit to 120°C. When the program indicated that the strain had reached a value of 0.1 mm/mm at a stage between the yield stress and the ultimate tensile stress, the test was paused, the specimen was unloaded and the temperature control unit was set to ambient temperature (approximately 34°C). After reaching this temperature and allowing several minutes for the specimen to reach equilibrium temperature, the test was resumed at the same cross-head velocity and the new temperature and pulled to fracture.

For the second set of tests, the test was conducted in three stages. Each stage was conducted with a difference in temperature change of 20°C. For each transition, when the program reached increments of 0.05 mm/mm, the test was paused, the specimen was

unloaded, and the temperature control unit was set to the new temperature before resuming the test. The first stage involved setting the temperature from -134 to -114°C as the strain reached approximately 0.05 mm/mm. The second stage involved setting the temperature from -114 to -94°C as the strain reached approximately 0.1 mm/mm. The third stage involved setting the temperature from -94 to -74°C as the strain reached approximately 0.15 mm/mm. The stress-strain curve for this procedure was plotted and recorded to calculate the difference in stress and strain during these jumps.

### 3.3.5 Strain Rate Change Tensile Testing

For the strain rate jump tests, a program was developed on the MTS TestSuite TW Elite graphing software templates with inputs such as sample thickness, gauge length, and strain rate, to unload the specimen, and spike the strain rate after a certain value of strain had been reached.

In these tests, the crosshead velocity was not set at a single rate to pull the samples to fracture, but rather a change in strain rate mid-test, with the purpose of the strain rate jumps to investigate the relation of the flow stress of the material with respect to strain rate (material strain rate sensitivity). The initial cross-head velocity and temperature was set as 1mm/min and 25°C, respectively. The test was continued until the program indicated that the extensometer had reached a distance of 1 mm. The template that was developed for the test then automatically jumped the cross-head velocity to 5 mm/min. Once the extensometer reached a distance of 2 mm, the cross-head velocity was automatically jumped to 10 mm/min and the specimen was pulled until fracture.

The second strain rate change test used the same process as described above, but as the tensile sample reached an extensometer distance of 1 mm, the cross-head velocity was changed from 1 mm/min to 100 mm/min and pulled until fracture.

### 3.4 Formability Testing

The formability of the AA5182-O aluminum alloy samples was investigated using a model 102 Erichsen sheet metal testing machine, as shown in **Figure 3.18**. A schematic of the cross-section of the Erichsen cupping test that was used is provided in **Figure 3.19**. To prepare samples for this work, Catia V5 Software was used to 3D model draft specimens, as provided in the appendices section. To obtain proper strain data to construct forming limit curves, care must be taken during the design stage of these samples. In order to develop an experimental FLC, a number of strain ratios are required. The details for design of these samples is provided in the next section. The strain data of these samples, along with a more detailed discussion of the results of the formability testing, is included in Chapter 6: *Future Work and Recommendations*.

Once the samples were designed and machined from the as-received sheet metal, grids were etched on to the specimens in the same method that is described in **Section 3.2**. The formability testing process, involved inserting these samples inside the side slot of the machine, positioning the sample centered on to the punch of the machine, and screwing down the holder to clamp the sample in place. Once held in place, the test was programmed to move the punch upwards, into the sample, at a drawing speed of 150 mm/min. The tests were automatically stopped when necking, or a crack, was sensed on the sample from force monitoring.

Samples were tested 3 times to collect an average data. After cupping tests were performed, grid analysis was conducted on each sample to construct a forming limit diagram.



**Figure 3.18** Erichsen sheet metal testing machine model 102.

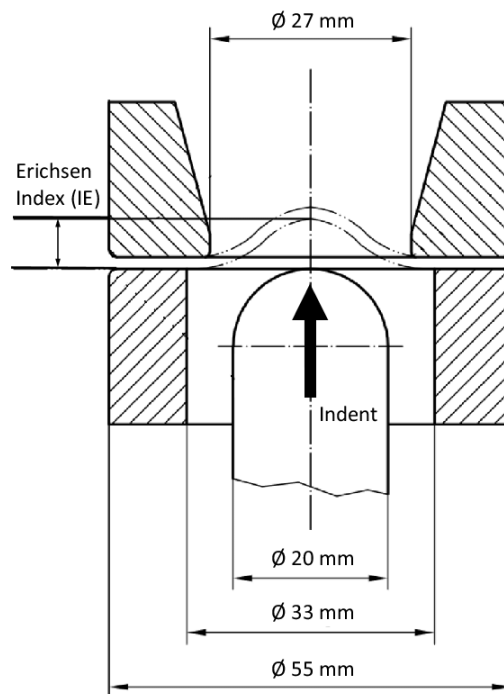


**Figure 3.19** Schematic of Erichsen cupping test (cross-section) [11]

Low temperature formability tests were performed by inserting the forming samples into a container of liquid nitrogen, while simultaneously attached to a live-reading thermocouple. The temperature of the aluminum reached a temperature of  $-40^{\circ}\text{C}$  and was given 5 minutes to reach an internal equilibrium temperature while inside the container of liquid nitrogen. Once this was achieved, the sample was carefully transferred to the Erichsen sheet metal testing machine using tongs. This step was done while the thermocouple was still attached to the sample, to ensure there was not a drastic change in temperature. The sample was then tested with the same process as described for the room temperature formability samples.

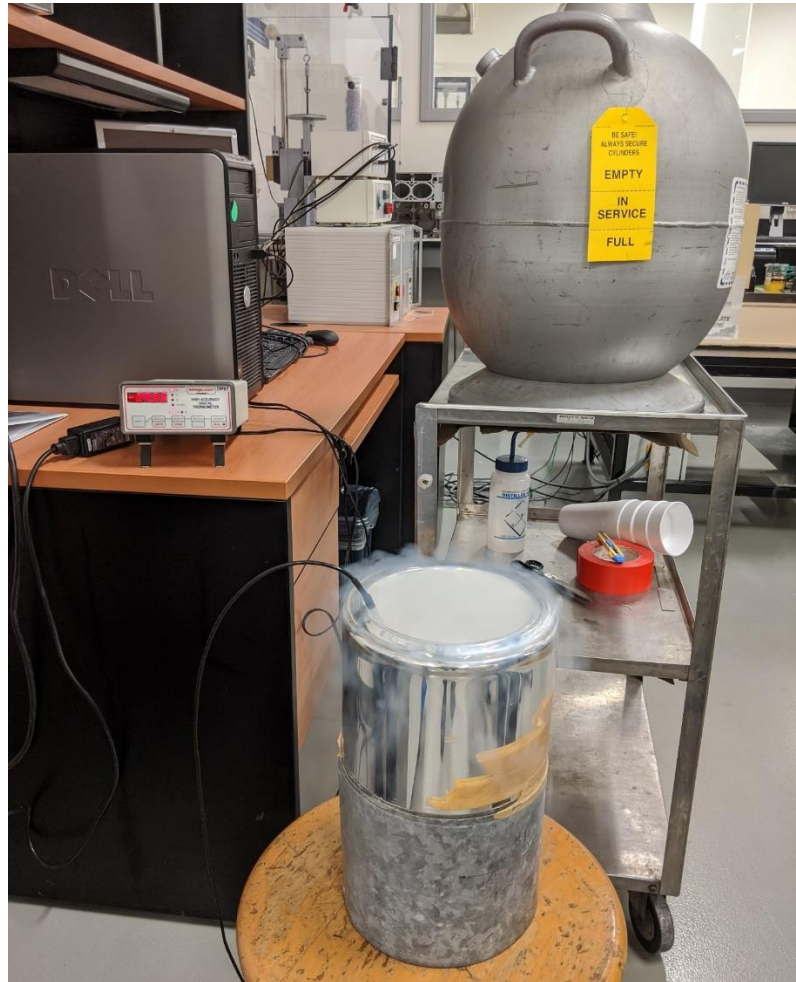


**Figure 3.20** Process for cooling samples for low temperature formability testing using a thermocouple, cryogenic dewar of liquid nitrogen, and cooling container.

### 3.4.1 Testing Equipment

Grid analysis was completed for each tested sample with a 1-mm-diameter circle grid pattern etched onto the surface. Grid analysis involved using an FMTI grid analyzer gun, as shown in **Figure 3.21**, along with the corresponding FMTI analysis software. An example of the FMTI analysis software screen, along with how the gun was able to view and measure strains from the grids, is provided in **Figure 3.22**.



**Figure 3.21** FMTI Systems grid analyzer hardware (grid analysis gun) [12].

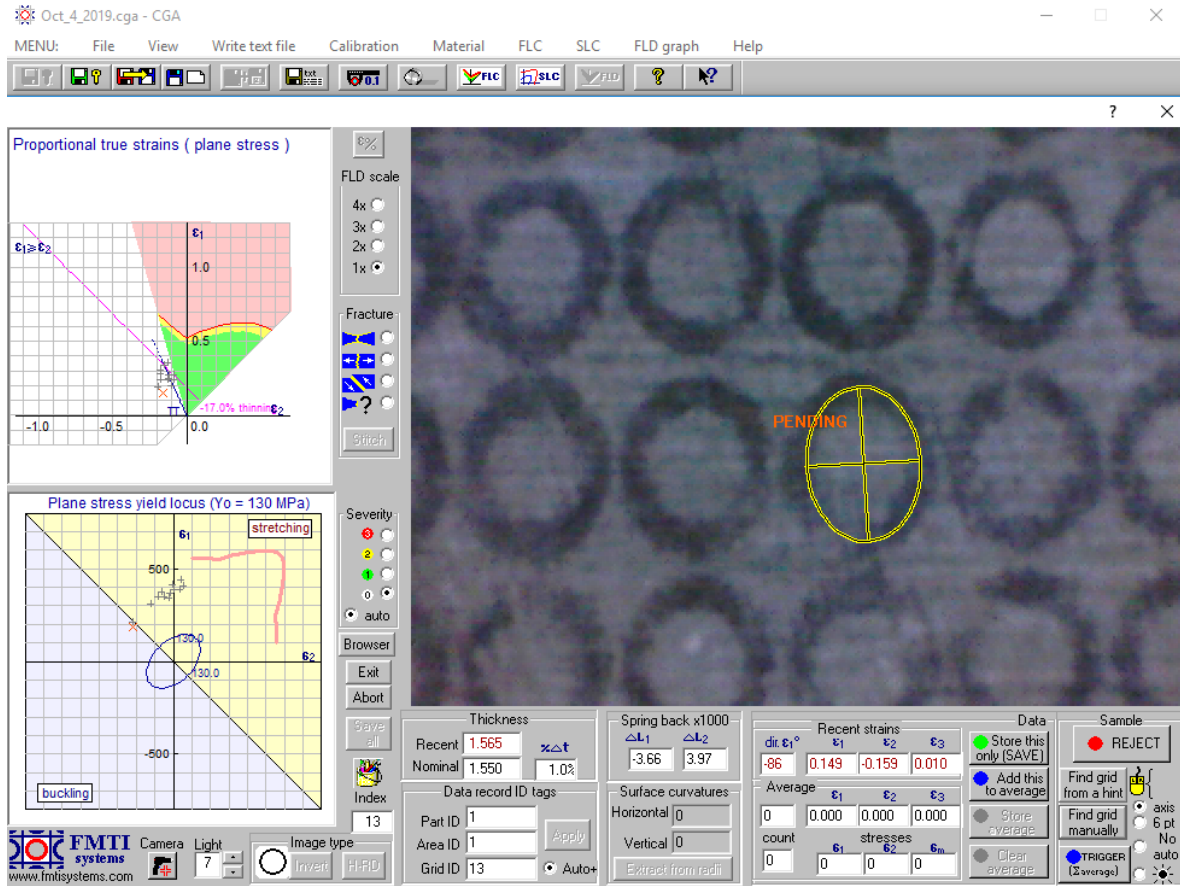
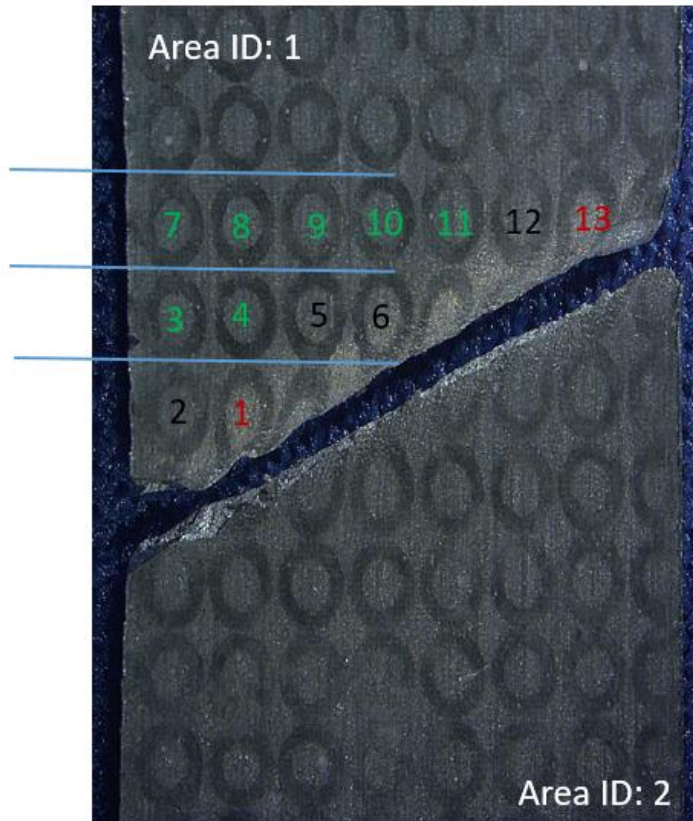


**Figure 3.22.** FMTI Systems grid analysis software screen example.

Due to the difficulty of sample design along with controlling the sensitivity of the Erichsen sheet metal testing machine, stopping the test during the necking stage and prior to fracture of the sample posed some challenges to research. These challenges are further discussed in recommendations and future work for the research. As a result, fracture measurements using grid stitching can be used to develop forming curves. The grid stitching function in FMTI is capable of removing the gap between fractured grids and measuring the fracture strain to determine if the type of fracture includes necking, normal rupture, or shear [12].

The following figure, **Figure 3.23**, gives a schematic of the fractured/failed, necking, and acceptable grids overlaid over a uniaxial tension sample that has been subjected to tensile testing at room temperature.

Part ID: 1



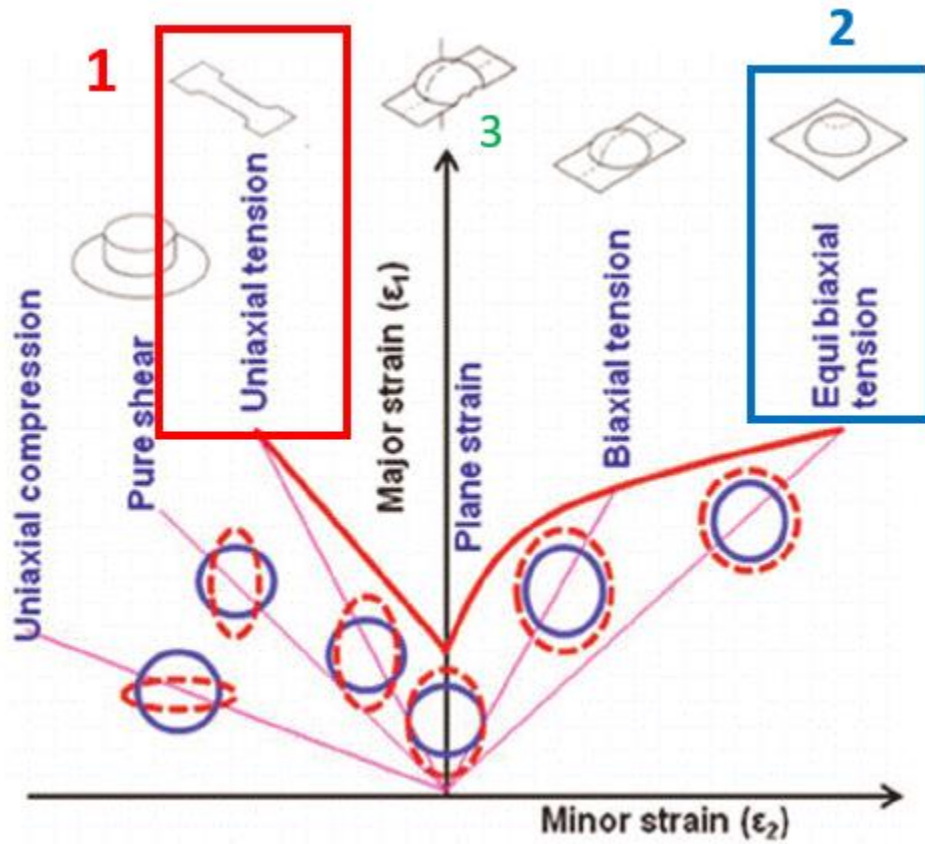
Fracture (Failed) , Neck , Acceptable

Figure 3.23. FMTI Systems grid analysis software screen example.

### 3.4.2 Specimen Geometries

In order to develop forming grids, there are a variety of strain paths that are used. These typically include uniaxial tension, plane strain, biaxial tension and equibiaxial tension data on a plot of the major strain versus the minor strain. **Figure 3.24** shows an

illustration of these strain paths and how they are used to develop a forming curve on a major strain-minor strain plot.



**Figure 3.24.** FMTI Systems grid analysis software screen example [13].

The two major samples that were developed in this work were uniaxial samples and equibiaxial tension samples. The CATIA drafts for all of the formability samples are provided in the appendices section. Each part tested was organized by Index, Part ID, Area ID, Grid ID, and Tag #. The FMTI software was then used to collect information on the thickness, major strain, and minor strain.

# Bibliography

- [1] 10M14 MECHANICAL SHEET METAL SHEAR: <https://www.roperwhitney.com/our-products/10m14-mechanical-sheet-metal-shear/>
- [2] G. V. Voort, “Metallography and Microstructure of Aluminum and Alloys,” <https://vacaero.com/information-resources/metallography-with-george-vander-voort/1217-metallography-and-microstructure-of-aluminum-and-alloys.html>
- [3] ZWICK/ROELL INDENTEC HARDNESS TESTING - VICKERS HARNESS TEST: [https://www.indentec.com/downloads/info\\_vickers\\_test.pdf](https://www.indentec.com/downloads/info_vickers_test.pdf)
- [4] SPECTROGRAPHIC LIMITED – BUEHLER MICROMET 2 HARDNESS TESTER <https://spectrographic.co.uk/products/buehler-micromet-2-hardness-tester-1>
- [5] ASTM E384-17 Standard Test Method for Microindentation Hardness of Materials <https://www.astm.org/standards/e384>
- [6] Omano OM159T - 40x-1,000x - Research Grade - Trinocular Compound Microscope  
<https://spwindustrial.com/omano-om159t-40x-1-000x-research-grade-trinocular-compound-microscope-infinity-corrcted-optics-plan-objective-lenses-halogen-illumination/>
- [7] F. Ozturk et. al. “Grid Marking and Measurement Methods for Sheet Metal Formability,” 5<sup>th</sup> International Conference and Exhibition on Design and Production of Machines and Dies/Molds, pp. 1-10, 2009.
- [8] ASTM E8/E8M-16 Standard Test Methods for Tension Testing of Metallic Materials [https://www.astm.org/e0008\\_e0008m-16.html](https://www.astm.org/e0008_e0008m-16.html)
- [9] O. Daghfaz, “Experimental and numerical study on mechanical properties of aluminum alloy under uniaxial tensile test,” *Frattura ed Integrità Strutturale*, vol. 39, pp. 263-273, 2017.
- [10] Epsilon extensometer 3542-050M-050-LT <https://www.epsilontech.com/products/axial-extensometer-model-3542/>
- [11] F. S. Sorce et. al. “Quantification of coating surface strains in Erichsen cupping tests,” *Journal of Materials Science*, vol. 54, issue 2, 2019.
- [12] FMTI SYSTEMS INC. HARDWARE <http://www.fmtisystems.com/videos.htm>

[13] S. K. Paul, M. Ganapathy, R. K. Verma, "Prediction of entire forming limit diagram from simple tensile material properties," *The Journal of Strain Analysis for Engineering Design*, vol. 48, issue 6, pp. 386-394, 2013.

## 4 Experimental Results

### 4.1 Material Characterization

#### 4.1.1 Hardness of AA5182-O at room temp.

Hardness tests were conducted using the Vickers hardness testing method and Vickers hardness equation (equation 18). Eight indents were created in eight different locations to determine an average hardness for the surface, longitudinal direction, and transverse direction of the sample, as shown in **Figure 4.1** and **Figure 4.2**. The results of these indents for each direction are provided in the appendices section. The surface hardness was calculated to be 70.36 HV with a standard deviation of 3.47. The longitudinal plane hardness was calculated to be 64.48 HV with a standard deviation of 3.89. The hardness calculated for the transverse plane of the sample was 69.37 HV with a standard deviation of 3.77.

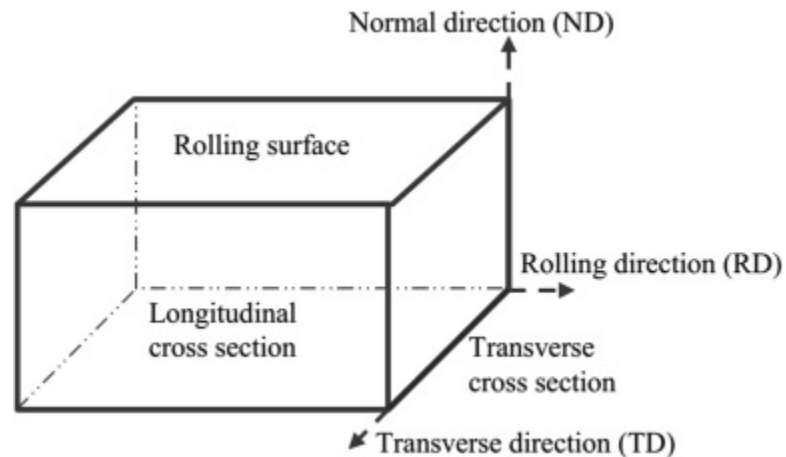


**Figure 4.1** Schematic showing nomenclature for directions.

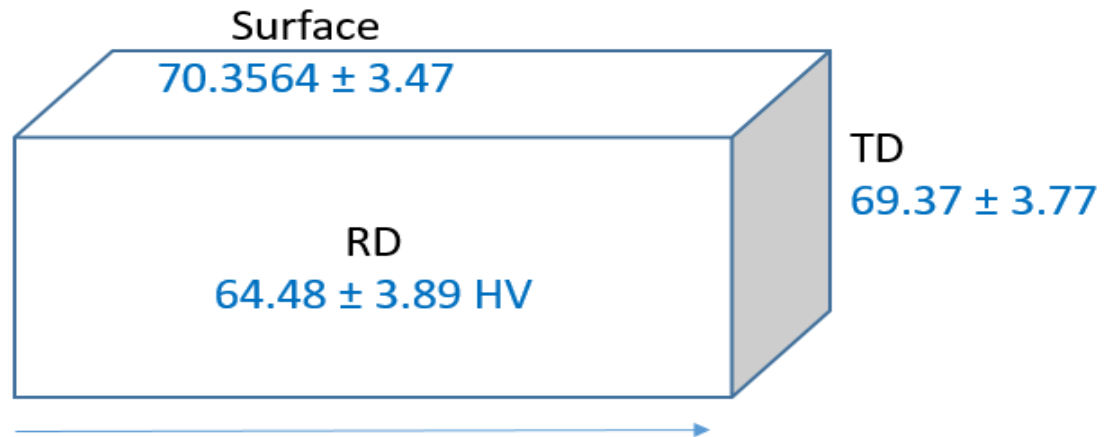


**Figure 4.2** Average hardness calculations and respective standard deviations for AA5182-O calculated for the rolling surface, rolling direction, and transverse direction of the sample.

#### 4.1.2 Microstructure of AA5182-O by OM, SEM, and EDS

Using the metallographic grinding and polishing procedures described in Chapter 3, microscopic images of the specimen on the rolling surface were taken with the Omano OM159T microscope at a magnification of 1000x magnification. These images, as shown and indicated in **Figure 4.3**, reveal the second-phase precipitates. These images were also used to ensure enough scratches were removed from the surface of the specimens before proceeding to SEM analysis.

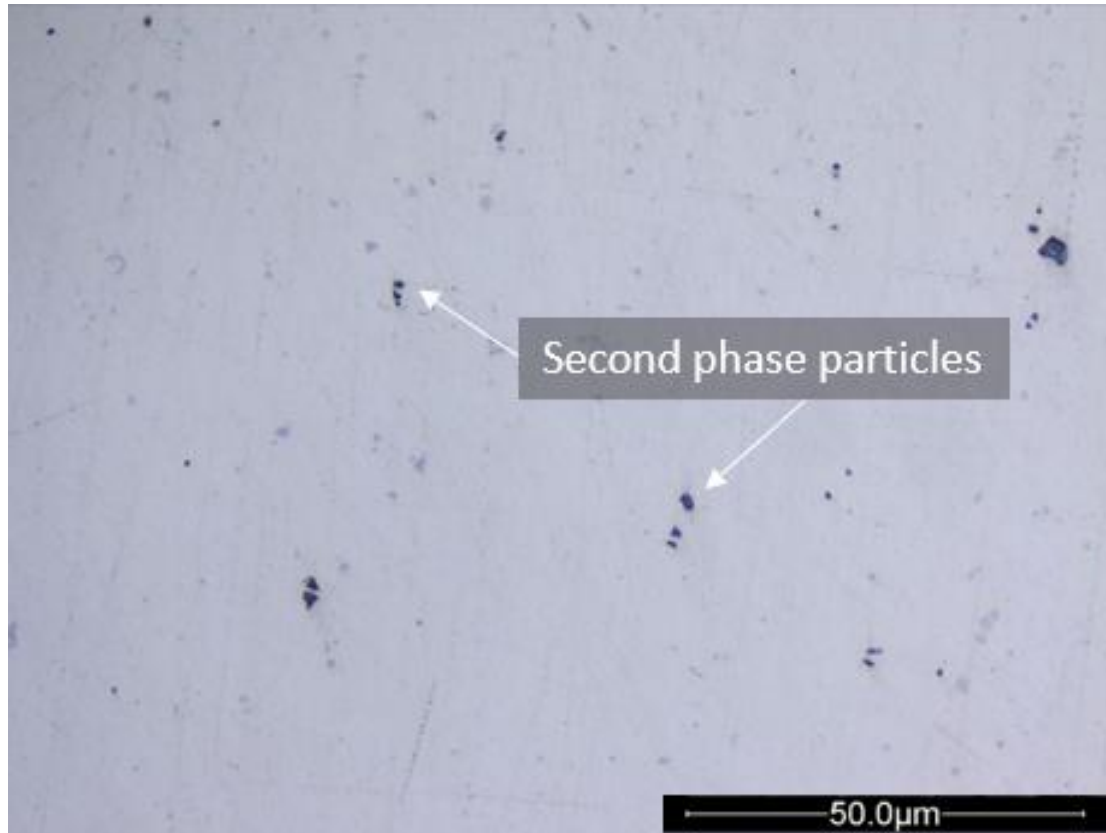


**Figure 4.3** Optical microscopy image of AA5182-O after metallographic grinding and polishing procedures at a magnification of 1000x magnification.

The second-phase precipitates appear as dark spots along the surface of the AA5182-O aluminum, as indicated by the arrows. Samples of the as-received AA5182-O aluminum alloy were then subjected to the etching procedure described in **Section 3.1.1**. Using the FEI Quanta 200 FEG scanning electron microscope, images were taken of the etched sample to observe and analyze the grain boundaries. **Figure 4.4** shows the SEM image of AA5182-O etched with concentric Keller's reagent and observed under 1000x magnification.

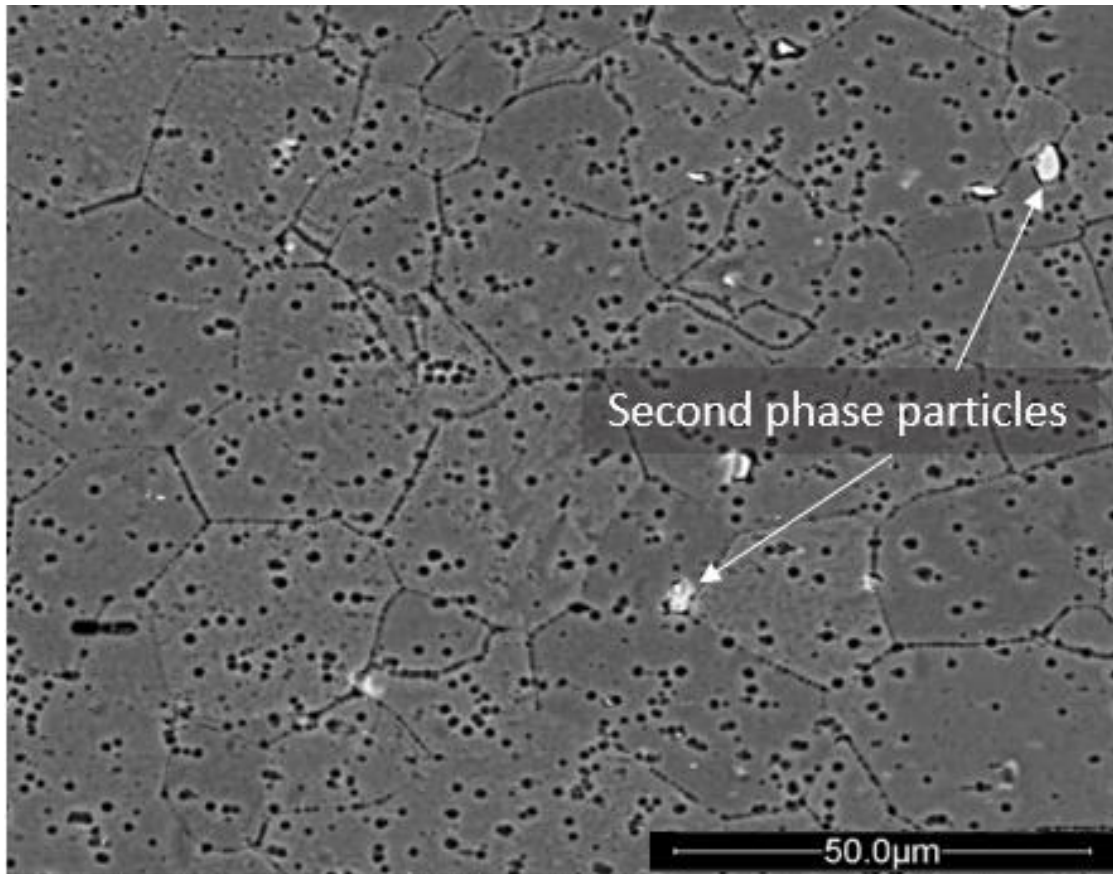


**Figure 4.4** SEM image of the etched surface of aluminum alloy AA5182-O showing the grain boundaries under 1000x magnification

Grain length, width, area, and the aspect ratio were determined using microscopic measurements of the grain boundaries from the SEM images of the etched surfaces of the as-received aluminium alloy. 10 locations were randomly selected and each grain area on the surface was magnified and measured. This process is further detailed in the appendices, along with data histograms. **Table 4.1** shows the average results for the calculations for the grain length, width, area and aspect ratio (the ratio of length 1 to length 2).

**Table 4.1** Average grain values calculated from initial material characterization of rolling surface for AA5182-O aluminum alloy.

Property	Average value	Units
Grain length	18.91	μm
Grain width	14.98	μm
Grain area	365.08	(μm) <sup>2</sup>
Aspect Ratio	1.39	--

The average grain length was approximated to be 18.91 μm. The average width was measured to be approximately 14.98 μm. The average grain area was calculated to be 365.08 (μm)<sup>2</sup>. The aspect ratio was calculated to be 1.39.

EDS analysis was conducted using the as-received specimens and the energy-dispersive X-ray EDAX (SiLi Detector) to collect information on the chemical composition of the aluminum alloy and the chemical composition of precipitates and second phase particles. **Figure 4.4** shows an image captured at a magnification of 10000x for the as-received specimen after tensile fracture at room temperature. Four spots were selected to obtain EDS information, Spots 1 and 3 are taken from locations containing a Mg<sub>2</sub>Si and Al<sub>3</sub>(Fe-Mn) particle, respectively, and spots 2 and 4, as indicated in **Figure 4.5**, are taken from the aluminum matrix. The settings for the EDAX SiLi Detector that were used to acquire the following information is provided in **Table 4.2**.

**Table 4.2** Settings for the EDAX SiLi Detector for EDS analysis.

Setting	Voltage	Mag.	Takeoff	Live Time	Amp Time	Resolution
Value (Unit)	15 (kV)	10000	35.8	30 (s)	7.68 (μs)	123.1 (eV)

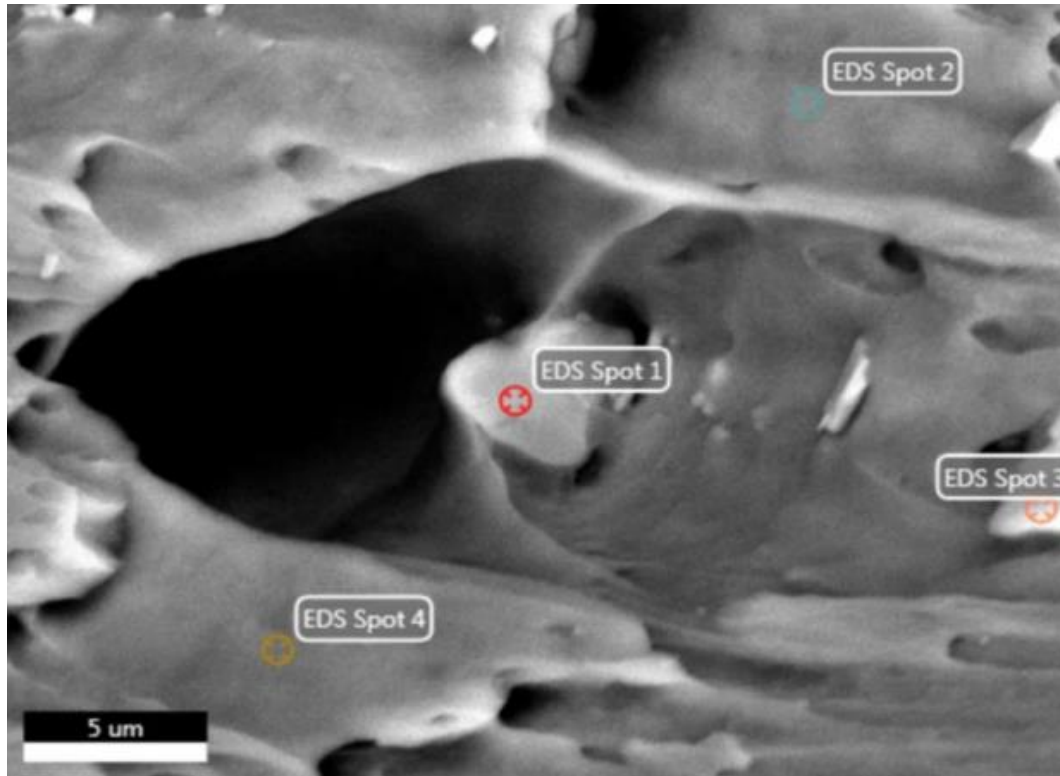


**Figure 4.5** EDS image captured using energy-dispersive X-ray EDAX (SiLi Detector) of AA5182 fractured specimen.

**Figures 4.6 through 4.9**, provide the element distribution graphs obtained using the described EDS techniques for the respective spots number 1, 2, 3, and 4, as labelled in **Figure 4.5**.

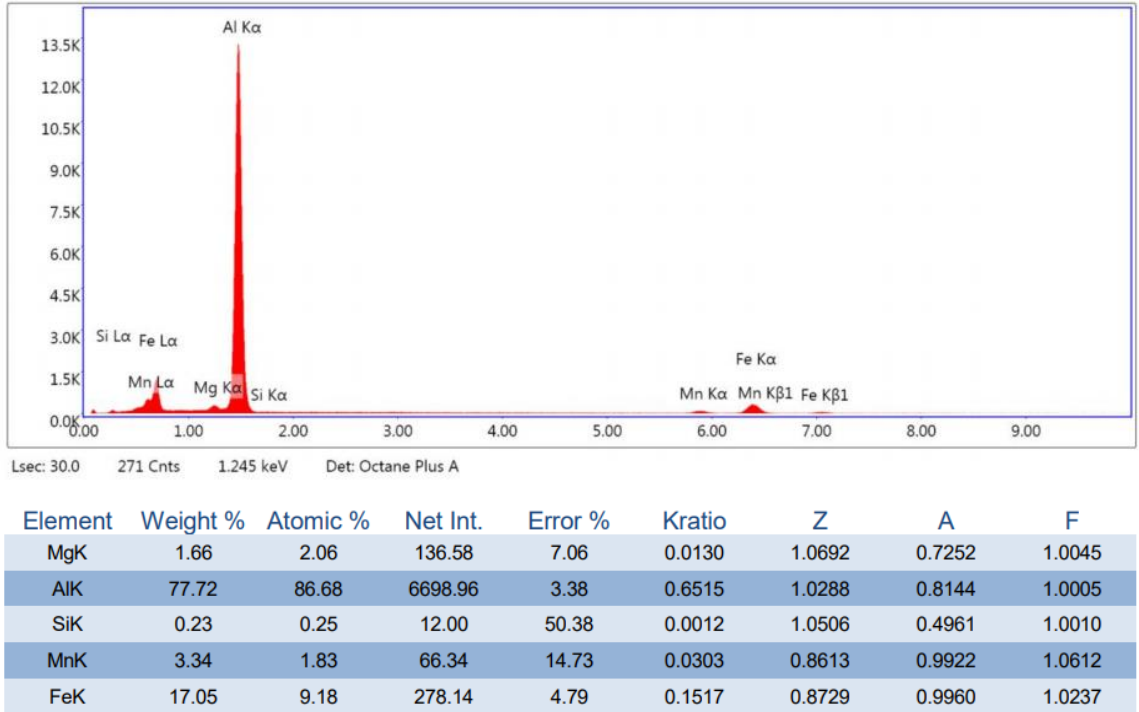
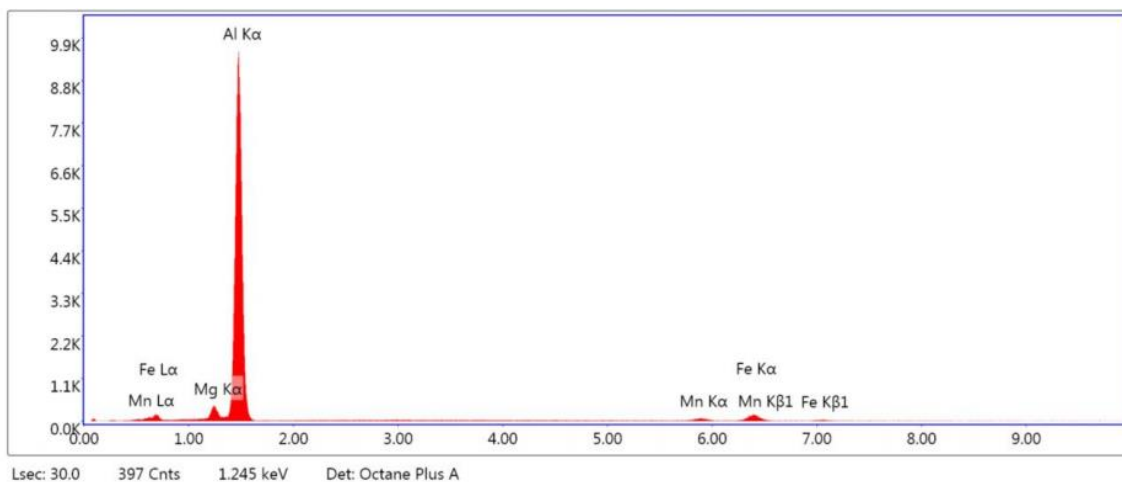


**Figure 4.6** Element distribution graph obtained from EDS analysis of spot 1

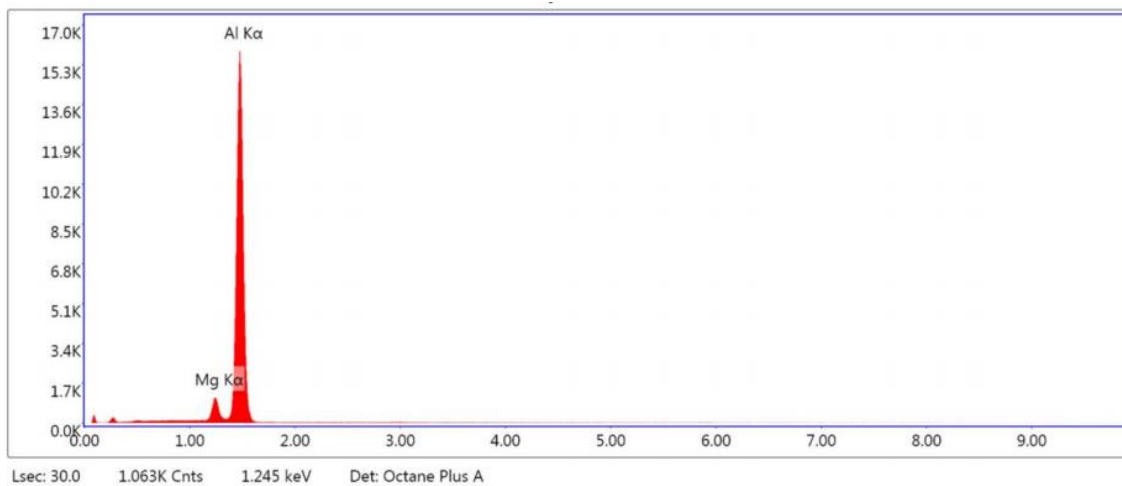


**Figure 4.7** Element distribution graph obtained from EDS analysis of spot 2



Element	Weight %	Atomic %	Net Int.	Error %	Kratio	Z	A	F
MgK	3.36	4.05	194.60	5.70	0.0275	1.0626	0.7662	1.0051
AlK	80.34	87.35	4714.05	3.26	0.6821	1.0223	0.8301	1.0004
MnK	4.24	2.26	55.80	14.87	0.0379	0.8552	0.9920	1.0544
FeK	12.07	6.34	131.99	6.64	0.1071	0.8666	0.9959	1.0285

**Figure 4.8** Element distribution graph obtained from EDS analysis of spot 3



Element	Weight %	Atomic %	Net Int.	Error %	Kratio	Z	A	F
MgK	5.83	6.42	542.44	2.86	0.0583	1.0372	0.9541	1.0105
AlK	94.17	93.58	7968.18	2.15	0.8776	0.9977	0.9340	1.0000

**Figure 4.9** Element distribution graph obtained from EDS analysis of spot 4

Using EDS techniques, as shown in **Figure 4.5**, the resulting data provided in **Figures 4.6** through **4.9**, and literature data for AA5182-O given in the literature survey, the chemical composition of the as-received aluminum alloy AA5182-O was determined and is provided in **Table 4.3**.

**Table 4.3** Chemical composition of the as-received AA5182-O aluminum alloy in wt%

<b>Material</b>	<b>Al</b>	<b>Mg</b>	<b>Mn</b>	<b>Fe</b>	<b>Si</b>	<b>Residuals</b>
AA5182-O	95.02	4.3	0.34	0.21	0.03	<0.1

## 4.2 Mechanical Properties

### 4.2.1 Room Temperature Tensile Testing

The engineering stress strain curve was determined using the tensile testing methodology described in **Section 3.3.1**. These samples were cut in parallel to the rolling direction. The stress-strain curve shown in **Figure 4.10** was obtained at an initial crosshead velocity of 0.084 mm/s and room temperature testing conditions. A 0.002 offset is applied to the graph to determine the elastic region and respective yield stress of the material.

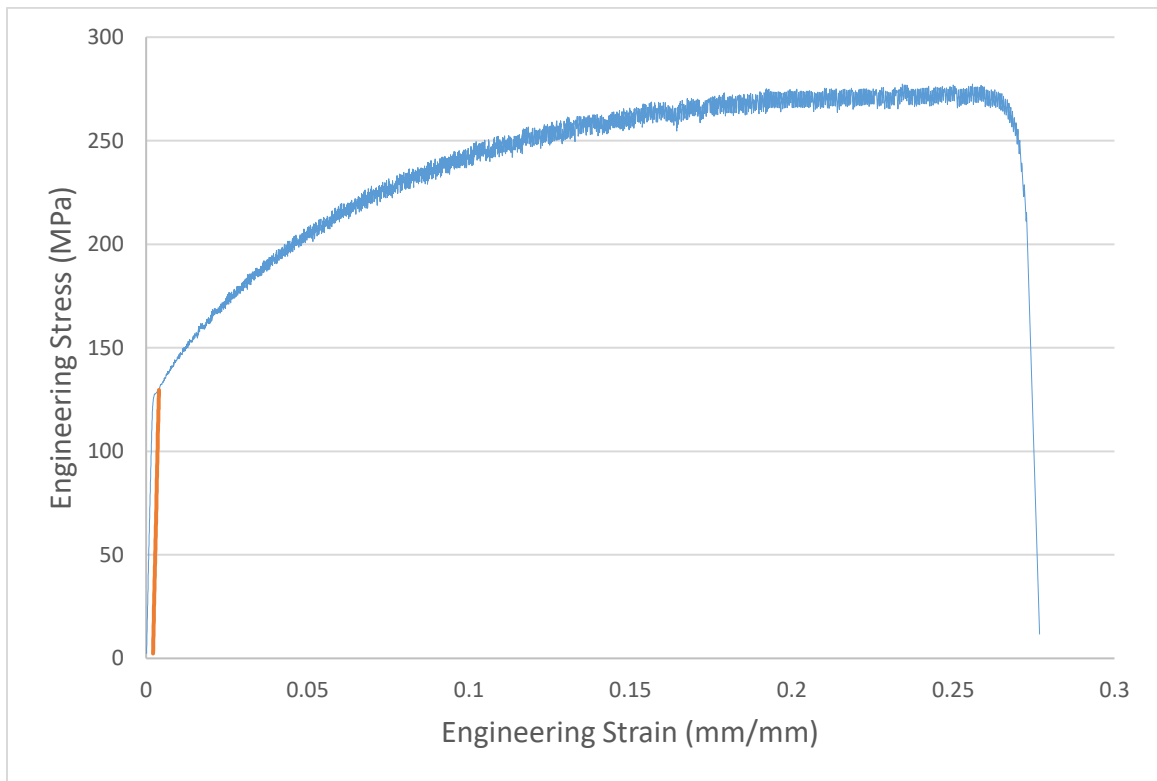


**Figure 4.10** Engineering stress-strain curve for aluminum alloy AA5182-O (rolling direction) obtained at ambient temperature and 0.002 offset of elastic region; respective strain rate  $1.9 \times 10^{-3} \text{ s}^{-1}$

$3 \text{ s}^{-1}$

Using the data obtained from the MTS TW elite program, the mechanical properties were collected and calculated using Formulas 6 through 9 as outlined in **Section 2.1.1**. These values are provided in the following table and used for comparison for subsequent low temperature and Cottrell-Stokes tensile testing. The appendices provide additional stress strain curves used for average calculations.

**Table 4.4** Average mechanical properties (rolling direction) obtained from the engineering stress strain curve for aluminum alloy AA5182 obtained at ambient temperature; respective strain rate  $1.9 \times 10^{-3} \text{ s}^{-1}$

Property	Value	St. Deviation
Elastic Modulus	69.9 GPa	±2.45
Yield Stress	129.6 MPa	±2.98
Ultimate Tensile Stress	279.2 MPa	±3.21
Uniform Elongation (strain, %)	23.7	±1.23
Total elongation (strain, %)	26.5	±1.42

## 4.2.2 Sub-Zero Temperature Tensile Testing

The engineering stress strain curve data at sub-zero temperatures was determined using the tensile testing methodology described in **Section 3.3.3**. The following representative stress strain curves in **Figures 4.11** through **4.15** were obtained at an initial crosshead velocity of 0.084 mm/s and -40, -80, -120, -160, and -196 °C temperature testing conditions respectively. **Figure 4.16** combines the results of these figures.

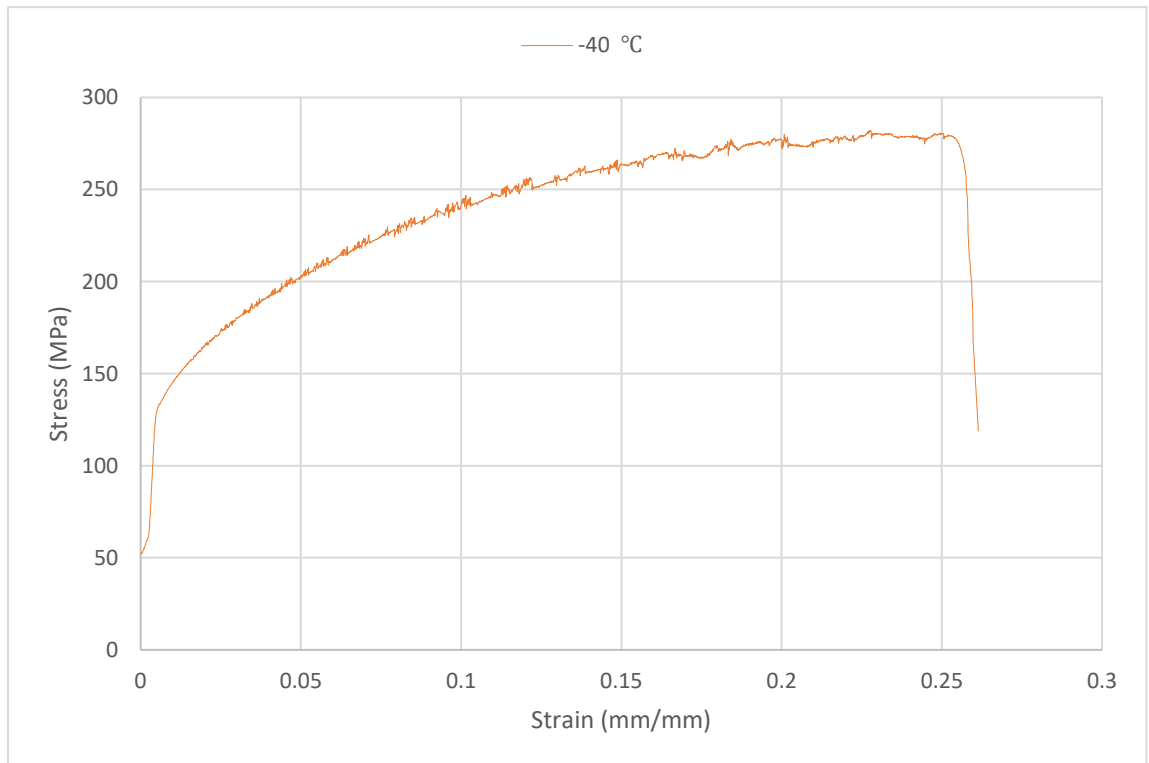


**Figure 4.11** Engineering Stress Strain Curves for aluminum alloy AA5182 (rolling direction) obtained at -40°C; respective strain rate  $1.9 \times 10^{-3} \text{ s}^{-1}$

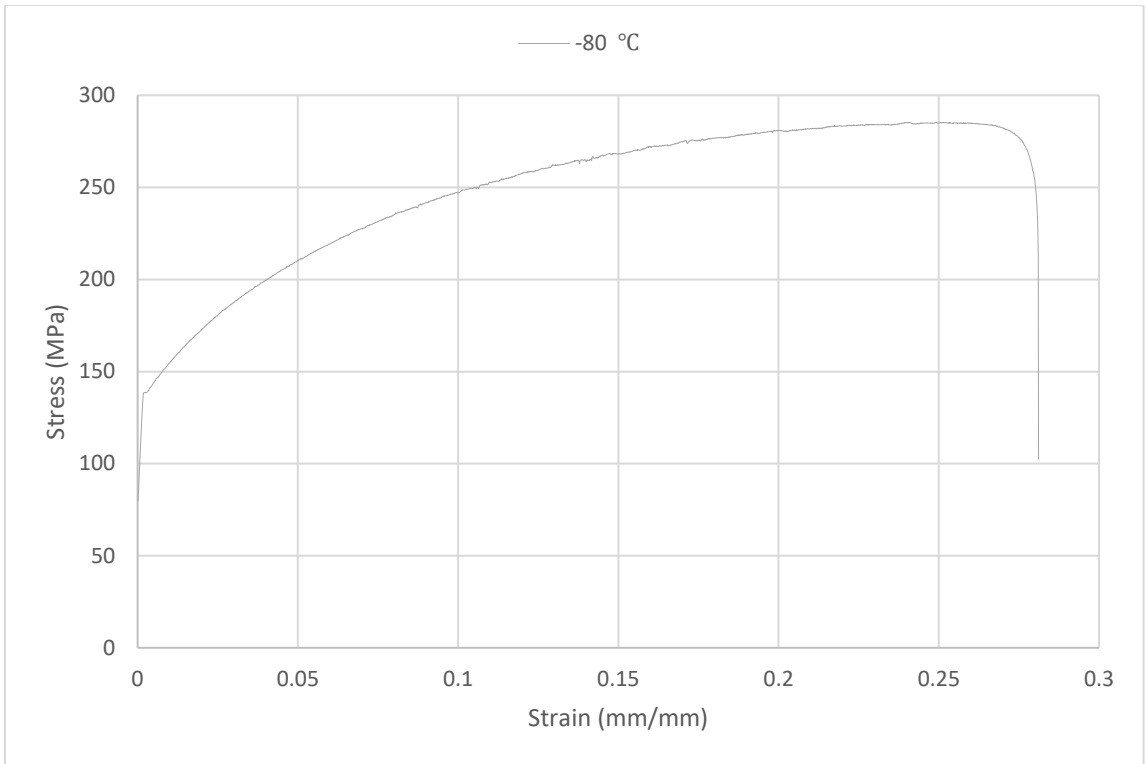


**Figure 4.12** Engineering Stress Strain Curves for aluminum alloy AA5182 (rolling direction) obtained at -80°C; respective strain rate  $1.9 \times 10^{-3} \text{ s}^{-1}$

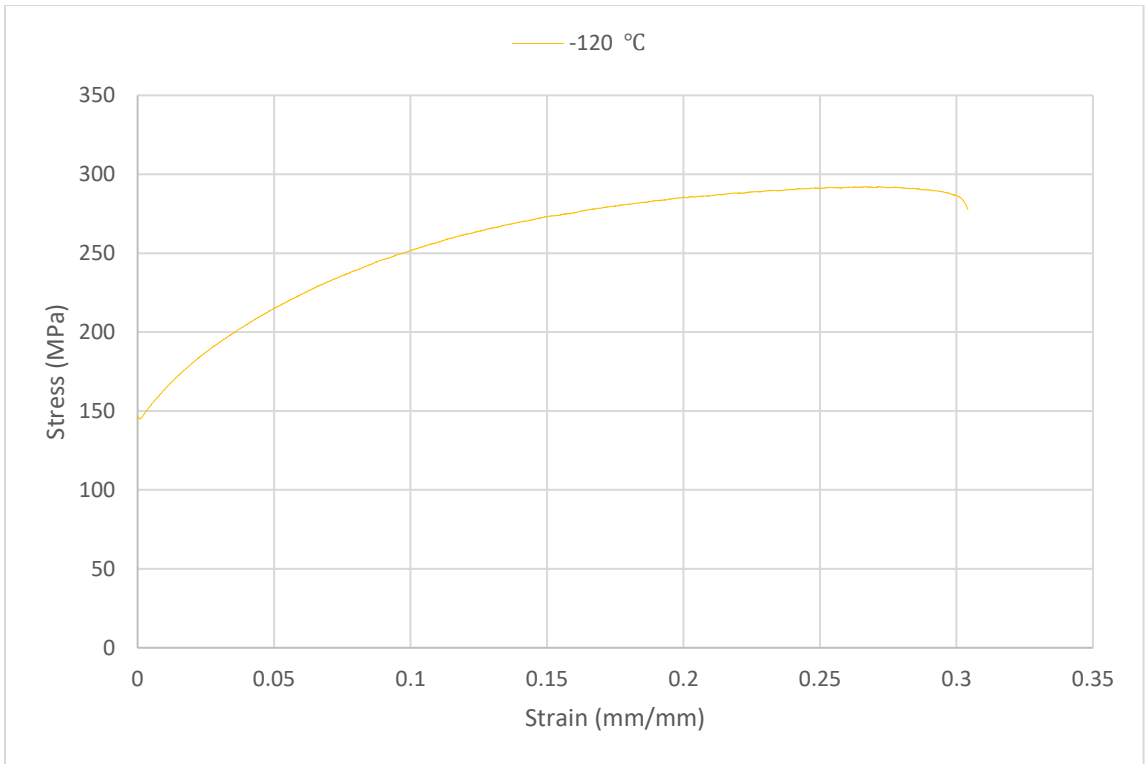


**Figure 4.13** Engineering Stress Strain Curves for aluminum alloy AA5182 (rolling direction) obtained at -120°C; respective strain rate  $1.9 \times 10^{-3} \text{ s}^{-1}$

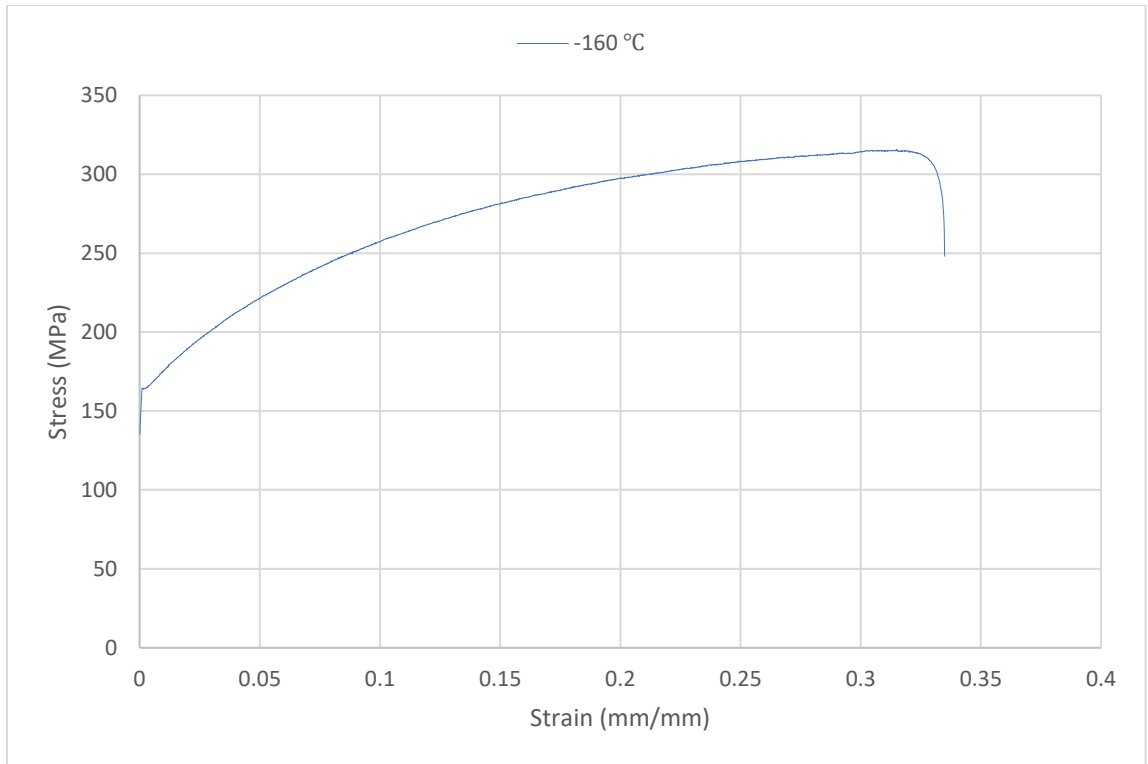


**Figure 4.14** Engineering Stress Strain Curves for aluminum alloy AA5182 (rolling direction) obtained at -160°C; respective strain rate  $1.9 \times 10^{-3} \text{ s}^{-1}$

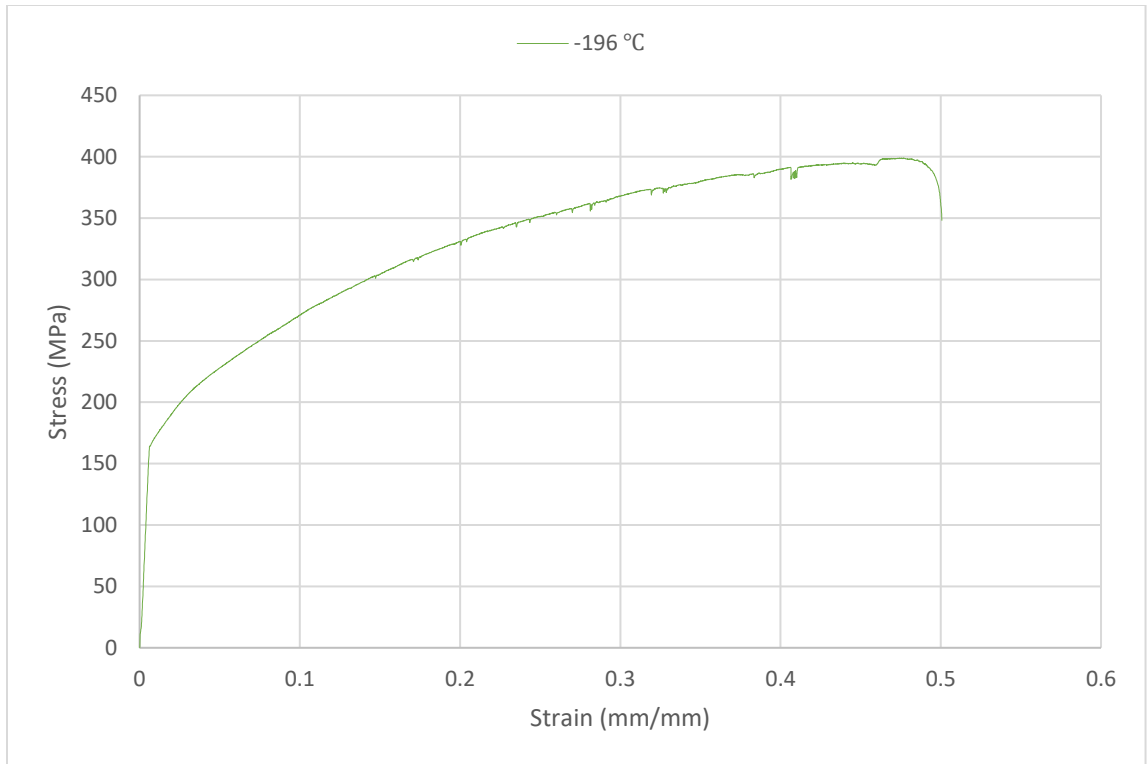


**Figure 4.15** Engineering Stress Strain Curves for aluminum alloy AA5182 (rolling direction) obtained at -196 °C; respective strain rate  $1.9 \times 10^{-3} \text{ s}^{-1}$

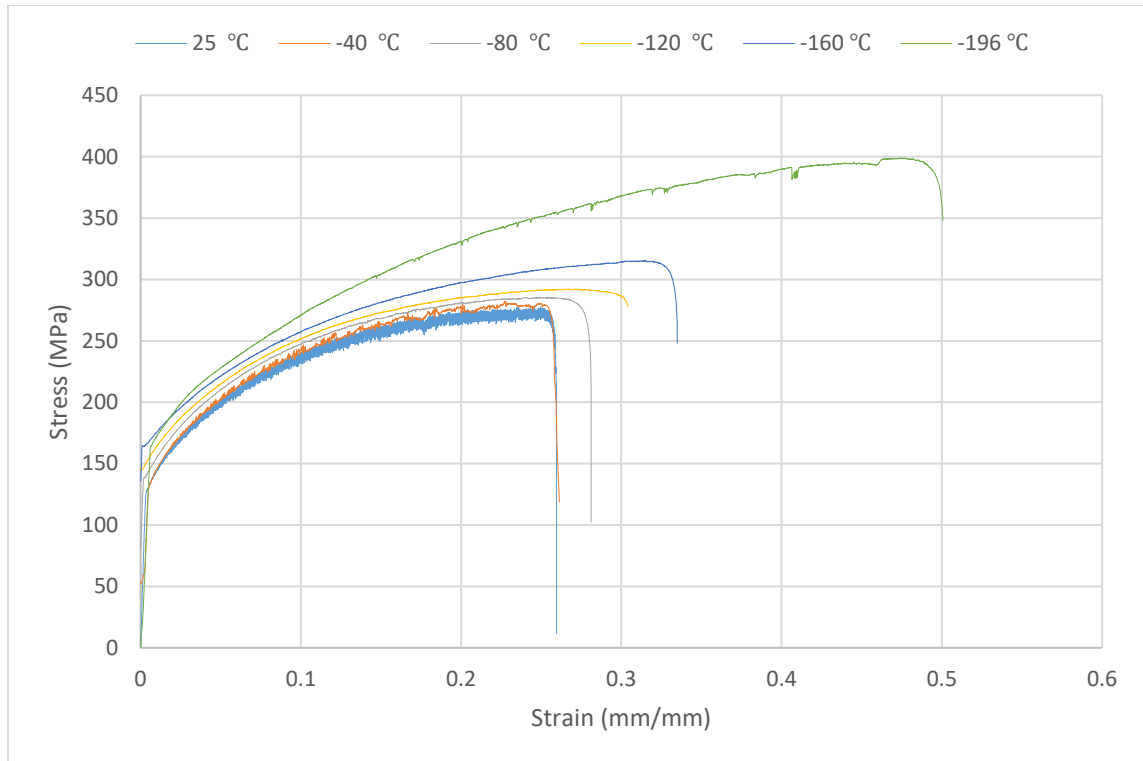


**Figure 4.16** Engineering Stress Strain Curves for aluminum alloy AA5182 (rolling direction) obtained at temperature points of from 25, -40, -80, -120, -160, and -196 °C; respective strain rate  $1.9 \times 10^{-3} \text{ s}^{-1}$

The yield stress, ultimate tensile stress, strain at necking, and strain at fracture are plotted as a function of temperature in **Figure 4.17** through **4.19** respectively. **Figure 4.17** shows a relatively constant yield stress, with a gradual increase as temperature decreases. The tensile stress of the material is observed to first increase gradually from RT as the temperature is decreased to -80°C. The tensile stress then increases significantly from -80°C to -160°C, and again increases even more drastically from -160°C to -196°C. **Figure 4.18** and **Figure 19** show that the strain at maximum load and the engineering fracture strain both follow the same trend of increasing as the temperature is decreased. The material is gaining both strength and ductility as the temperature is decreased. These results are discussed further in Chapter 5.

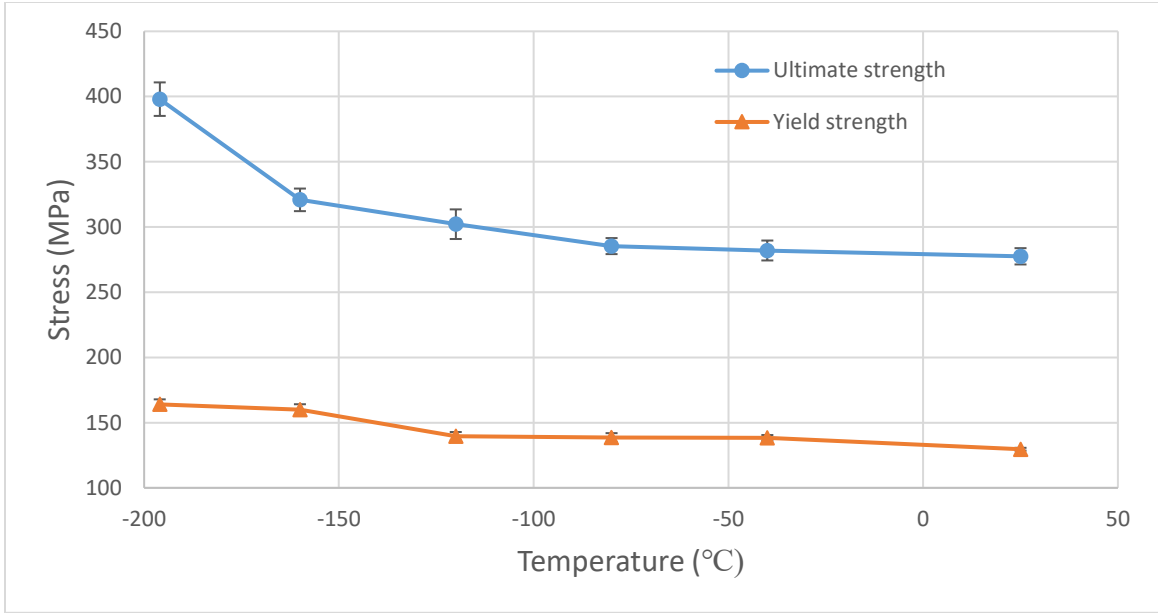


**Figure 4.17** Yield stress and ultimate tensile stress obtained in uniaxial tension at values from 25, -40, -80, -120, -160, and -196°C tensile tests.

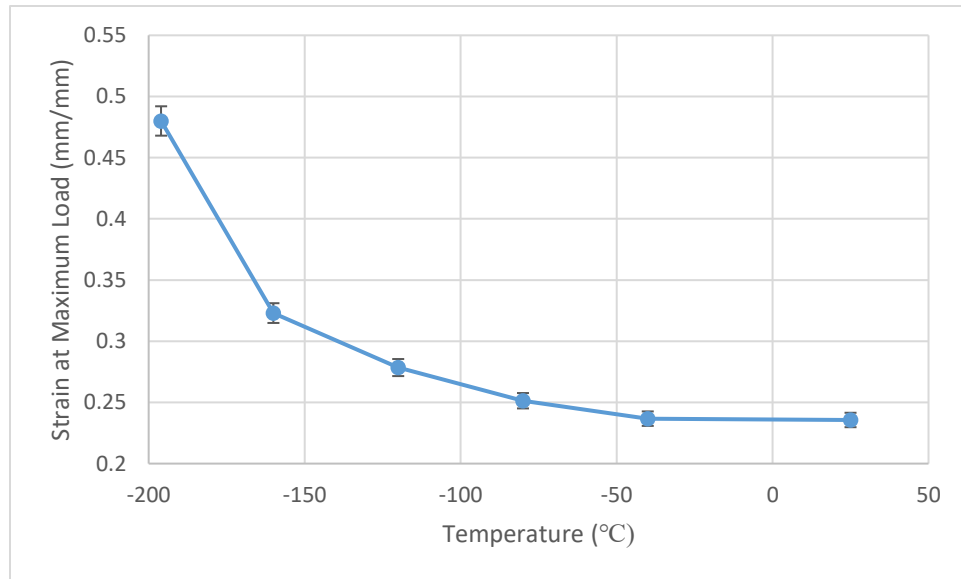


**Figure 4.18** Strain at maximum load values from 25, -40, -80, -120, -160, and -196 °C

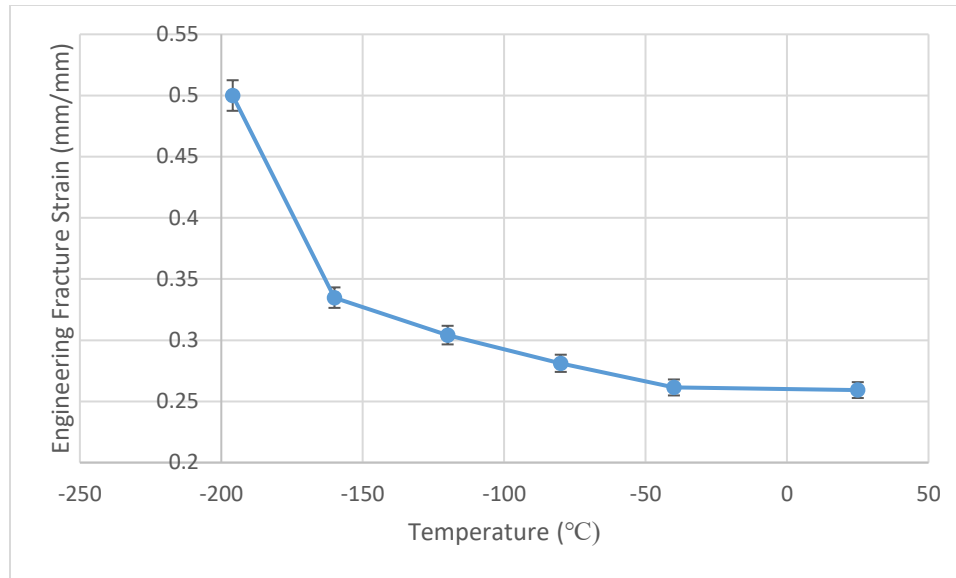


**Figure 4.19** Engineering fracture strain average values from 25, -40, -80, -120, -160, and -196 °C

To determine more information on the effect of temperature on the mechanical properties, specifically strain hardening and work hardening rates, the strain hardening exponent was mapped as a function of uniform elongation of aluminum alloy AA5182 at temperature points of 25, -40, -80, -120, -160. and -196 °C in **Figure 4.20** and **Figure 4.21** respectively.

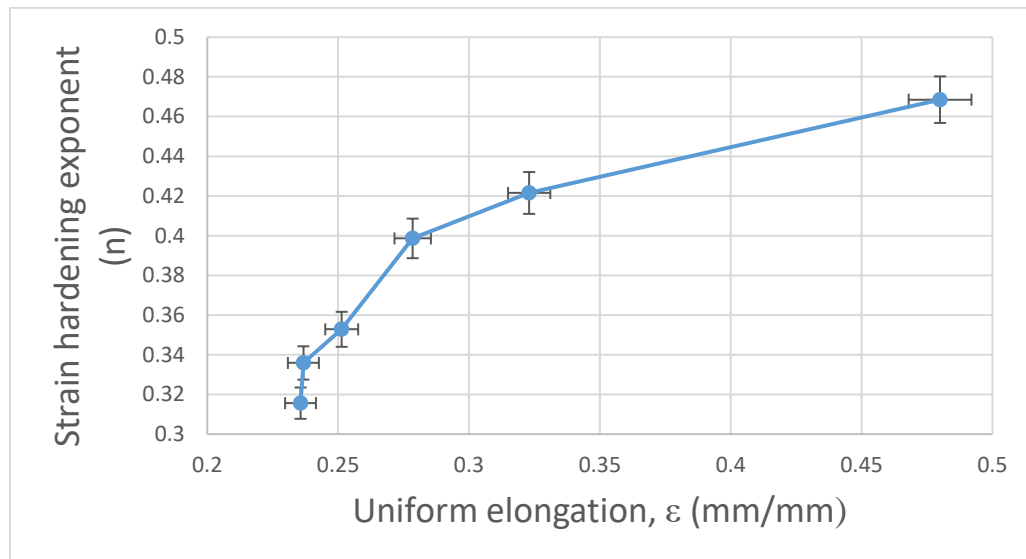


**Figure 4.20** Strain hardening exponent mapped as a function of uniform elongation of aluminum alloy AA5182 obtained at temperature points of 25, -40, -80, -120, -160. and -196 °C

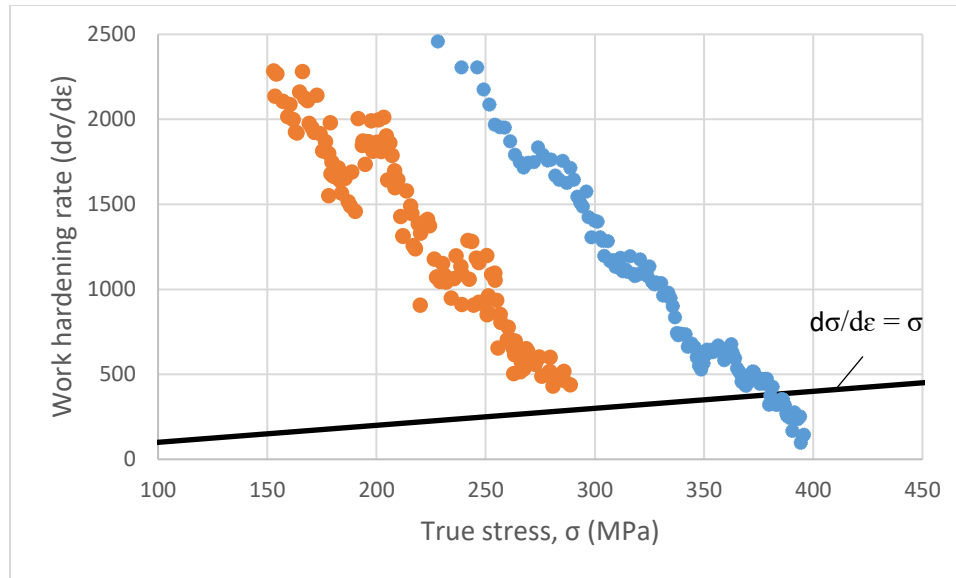


**Figure 4.21** Work hardening rate mapped as a function of true stress for aluminum alloy AA5182 obtained at temperature points of 25 and -196°C

**Figure 4.21** provides the work hardening rate as a function of true stress for tensile samples tested at 25 and -196°C. This plot, referred to as the Kocks-Mecking model, provides significant information about the material behaviour of AA5182-O and flow stress dependence on temperature. Both the slope (k-value) of the data and the relationship with the Considère criterion are important behaviors to analyze. There are three important details that can be observed from the graph. The slope of the -196°C data is observed to be lower than the slope of the 25°C data. It is also observed that the -196°C data is more consistent with less variation (standard deviation) in values. The final observation is that the -196°C data fractures when the Considère's criterion for necking is met; as opposed to the 25°C data which fractures prematurely before this criterion is met. These results are further discussed in Chapter 5.

**Figures 4.10** through **Figure 4.15** show a trend of the serrations of the stress-strain curves from the tensile tests decreasing as the temperature is decreased. **Figure 4.22**, shows the stress-strain curve for a tensile sample tested at 120°C and **Figure 4.23** illustrates a summation of the room temperature, low temperature, and 120°C stress-strain curves combined. This figure illustrates that the stress-strain curves become uniform at lower temperatures (approximately below -80°C) as well as higher temperatures (around 120°C).

These changes in serrations, as well as the trends of mechanical properties plotted, are further discussed in Chapter 5. It also shows that although testing AA5182-O at higher temperatures (120°C) reduces the non-uniform deformation and increases the ductility of the material (engineering strain), it does not reach the maximum flow stress or the increased final fracture that testing at lower temperatures (below -80°C) is capable of achieving.

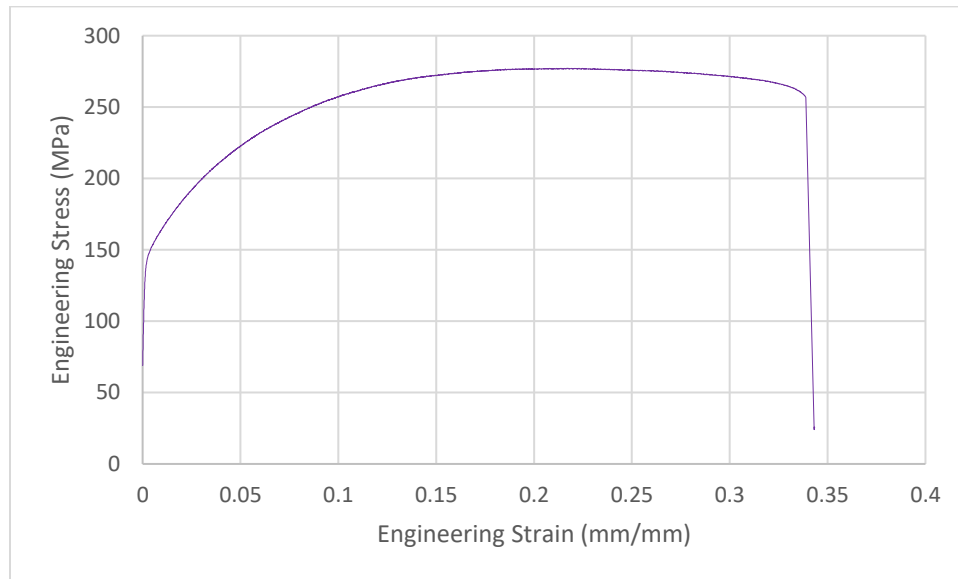


**Figure 4.22** Engineering Stress Strain Curves for aluminum alloy AA5182 (rolling direction) obtained at temperature 120°C; respective strain rate  $1.9 \times 10^{-3} \text{ s}^{-1}$

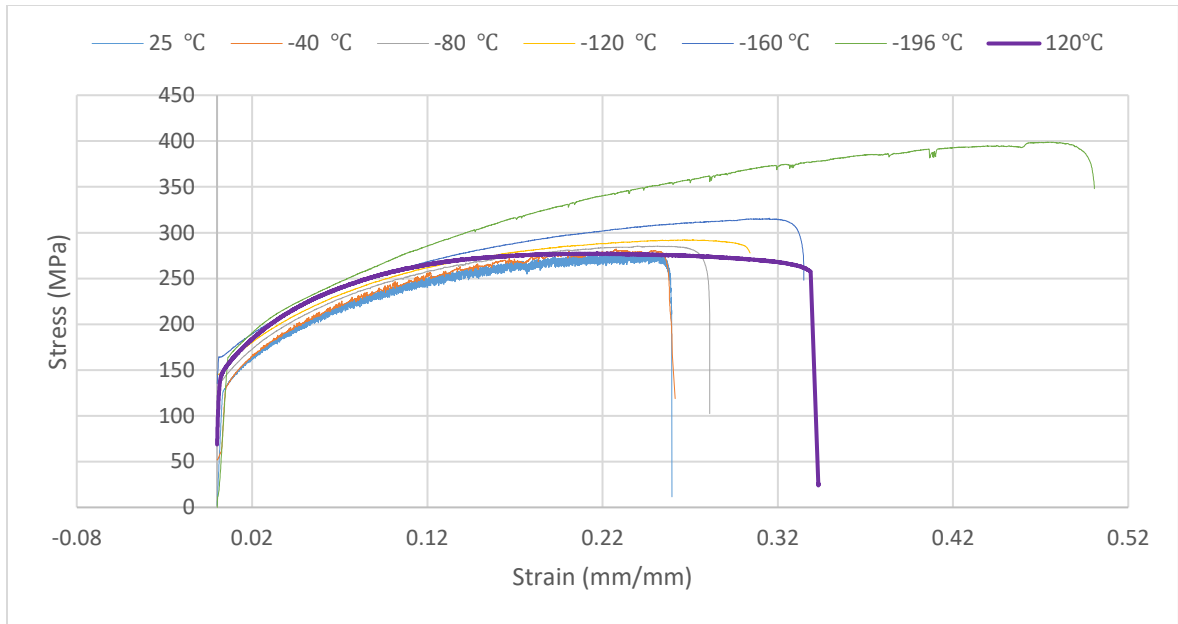


**Figure 4.23** Engineering Stress Strain Curves for aluminum alloy AA5182 (rolling direction) obtained at temperature points of from 25, -40, -80, -120, -160, -196, and 120°C; crosshead velocity of 0.084 mm/s (respective strain rate  $1.9 \times 10^{-3} \text{ s}^{-1}$ ).

### 4.3 Fractography

**Figure 4.24** a through f, shows the tensile samples post-fracture at temperature of 25, -40, -80, -120, -160. and -196 °C respectively, and a crosshead velocity of 0.084 mm/s.

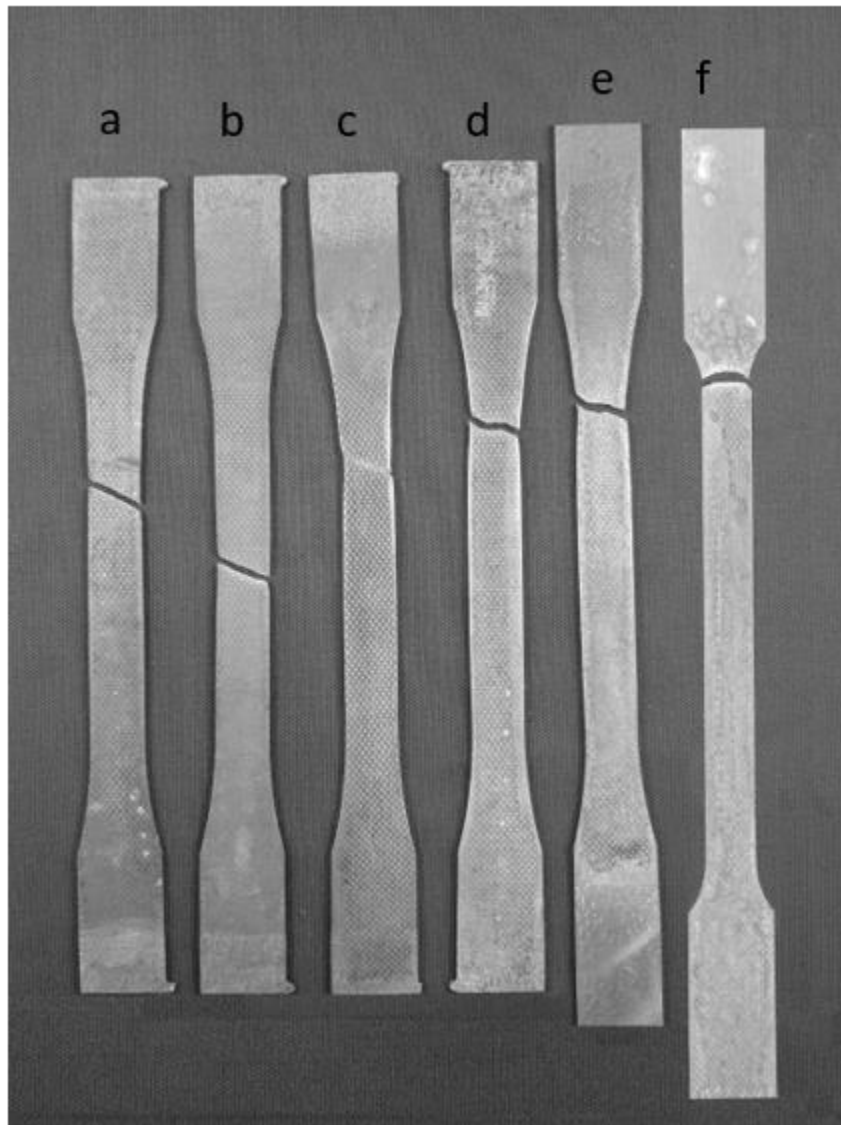


**Figure 4.24** Tensile samples fractured at temperature of a-25, b-40, c-80, d-120, e -160. and f-196°C respectively, and a crosshead velocity of 0.084 mm/s (strain rate  $1.9 \times 10^{-3} \text{ s}^{-1}$ ).

The following Figure, **Figure 4.25**, shows the angle of fracture measured from reference from parallel to the gauge length of the fracture of three sets of samples at each temperature. Magnified images of these sample fracture angles are provided in the Appendices.

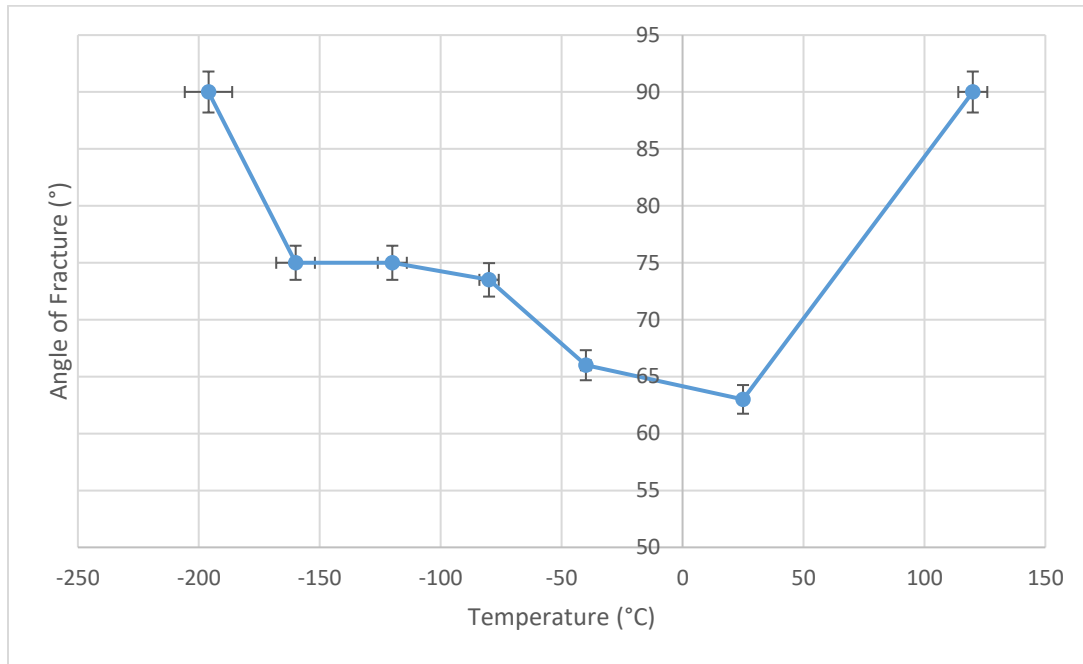


**Figure 4.25** Average measured angle of fracture mapped as a function of temperature at 25, -40, -80, -120, -160. and -196°C

Some images of the fracture surface were taken for each sample and Autopano Pro software was used to stitch the images together. These images were used to locate areas of interest for further SEM investigation, such as dense areas of dimples, or areas that appear out of the ordinary. The secondary purpose for these images was to measure the average area of reduction after fracture.

**Figure 4.26** shows a stitched image of the full BSE SEM fracture surface for AA5182-O after experiencing a ductile fracture from tensile testing at a temperature of -160°C and a crosshead velocity of 0.084 mm/s. **Figures 6.12** through **6.21** in the appendices show some stitched BSE SEM images and some magnified fracture surface images from tensile testing at a crosshead velocity of 0.084 mm/s and temperature of 25, -40, -80, -120, -160. and -196°C respectively.

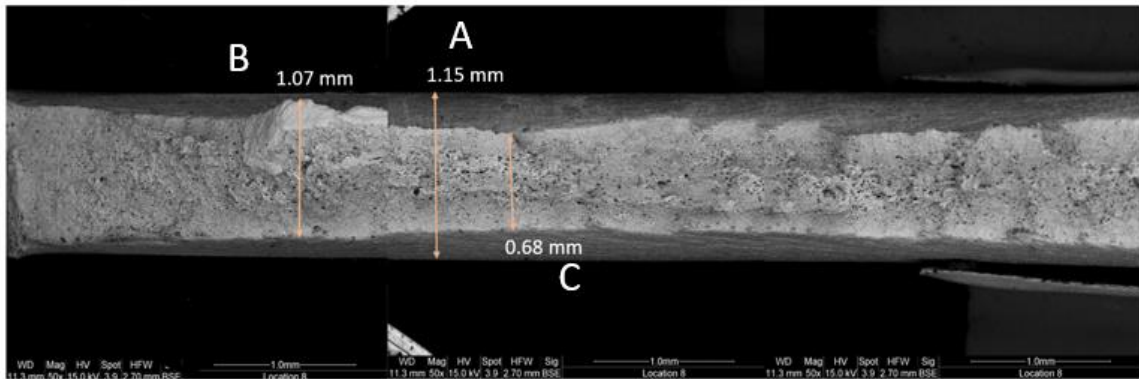


**Figure 4.26** BSE SEM image of AA5182-O after experiencing a ductile fracture from tensile testing at a temperature of  $-160^{\circ}\text{C}$  and a crosshead velocity of  $0.084\text{ mm/s}$ .

In these figures, the samples are measured at 10 different locations to determine the average thickness of the material in the area of uniform deformation (an example of these measurements is marked by **A**). The longest and shortest fractured edge were also measured and recorded (examples of these measurements are marked by **B** and **C** respectively). These measurements were taken to investigate the changes in the deformation fracture area. Results for these measurements are provided in the appendices. This process was repeated for tensile samples at each testing temperature ( $25$ ,  $-40$ ,  $-80$ ,  $-120$ ,  $-160$ , and  $-196^{\circ}\text{C}$ ) and provided in the Appendices.

To analyze the average dimple sizes, grids were overlaid on different areas of the fracture surface. Each point of the grid was used as a data point, with 10 different areas selected from each population of temperatures. Using these points, average dimple radius, length, and area calculations were measured from the images. From this data, graphs of the average dimple radius, length, area, and aspect ratio, were mapped as a function of temperature. **Figures A.4** through **A.7** provide the histograms of the dimple measurement data.

**Figure 4.27** shows the grid used for the purpose of this method of calculating the average sizes from a selection of locations on the fracture surface.

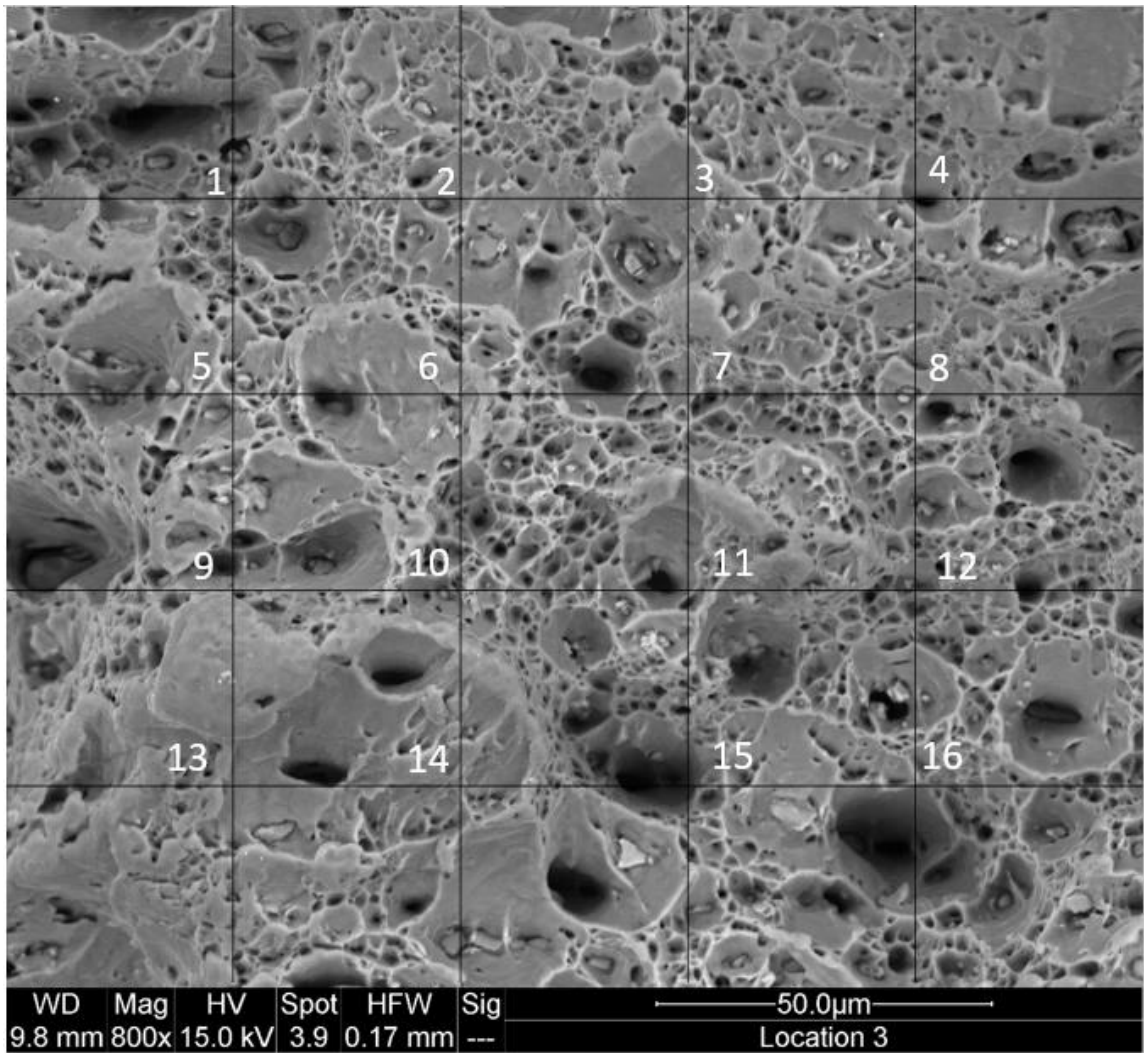


**Figure 4.27** SEM image of fractured tensile sample (rolling direction; -160°C; 0.084 mm/s) at 800x magnification with grid overlay.

**Figure 4.28** shows the average aspect ratio of dimples for aluminum alloy AA5182 obtained at temperature points of from 25, -40, -80, -120, -160. and -196 °C.

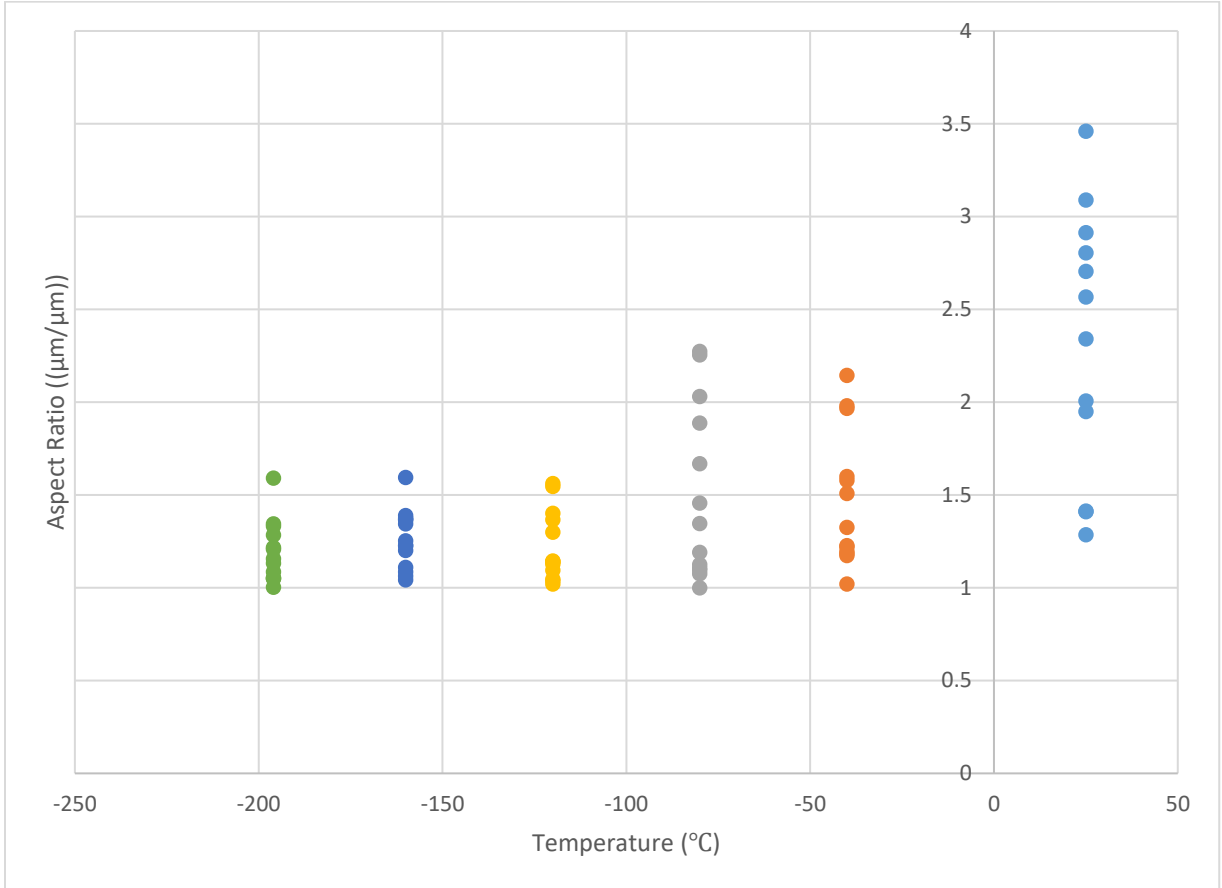


**Figure 4.28** The average aspect ratio of dimples for aluminum alloy AA5182 obtained at temperature points of from 25, -40, -80, -120, -160. and -196 °C.

The aspect ratio (ratio between the two lengths) decreases as the temperature decreases. It is observed that the dimples become more equiaxed and consistent as temperature is decreased. The shear fracture to void coalescence fracture is supported by this and further discussed in Chapter 5.

**Figure 4.29** shows the aspect ratio measured for aluminum alloy AA5182 obtained at temperature points of from 25, -40, -80, -120, -160. and -196 °C with a box plot and standard deviation values. These values are provided in the Appendices.

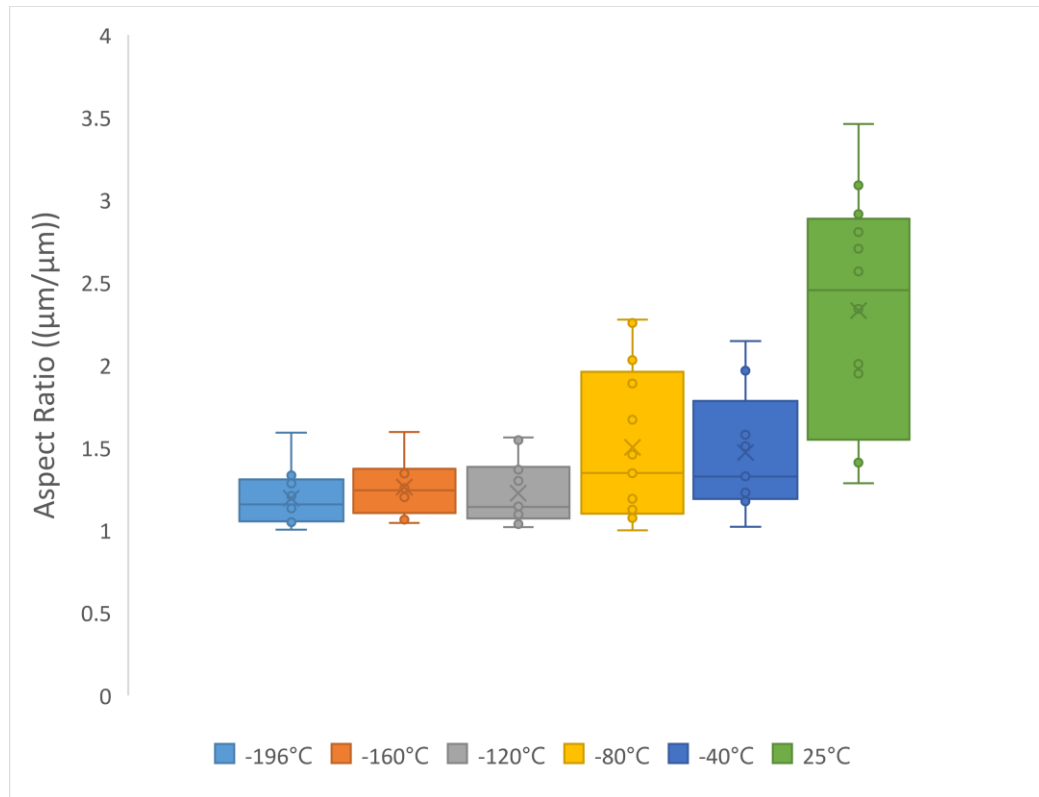


**Figure 4.29** The average aspect ratio of dimples with standard deviation for aluminum alloy AA5182 obtained at temperature points of from 25, -40, -80, -120, -160. and -196 °C.

**Figure 4.30** and **Figure 4.31** shows the average dimple area and standard deviation, respectively, measured for aluminum alloy AA5182 obtained at temperature points of from 25, -40, -80, -120, -160. and -196 °C.

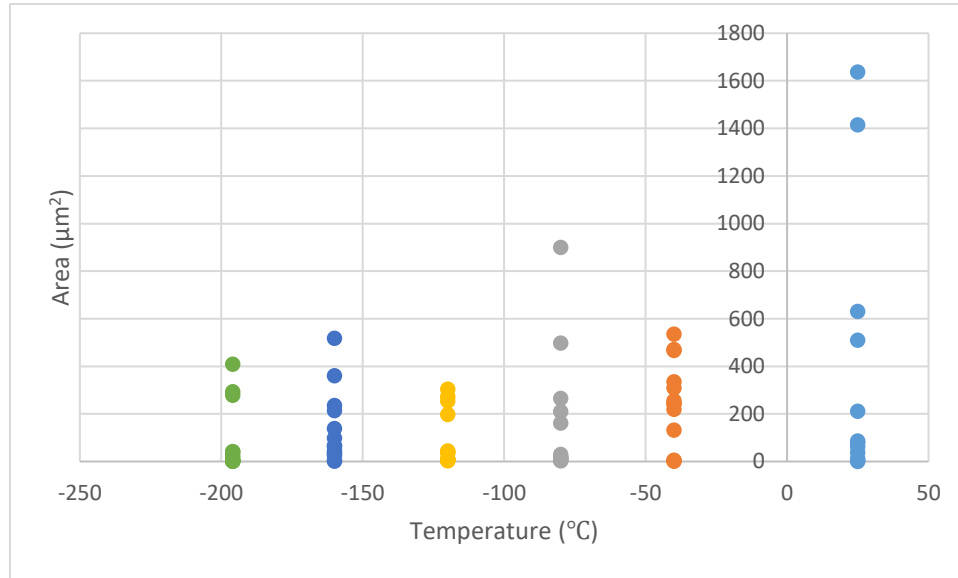


**Figure 4.30** The average dimple area ( $\pi \times \text{radius}^2$ ) measured for aluminum alloy AA5182 obtained at temperature points of from 25, -40, -80, -120, -160. and -196 °C.

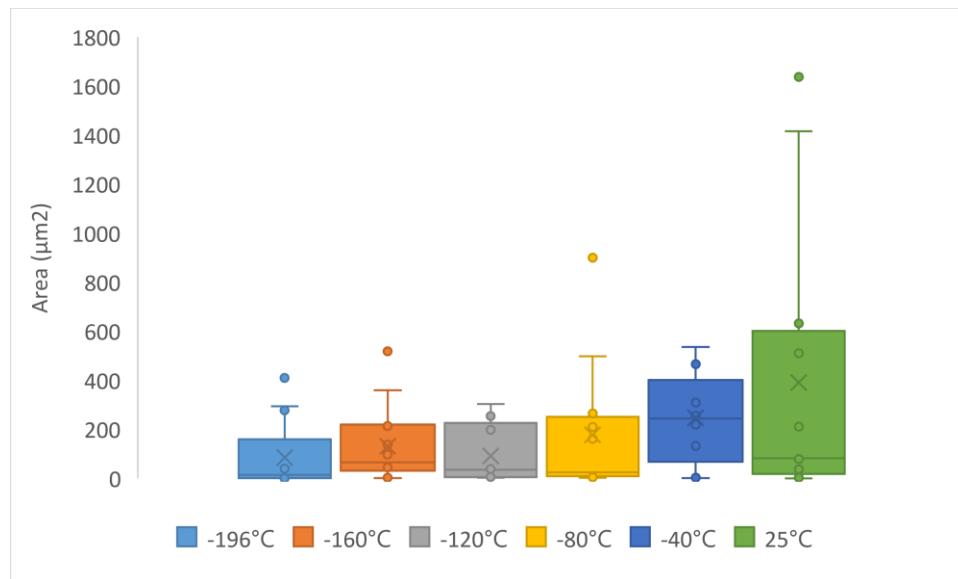


**Figure 4.31** The average dimple area ( $\pi \times \text{radius}^2$ ) measured with standard deviation for aluminum alloy AA5182 obtained at temperature points of from 25, -40, -80, -120, -160. and -196 °C.

**Figure 4.32** shows the BSE SEM image of AA5182-O after experiencing a ductile fracture from tensile testing at a temperature of 25°C and a crosshead velocity of 0.084 mm/s with arrows indicating the particles observed along the side walls of the dimples at 800x magnification. **Figure 4.33** shows the BSE SEM image of AA5182-O after experiencing a ductile fracture from tensile testing at a temperature of 25°C and a crosshead velocity of 0.084 mm/s showing parabola shaped dimples observed at 2000x magnification indicating parabolic shaped dimples.

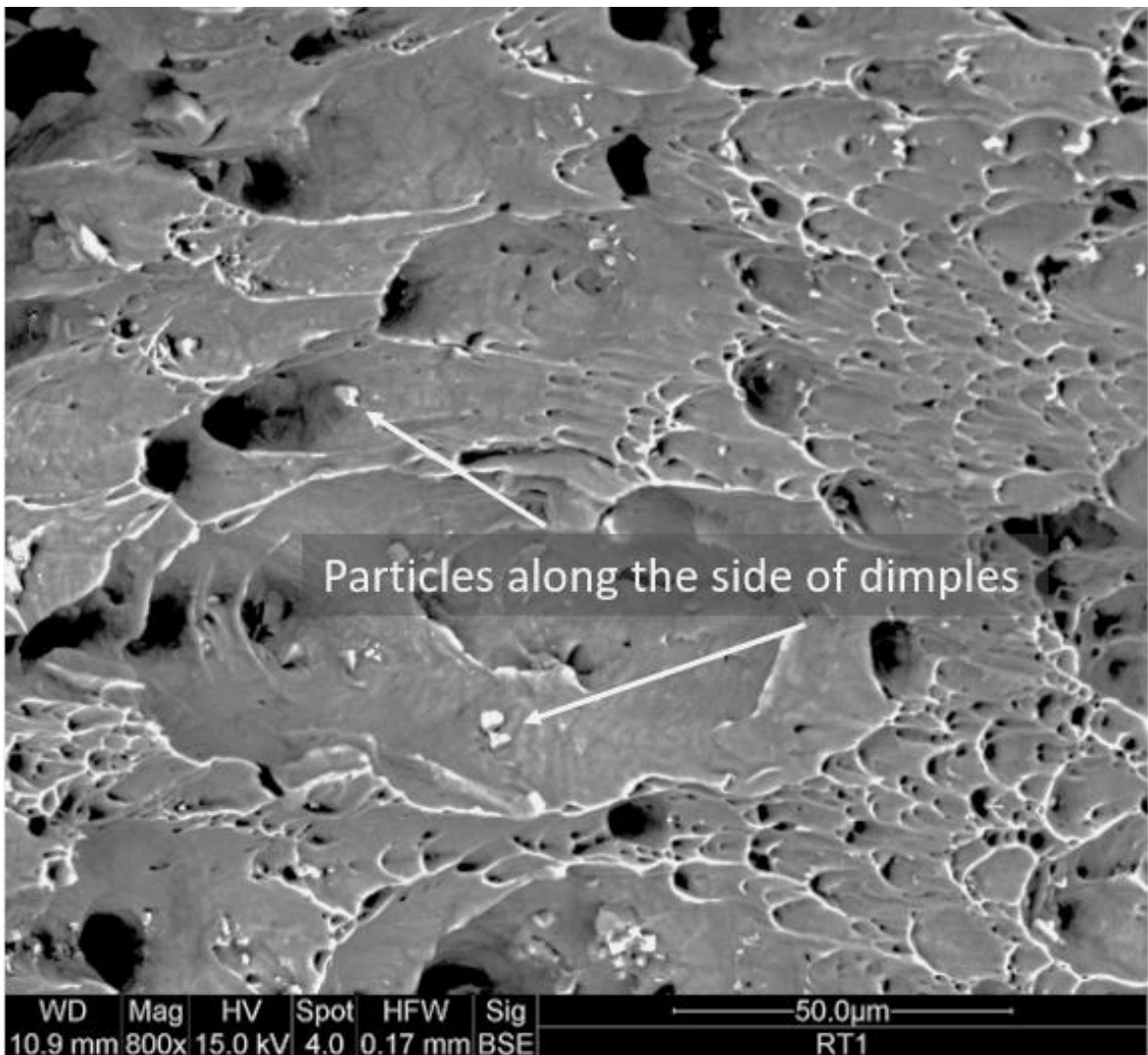


**Figure 4.32** BSE SEM image of ductile fracture of AA5182 at X800 magnification at 25°C

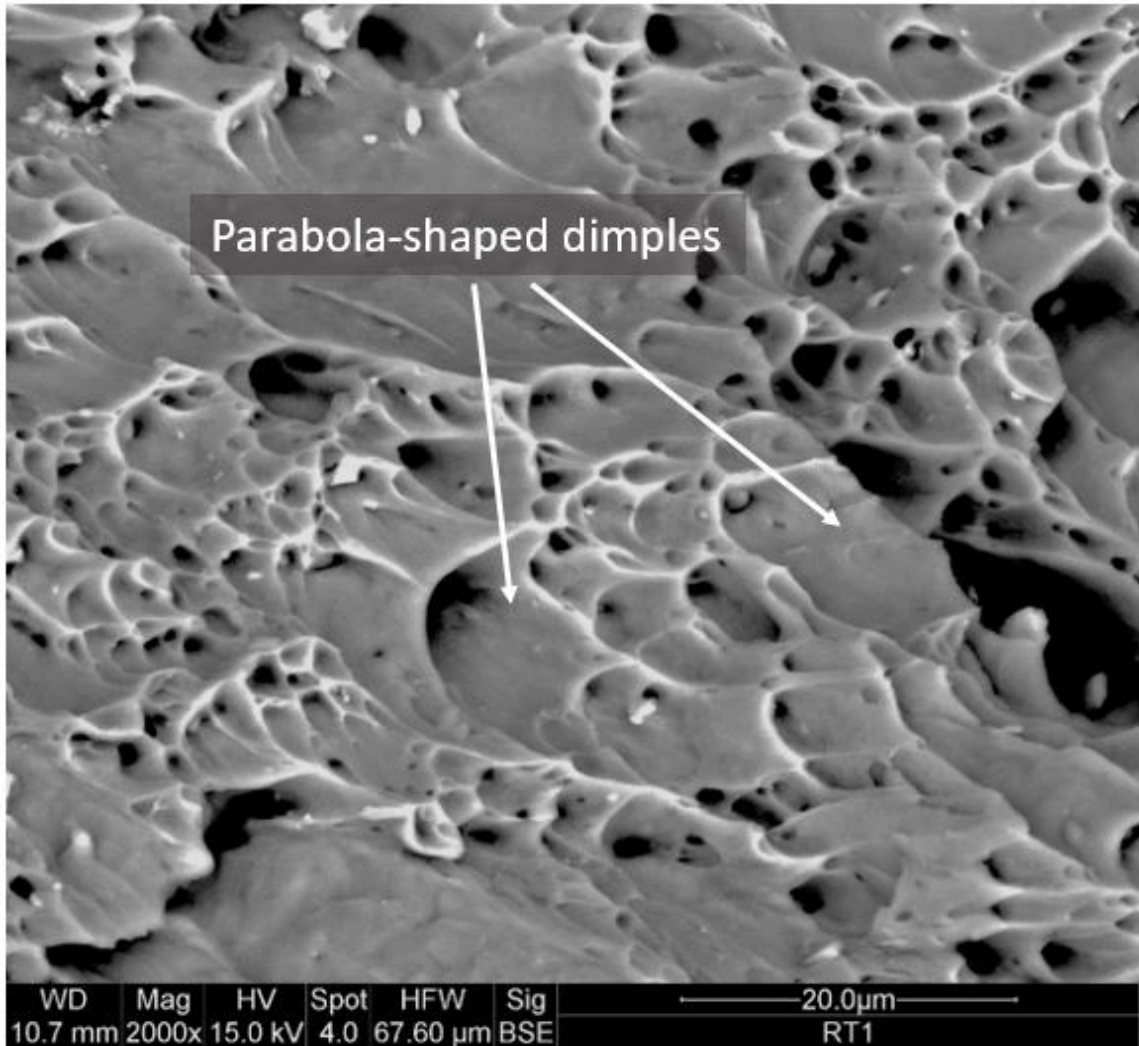


**Figure 4.33** BSE SEM image of ductile fracture of AA5182 at X2000 magnification at 25°C

These figures are in contrast against the -160°C tensile sample in **Figure 4.34** and **Figure 4.35** which show equiaxed dimples and broken particles located at the bottom of dimples respectively.

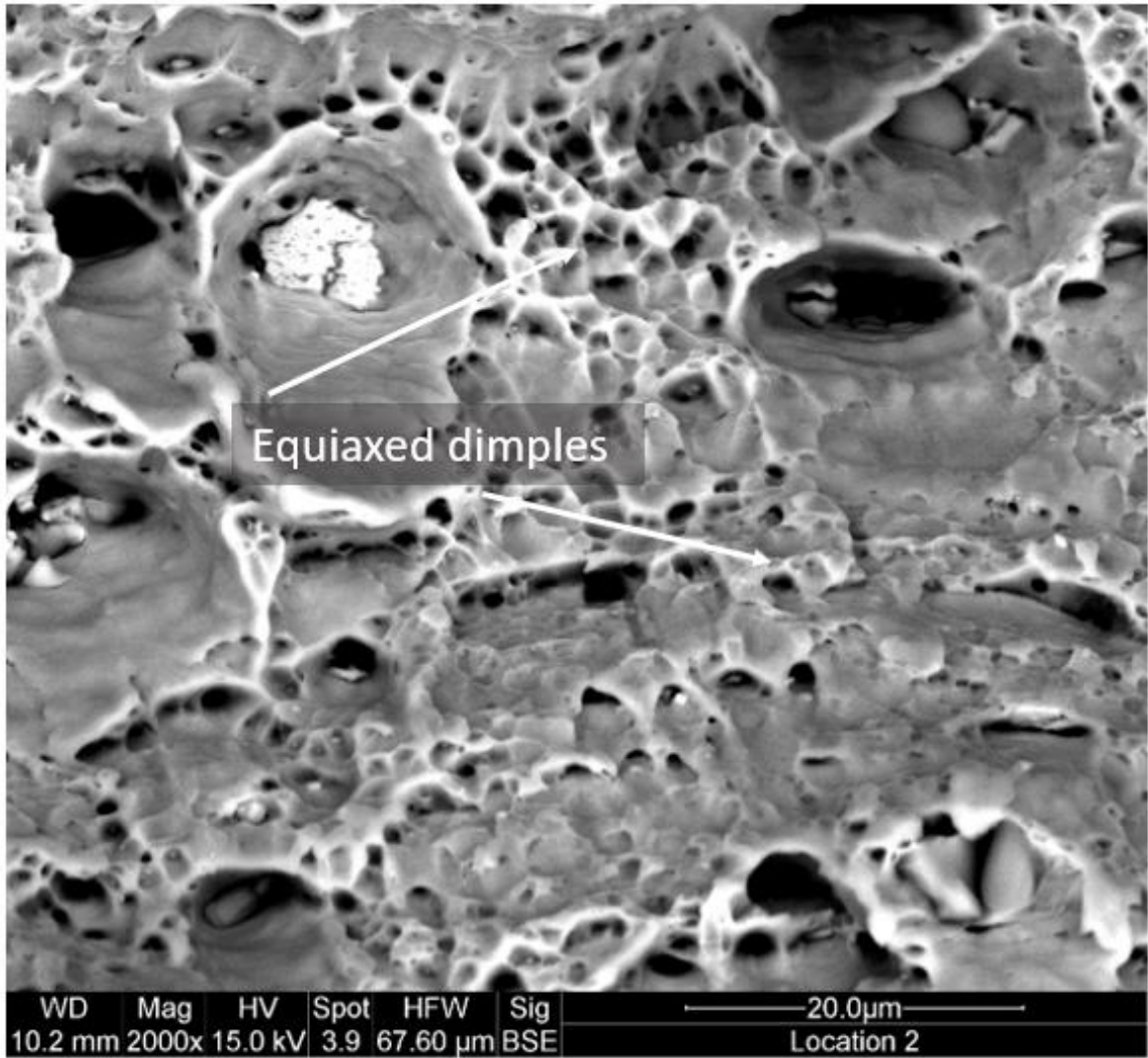


**Figure 4.34** BSE SEM image of ductile fracture of AA5182 at X2000 magnification at -160°C.

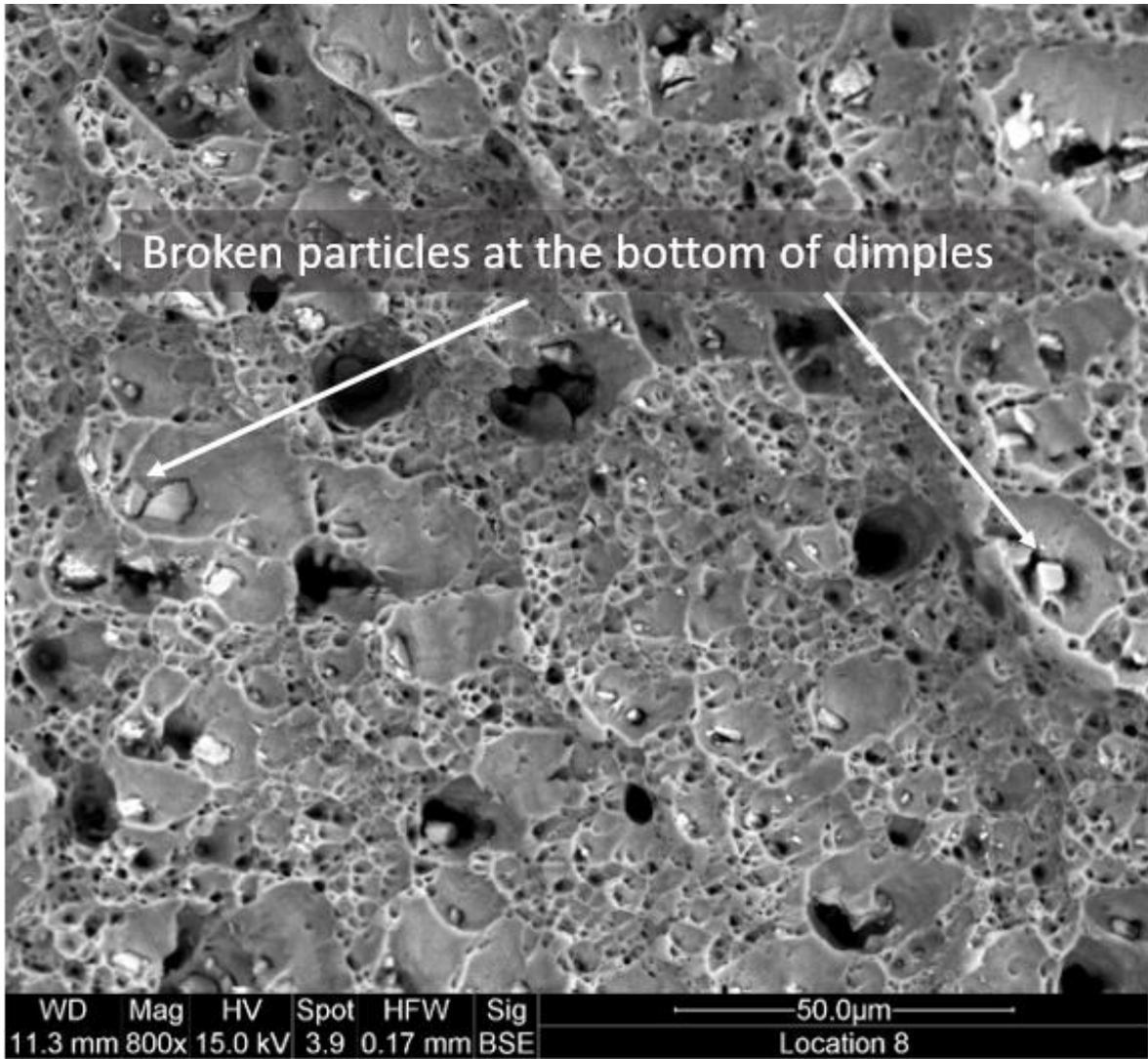


**Figure 4.35** BSE SEM image of ductile fracture of AA5182 at X800 magnification at -160°C

**Figures 4.36 through 4.40** show a gradual trend as the temperature is lowered from 25°C to -196°C, the shape of the dimples transitions from parabolic to equiaxed as the temperature is decreased. As the temperature is lowered below -80°C, more broken particles are observed (the quantity of these broken particles appear to increase as the temperature is decreased).

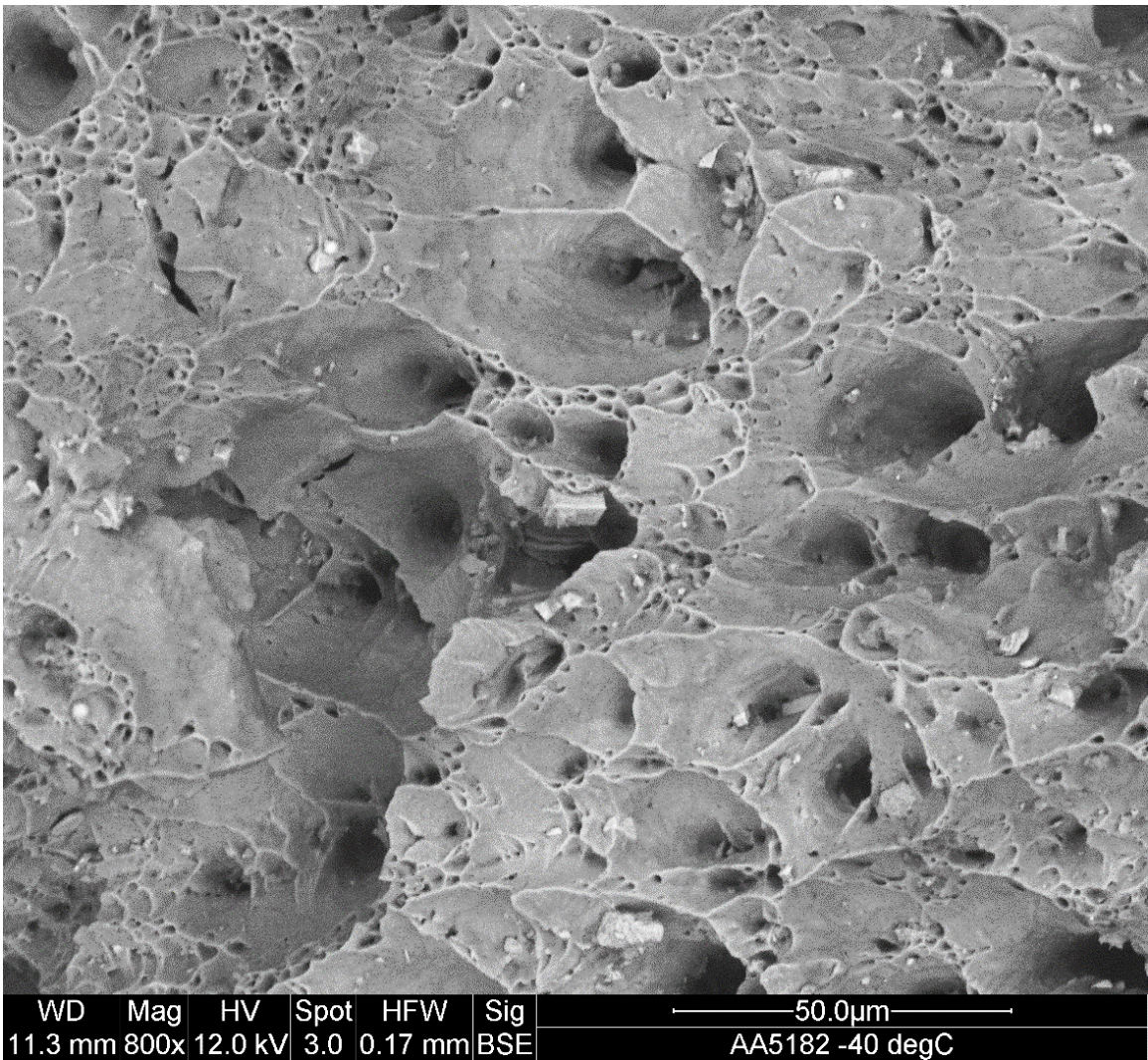


**Figure 4.36** BSE SEM image of ductile fracture of AA5182 at X800 magnification at -40°C

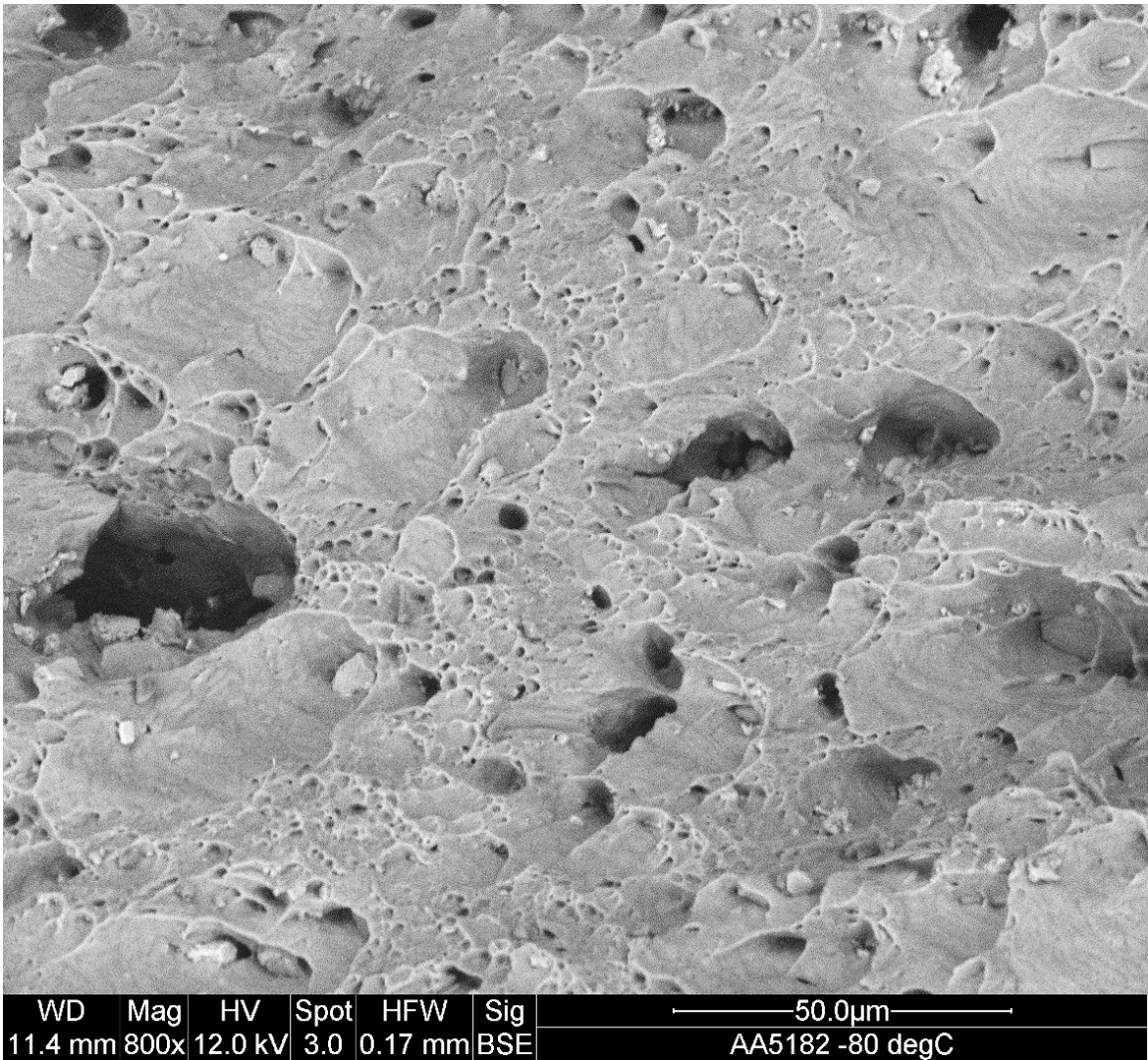


**Figure 4.37** BSE SEM image of ductile fracture of AA5182 at X800 magnification at -80°C

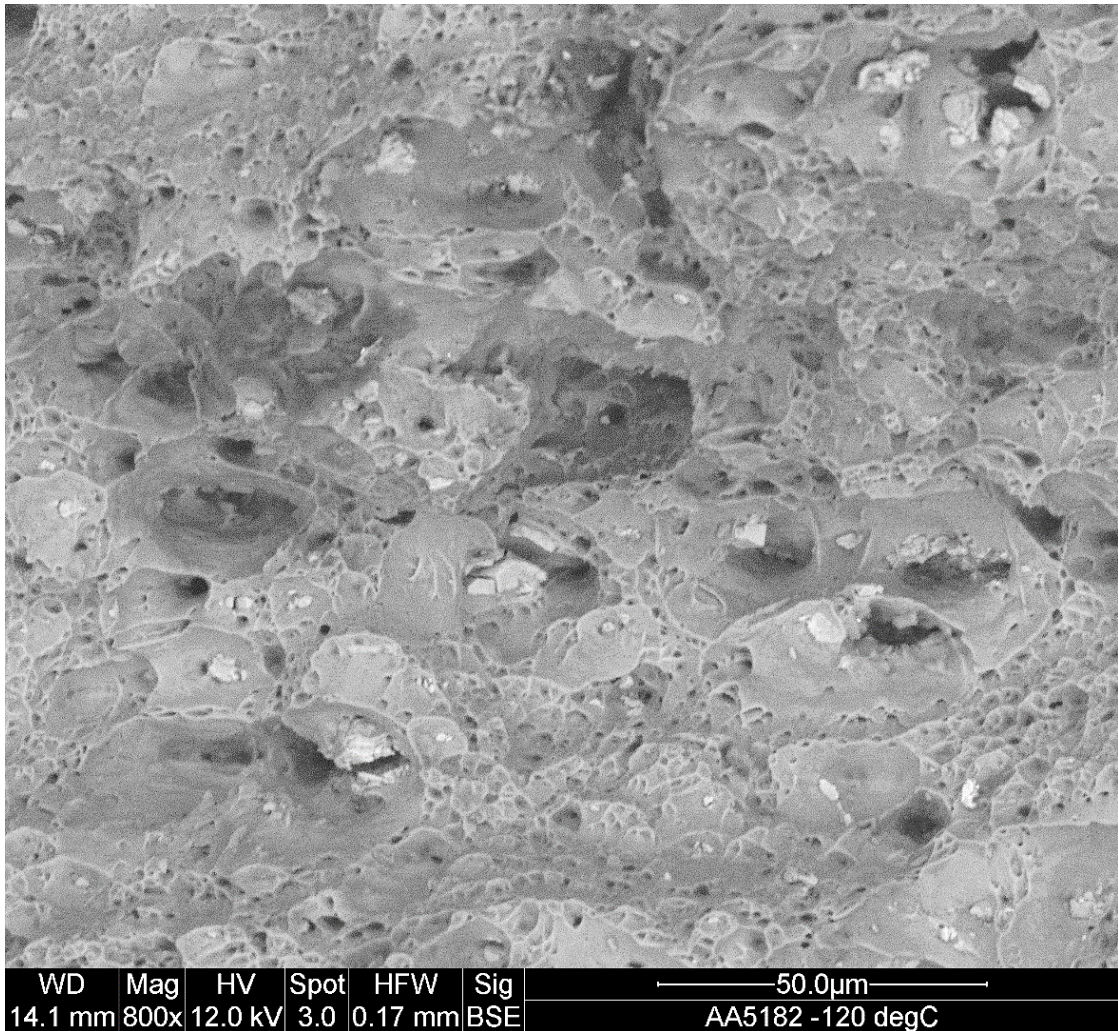


**Figure 4.38** BSE SEM image of ductile fracture of AA5182 at X800 magnification at -120°C

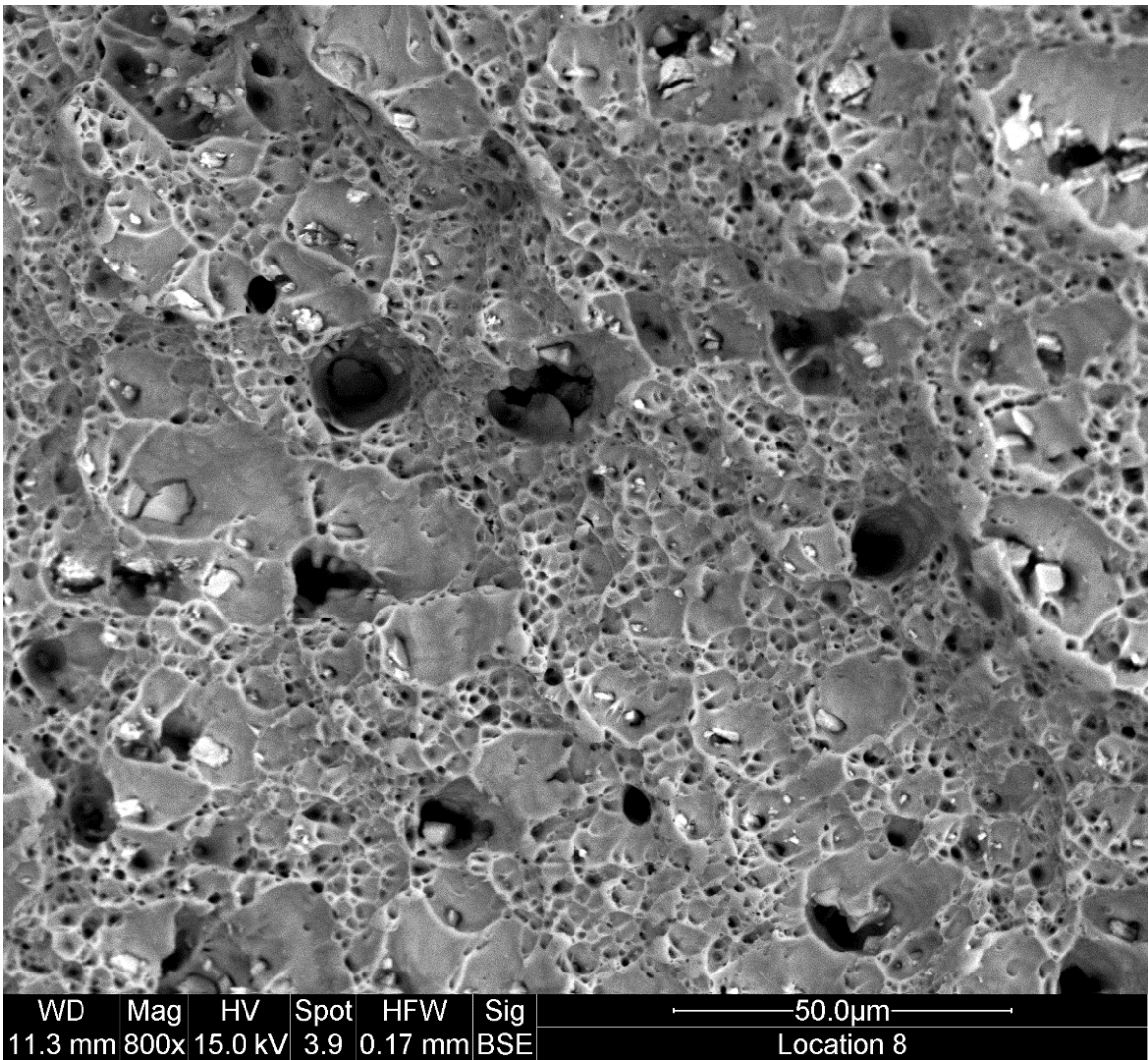


**Figure 4.39** BSE SEM image of ductile fracture of AA5182 at X800 magnification at -160°C

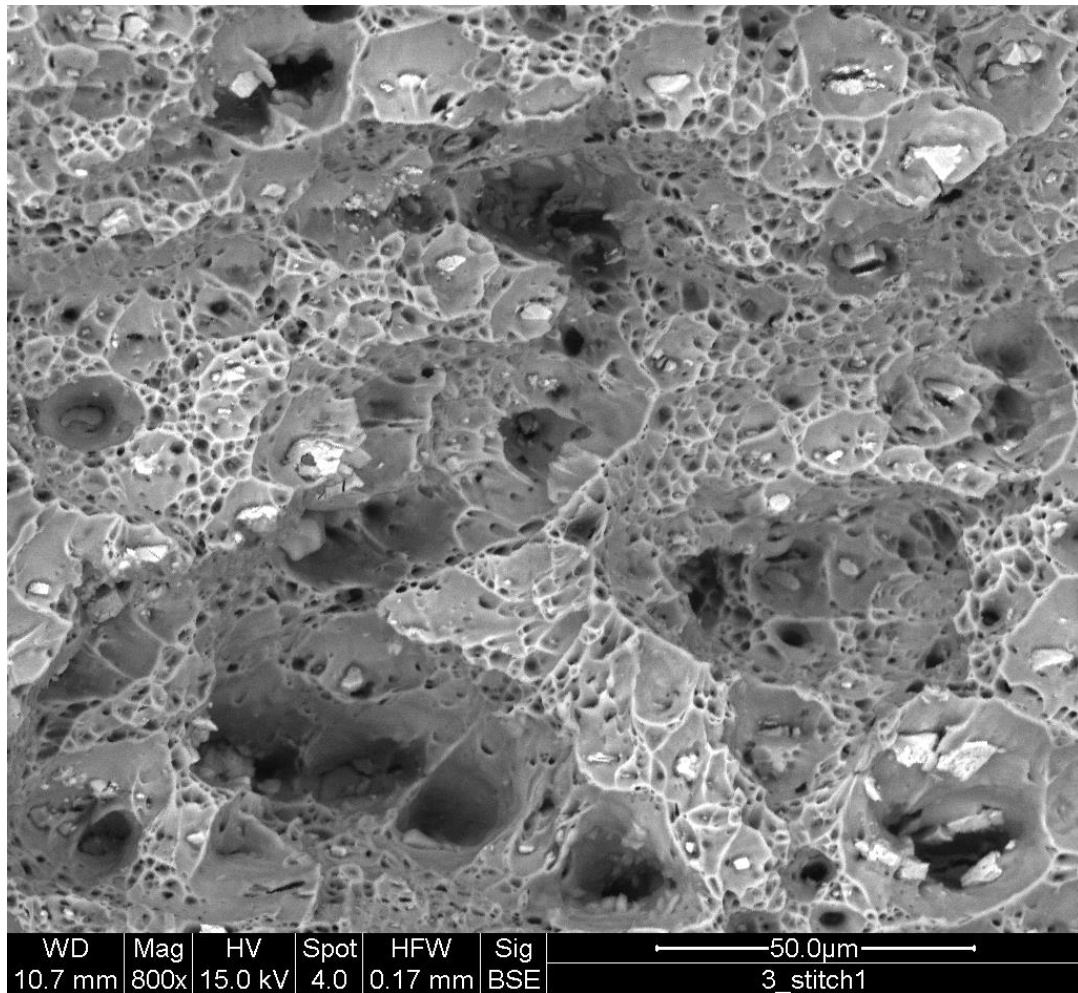


**Figure 4.40** BSE SEM image of ductile fracture of AA5182 at X800 magnification at -196°C

It is also observed that as the temperature decreases, the size of the dimples appear to decrease and becomes more consistent in measurements. In SEM images at 25°C, dimples appear to be disconnected by large shear areas. In the SEM images at -196°C, void coalescence appears to be the mechanism for fracture as intervoid ligaments seem to connect equiaxed voids together. These fracture surfaces and possible fracture mechanisms are discussed further in Chapter 5. Additional SEM images are provided in the Appendices.

## 4.4 Cottrell-Stokes Testing

### 4.4.1 Temperature Change Tensile Testing

The process of Cottrell-Stokes testing involved conducting initial tensile tests to obtain stress-strain curves for each interval temperature to identify the regions of flow stress and points of interest at specific strain values. Two sets of tests were conducted. The first set was a preliminary trial for developing a Cottrell-Stokes procedure and involved developing stress-strain curves at room temperature and 120°C. The secondary set of tests involved testing at lower temperatures. For these tests, stress-strain curves were developed at 25 C and -40, -80, -120, and -160°C. For the first set of tests, the room temperature tensile curve results are provided in **Figure 4.10** at a crosshead velocity of 0.084 mm/s. The following figure, **Figure 4.41**, provides the engineering stress-strain curve at 120°C temperature and an initial crosshead velocity of 0.084 mm/s.

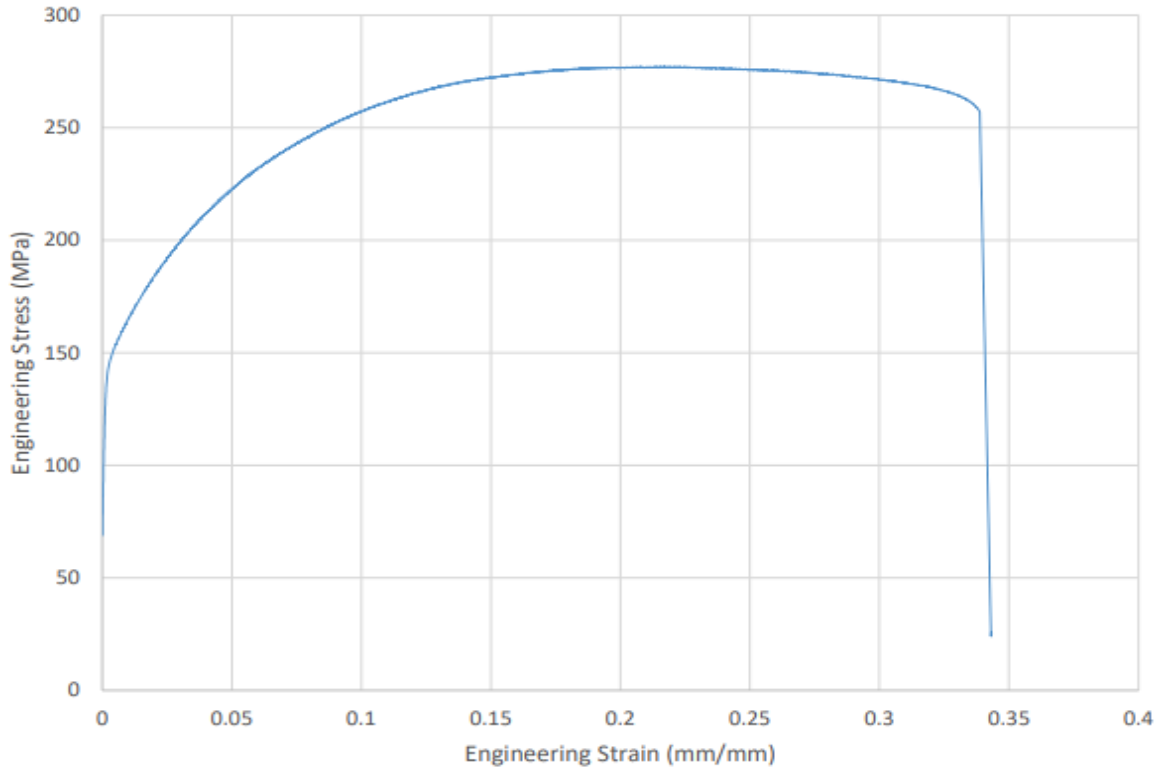


**Figure 4.41** Engineering Stress Strain Curve for aluminum alloy AA5182 obtained at 120°C and crosshead velocity of 0.084 mm/s

**Figure 4.42**, provides the Cottrell-Stokes plot of the engineering stress-strain curve. A magnified version of this curve is provided in the appendices section in **Figure A.59**.

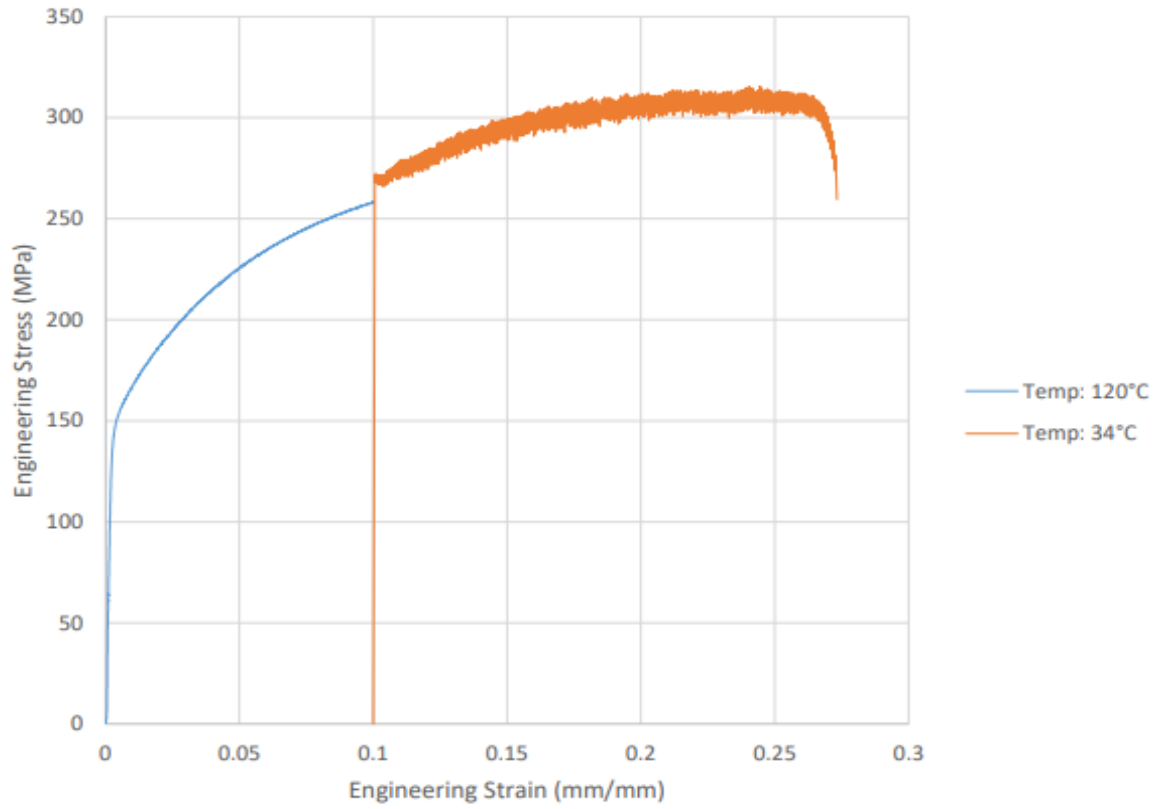


**Figure 4.42** Cottrell-Stokes Engineering Stress Strain curve for temperature change tests from 120°C to 34°C.

The following figure, **Figure 4.43**, provides the engineering stress-strain curve at 0.084 mm/s and temperature intervals as provided in **Table 4.5**.

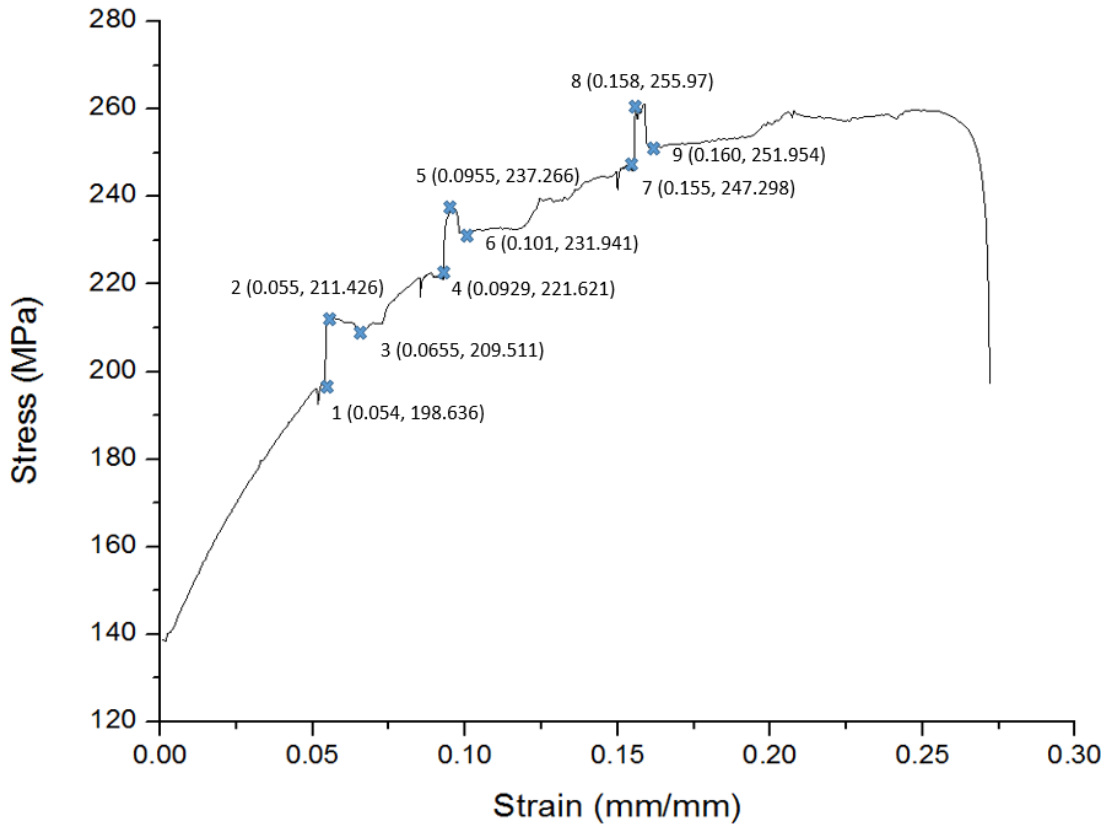


**Figure 4.43** Cottrell-Stokes Engineering Stress Strain curve for  $\Delta 20^{\circ}\text{C}$  temperature jump tests.

**Table 4.5** Internal Data for Cottrell-Stokes  $\Delta 20^{\circ}\text{C}$  temperature jump tests

Interval Temperature	$\Delta\text{Temp}$	$\Delta\text{Stress}$	$\Delta\text{Strain}$
1) -134 to -114 (Points 1-3)	$20^{\circ}\text{C}$	10.875 MPa	0.0115 mm/mm
2) -114 to -94 (Points 4-6)	$20^{\circ}\text{C}$	10.32 MPa	0.0081 mm/mm
3) -94 to -74 (Points 7-9)	$20^{\circ}\text{C}$	4.656 MPa	0.005 mm/mm

The three stages were plotted using the change in stress as a function of temperature in the following graph.

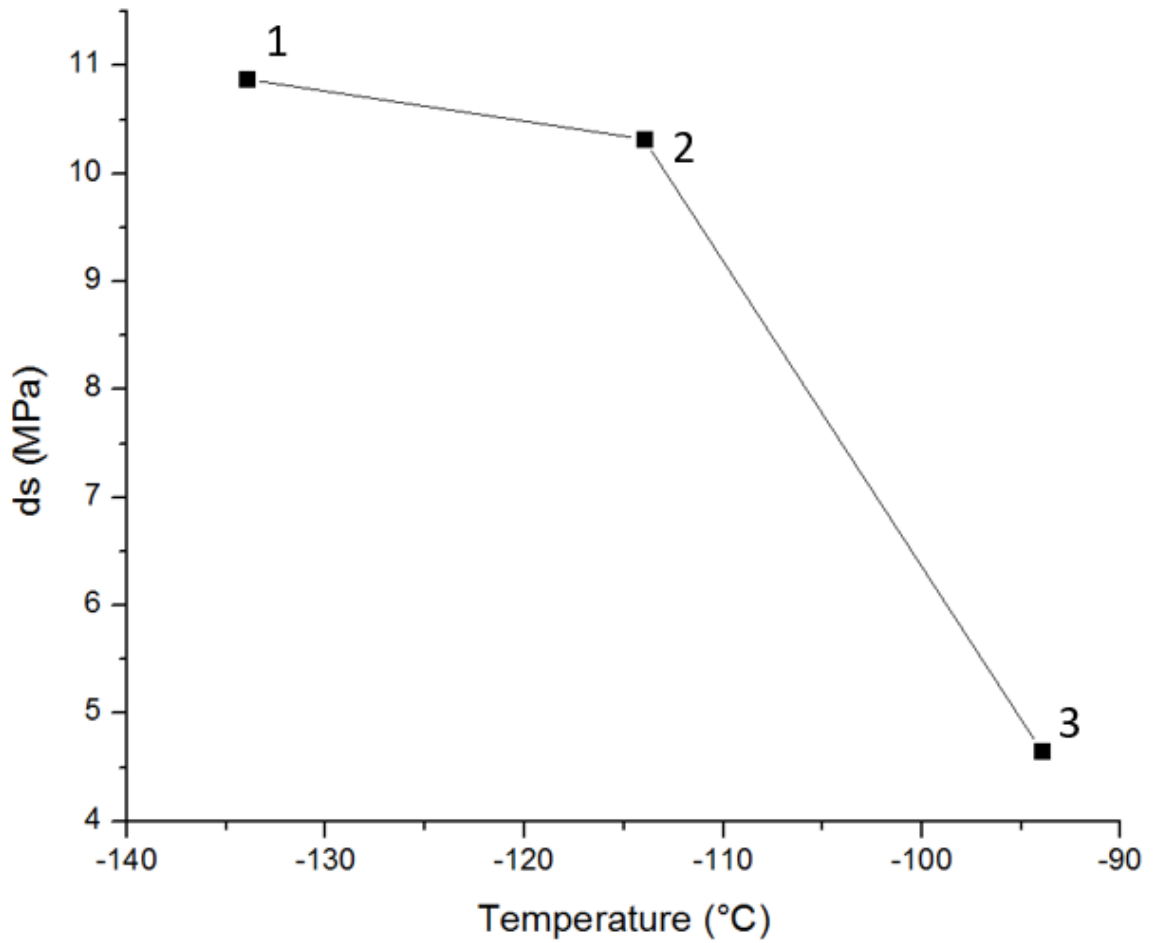


**Figure 4.44** Interval plot of the change in stress as a function of temperature for  $\Delta 20^\circ\text{C}$  temperature jump tests

## 4.4.2 Strain Rate Change Tensile Testing

In the first set of tests, the cross-head velocity was not set at a single rate to pull the samples to fracture. The full load versus extensometer displacement curve for this test is magnified and provided in the appendices in **Figure A.59**. The initial cross-head velocity and temperature was set as 1mm/min and 25°C, respectively. A reference load-displacement curve was obtained at 1 mm/min and 25°C and provided in **Figure 4.45**. The test was continued until the program indicated that the extensometer had reached a distance of 1 mm, as shown in **Figure 4.46**. The template that was developed for the test then automatically jumped the cross-head velocity to 5 mm/min, as shown in **Figure 4.47**. Once the extensometer reached a distance of 2 mm, the cross-head velocity was automatically jumped to 10 mm/min and the specimen was pulled until fracture, as shown in **Figure 4.48**.

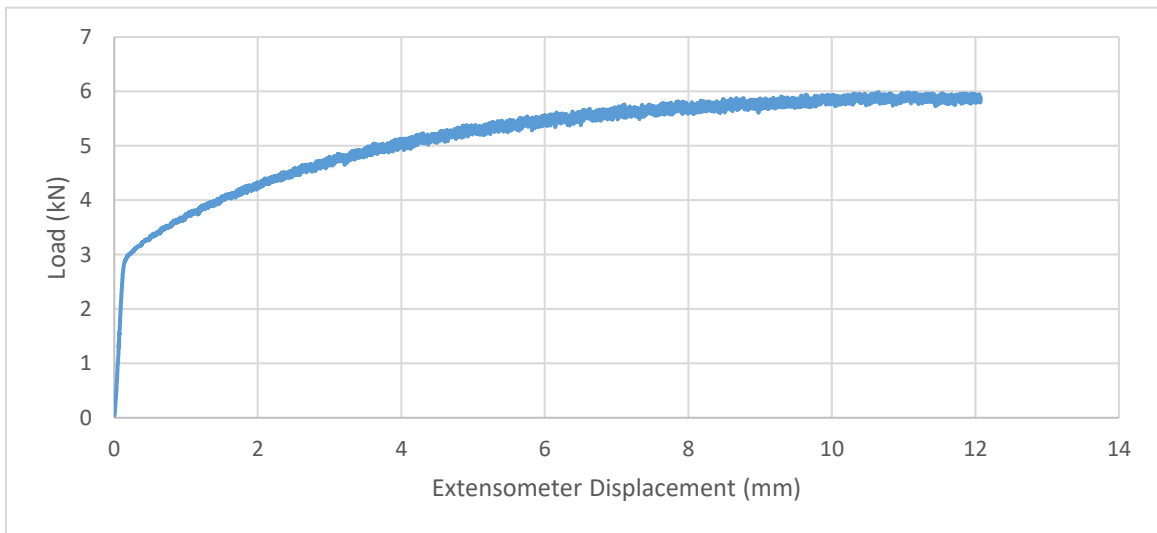


**Figure 4.45** Initial load-displacement curve obtained at 1 mm/min and 25°C

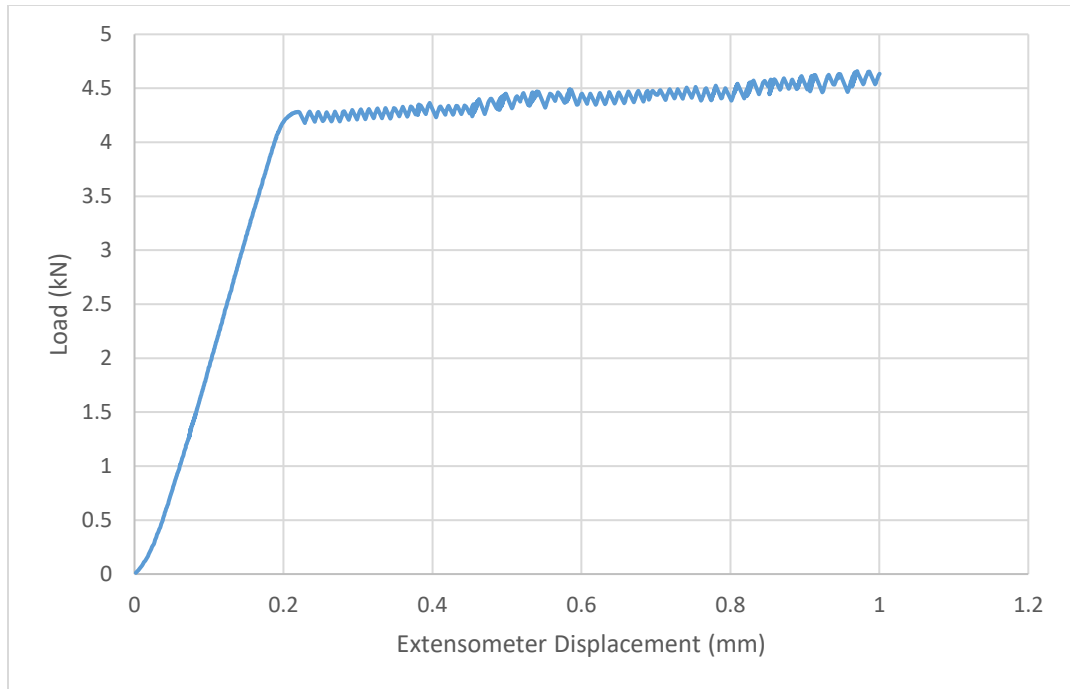


**Figure 4.46** Section 1 of Cottrell-Stokes load-displacement curve for strain rate jump tests of 1 mm/min to 5 mm/min (at 1 mm displacement) from 0 to 1 mm extensometer displacement.

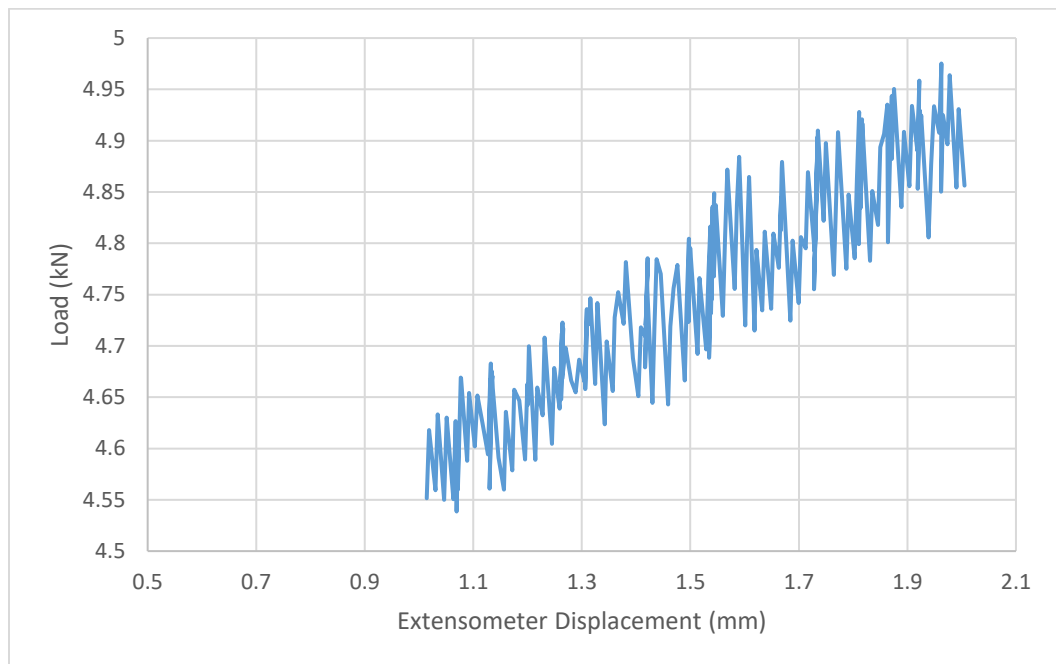


**Figure 4.47** Section 2 of Cottrell-Stokes load-displacement curve for strain rate jump tests of 5 mm/min to 10 mm/min (at 2 mm displacement) from 1 to 2 mm extensometer displacement.

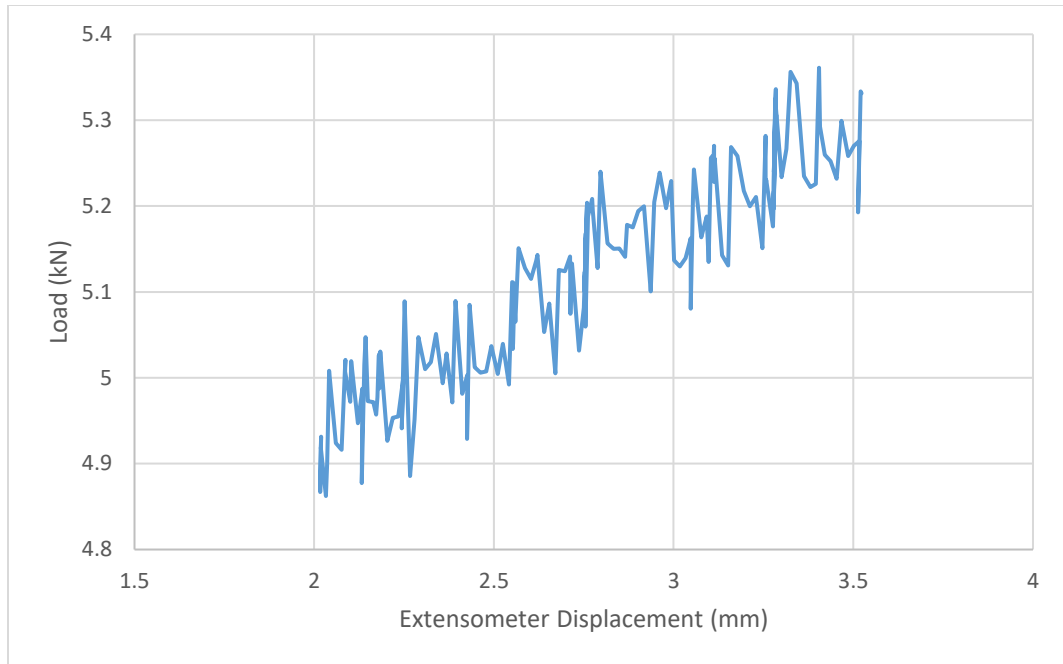


**Figure 4.48** Section 3 of Cottrell-Stokes load-displacement curve for strain rate jump tests of 10 mm/min (at 2 mm displacement) from 2 mm to fracture.

The second strain rate change test used the same process as described above, but as the tensile sample reached an extensometer distance of 1 mm, the cross-head velocity was changed from 1 mm/min to 100 mm/min and pulled until fracture, as shown in **Figure 4.49**.

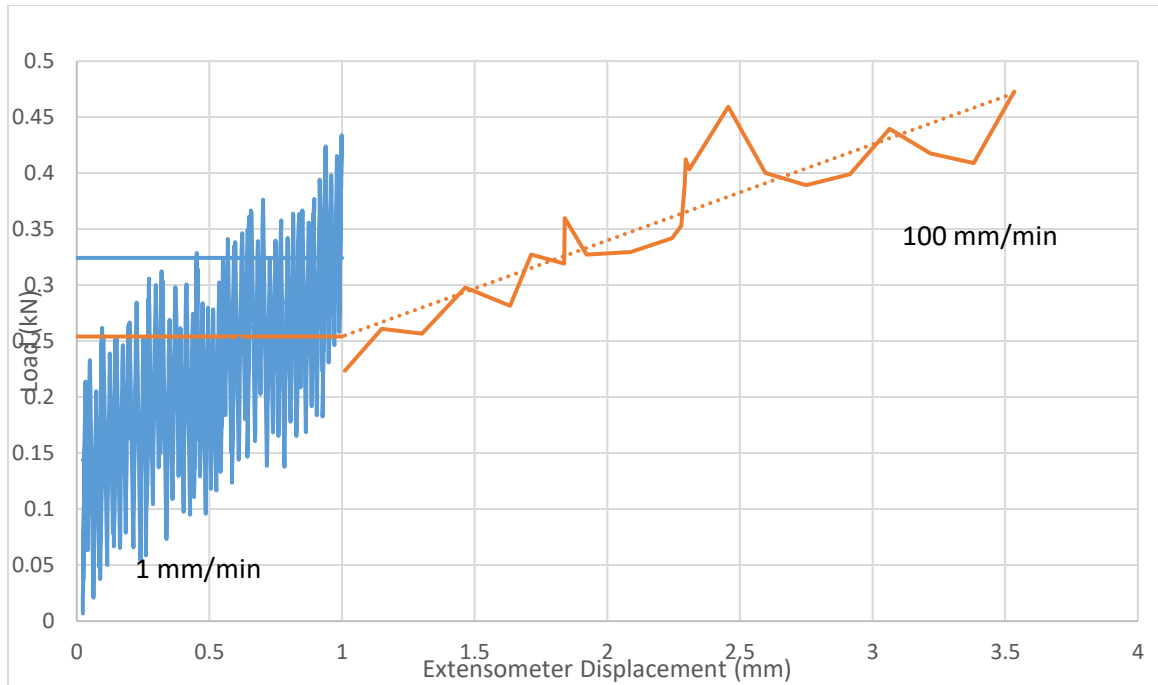


**Figure 4.49** Segment of the load-displacement curve for aluminum alloy AA5182 obtained at 25°C and a strain rate change of 1mm/min to 100 mm/min.

The jump test calculations for both sets of tests are provided in the appendices of the report in **Section A.3**.

## 5 Discussion

### 5.1 Microstructure

The microstructure of the as-received AA5182-O aluminum alloy was analyzed using OM, SEM, and EDS techniques. OM images were captured after metallographic grinding and polishing procedures, and secondary particles were observed at 1000x magnification. Through EDS analysis, two groups of second phase particles were observed (Fe,Mn)- and (Mg,Si)- enriched intermetallic particles. Particularly,  $\text{Al}_3(\text{Fe-Mn})$  and  $\text{Mg}_2\text{Si}$  particles were detected.

The average grain length was approximated to be 18.91  $\mu\text{m}$ . The average grain length was measured to be approximately 14.98  $\mu\text{m}$ . The average grain area was calculated to be 365.08 ( $\mu\text{m}$ )<sup>2</sup>. The aspect ratio was calculated to be 1.39. The surface hardness was calculated to be 70.36 HV with a standard deviation of 3.47. The rolling direction hardness was calculated to be 64.48 HV with a standard deviation of 3.89. The hardness calculated for the transverse direction of the sample was 69.37 HV with a standard deviation of 3.77. These values were comparable to standard literature data of aluminum alloys AA5182-O [1, 2].

The EDS analysis conducted using the as-received specimens and the energy-dispersive X-ray EDAX (SiLi Detector) was used to determine not only the chemical composition of precipitates and second phase particles, but the chemical composition of the as-received AA5182-O aluminum alloy. The chemical composition was observed and calculated as approximately 95.02% Al, 4.3% Mg, 0.34% Mn, 0.21% Fe, 0.03% Si. These values were also comparable to standard literature data of aluminum alloy AA5182-O compositions [1, 2].

## 5.2 Mechanical Properties

### 5.2.1 Room Temperature Tensile Testing

From the tensile tests conducted at room temperature it can be observed that the mechanical properties of the aluminum alloy AA5182-O behave comparably to data collected from literature [1, 2]. The standard deviations for these values are provided in the appendices section. For the yield stress, the average value at room temperature was determined to be 129.6 MPa using the 0.002 offset method. This value is in agreement with Lloyd's [3] prediction of the yield stress of three 5xxx-series aluminum alloys in the plot, **Figure 2.2**, with experimental yield stress.

### 5.2.2 Sub-Zero Temperature Tensile Testing

From the tensile tests in **Figure 4.16**, it can be observed that both the yield stress and tensile stress are enhanced in aluminum alloy AA5182-O as the temperature is reduced from RT to -196°C. There was a small rise in the yield stress at cryogenic temperature for the samples of 129.6 to 164 MPa from RT to -196°C, respectively, an approximate increase of 26.5%. The ultimate tensile stress was observed to increase from 277.5 to 398 MPa as the temperature was reduced from RT to -196°C, an approximate 43.42% increase.

For aluminum alloy AA5182-O, the onset of plastic deformation is notably influenced by the testing temperature as shown in previous studies such as that of Schneider et al. [1]. When observing studies of pure aluminum, or an alloy such as AA1085 with very little alloying elements,

the onset of plastic deformation is only mildly influenced by temperature [4]. **Figure 4.17** shows a relatively constant yield stress, with a gradual increase as temperature decreases. FCC metals are known to often only have mild influences to yield stress based on temperature changes [5]. In some studies, the difference in yield stress as the temperature is decreased below sub-zero temperatures has been attributed to the thermally activated obstacle strength which derives from solid solution hardening of AA 5182-O materials [4].

The tensile stress of the material is observed to first increase gradually from RT as the temperature is decreased to  $-80^{\circ}\text{C}$ . The tensile stress then increases significantly from  $-80^{\circ}\text{C}$  to  $-160^{\circ}\text{C}$ , and again increases even more drastically from  $-160^{\circ}\text{C}$  to  $-196^{\circ}\text{C}$ . It is possible that the increase in tensile stress is a result of both the suppression in DSA (and therefore more uniform dislocation mobility), as well as higher strain hardening rates at lower temperatures. Higher strain hardening rates provide the material with an increase in strength during tensile testing.

The engineering fracture strain followed an even greater trend from 0.2593 to 0.5 mm/mm, as the temperature was reduced from RT to  $-196^{\circ}\text{C}$ , an approximate 92.83% increase. Similarly, the uniform elongation was observed to increase from 0.2356 to 0.48 mm/mm, as the temperature was reduced from RT to  $-196^{\circ}\text{C}$ , an approximate 103.7% increase. **Figure 4.18** and **Figure 4.19** show that the strain at maximum load and the fracture strain both follow the same trend of increasing as the temperature is decreased. The material is gaining both strength and ductility as the temperature is decreased. The increase in elongation is also linked to an observed reduction in DSA as the temperature is decreased. As dislocation mobility is reduced (and spends less time becoming pinned and temporarily arrested [4]), the deformation appears to become more uniform as observed in the stress-strain curves, the increased strain, as well as further observed in the fracture surfaces of the specimens. This shows that the increase in fracture strain of the material is related to a reduction in the PLC effect and points to an interaction occurring between the solute and dislocations that provides homogenous deformation conditions and possibly a higher potential for necking to occur before fracture.

**Figure 4.21** provides the work hardening rate as a function of true stress for samples tensile tested at 25 and  $-196^{\circ}\text{C}$ . This plot, referred to as the Kocks-Mecking model,

provides significant information about the material behaviour of AA5182-O and flow stress dependence on temperature. Both the slope (k-value) of the data and the relationship with the Considère criterion are important behaviors to analyze. There are three important details that can be observed from the graph. The slope of the -196°C data is observed to be lower than the slope of the 25°C data and results in higher tensile stress being achieved. The slope for -196°C being less than the slope for the 25°C data is an indication that the strain hardening is increased (typically a consequence of higher dislocation densities). It is also observed that the -196°C data is more consistent with less variation (standard deviation) in values as a result of the reduction in DSA and PLC phenomenon. The final observation is that the -196°C data fractures when the Considère's criterion for necking is met; as opposed to the 25°C data which fractures prematurely before this criterion is met. The Considère's criterion is marked to show the onset of necking. This data shows that necking occurs in -196°C and does not appear to occur in 25°C.

From this graph, it is observed that the evolution of the work hardening rate at both temperatures is similar until the slope of Considère's criterion, that is to say that the load reaches its maximum point. At room temperature, this occurs when the work hardening rate falls to about 430 MPa, at which point it is still higher than the corresponding flow stress, around 275 MPa. In addition, the strain at maximum load is 0.23, which is considerably below the strain hardening exponent of 0.30 of the material. For the material at -196°C, however, the work hardening rate at the onset of necking (Considère's criterion) equals the flow stress and the necking strain is even higher. This suggests that dynamic strain aging reduces uniform ductility at room temperature by triggering an early onset of necking. It follows that the sub-zero temperature testing provides higher work hardening capacity and more homogenous deformation behaviour, resulting in higher ductility of the material. This is further supported by the fracture angles and fracture surfaces of the samples, discussed in **Section 5.2.3**.

### 5.2.3 Fractography

Analysis of the fracture behaviour of AA5182-O at temperatures of 25, -40, -80, -120, -160, and -196°C, included measurements of final fracture geometry, dimple measurements, and dimple/particle characteristic observations. To investigate final fracture geometric characteristics, the fracture angle was measured and notably dependent on the temperature. At room temperature and -40°C, the fracture angle is 63-66° and displaying characteristics of macroscopic plastic localization dominated failure (**Figure 2.9** mechanism 2 and 3) [5]. This fracture mechanism is typical of ductile solids that fail as a result of plastic localization in shear bands [2]. These shear bands can often be caused by dislocation slipping or softening mechanisms. As localized plastic deformation occurs inside of these bands, void coalescence will occur until final fracture. For these mechanisms, compared to mechanisms 3, 4, and 5 from Figure 2.9, this mechanism is mostly attributed to cases of failure by localized plastic shear without necking [8].

There is a clear transition from shear failure to more ductile tearing as the temperature is decreased. In **Figure 4.24 c**, the sample tested at -80°C, there appears to be a combination of diagonal localized shear fracture and ductile tearing from void coalescence. This illustrates a transition to a more void coalescence dominated failure and overall increase in ductility, supported by the increase in fracture strain achieved during tensile testing. Ductile fracture aspects are even more apparent in **Figure 4.24d, e, and f.**, where necking occurs in the direction of the thickness after uniform elongation. This is supported by the widened plastically deformed zone and increased necking strain the previous tensile analysis.

The SEM images in **Figures 4.32** through **4.40** also show change from diagonal localized shear fracture to ductile tearing. These failure mechanisms are observed through a transition from parabolic dimples at 25°C to equiaxial dimples at temperatures below -

80°C. Parabolic dimples are often traits of shear failure, where the material experiences high amounts of localized plastic flow. In this mechanism, dislocations are getting caught by the solutes inside the aluminum matrix and experiencing arrested dislocation mobility. As a result of very limited void nucleations sites, the specimen fails by plastic localization (commonly in the form of shear bands). The equiaxial dimples observed at sub-zero temperatures are characteristics typical for failures dominated by void growth and coalescence (highly ductile tearing) [6].

SEM images at 25 and -40°C also exhibit particles ( $Mg_2Si$ ) embedded in the walls of the dimples. This is another characteristic that is typical of shear deformation. In this mechanism, decohesion between the particles and the matrix is caused by shear deformation (plastic shear strain) and resulting in fracture surfaces with parabolic shaped dimples [9]. At temperatures at and below -80°C, the SEM figures show a combination of decohesion of the particle and matrix interface, as well as particle cracking. Both of these mechanisms are typical of void nucleation around inclusions and accompanied by spherical dimples [9]. These particles were found to be  $Al_3(Fe, Mn)$  particles that were mostly observed cracked along the center of the particle. Deformation at lower temperatures promotes both cracking and debonding due to increased work hardening rates. Small particles (such as the  $Mg_2Si$ ) tend to be spherical or equiaxed and tend to cause inner fracture due to the pile-up of dislocations at the particle-matrix interface. There are more cracked  $Al_3(Fe, Mn)$  particles observed at the bottom of the sub-zero temperature samples as well, suggesting that microcracks dominate the failure mode and not localized plastic deformation in the matrix.

From the measurements of the average aspect ratio measured for the dimples as the temperature was decreased from RT to -196°C, as the temperature decreases, the measurement of the aspect ratio becomes more uniform. It is also observed that the dimples become more equiaxed during the fracture. As shown in the RT SEM images, a large number of dimples are associated with considerable plastic deformation. However, the low temperature dimples have clear differences such as area and population. **Figure 4.30** illustrates a plot of the dimple area as a function of temperature. As the temperature is decreased, it is observed that dimples are measured at relatively smaller sizes. As the

dimple size decreased, the number of dimples increased at cryogenic temperature. Studies show that, prior to fracture, dislocation structures within crystalline materials destabilize. This occurrence is caused by intensive flow localization in relative soft areas [4]. Subsequently, this leads to nucleation and growth of microvoids, macroscopic necking, and finally failure [9].

### 5.3 Cottrell-Stokes Testing

The Cottrell-Stokes method was used to investigate the temperature dependence of flow stress for the AA5182-O alloy. The difference in flow stress was measured and analyzed through two separate methods. The first method was a temperature change test. This method involves tensile testing a specimen and changing the temperature mid-test while holding the dislocation distribution constant (using the same material as opposed to conducting two separate tests with two separate test specimens and two unique dislocation distributions). During the temperature change test from 120°C to 34°C, the increase in flow stress is measured to be approximately 20 MPa, and there is a significant change from a uniform stress-strain curve at 120°C to serrations at 34°C (non-uniform stress-strain). The change in flow stress as the temperature changes, along with the change in the behaviour of the flow stress (uniform to non-uniform), this material shows a clear dependence on the temperature.

Similarly, using strain-rate jump tests, the behaviour of the material and dislocation mobility is investigated using a method which investigates the strain-rate sensitivity of a material while holding the dislocation distribution constant (using the same material as opposed to conducting two separate tests with two separate test specimens and two unique dislocation distributions). The jump in stress and change in stress-strain behaviour also reveals the change in dislocation mobility behaviour with regard to changes in strain.

The stress-strain curve of a strain jump from 1 mm/min to 100 mm/min shows a significant decrease in serrations at the higher strain rate. Specifically, referring to the serration type data in **Figures 2.18** and **Figure 2.19**, these serrations appear to transition from Type C serrations (at 1 mm/min) to Type A serrations (100 mm/min). It was discussed in Chapter 2 that these PLC band types are dependent on both temperature and strain rate. The behaviour exhibited by the serrations is aligned with the literature conducted by Aik-Amokhtar where type C bands were observed for lower strain rates (approximately  $4 \times 10^{-5} \text{ s}^{-1}$ ) and type A bands were observed at higher strain rates (approximately  $5 \times 10^{-2} \text{ s}^{-1}$ ) [10]. In this test,  $m$  (the strain rate sensitivity) is calculated to be negative. Compared to the set of jump tests presented in **Figure A.60**, where the tests are first changed from 1 mm/min to 5 mm/min at 1 mm extensometer displacement, and then changed a second time from 5 mm/min to 10 mm/min at 2 mm extensometer displacement,  $m$  is calculated to be negative.

These results support the theory that as  $m$ , the strain rate sensitivity, is negative, the material is in the regime of DSA and PLC bands are present. During high strain rate deformation, cluster sizes are smaller and junction strength is lower. At lower strain rates, cluster sizes are larger and the mechanism discussed in the literature review of mobile dislocations becoming temporarily arrested at forest dislocation clusters can be observed through non-uniform dislocation mobility. Solute atoms diffuse and pin the mobile dislocations, leading to nSRS, (negative  $m$ ), manifestations of serrations in the stress-strain curves, and PLC bands along the material.

# Bibliography

- [1] R. Schneider, B. Heine, R.J. Grant, R. Kelsch, F. Gertsner, T. Hagele, “Low Temperature Mechanical Properties of Wrought Aluminum Alloys Applicable to the Automotive Sector, Magazine WOMag, 2013.
- [2] M. F. Ashby, D. R. H. Jones, “Light Alloys,” Engineering Materials 2: An Introduction to Microstructures and Processing, 4th ed., pp. 111, 2013.
- [3] D.J. Lloyd and S.A. Court, Mater. Sci. and Tech., 19, 1349-1354, 2003.
- [4] B. Gruber, et. al., “Mechanism of low temperature deformation in aluminum alloys,” Materials Science and Engineering: A, vol. 795, 139935, 2020.
- [5] G. E. Dieter, G. Ellwood, D. Bacon, “Mechanical Metallurgy,” vol. 3, New York: McGraw-Hill Education, 1976.
- [6] C. Tekoglu, J.W. Hutchinson, T. Pardoen, “On localization and void coalescence as a precursor to ductile fracture,” Philosophical Transactions of the Royal Society A Mathematical Physical and Engineering Sciences, vol. 373, 2015.
- [7] A.S. Bhuwal, T. Liu, I. Ashcroft, W. Sun, “Localization and coalescence of imperfect planar FCC truss lattice metamaterials under multiaxial loadings,” Mechanics of Materials, vol. 160, 103996, 2021.
- [8] L. Zhichao, M. X. Huang, “Revealing the Fracture Mechanism of Twinning-Induced Plasticity Steels,” Steel Research International, vol. 89, 1700433, 2018.
- [9] A. Jenab, D. E. Green, A. T. Alpas, “Microscopic investigated of failure mechanisms in AA5182-O sheets subjected to electro-hydraulic forming,” Materials Science and Engineering A, Volume 691, pp. 31-41, 2017.
- [10] H. Ait-Amokhtar, C. Fressengeas, Crossover from continuous to discontinuous propagation in the Portevin-Le Chatelier effect, Acta Materialia, Volume 58, Issue 4, pp. 1342-1349, 2010.

## 6 Conclusions and Future Work

### 6.1 Conclusions

The favorable weight, strength, weldability, and corrosion resistance properties of aluminum-magnesium alloys, such as AA5182-O, are suitable for automotive and aerospace applications that require a high strength-to-weight ratio and protection from extreme conditions. The continued research and usage of these alloys can only further reduce the overall fuel consumption and greenhouse gas emissions of these industries. However, these alloys are often lacking in formability capabilities when compared to modern high strength steels. In recent studies, sub-zero temperature has been presented as a method of forming that can help overcome the PLC effect present in 5xxx-series aluminum alloys at room temperature. Although there are current trends that show the increase in mechanical properties (stress, elongation, etc.) at sub-zero temperatures, the mechanical and microscopic levels of insight on these mechanisms are still currently being studied.

A change in deformation mechanisms and fracture behaviour is observed in both the mechanical properties of the material, as well as the fracture analysis of the samples. There is an overall increase observed in the ultimate tensile stress, yield stress, fracture strain, and strain at maximum load as testing temperatures are decreased from RT to sub-zero temperatures. PLC bands cause non-homogenous strain in the material that triggers an early onset of failure. The suppression of the PLC effect and the DSA process, increases the work hardening capacity and as a result, increases the ductility.

Fracture behaviour from SEM and EDS analysis reveal a transition from plastic shear deformation at RT to more ductile tearing at sub-zero temperatures. This is observed through a transition of parabolic dimples at RT (characteristic of shear loading) to more equiaxed dimples (characteristic of void growth and coalescence failure). At sub-zero temperatures, this is further supported by a reduction in dimple area and suggests an

increase in dislocations (in agreeance with an increase in work hardening capacity at sub-zero temperatures). The observed changes in plastic deformation, along with the changes in fracture behaviour from RT to sub-zero temperatures, suggests a more homogenous mechanism of failure is caused by the suppression of DSA and the PLC effect.

## 6.2 Future Work

Future work for this research is recommended in the following points to further investigate and understand the mechanisms behind the improvement of mechanical behaviour of AA5182-O at sub-zero temperatures:

### 6.2.1 Sub-Zero Temperature Tensile Testing

- i. A condensed environmental chamber, capable of holding liquid nitrogen around the MTS tensile testing machine, could be purchased or designed to perform -196°C temperatures during uniaxial tensile testing. Although tensile tests in this study were capable of reaching this temperature using a small liquid-nitrogen bath, there were some movements in the stress-strain curve corresponding to times where the bath was re-filled with liquid nitrogen during the tests. Recommendation for this setup: automated through an environmental chamber that can hold the liquid nitrogen for the duration of the tests. Although the test results from the sub-zero temperature tests were repeatable and in agreeance with the literature survey, these minor movements in the stress-strain curves can be further reduced.

## 6.2.2 Sub-Zero Formability Testing

- i. An environmental chamber, capable of dispersing and holding liquid nitrogen around the Erichsen sheet metal testing machine, could be purchased, or designed, to perform sub-zero temperatures tests to investigate formability behaviour as temperature is decreased. This will simplify the method for performing the formability testing as well as reduce standard deviation between samples.
- ii. There is continued work that is recommended on the sample designs for Erichsen sheet metal cupping tests to investigate strain paths at sub-zero temperatures and the development of a forming limit diagram at sub-zero temperatures. Initial specimens were designed, tested, and provided in the Appendices section of the report under *Section A.4*.
- iii. Attention is advised for the length of time that the specimens are tested for in the Erichsen sheet metal cupping tests. It is recommended to run the samples through the test and stop the testing process when necking occurs on the specimen (prior to fracture). This has been completed for some samples (provided in the Appendices *Section A.4*) and possible through the design of the testing method. Detecting the necking of the material prior to fracture is recommended to improve the accuracy of the results for the forming limit diagram data.

## 6.2.3 Fractography

- i. SEM and TEM Analysis is recommended for the  $\Delta$  strain rate and  $\Delta$  temperature tests. This can strengthen the microscopic analysis for the overall study. Fractography on the Cottrell-Stokes testing samples can provide further information on the differences between reversible and irreversible changes of

flow stress with temperature and how the micro-mechanisms for these samples behave.

- ii. Further analysis of SEM images is recommended to obtain statistical information on types of secondary particles and a map of their behaviour with respect to temperature. TEM analysis is recommended to analyze dislocation behaviour and plot findings with respect to temperature. This will provide further information on the interactions occurring between dislocations and secondary particles as temperature is decreased.

# Appendices

## A.1 Material Characterization

### A.1.2 Hardness Testing

**Table A.1** AA5182-O average surface hardness measurements and calculations (load 25 gf)

Indent	D1 ( $\mu\text{m}$ )	D2 ( $\mu\text{m}$ )	D ( $\mu\text{m}$ )	D (mm)	HV	MPa
1	25	25.5	25.25	0.02525	72.6988	712.957
2	25.5	26	25.75	0.02575	69.9029	685.538
3	26.5	25.5	26	0.026	68.5651	672.418
4	27	26.5	26.75	0.02675	64.7742	635.241
5	25	26	25.5	0.0255	71.2803	699.046
6	26.5	26	26.25	0.02625	67.2653	659.671
7	24.5	25	24.75	0.02475	75.6657	742.054
8	25.5	25	25.25	0.02525	72.6988	712.957
Average					70.3564	689.985
Std. Deviation					3.46711	34.002

**Table A.2** AA5182-O longitudinal direction hardness measurements and calculations  
(load 25 gf)

Indent	D1 (μm)	D2 (μm)	D (μm)	D (mm)	HV	MPa
1	27	28.5	27.75	0.02775	60.1899	590.283
2	27.5	28.5	28	0.028	59.1199	579.789
3	26.5	25.5	26	0.026	68.5651	672.418
4	26	26.5	26.25	0.02625	67.2653	659.671
5	27	26.5	26.75	0.02675	64.7742	635.241
6	26	25.5	25.75	0.02575	69.9029	685.538
7	27.5	26.5	27	0.027	63.5802	623.531
8	27	27.5	27.25	0.02725	62.419	612.143
Average					64.4771	632.327
Std. Deviation					3.89383	38.1868

**Table A.3** AA5182-O transverse direction surface hardness measurements and  
calculations (load 25 gf)

Indent	D1 (μm)	D2 (μm)	D (μm)	D (mm)	HV	MPa
1	26	27.5	26.75	0.02675	64.7742	635.241
2	27	27.5	27.25	0.02725	62.419	612.143
3	26	25	25.5	0.0255	71.2803	699.046
4	25	25.5	25.25	0.02525	72.6988	712.957
5	26.5	25	25.75	0.02575	69.9029	685.538
6	25.5	26	25.75	0.02575	69.9029	685.538
7	25	25.5	25.25	0.02525	72.6988	712.957
8	26	25	25.5	0.0255	71.2803	699.046
Average					69.3696	680.308
Std. Deviation					3.76953	36.9677

### A.1.3 OM, SEM, and EDS

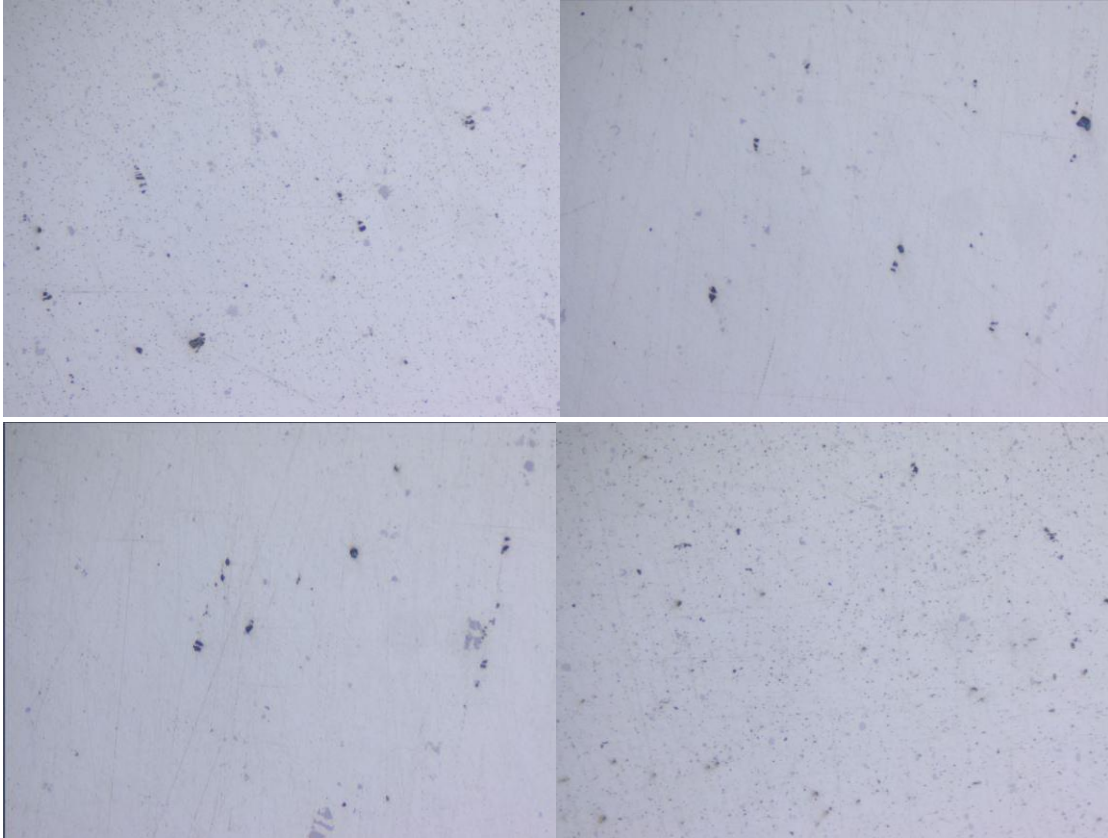


**Figure A.1** Optical microscopy image of AA5182-O after metallographic grinding and polishing procedures at a magnification of 1000x magnification.

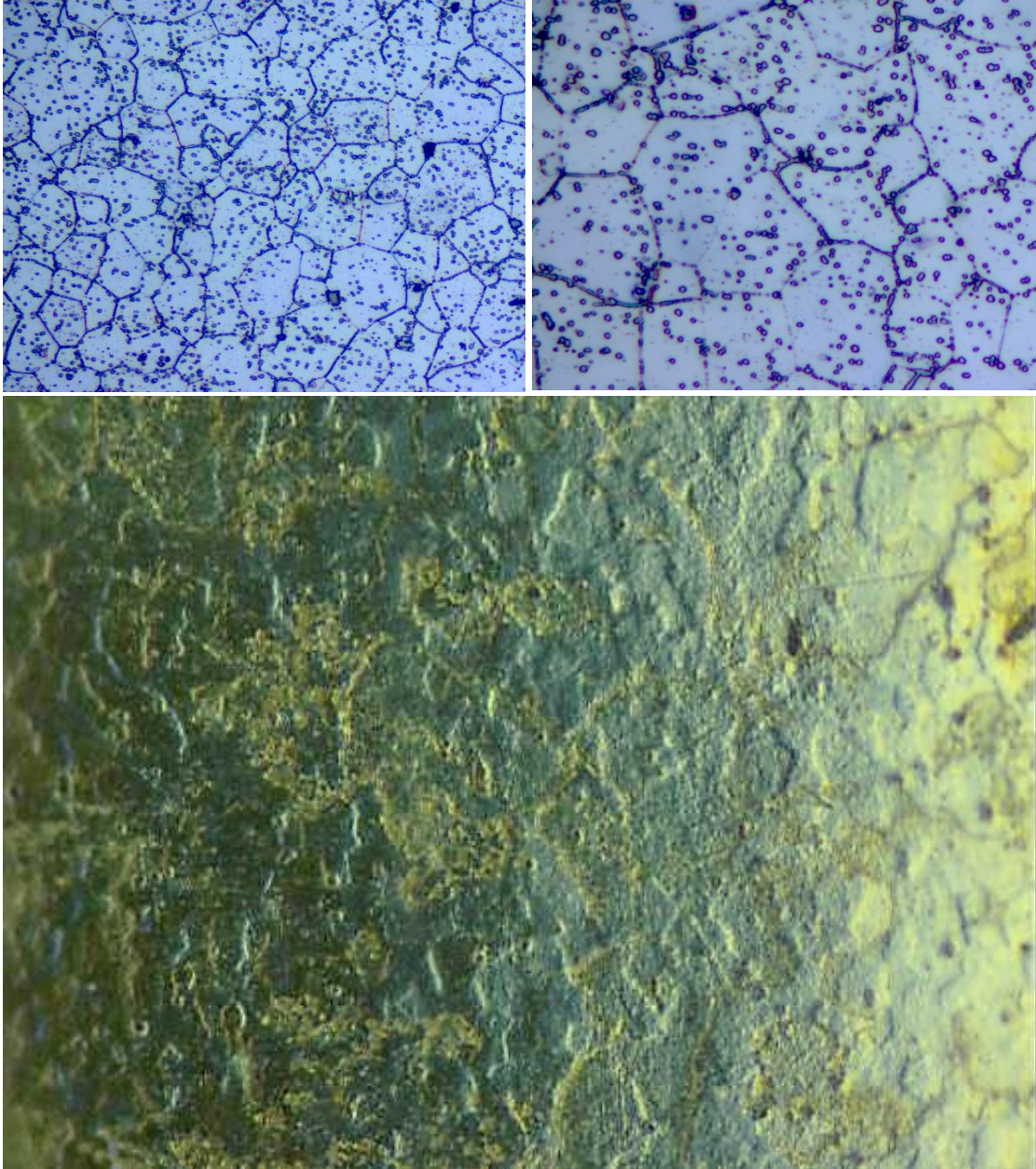


**Figure A.2** Optical microscopy images of AA5182-O after metallographic grinding and polishing and etching procedures at a magnification of 1000x magnification.

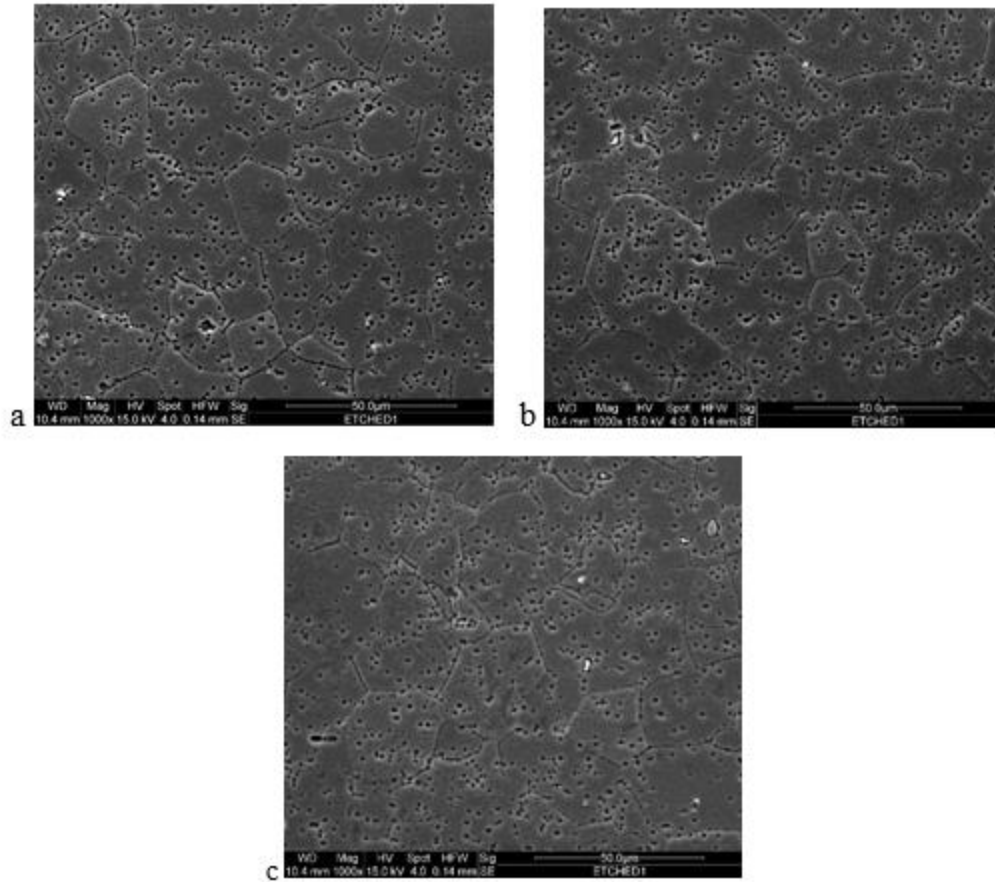


**Figure A.3** SEM images of as-received **(a)** Etched 5182\_SE\_1000x\_001 **(b)** Etched 5182\_SE\_1000x\_002 and **(c)** Etched 5182\_SE\_1000x\_004 (Method 1)

**Table A.4** AA5182-O average length measurements from *Figure A.3* SEM images.

File Name	Length ( $\mu\text{m}$ )	Width ( $\mu\text{m}$ )	Area ( $\mu\text{m}^2$ )	Aspect Ratio (L/W)
Etched 5182_SE_1000x_001	18.91	14.98481481	365.0812	1.26219
Etched 5182_SE_1000x_002	16.85518519	13.60111111	279.3535481	1.23925
Etched 5182_SE-1000x_004	18.38064516	14.28774194	302.3386935	1.28646

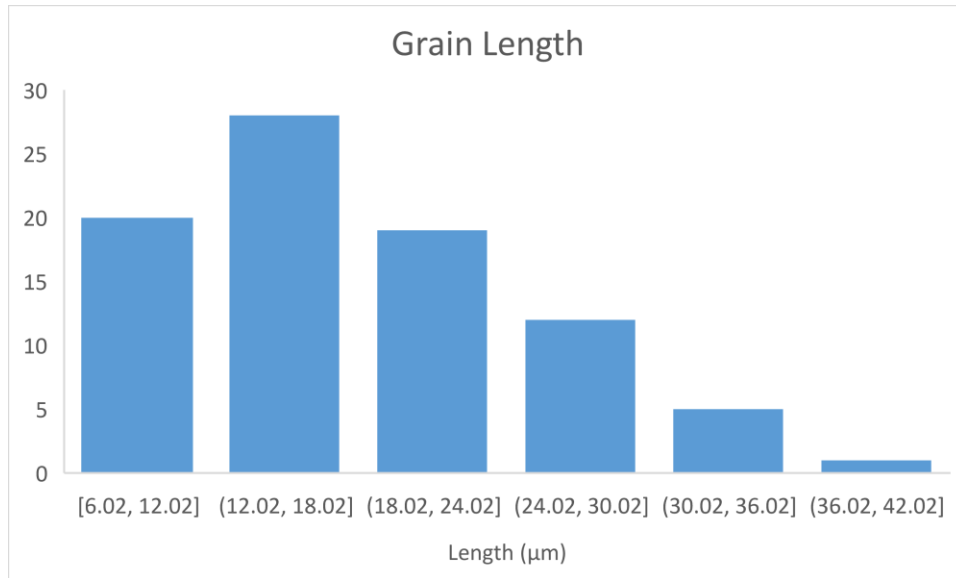


**Figure A.4** Average grain length measurements of as-received AA5182-O

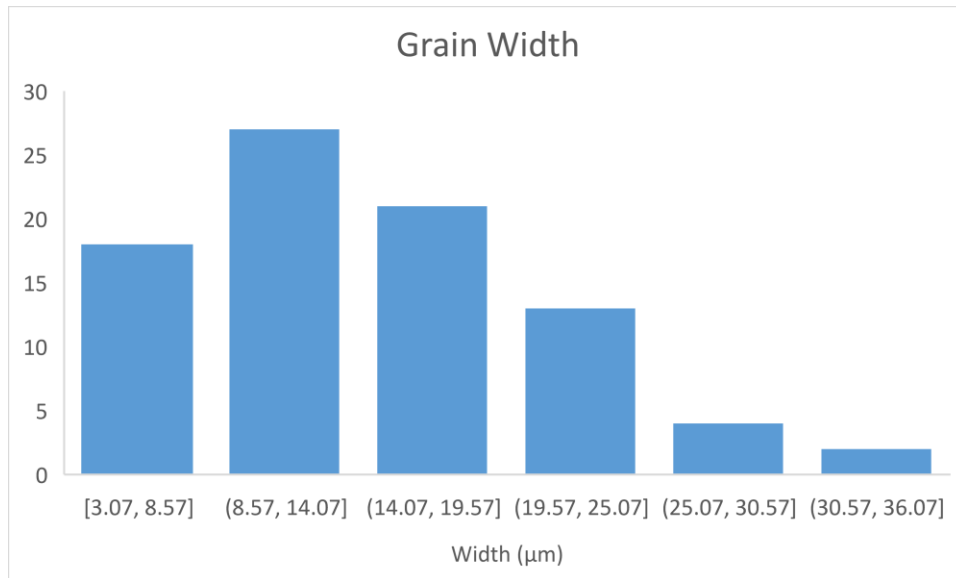


**Figure A.5** Average grain width measurements of as-received AA5182-O

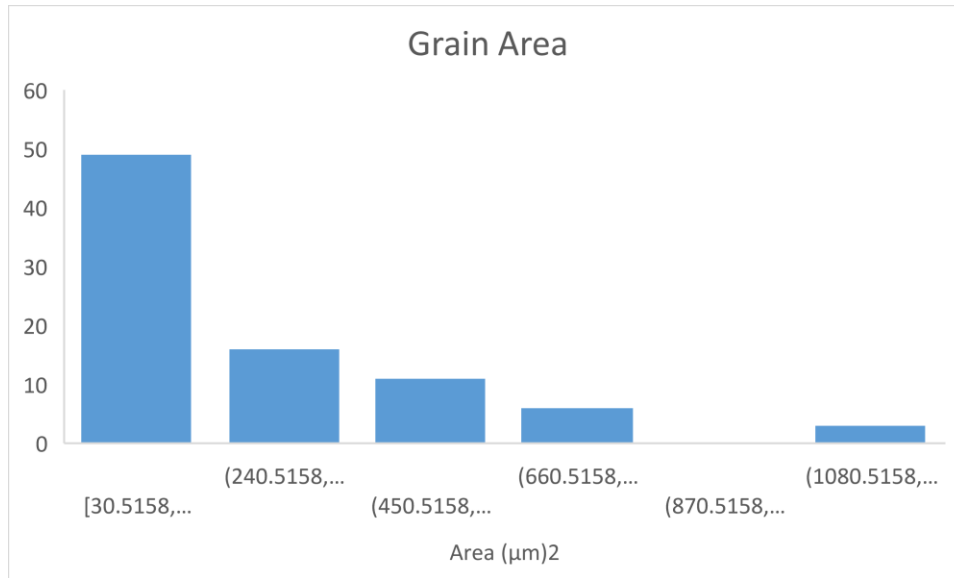


**Figure A.6** Average grain area measurements of as-received AA5182-O

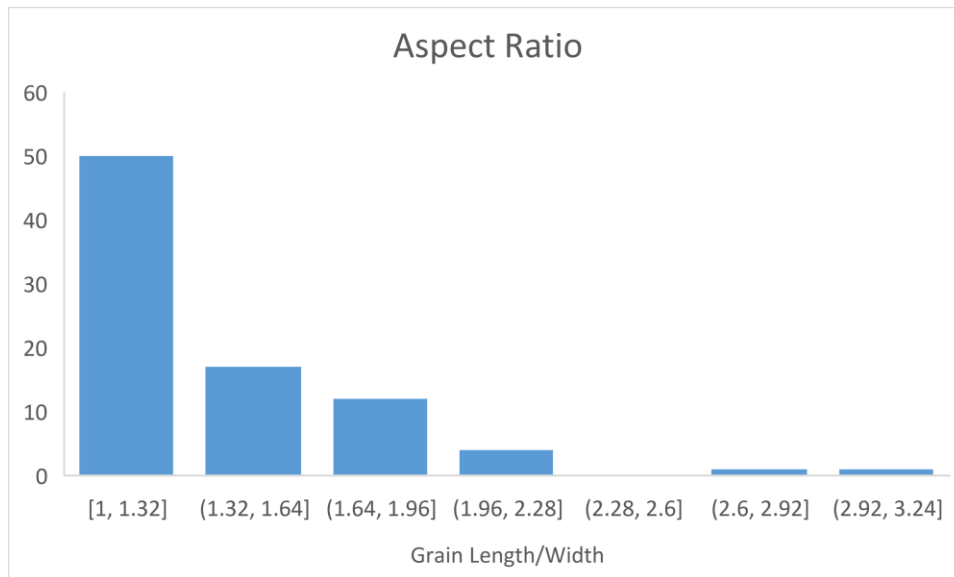


**Figure A.7** Average grain aspect ratio measurements of as-received AA5182-O

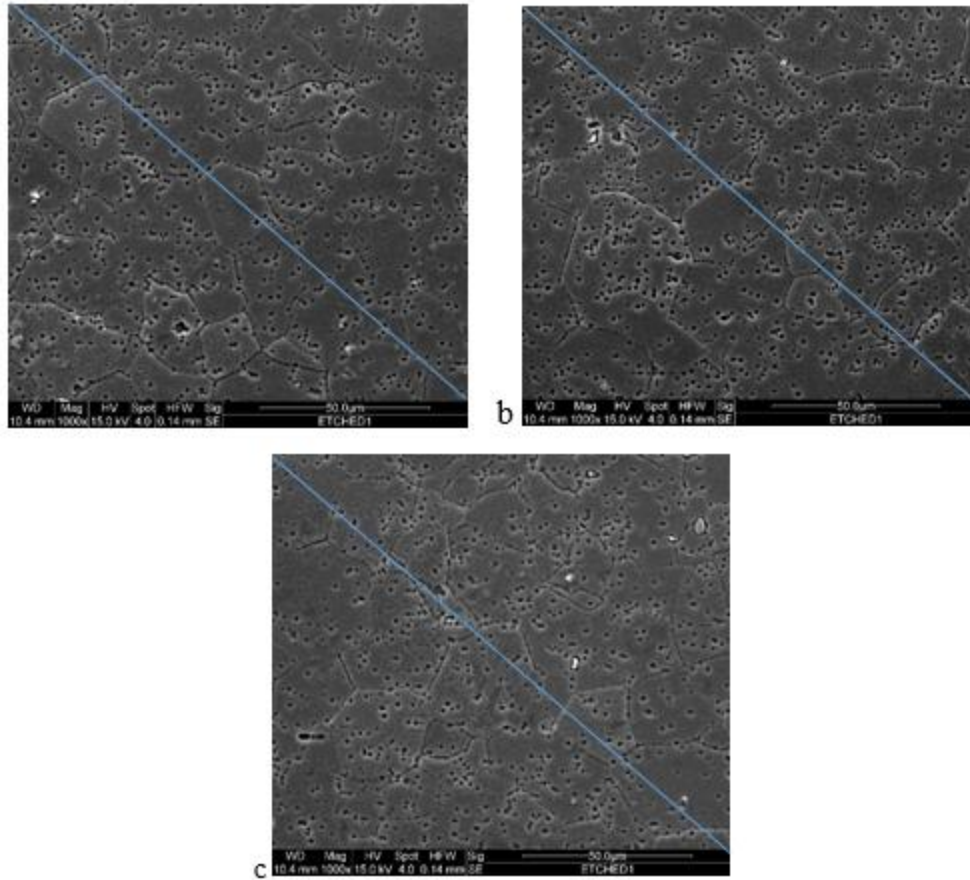


**Figure A.8** SEM images of as-received (a) Etched 5182\_SE\_1000x\_001 (b) Etched 5182\_SE\_1000x\_002 and (c) Etched 5182\_SE\_1000x\_004 (Method 2)

**Table A.5** AA5182-O average length measurements from *Figure A.8* SEM images.

File Name	Length ( $\mu\text{m}$ )
Etched 5182_SE_1000x_001	19.255514
Etched 5182_SE_1000x_002	16.454615
Etched 5182_SE-1000x_004	18.546895

**Table A.6** AA5182-O reference measurements from *Figure A.8* SEM images.

File Name	Grain #	Length (μm)	Width (μm)	Area (μm) <sup>2</sup>	Aspect Ratio (L/W)
Etched 5182_SE_1000x_001	1	22.99	15.88	365.0812	1.447732997
Etched 5182_SE_1000x_001	2	18.88	9.85	185.968	1.916751269
Etched 5182_SE_1000x_001	3	19.27	17.65	340.1155	1.091784703
Etched 5182_SE_1000x_001	4	9.75	6.73	65.6175	1.448736999
Etched 5182_SE_1000x_001	5	24.11	20.04	483.1644	1.203093812
Etched 5182_SE_1000x_001	6	34.5	34.17	1178.865	1.009657594
Etched 5182_SE_1000x_001	7	22.34	10.17	227.1978	2.196656834
Etched 5182_SE_1000x_001	8	15.56	15.12	235.2672	1.029100529
Etched 5182_SE_1000x_001	9	16.05	14.77	237.0585	1.086662153
Etched 5182_SE_1000x_001	10	17.36	16.01	277.9336	1.084322299
Etched 5182_SE_1000x_001	11	11.25	9.45	106.3125	1.19047619
Etched 5182_SE_1000x_001	12	15.98	8.98	143.5004	1.779510022
Etched 5182_SE_1000x_001	13	27.45	27.18	746.091	1.009933775
Etched 5182_SE_1000x_001	14	20.69	17.85	369.3165	1.159103641
Etched 5182_SE_1000x_001	15	18.25	17.85	325.7625	1.022408964
Etched 5182_SE_1000x_001	16	41.04	29.81	1223.4024	1.376719222
Etched 5182_SE_1000x_001	17	23.87	20.52	489.8124	1.163255361
Etched 5182_SE_1000x_001	18	9.27	9.22	85.4694	1.005422993
Etched 5182_SE_1000x_001	19	13.37	13.35	178.4895	1.001498127
Etched 5182_SE_1000x_001	20	22.51	16.28	366.4628	1.382678133
Etched 5182_SE_1000x_001	21	20.28	14.55	295.074	1.393814433
Etched 5182_SE_1000x_001	22	12.01	9.61	115.4161	1.249739854

Etched					
5182_SE_1000x_001	23	24.92	22.33	556.4636	1.115987461
Etched					
5182_SE_1000x_001	24	8.25	4.72	38.94	1.747881356
Etched					
5182_SE_1000x_001	25	9.94	3.07	30.5158	3.237785016
Etched					
5182_SE_1000x_001	26	13.88	8.18	113.5384	1.696821516
Etched					
5182_SE_1000x_001	27	16.8	11.25	189	1.493333333
Etched					
5182_SE_1000x_002	28	25.15	14.48	364.172	1.736878453
Etched					
5182_SE_1000x_002	29	28.18	27.15	765.087	1.037937385
Etched					
5182_SE_1000x_002	30	10.1	8.2	82.82	1.231707317
Etched					
5182_SE_1000x_002	31	17.52	16.65	291.708	1.052252252
Etched					
5182_SE_1000x_002	32	9.5	9.5	90.25	1
Etched					
5182_SE_1000x_002	33	21.75	21.63	470.4525	1.00554785
Etched					
5182_SE_1000x_002	34	14.24	12.19	173.5856	1.168170632
Etched					
5182_SE_1000x_002	35	7.27	5.47	39.7669	1.329067642
Etched					
5182_SE_1000x_002	36	14.76	12.88	190.1088	1.145962733
Etched					
5182_SE_1000x_002	37	14.77	13.25	195.7025	1.114716981
Etched					
5182_SE_1000x_002	38	8.51	4.21	35.8271	2.021377672
Etched					
5182_SE_1000x_002	39	19.77	11.28	223.0056	1.752659574
Etched					
5182_SE_1000x_002	40	11.63	5.2	60.476	2.236538462
Etched					
5182_SE_1000x_002	41	23.29	19.01	442.7429	1.225144661
Etched					
5182_SE_1000x_002	42	33.78	22.92	774.2376	1.47382199
Etched					
5182_SE_1000x_002	43	6.02	6.02	36.2404	1
Etched					
5182_SE_1000x_002	44	35.58	33.72	1199.7576	1.055160142
Etched					
5182_SE_1000x_002	45	24.63	18.45	454.4235	1.33495935
Etched					
5182_SE_1000x_002	46	14.92	14.61	217.9812	1.021218344
Etched					
5182_SE_1000x_002	47	7.92	6.23	49.3416	1.271268058

Etched					
5182_SE_1000x_002	48	21.85	17.82	389.367	1.226150393
Etched					
5182_SE_1000x_002	49	19.86	16.23	322.3278	1.223659889
Etched					
5182_SE_1000x_002	50	16.81	12.34	207.4354	1.362236629
Etched					
5182_SE_1000x_002	51	12.94	11.78	152.4332	1.098471986
Etched					
5182_SE_1000x_002	52	9.57	3.52	33.6864	2.71875
Etched					
5182_SE_1000x_002	53	12.97	12.16	157.7152	1.066611842
Etched					
5182_SE_1000x_002	54	11.8	10.33	121.894	1.142303969
Etched					
5182_SE_1000x_004	55	22.97	20.69	475.2493	1.110198163
Etched					
5182_SE_1000x_004	56	14.72	8.73	128.5056	1.686139748
Etched					
5182_SE_1000x_004	57	10.22	8.25	84.315	1.238787879
Etched					
5182_SE_1000x_004	58	14	12.61	176.54	1.110229976
Etched					
5182_SE_1000x_004	59	15.02	14.42	216.5884	1.041608877
Etched					
5182_SE_1000x_004	60	23.95	22.32	534.564	1.073028674
Etched					
5182_SE_1000x_004	61	7.87	7.22	56.8214	1.090027701
Etched					
5182_SE_1000x_004	62	10.63	10	106.3	1.063
Etched					
5182_SE_1000x_004	63	29.24	26.02	760.8248	1.123750961
Etched					
5182_SE_1000x_004	64	25.79	24.76	638.5604	1.041599354
Etched					
5182_SE_1000x_004	65	15.21	7.68	116.8128	1.98046875
Etched					
5182_SE_1000x_004	66	15.45	10.27	158.6715	1.504381694
Etched					
5182_SE_1000x_004	67	26.1	19.31	503.991	1.351631279
Etched					
5182_SE_1000x_004	68	13.06	7.88	102.9128	1.657360406
Etched					
5182_SE_1000x_004	69	13.97	13.17	183.9849	1.060744115
Etched					
5182_SE_1000x_004	70	14.04	10.7	150.228	1.312149533
Etched					
5182_SE_1000x_004	71	22.75	15.55	353.7625	1.463022508
Etched					
5182_SE_1000x_004	72	10.74	5.75	61.755	1.867826087

Etched 5182_SE_1000x_004	73	24.85	16.84	418.474	1.475653207
Etched 5182_SE_1000x_004	74	28.83	24.77	714.1191	1.163907953
Etched 5182_SE_1000x_004	75	15.22	13.21	201.0562	1.152157456
Etched 5182_SE_1000x_004	76	14.09	8.35	117.6515	1.68742515
Etched 5182_SE_1000x_004	77	32.45	19.85	644.1325	1.634760705
Etched 5182_SE_1000x_004	78	7.99	4.32	34.5168	1.849537037
Etched 5182_SE_1000x_004	79	13.34	8.95	119.393	1.490502793
Etched 5182_SE_1000x_004	80	24.58	22.8	560.424	1.078070175
Etched 5182_SE_1000x_004	81	13.03	8.93	116.3579	1.45912654
Etched 5182_SE_1000x_004	82	35.84	20.14	721.8176	1.779543198
Etched 5182_SE_1000x_004	83	19.55	17.52	342.516	1.11586758
Etched 5182_SE_1000x_004	84	20.25	19.89	402.7725	1.018099548
Etched 5182_SE_1000x_004	85	14.05	12.02	168.881	1.168885191

## A.2 Fractography



**Figure A.9** Tensile sample fractured at temperature of 120°C



**Figure A.10** Tensile sample fractured at temperature of 25°C

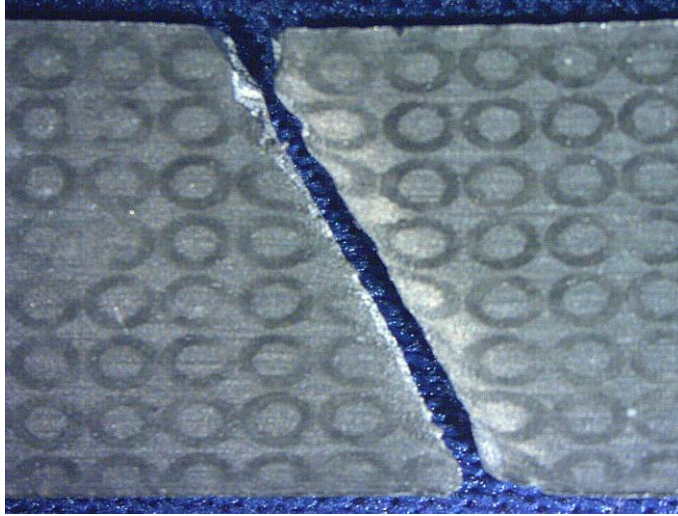


**Figure A.11** Tensile sample fractured at temperature of  $-40^{\circ}\text{C}$

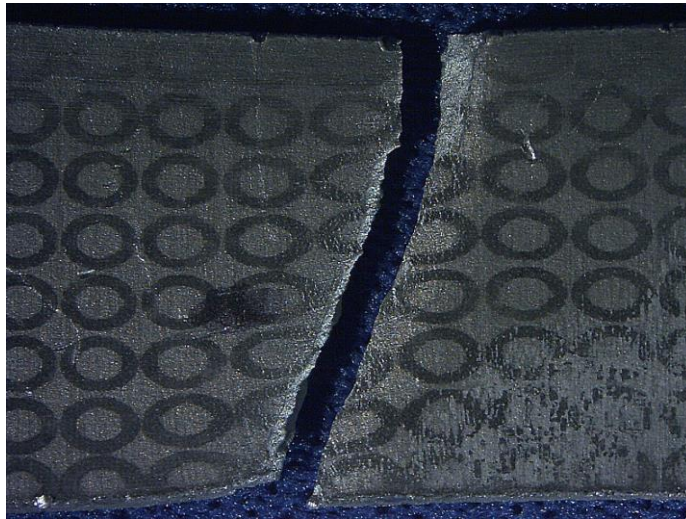


**Figure A.12** Tensile sample fractured at temperature of  $-80^{\circ}\text{C}$

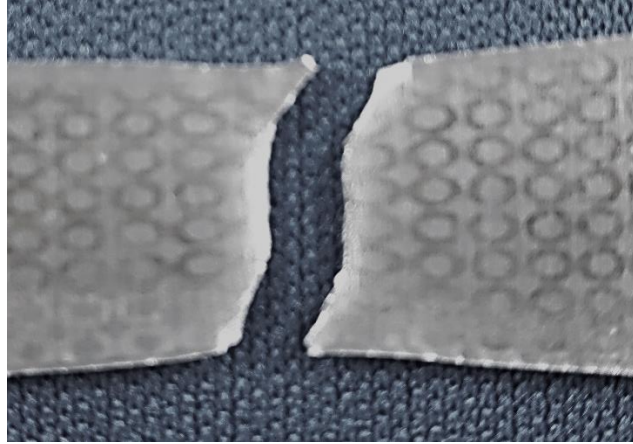


**Figure A.13** Tensile sample fractured at temperature of  $-120^{\circ}\text{C}$

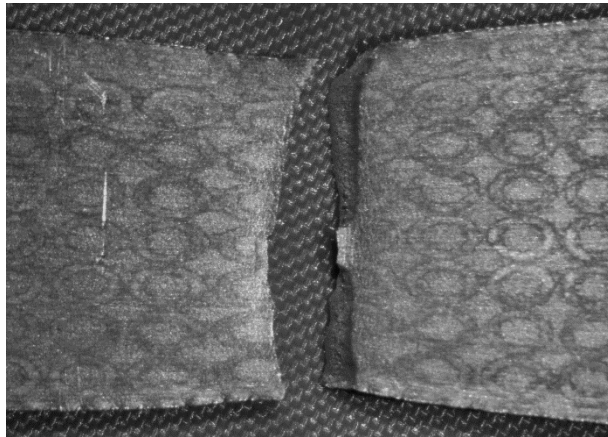


**Figure A.14** Tensile sample fractured at temperature of  $-160^{\circ}\text{C}$

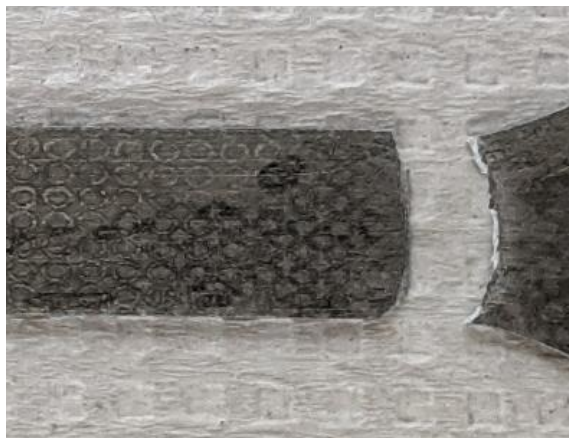


**Figure A.15** Tensile sample fractured at temperature of  $-196^{\circ}\text{C}$

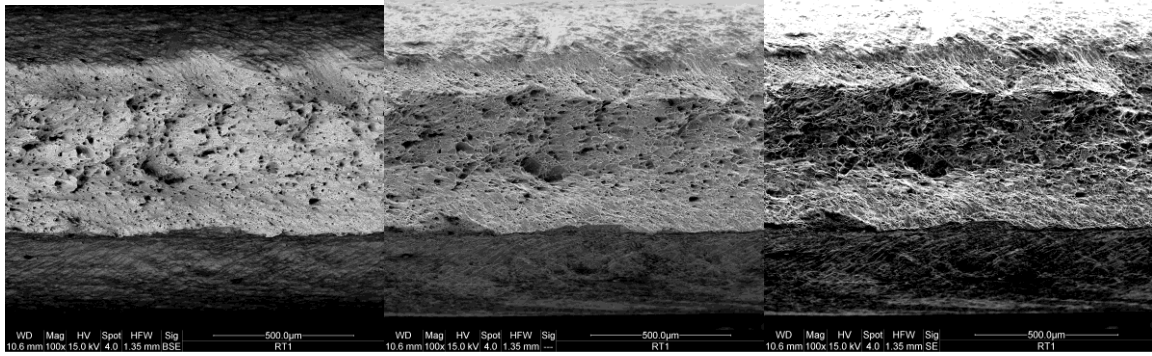


**Figure A.16** BSE SEM image of AA5182-O after experiencing a ductile fracture from tensile testing at a temperature of 25°C and a crosshead velocity of 0.084 mm/s

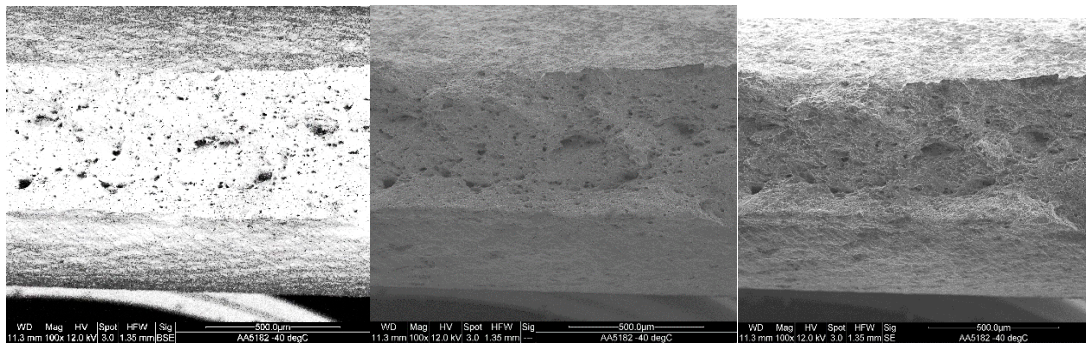


**Figure A.17** BSE SEM image of AA5182-O after experiencing a ductile fracture from tensile testing at a temperature of -40°C and a crosshead velocity of 0.084 mm/s

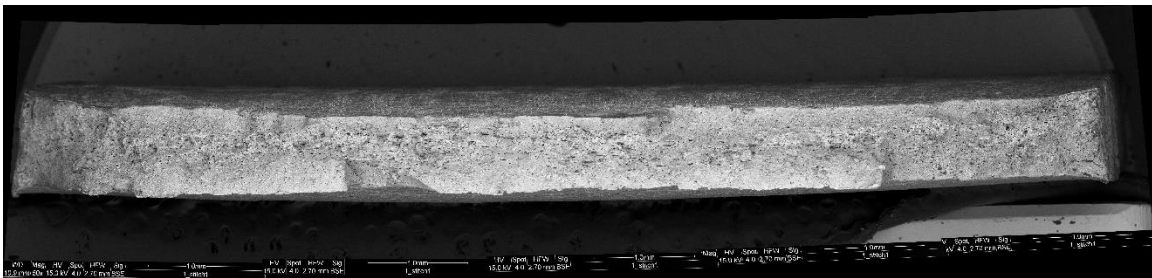


**Figure A.18** BSE SEM image of AA5182-O after experiencing a ductile fracture from tensile testing at a temperature of -80°C and a crosshead velocity of 0.084 mm/s.

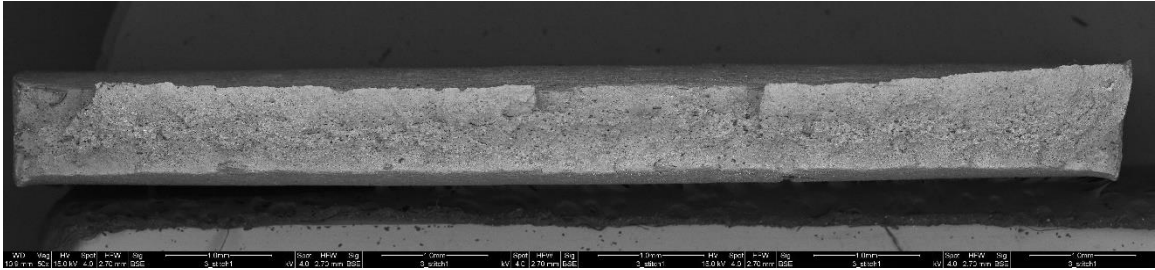


**Figure A.19** BSE SEM image of AA5182-O after experiencing a ductile fracture from tensile testing at a temperature of  $-120^{\circ}\text{C}$  and a crosshead velocity of  $0.084\text{ mm/s}$ .

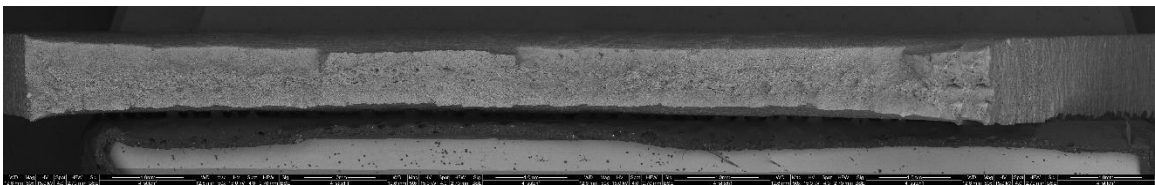


**Figure A.20** BSE SEM image of AA5182-O after experiencing a ductile fracture from tensile testing at a temperature of  $-196^{\circ}\text{C}$  and a crosshead velocity of  $0.084\text{ mm/s}$ .

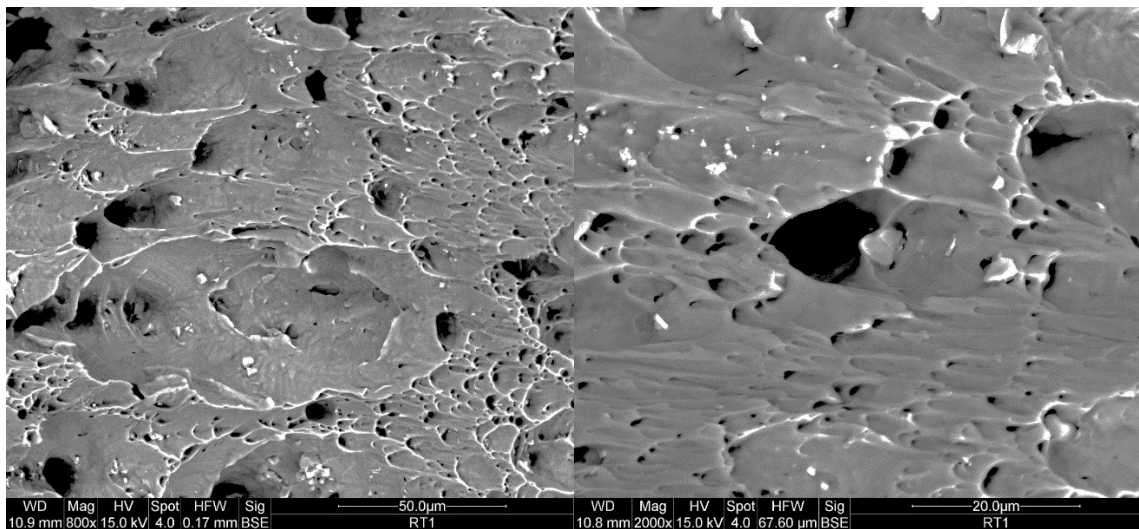


**Figure A.21** BSE SEM image of AA5182-O after experiencing a ductile fracture from tensile testing at a temperature of  $-40^{\circ}\text{C}$  and a crosshead velocity of  $0.084\text{ mm/s}$ .

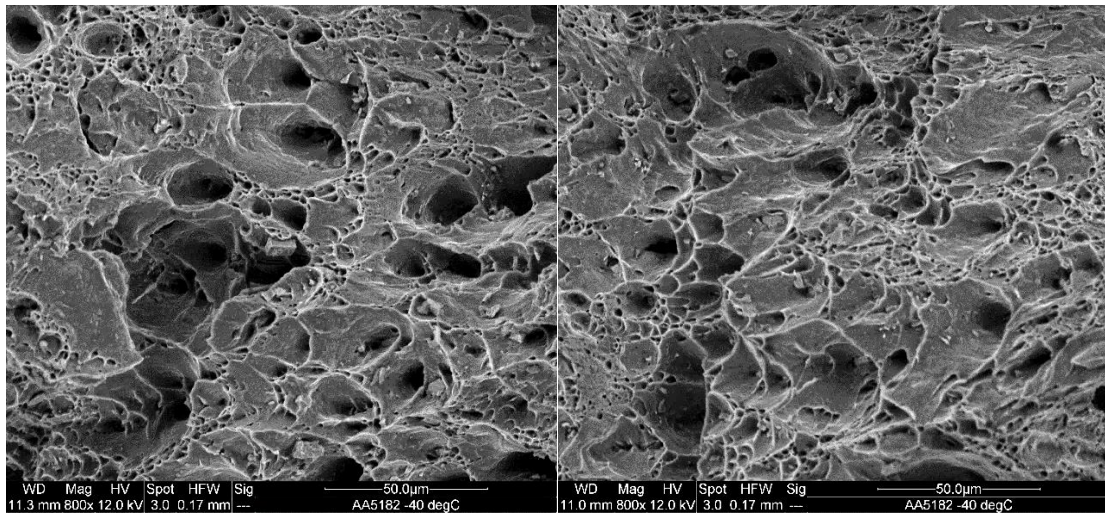


**Figure A.22** BSE SEM image of AA5182-O after experiencing a ductile fracture from tensile testing at a temperature of  $-40^{\circ}\text{C}$  and a crosshead velocity of  $0.084\text{ mm/s}$ .

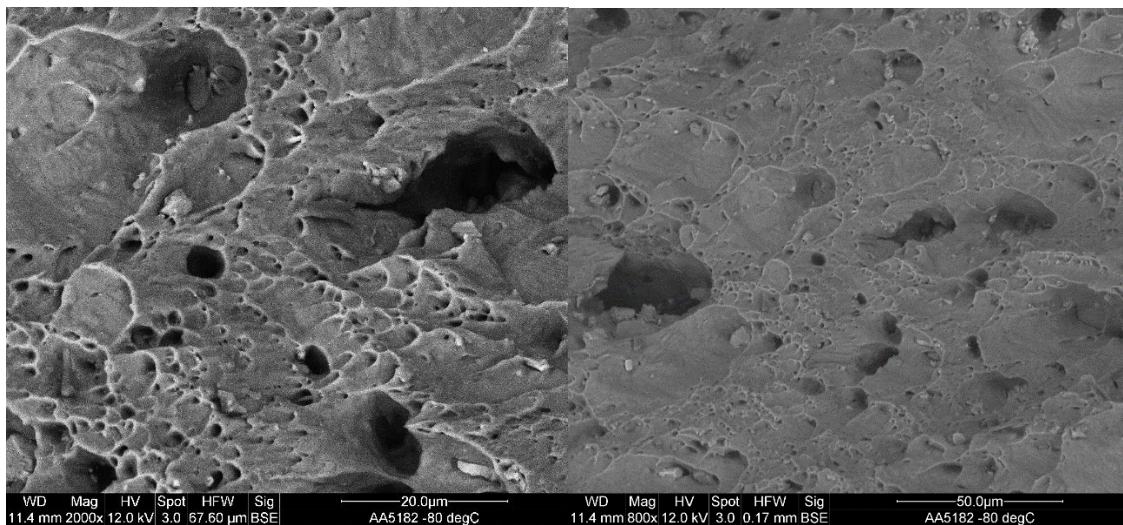


**Figure A.23** BSE SEM image of AA5182-O after experiencing a ductile fracture from tensile testing at a temperature of  $-80^{\circ}\text{C}$  and a crosshead velocity of  $0.084\text{ mm/s}$ .

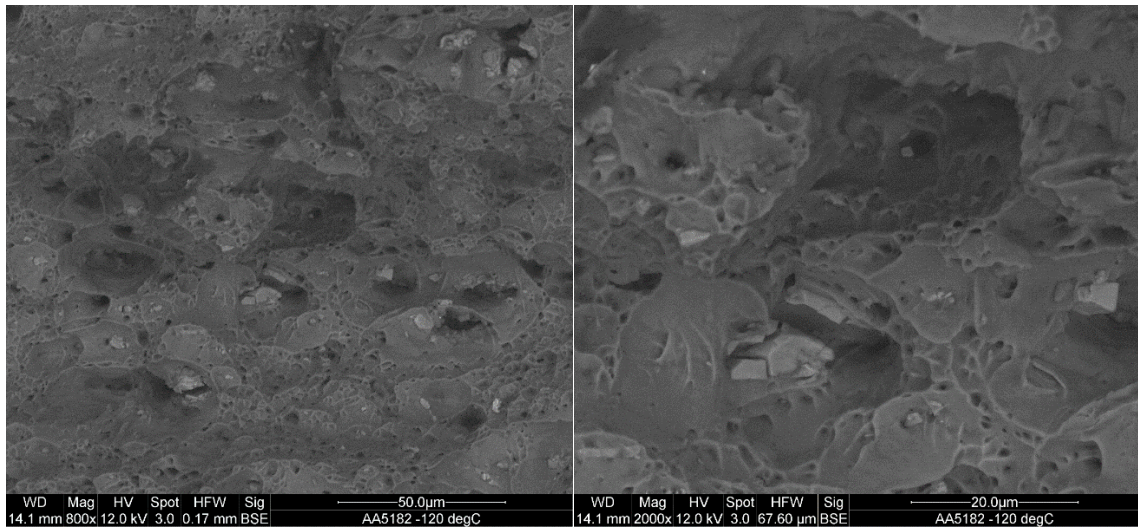


**Figure A.24** BSE SEM image of AA5182-O after experiencing a ductile fracture from tensile testing at a temperature of  $-80^{\circ}\text{C}$  and a crosshead velocity of  $0.084\text{ mm/s}$ .

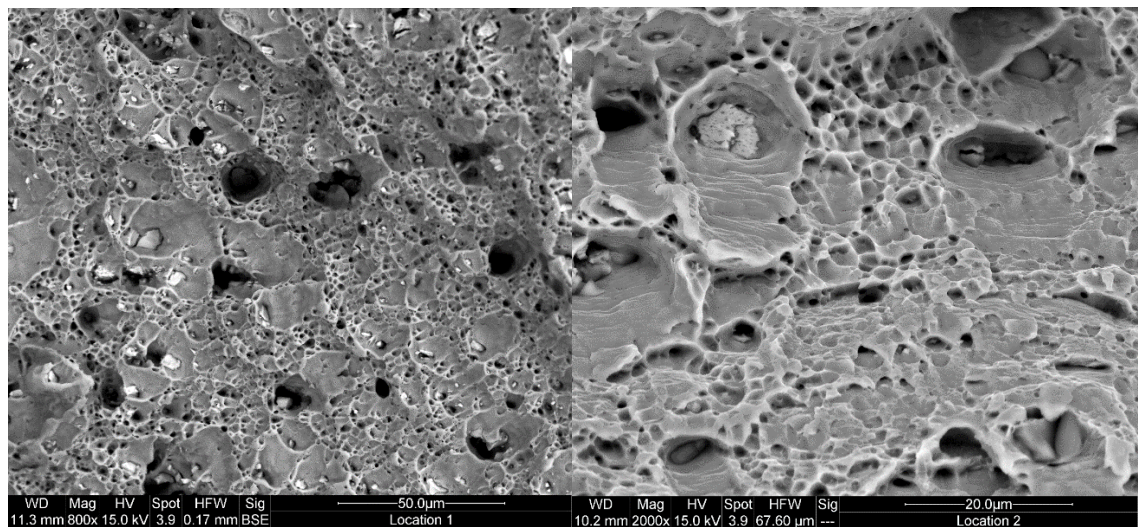


**Figure A.25** BSE SEM image of AA5182-O after experiencing a ductile fracture from tensile testing at a temperature of  $-80^{\circ}\text{C}$  and a crosshead velocity of  $0.084\text{ mm/s}$ .

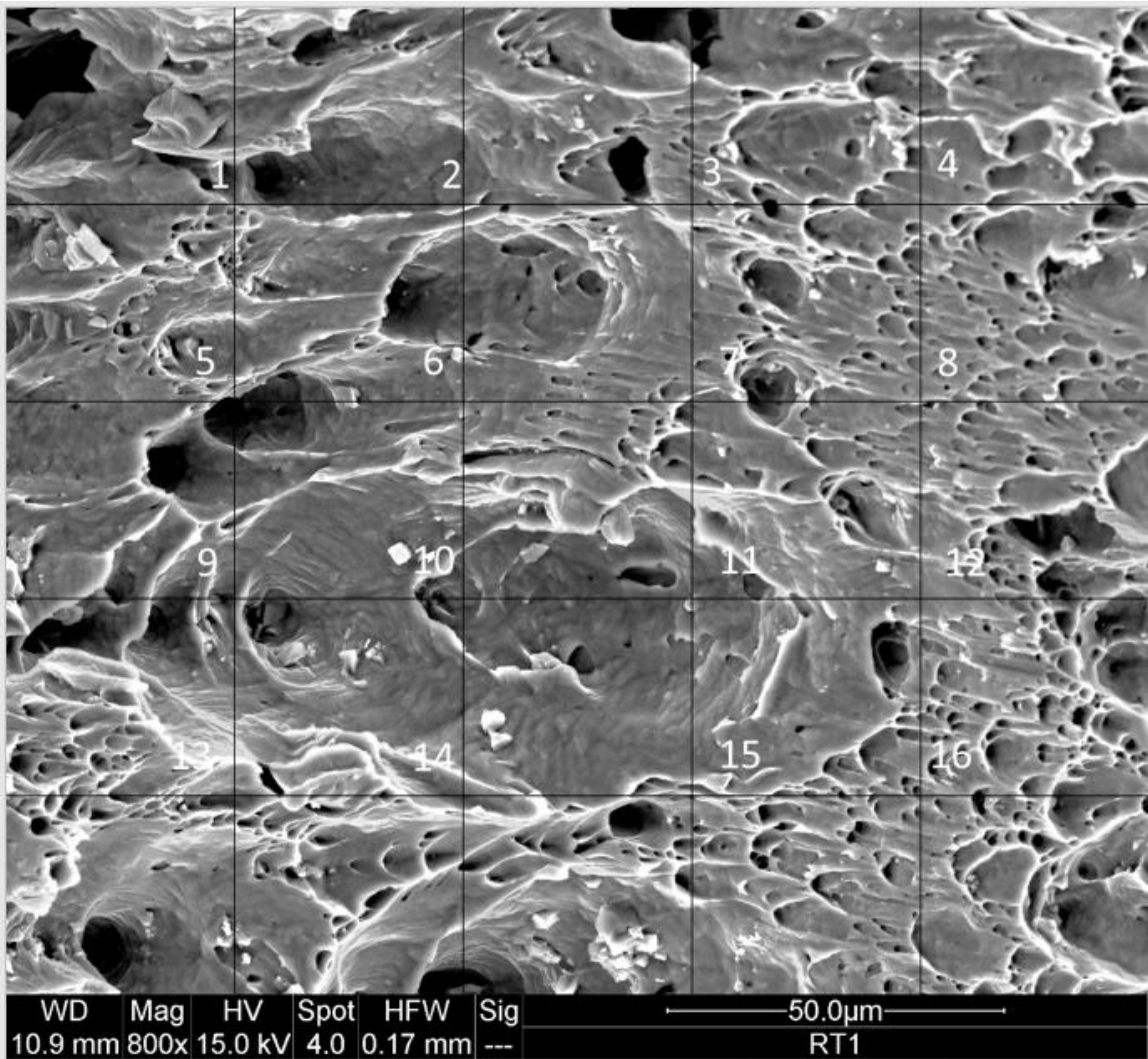


**Figure A.26** Mixed-signal SEM image of AA5182-O after experiencing a ductile fracture from tensile testing at a temperature of 25°C and a crosshead velocity of 0.084 mm/s with overlaid square grid for dimple measurements.

**Table A.7** AA5182-O reference measurements from *Figure A.26* SEM image.

Temp (°C)	Spot	Length 1 (mm)	Length 2 (mm)	Radius (average) (mm)	Area (mm <sup>2</sup> )	Characteristics/Notes
25	1	5.41	7.65	6.53	42.6409	next to some larger particles
25	2	33.88	14.47	24.175	584.43063	long elongated, particle inside the hole
25	3	22.39	8.72	15.555	241.95803	surrounded by lots of smaller dimples
25	4	12.36	4.57	8.465	71.656225	small elongated dimple
25	5	39.65	14.13	26.89	723.0721	very elongated, particle in the wall
25	6					n/a
25	7	14.22	4.88	9.55	91.2025	medium elongated dimple
25	8	5.71	1.65	3.68	13.5424	small elongated dimple
25	9	45.28	35.22	40.25	1620.0625	lots of dimples combined, some particles at the bottom and small white particles in the wall
25	10	57.23	29.35	43.29	1874.0241	lots of dimples combined, multiple particles in the wall
25	11					refer to 10
25	12					n/a
25	13	12.86	6.41	9.635	92.833225	some smaller dimples combined
25	14					n/a
25	15	0.78	1.1	0.94	0.8836	small dimple
25	16	3.12	1.01	2.065	4.264225	small elongated dimple

**Table A.8** AA5182-O conversion reference measurements from *Figure A.26* SEM images.

Temp (°C)	Spot	Length 1 (μm)	Length 2 (μm)	Radius (average) (μm)	Area (μm <sup>2</sup> )
25	1	5.0560748	7.1495327	6.1028037	37.244213
25	2	31.663551	13.523364	22.593458	510.46434
25	3	20.925234	8.1495327	14.537383	211.33551
25	4	11.551402	4.271028	7.911215	62.587322
25	5	37.056075	13.205607	25.130841	631.55918
25	6				
25	7	13.28972	4.5607477	8.9252336	79.659796
25	8	5.3364486	1.5420561	3.4392523	11.828457
25	9	42.317757	32.915888	37.616822	1415.0253
25	10	53.485981	27.429907	40.457944	1636.8452
25	11				
25	12				
25	13	12.018692	5.9906542	9.0046729	86.760023
25	14				
25	15	0.728972	1.0280374	0.8785047	0.7717705
25	16	2.9158879	0.9439252	1.9299065	3.7245393

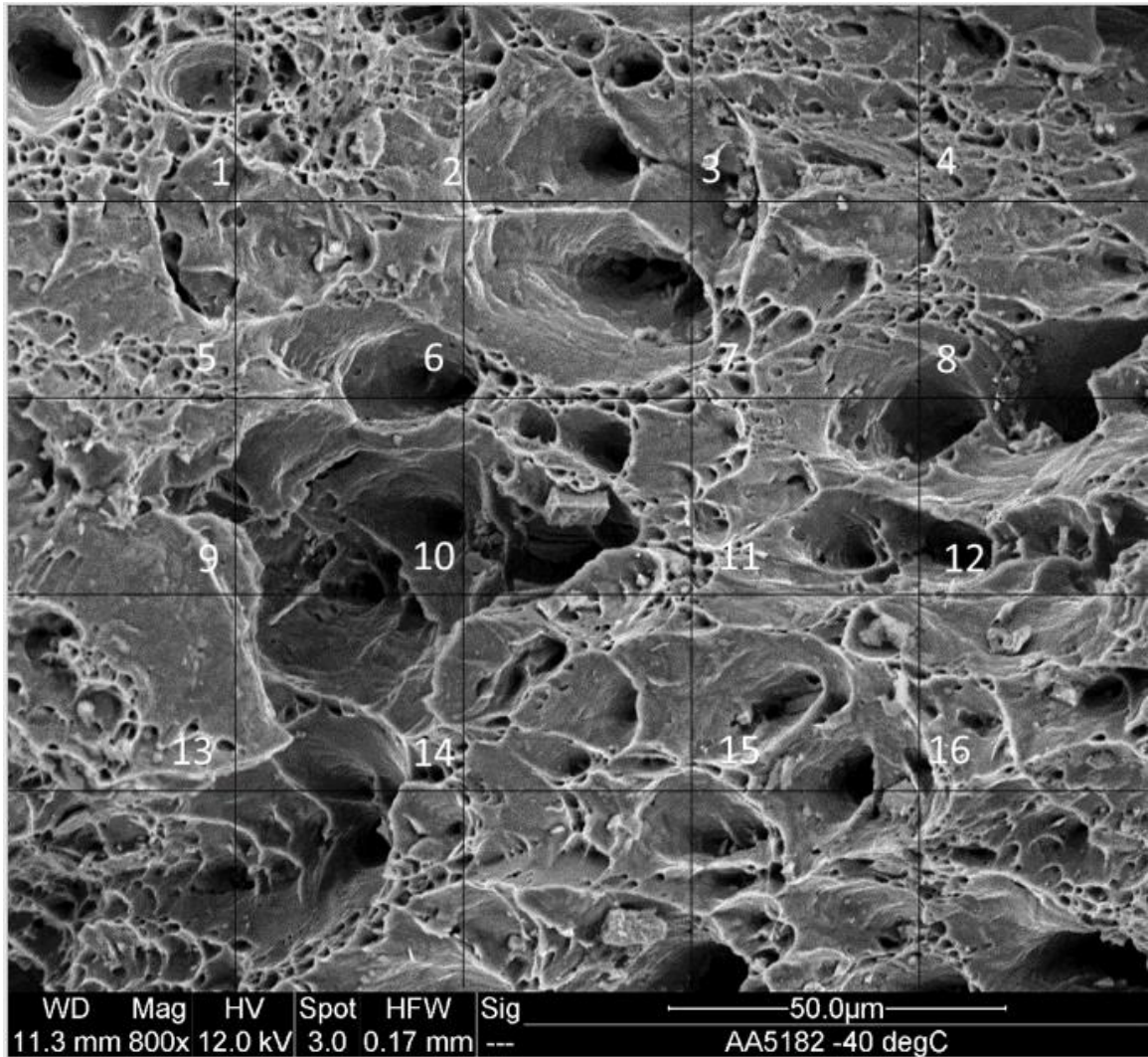


**Figure A.27** Mixed-signal SEM image of AA5182-O after experiencing a ductile fracture from tensile testing at a temperature of -40°C and a crosshead velocity of 0.084 mm/s with overlaid square grid for dimple measurements.

**Table A.9** AA5182-O reference measurements from *Figure A.27* SEM images.

Temp (°C)	Spot	Length 1 (mm)	Length 2 (mm)	Radius (average) (mm)	Area (mm <sup>2</sup> )	Characteristics/Notes
-40	1	21.29	28.24	24.765	613.30523	small particle on the wall, cant see the bottom due to shear angle
-40	2	25.29	21.14	23.215	538.93623	small particle on the wall, cant see the bottom due to shear angle
-40	3	15.04	18.46	16.75	280.5625	lots of clustered small particles
-40	4	20.99	10.67	15.83	250.5889	small particle on the wall, cant see the bottom due to shear angle
-40	5					n/a
-40	6	19.71	13.56	16.635	276.72323	two dimples inside, might be a particle in the bottom
-40	7	3.04	1.9	2.47	6.1009	small dimple
-40	8	15.65	18.55	17.1	292.41	very small particles in wall
-40	9					n/a
-40	10	13.15	26.05	19.6	384.16	next to some larger dimples, almost combined, a large rectangular particle in the wall
-40	11	1.45	2.29	1.87	3.4969	lots of very tiny particles in the area
-40	12	16.8	7.83	12.315	151.65923	lots of medium sized dimples in this area
-40	13	19.02	18.64	18.83	354.5689	lots of almost combined dimples in this region
-40	14	1.43	1.68	1.555	2.418025	small dimple
-40	15	20	13.26	16.63	276.5569	particle in he wall, almost rectangular shaped
-40	16	25.42	20.81	23.115	534.30323	lots of dimples combined, lots of particles along the walls

**Table A.10** AA5182-O conversion reference measurements from *Figure A.27* SEM images.

Temp (°C)	Spot	Length 1 (μm)	Length 2 (μm)	Radius (average) (μm)	Area (μm <sup>2</sup> )
-40	1	19.897196	26.392523	23.14486	535.68454
-40	2	23.635514	19.757009	21.696262	470.72777
-40	3	14.056075	17.252336	15.654206	245.05415
-40	4	19.616822	9.9719626	14.794393	218.87405
-40	5				
-40	6				
-40	7	2.8411215	1.7757009	2.3084112	5.3287623
-40	8	14.626168	17.336449	15.981308	255.40222
-40	9				
-40	10	12.28972	24.345794	18.317757	335.54022
-40	11	1.3551402	2.1401869	1.7476636	3.0543279
-40	12	15.700935	7.317757	11.509346	132.46504
-40	13	17.775701	17.420561	17.598131	309.69421
-40	14	1.3364486	1.5700935	1.453271	2.1119967
-40	15	18.691589	12.392523	15.542056	241.55551
-40	16	23.757009	19.448598	21.602804	466.68113

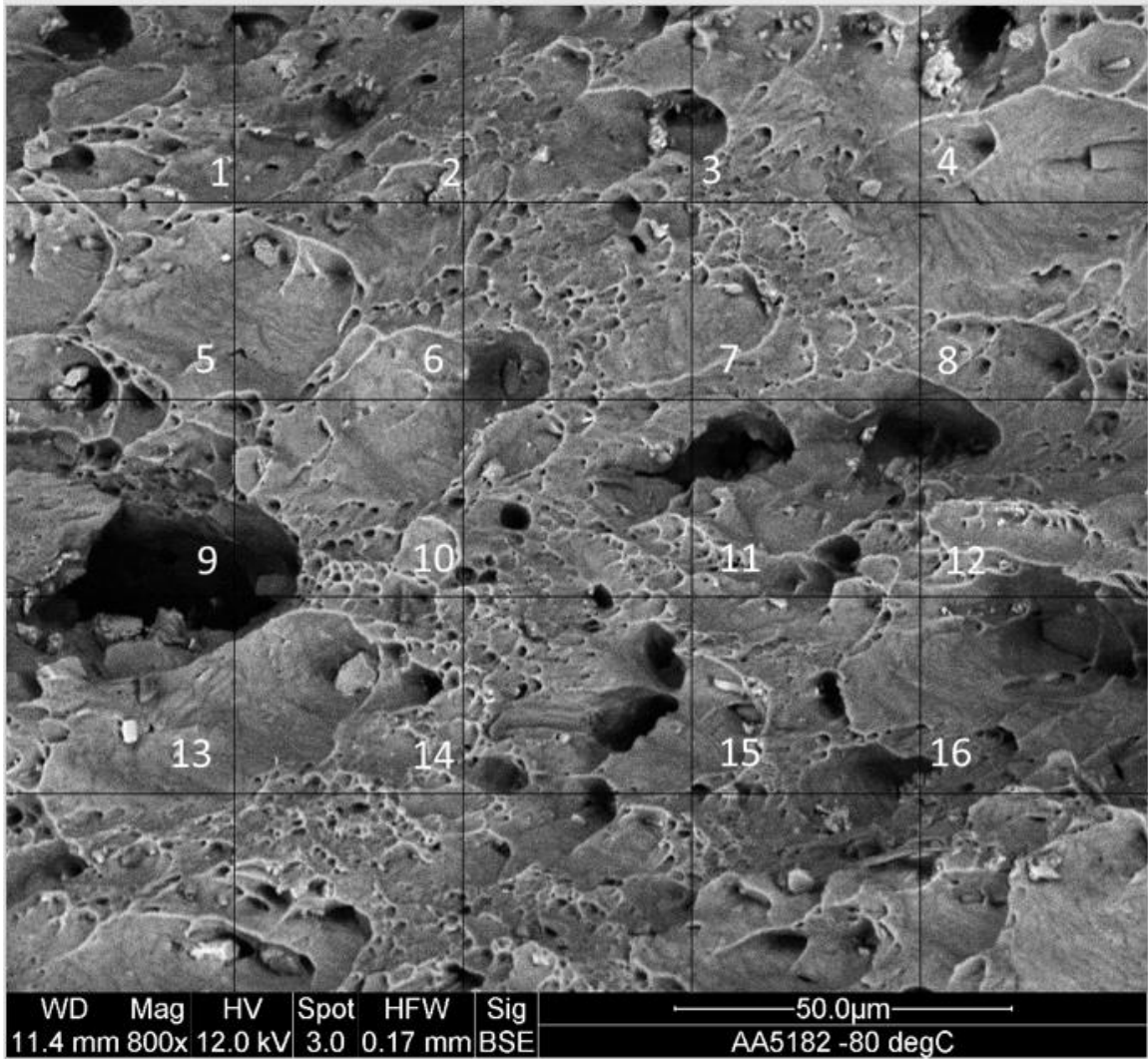


**Figure A.28** BSE SEM image of AA5182-O after experiencing a ductile fracture from tensile testing at a temperature of -80°C and a crosshead velocity of 0.084 mm/s with overlaid square grid for dimple measurements.

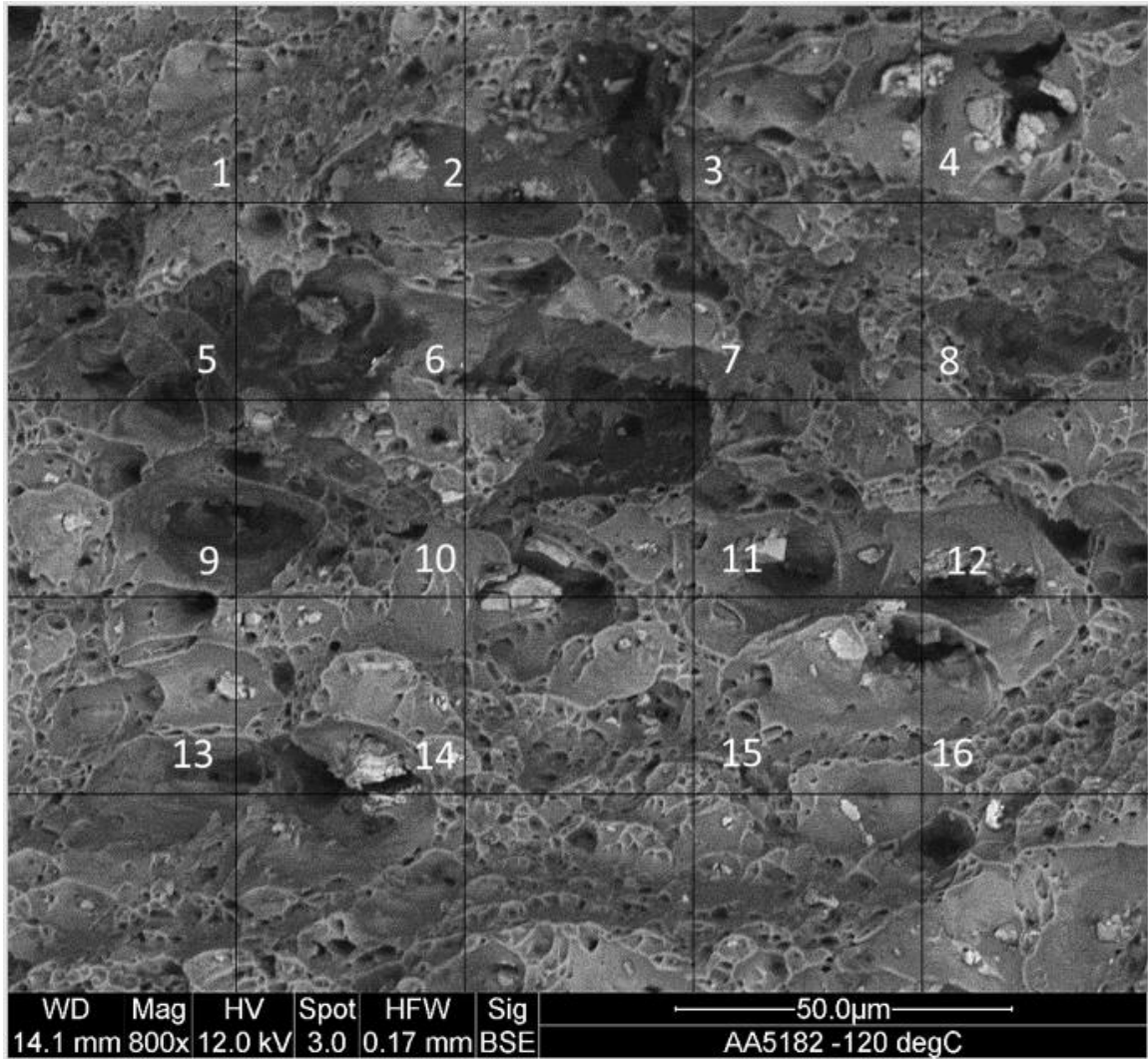


**Figure A.29** BSE SEM image of AA5182-O after experiencing a ductile fracture from tensile testing at a temperature of -120°C and a crosshead velocity of 0.084 mm/s with overlaid square grid for dimple measurements.

**Table A.11** AA5182-O reference measurements from *Figure A.28* SEM images.

Temp (°C)	Spot	Length 1 (mm)	Length 2 (mm)	Radius (average) (mm)	Area (mm <sup>2</sup> )
-80	1	12.84	17.29	15.065	226.95423
-80	2	1.84	1.84	1.84	3.3856
-80	3	6.92	6.15	6.535	42.706225
-80	4	11.79	26.82	19.305	372.68303
-80	5	5.45	4.92	5.185	26.884225
-80	6	17.47	35.48	26.475	700.92563
-80	7				
-80	8	15.7	18.7	17.2	295.84
-80	9	41.69	24.98	33.335	1111.2222
-80	10	4.51	4.85	4.68	21.9024
-80	11	3.14	5.93	4.535	20.566225
-80	12				
-80	13	49.31	21.86	35.585	1266.2922
-80	14				
-80	15	3.34	3.05	3.195	10.208025
-80	16	3.28	2.25	2.765	7.645225

**Table A.12** AA5182-O conversion reference measurements from *Figure A.28* SEM images.

Temp (°C)	Spot	Length 1 (μm)	Length 2 (μm)	Radius (average) (μm)	Area (μm <sup>2</sup> )
-80	1	10.826307	14.578415	12.702361	161.34997
-80	2	1.5514334	1.5514334	1.5514334	2.4069456
-80	3	5.8347386	5.1854975	5.510118	30.361401
-80	4	9.9409781	22.613828	16.277403	264.95385
-80	5	4.5952782	4.148398	4.3718381	19.112968
-80	6	14.730185	29.915683	22.322934	498.31339
-80	7				
-80	8	13.237774	15.767285	14.50253	210.32336
-80	9	35.151771	21.062395		
-80	10	3.8026981	4.0893761	3.9460371	15.571209
-80	11	2.6475548	5	3.8237774	14.621274
-80	12				
-80	13	41.576728	18.431703	30.004216	900.25297
-80	14				
-80	15	2.8161889	2.5716695	2.6939292	7.2572544
-80	16	2.7655987	1.8971332	2.3313659	5.4352671

**Table A.13** AA5182-O reference measurements from *Figure A.29* SEM images.

Temp (°C)	Spot	Length 1 (mm)	Length 2 (mm)	Radius (average) (mm)	Area (mm <sup>2</sup> )
-120	1	2.52	1.63	2.075	4.305625
-120	2	18.3	20.95	19.625	385.14063
-120	3	2.76	3.15	2.955	8.732025
-120	4	3.02	2.65	2.835	8.037225
-120	5	6.22	9.72	7.97	63.5209
-120	6				
-120	7				
-120	8	6.96	7.1	7.03	49.4209
-120	9	7.52	7.24	7.38	54.4644
-120	10	22.11	15.78	18.945	358.91303
-120	11	3.2	4.16	3.68	13.5424
-120	12				
-120	13	19.45	21.95	20.7	428.49
-120	14	2.83	3.1	2.965	8.791225
-120	15	4.02	3.84	3.93	15.4449
-120	16	14.13	19.33	16.73	279.8929

**Table A.14** AA5182-O conversion reference measurements from *Figure A.29* SEM images.

Temp (°C)	Spot	Length 1 (μm)	Length 2 (μm)	Radius (average) (μm)	Area (μm <sup>2</sup> )
-120	1	2.1212121	1.3720539	1.746633	3.0507268
-120	2	15.40404	17.63468	16.51936	272.88926
-120	3	2.3232323	2.6515152	2.4873737	6.1870281
-120	4	2.5420875	2.2306397	2.3863636	5.6947314
-120	5	5.2356902	8.1818182	6.7087542	45.007383
-120	6				
-120	7				
-120	8	5.8585859	5.976431	5.9175084	35.016906
-120	9	6.3299663	6.0942761	6.2121212	38.59045
-120	10	18.611111	13.282828	15.94697	254.30584
-120	11	2.6936027	3.5016835	3.0976431	9.5953928
-120	12				
-120	13	16.372054	18.476431	17.424242	303.60422
-120	14	2.3821549	2.6094276	2.4957912	6.2289739
-120	15	3.3838384	3.2323232	3.3080808	10.943399
-120	16	11.893939	16.271044	14.082492	198.31657

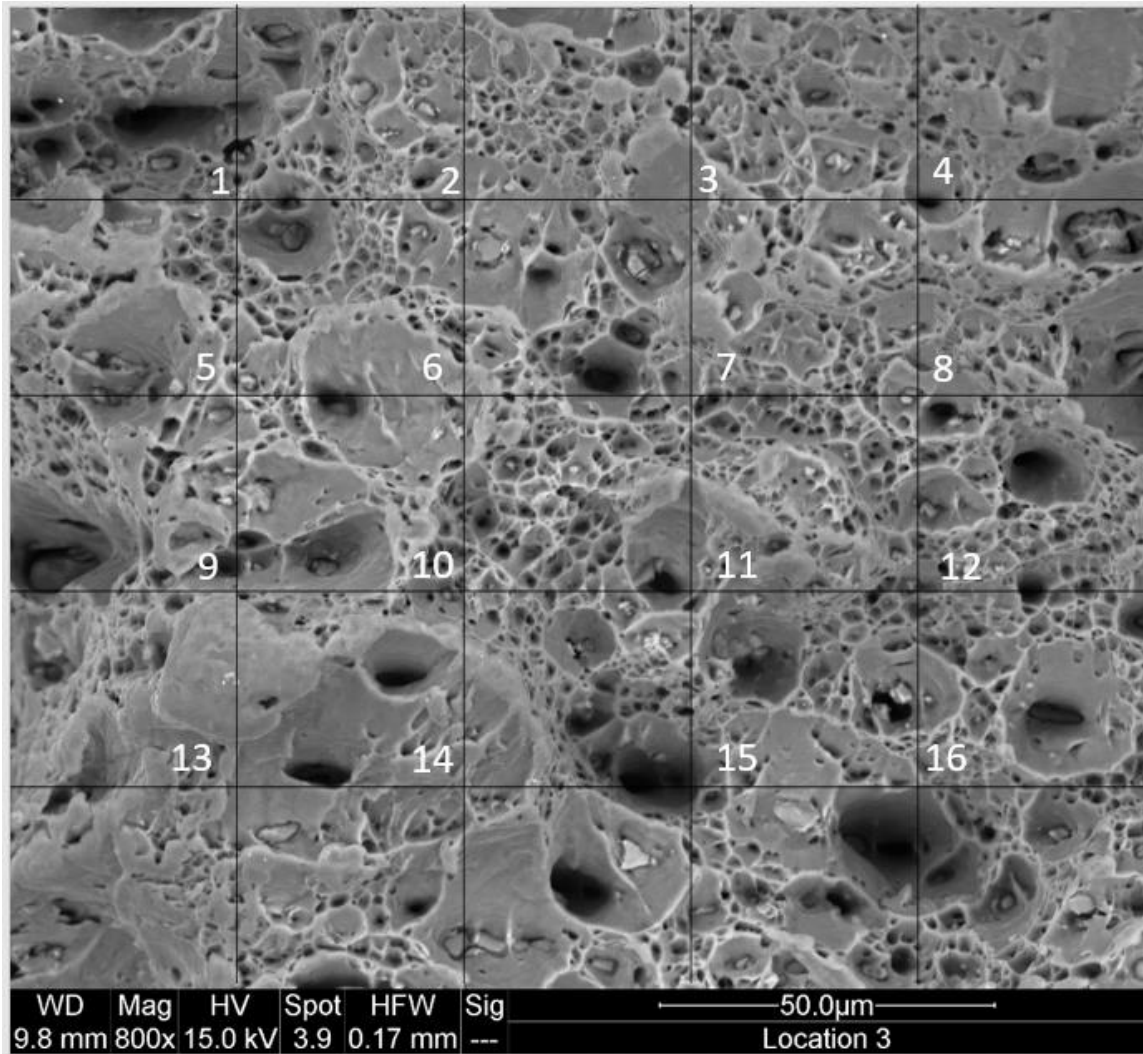


**Figure A.30** BSE SEM image of AA5182-O after experiencing a ductile fracture from tensile testing at a temperature of -160°C and a crosshead velocity of 0.084 mm/s with overlaid square grid for dimple measurements.

**Table A.15** AA5182-O reference measurements from *Figure A.30* SEM images.

Temp (°C)	Spot	Length 1 (mm)	Length 2 (mm)	Radius (average) (mm)	Area (mm <sup>2</sup> )	Characteristics/Notes
-160	1	1.78	2.45	2.115	4.473225	Small dimple
-160	2	9.48	7.89	8.685	75.429225	Particle in the bottom, somewhat joined to another dimple
-160	3	20.16	12.64	16.4	268.96	Maybe a particle at the bottom and broken white particle in walls, somewhat elongated to one side and joined to another dimple
-160	4	10.14	11.02	10.58	111.9364	Very circular, might be a particle at the bottom
-160	5	10.06	7.24	8.65	74.8225	Some smaller dimples inside, white particle wall/inside
-160	6	28.13	20.59	24.36	593.4096	Particle in the bottom, some small particles on the wall
-160	7	5.86	6.51	6.185	38.254225	No particles, somewhat smaller sized
-160	8	6.51	8	7.255	52.635025	Joined to another dimple, white broken particles in sides
-160	9	7.2	5.74	6.47	41.8609	Might be a particle at the bottom
-160	10	0.93	1.25	1.09	1.1881	Small dimple
-160	11	12.2	12.98	12.59	158.5081	Broken particle on the side wall, some smaller dimples along the side
-160	12	5.28	5.51	5.395	29.106025	Small broken particle inside on the wall
-160	13					n/a
-160	14					n/a
-160	15	14.07	17.26	15.665	245.39223	some broken particles on the wall
-160	16	17.14	23.48	20.31	412.4961	Particle in the bottom, joined to another dimple, one broken on wall

**Table A.16** AA5182-O reference measurements from *Figure A.30* SEM images.

Temp (°C)	Spot	Length 1 (μm)	Length 2 (μm)	Radius (average) (μm)	Area (μm <sup>2</sup> )
-160	1	1.6635514	2.2897196	1.9766355	3.907088
-160	2	8.8598131	7.3738318	8.1168224	65.882806
-160	3	18.841121	11.813084	15.327103	234.92008
-160	4	9.4766355	10.299065	9.8878505	97.769587
-160	5	9.4018692	6.7663551	8.0841121	65.352869
-160	6	26.28972	19.242991	22.766355	518.30693
-160	7	5.4766355	6.0841121	5.7803738	33.412722
-160	8	6.0841121	7.4766355	6.7803738	45.973469
-160	9	6.728972	5.364486	6.046729	36.562931
-160	10	0.8691589	1.1682243	1.0186916	1.0377326
-160	11	11.401869	12.130841	11.766355	138.44711
-160	12	4.9345794	5.1495327	5.0420561	25.422329
-160	13				
-160	14				
-160	15	13.149533	16.130841	14.640187	214.33507
-160	16	16.018692	21.943925	18.981308	360.29007

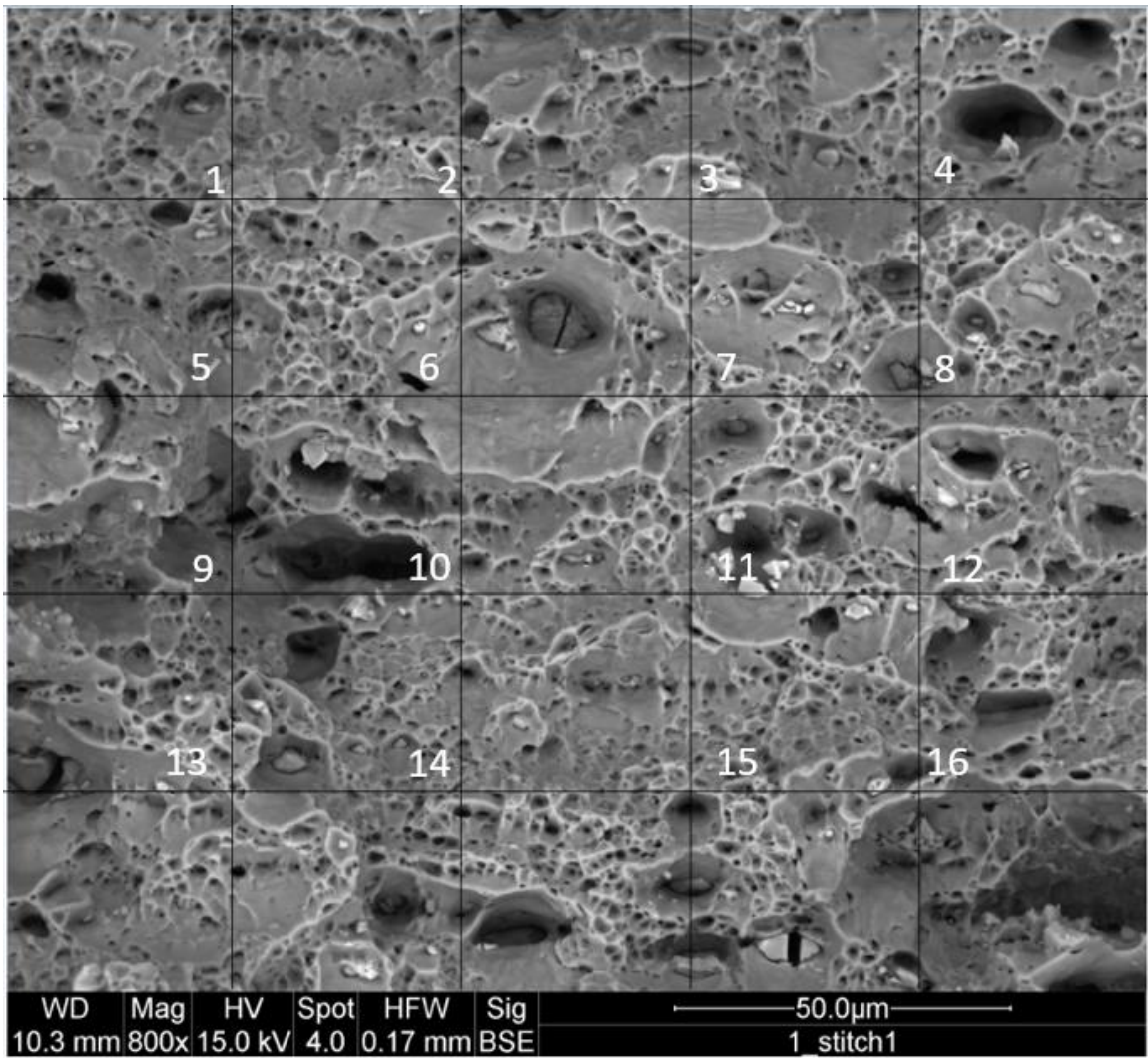


**Figure A.31** BSE SEM image of AA5182-O after experiencing a ductile fracture from tensile testing at a temperature of -196°C and a crosshead velocity of 0.084 mm/s with overlaid square grid for dimple measurements.

**Table A.17** AA5182-O reference measurements from *Figure A.31* SEM images.

Temp (°C)	Spot	Length 1 (mm)	Length 2 (mm)	Radius (average) (mm)	Area (mm <sup>2</sup> )	Characteristics/Notes
-196	1	0.95	1.1	1.025	1.050625	Small dimple
-196	2	1.2	1.45	1.325	1.755625	Small dimple
-196	3	18.23	11.46	14.845	220.37403	Maybe a particle at the bottom and broken white particle in walls, somewhat elongated to one side and joined to another dimple
-196	4	5.02	3.91	4.465	19.936225	Possibly joined to another dimple with sharp white particle embedded in the wall
-196	5					n/a
-196	6					n/a
-196	7	3.41	3.56	3.485	12.145225	Small dimple
-196	8	14.87	15.65	15.26	232.8676	Particle at the bottom, possibly one white particle embedded in the wall
-196	9					n/a
-196	10	0.93	1.25	1.09	1.1881	Small dimple
-196	11	18.04	17.98	18.01	324.3601	Multiple white (broken?) particles embedded in the walls
-196	12					n/a
-196	13	1.68	1.26	1.47	2.1609	Small dimple
-196	14					n/a
-196	15	5.54	6.02	5.78	33.4084	Equiaxed dimple
-196	16	1.08	1.25	1.165	1.357225	Small dimple

**Table A.18** AA5182-O conversion reference measurements from *Figure A.31* SEM images.

Temp (°C)	Spot	Length 1 (μm)	Length 2 (μm)	Radius (average) (μm)	Area (μm <sup>2</sup> )
-196	1	1.0674157	1.2359551	1.1516854	1.3263792
-196	2	1.3483146	1.6292135	1.488764	2.2164184
-196	3	20.483146	12.876404	16.679775	278.2149
-196	4	5.6404494	4.3932584	5.0168539	25.168823
-196	5				
-196	6				
-196	7	3.8314607	4	3.9157303	15.332944
-196	8	16.707865	17.58427	17.146067	293.98763
-196	9	1.0449438	1.4044944	1.2247191	1.4999369
-196	10	20.269663	20.202247	20.235955	409.49388
-196	11	1.247191	1.1011236	1.1741573	1.3786454
-196	12				
-196	13	1.8876404	1.4157303	1.6516854	2.7280646
-196	14	7	5.752809	6.3764045	40.658534
-196	15	6.2247191	6.7640449	6.494382	42.176998
-196	16	1.2134831	1.4044944	1.3089888	1.7134516

## A.3 Tensile Data

### A.3.1 Anisotropy

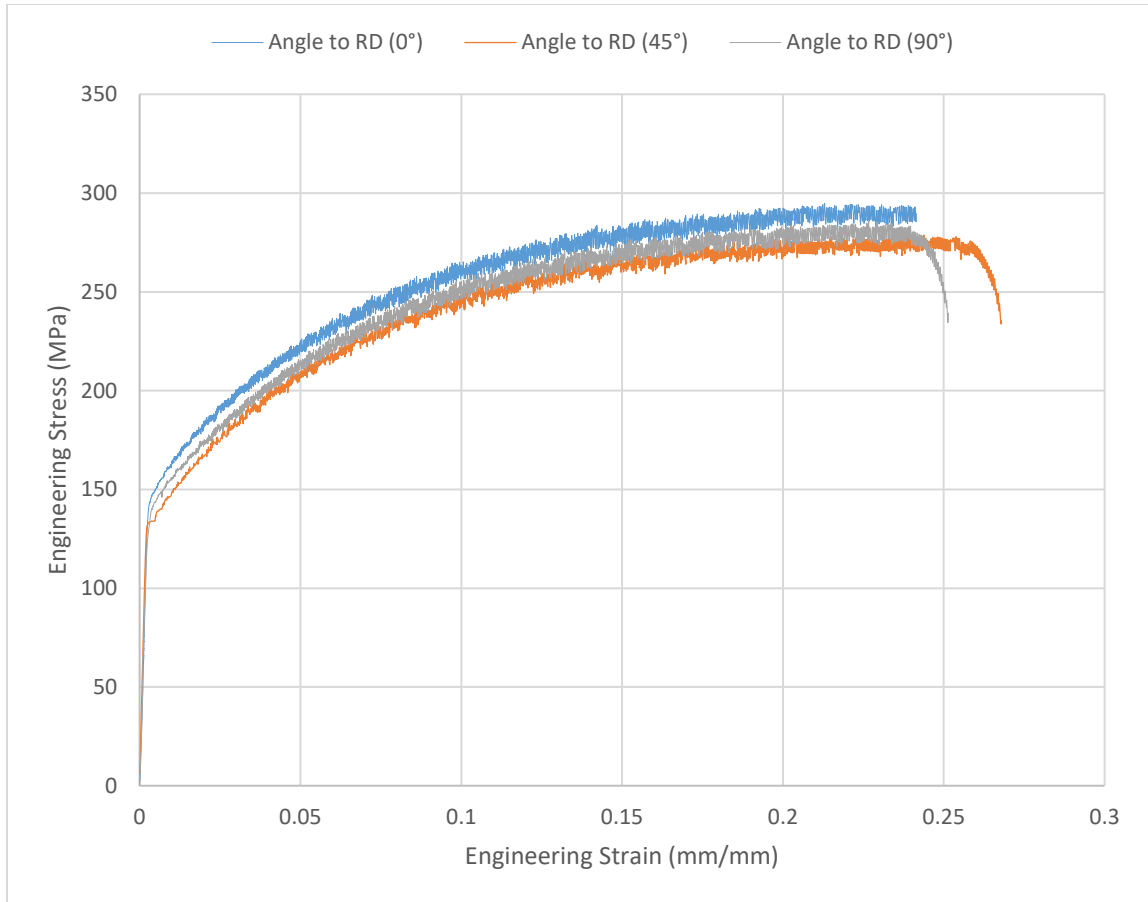


**Figure A.32** Engineering stress-strain curves for AA5182-O at strain rate average of  $0.0005 \text{ s}^{-1}$  and temperature  $25^\circ\text{C}$  with samples cut in the rolling direction ( $0^\circ$ ), perpendicular ( $90^\circ$ ) to the rolling direction, and  $45^\circ$  from the rolling direction.

**Table A.19.** Mechanical property values obtained from the data shown in Figure A.32. (Anisotropy data).

Sample Angle to RD	Elastic Modulus (GPa)	Yield Stress (MPa)	Ultimate Tensile Stress (MPa)	Uniform Elongation (strain, %)	Total elongation (strain, %)
( $0^\circ$ )	69.85	134.1	294.91	0.2129	0.248
( $45^\circ$ )	70.02	132.8	279.16	0.2398	0.261
( $90^\circ$ )	69.73	131.6	285.99	0.2267	0.251

### A.3.2 Room Temperature Tensile Testing

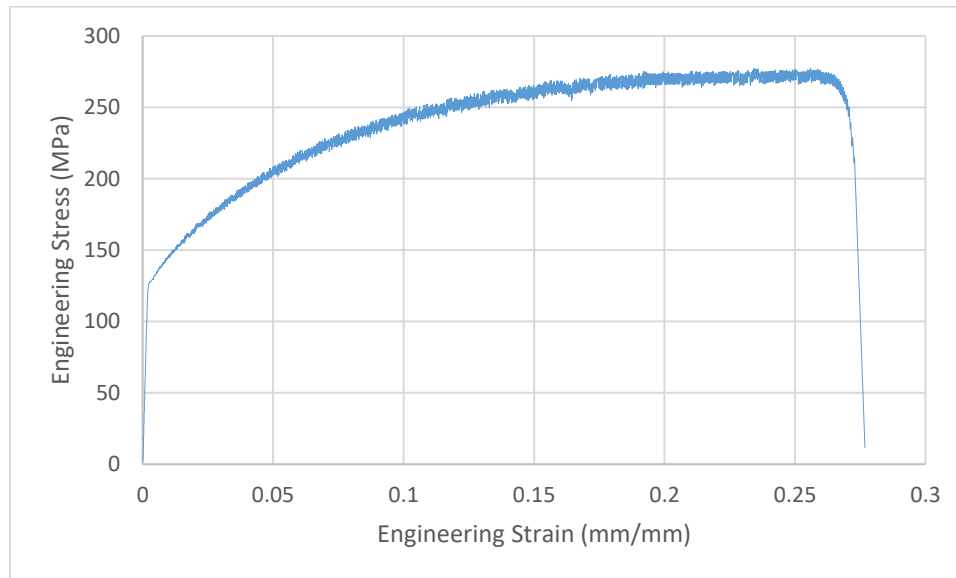


**Figure A.33** Engineering stress-strain curve for AA5182-O at strain rate average of  $0.0005 \text{ s}^{-1}$  and temperature  $25^\circ\text{C}$ .

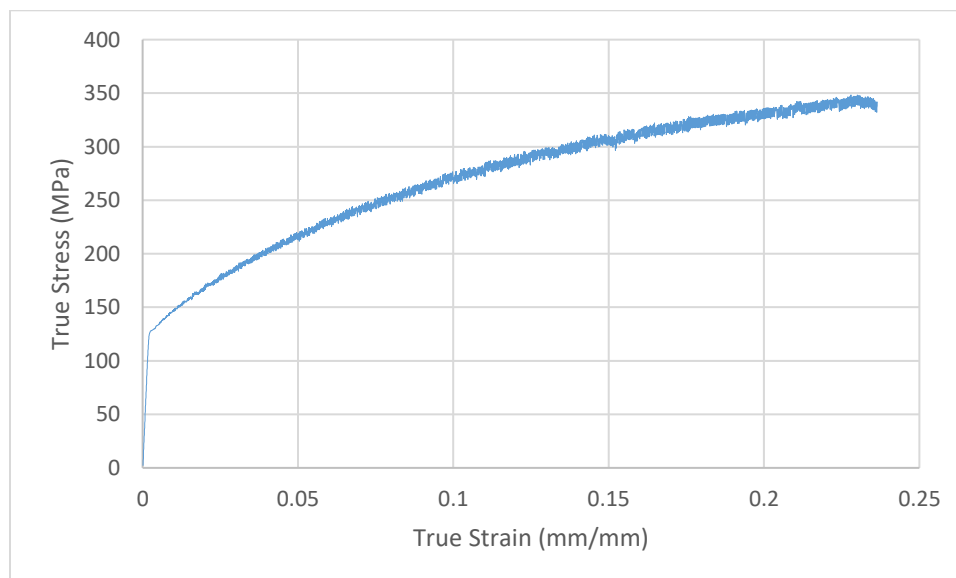


**Figure A.34** True stress-strain curve for AA5182-O at strain rate average of  $0.0005 \text{ s}^{-1}$  and temperature  $25^\circ\text{C}$ .

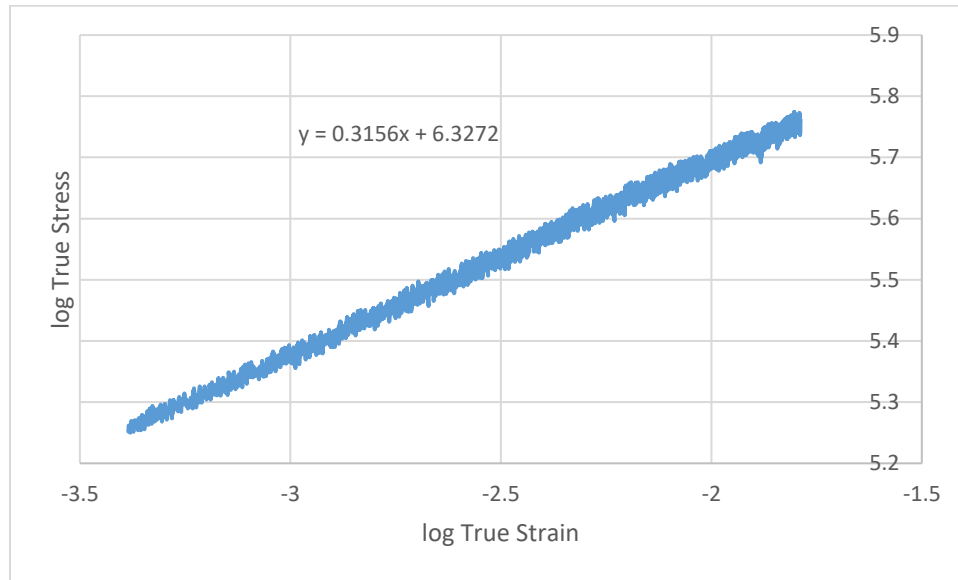


**Figure A.35** Log of true stress-true strain to determine average strain hardening exponent (n-slope displayed on the plot).

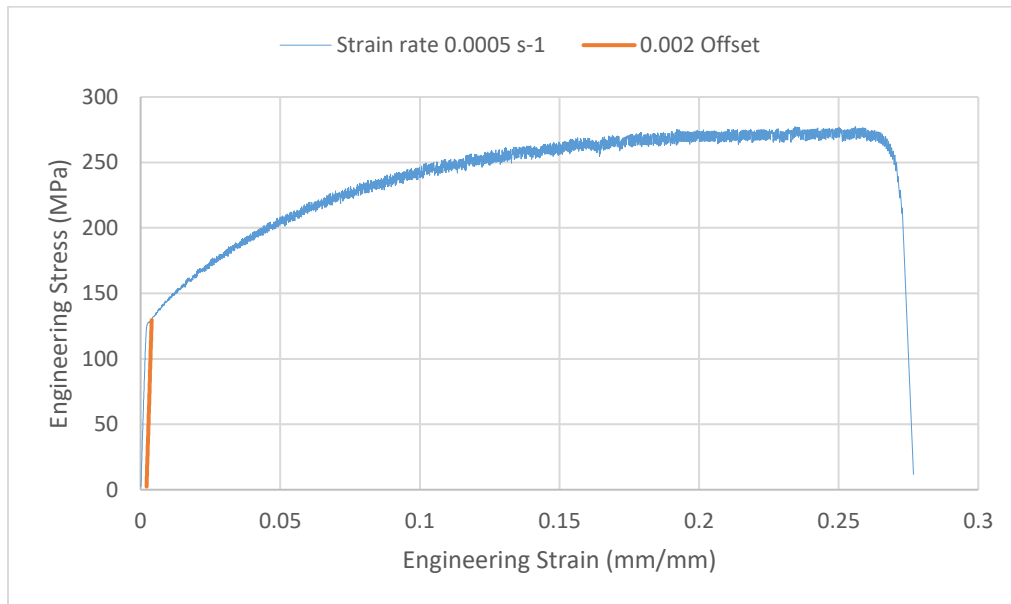


**Figure A.36** Engineering stress-strain curve for AA5182-O at strain rate average of 0.0005 s<sup>-1</sup> and temperature 25°C with 0.002 offset (for yield stress determination).

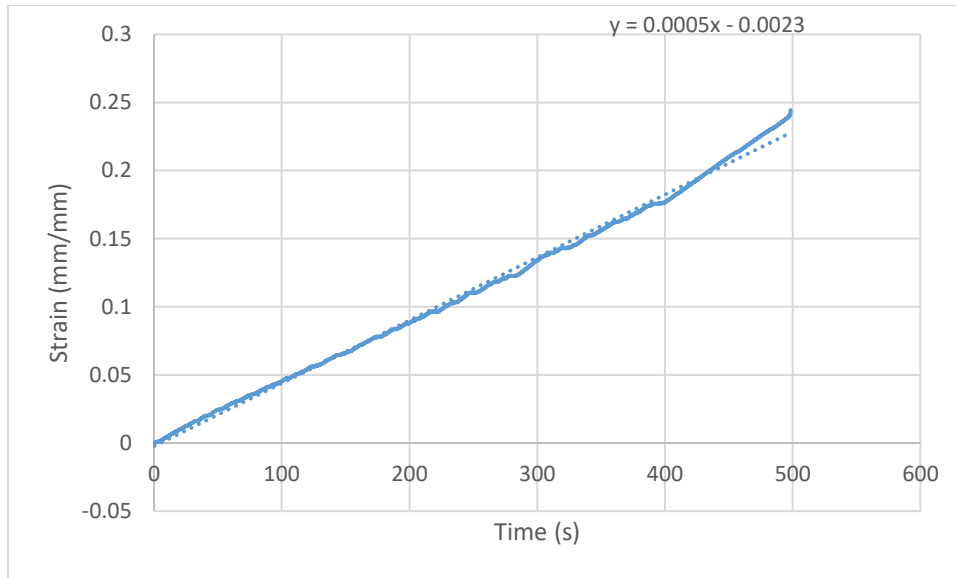


**Figure A.37** Strain mapped as a function of time to determine average strain rate (slope) of the test for AA5182-O at strain rate average of  $0.0005 \text{ s}^{-1}$  and temperature  $25^\circ\text{C}$ .

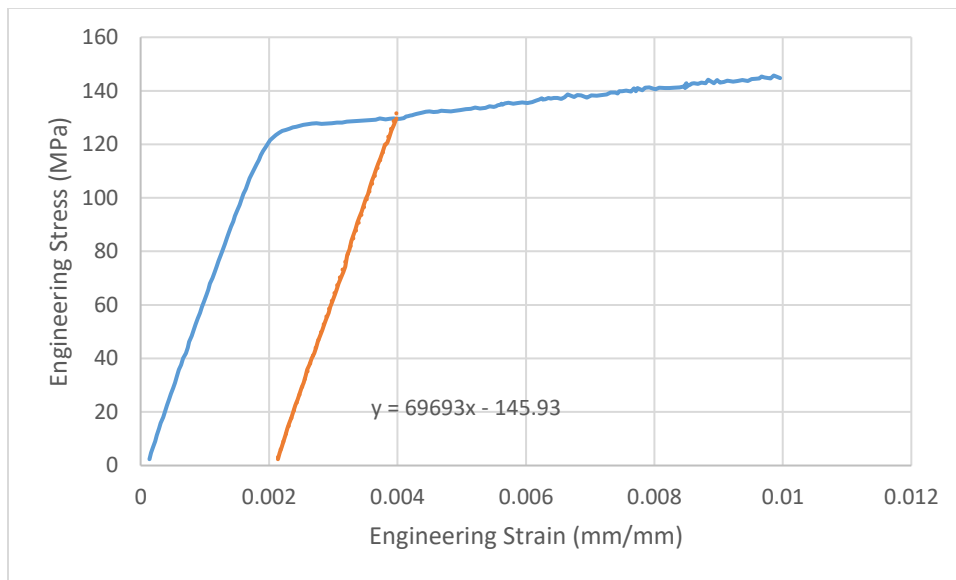


**Figure A.38** Magnified engineering stress-strain curve for AA5182-O at strain rate average of  $0.0005 \text{ s}^{-1}$  and temperature  $25^\circ\text{C}$  with 0.002 offset (elastic modulus=slope, intersection=yield stress) with equation displayed on the graph.

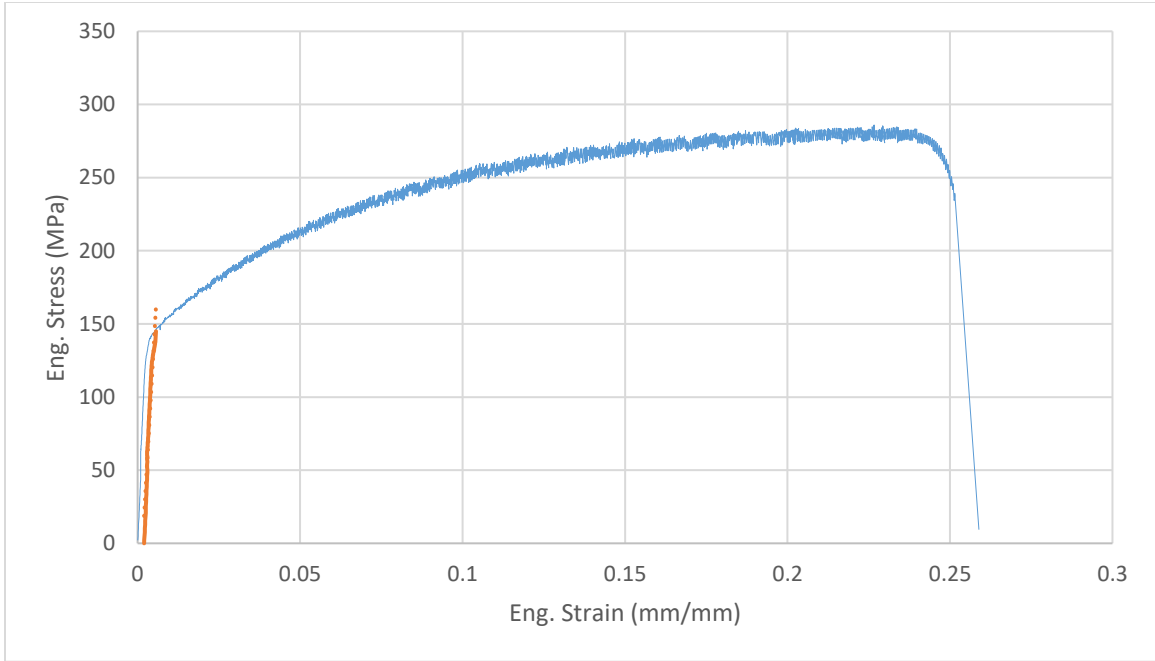


**Figure A.39** Engineering stress-strain curve for AA5182-O at strain rate average of  $0.001 \text{ s}^{-1}$  and temperature  $25^\circ\text{C}$  with 0.002 offset (for yield stress determination).

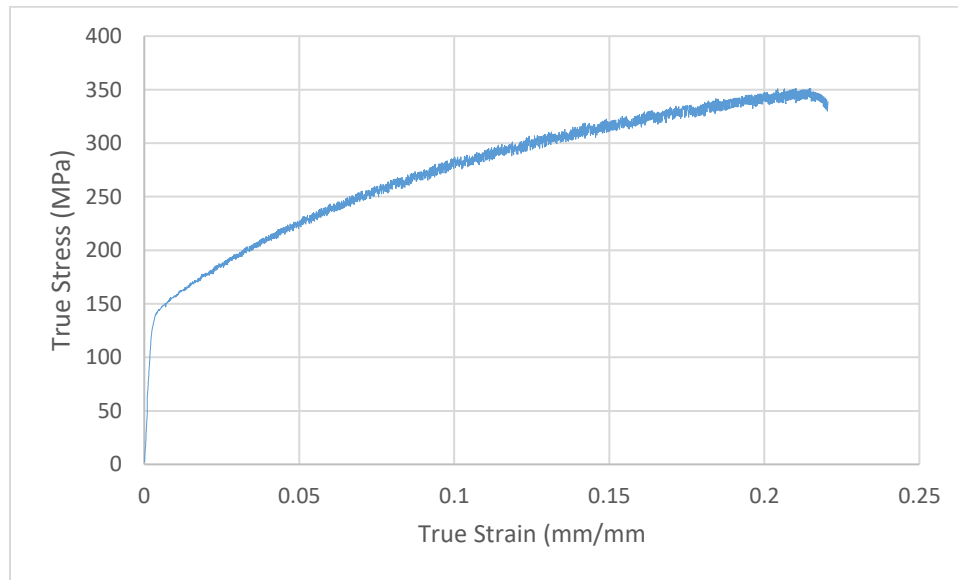


**Figure A.40** True stress-strain curve for AA5182-O at strain rate average of  $0.001 \text{ s}^{-1}$  and temperature  $25^\circ\text{C}$ .

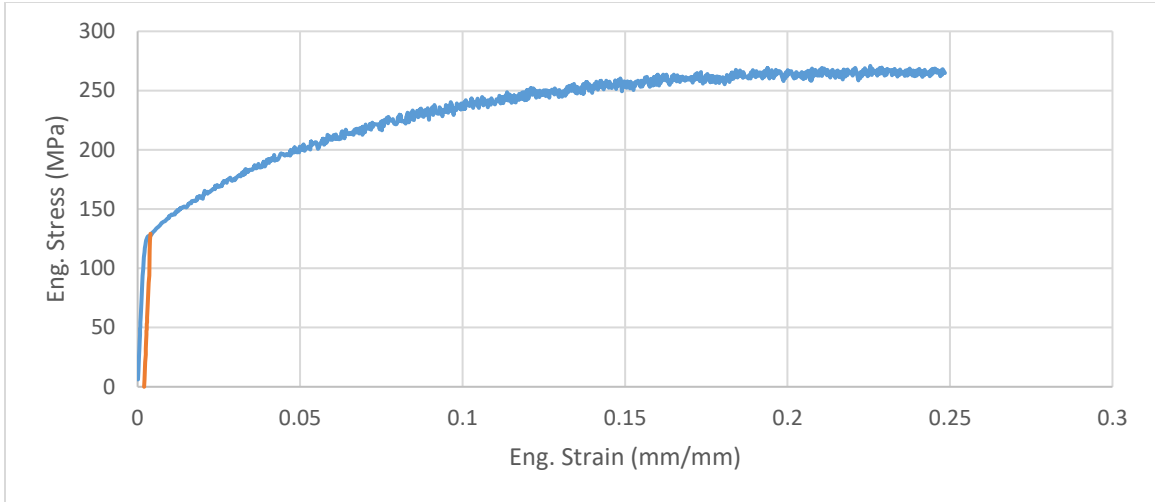


**Figure A.41** Engineering stress-strain curve for AA5182-O at strain rate average of  $0.0019 \text{ s}^{-1}$  and temperature  $25^\circ\text{C}$  with 0.002 offset (for yield stress determination).

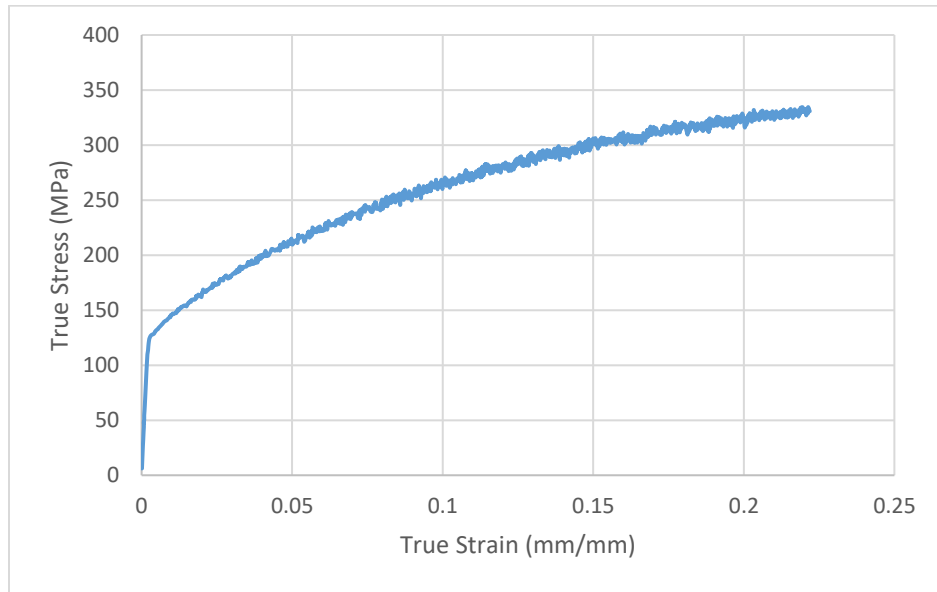


**Figure A.42** True stress-strain curve for AA5182-O at strain rate average of  $0.0019 \text{ s}^{-1}$  and temperature  $25^\circ\text{C}$ .

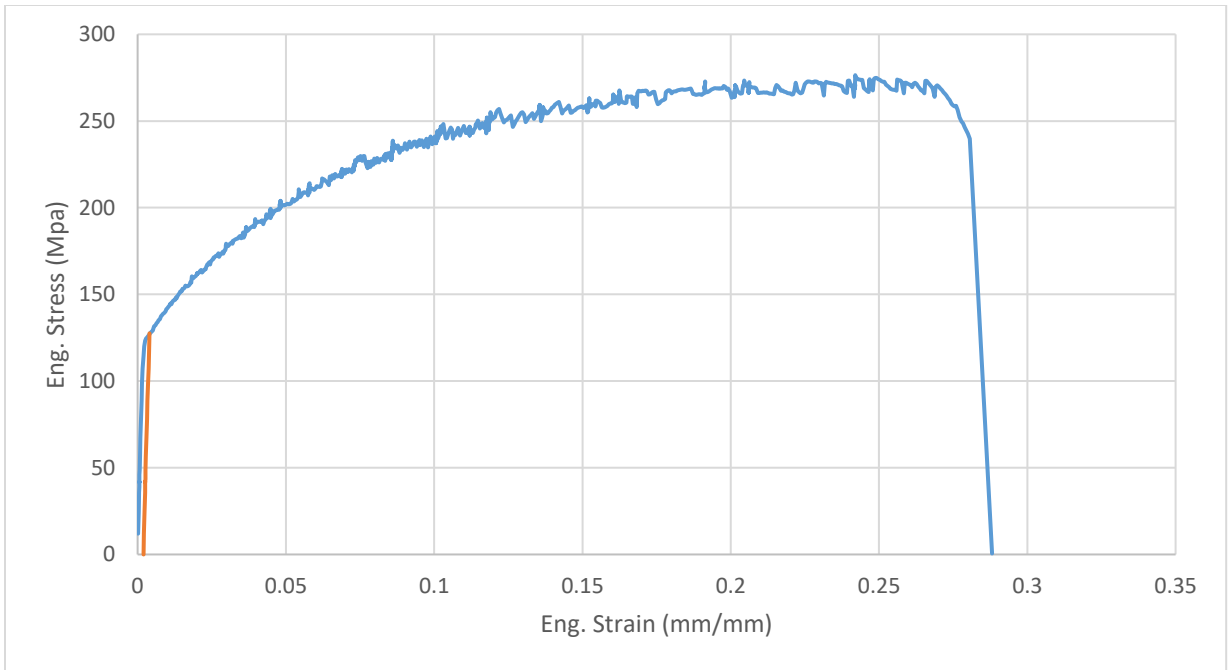


**Figure A.43** Engineering stress-strain curve for AA5182-O at strain rate average of  $0.0031 \text{ s}^{-1}$  and temperature  $25^\circ\text{C}$  with 0.002 offset (for yield stress determination).

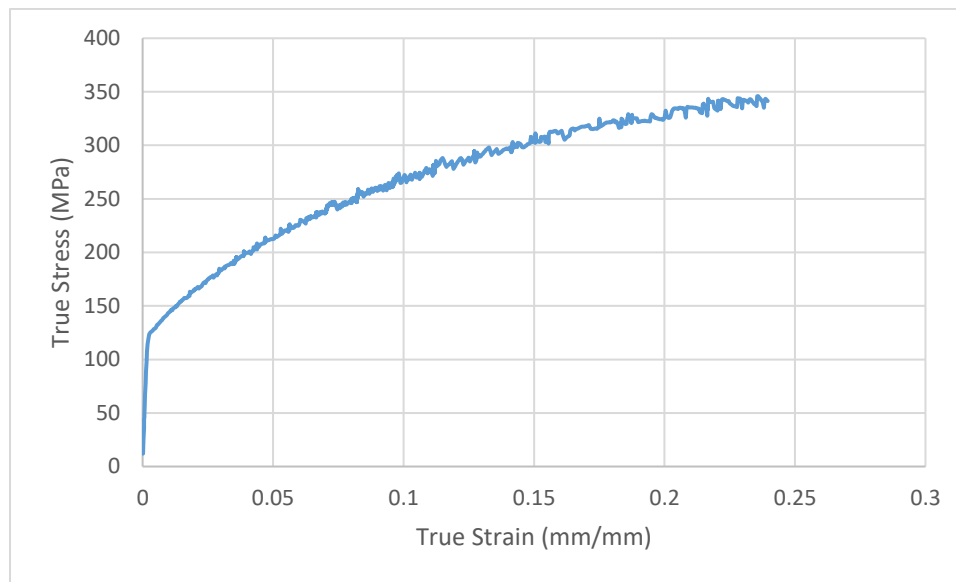


**Figure A.44** True stress-strain curve for AA5182-O at strain rate average of  $0.0031 \text{ s}^{-1}$  and temperature  $25^\circ\text{C}$ .

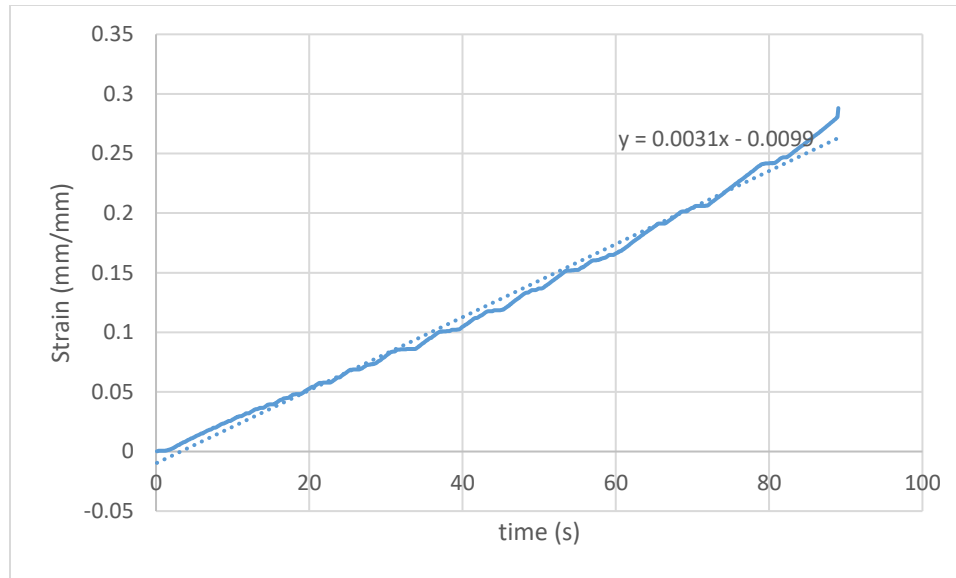


**Figure A.45** Strain mapped as a function of time to determine average strain rate (slope) of the test for AA6061 at strain rate average of  $0.0031 \text{ s}^{-1}$  and temperature  $25^\circ\text{C}$ .

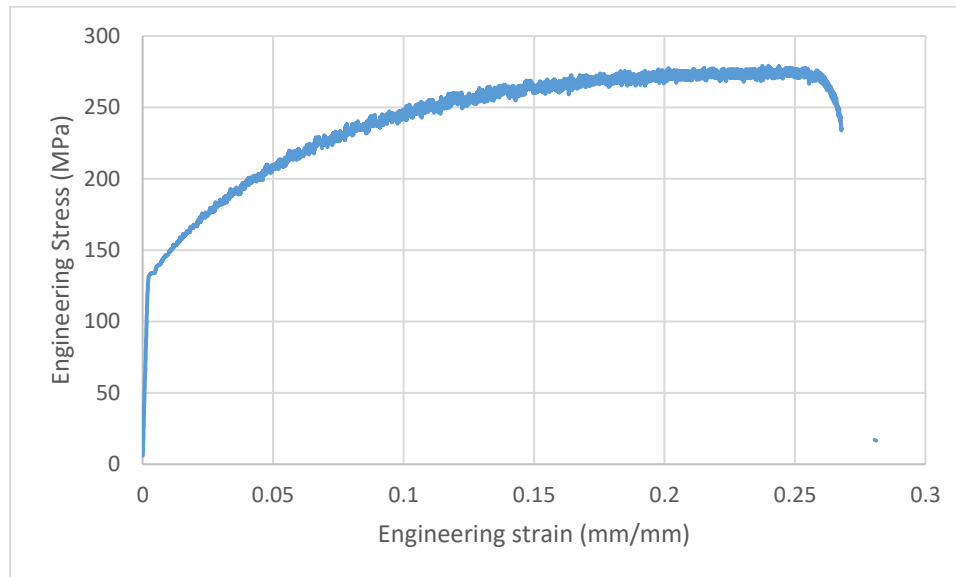


**Figure A.46** Engineering stress-strain curve for AA5182-O at strain rate average of  $0.0019 \text{ s}^{-1}$  and temperature  $25^\circ\text{C}$  ( $0.084 \text{ mm/s}$ ).

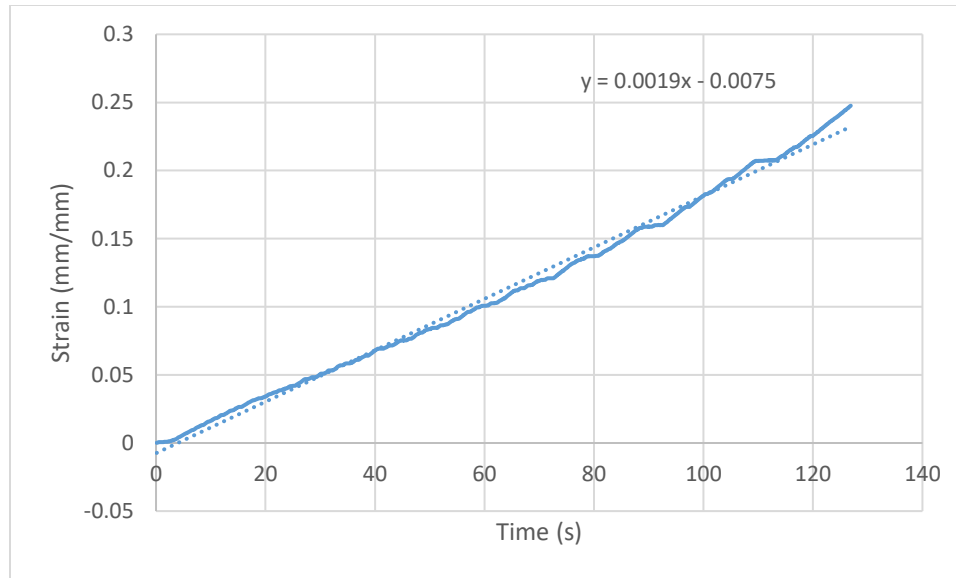


**Figure A.47** Strain mapped as a function of time to determine average strain rate (slope) of the test for AA5182-O at strain rate average of  $0.0019 \text{ s}^{-1}$  and temperature  $25^\circ\text{C}$ .

### A.3.3 Sub-Zero Temperature Tensile Testing

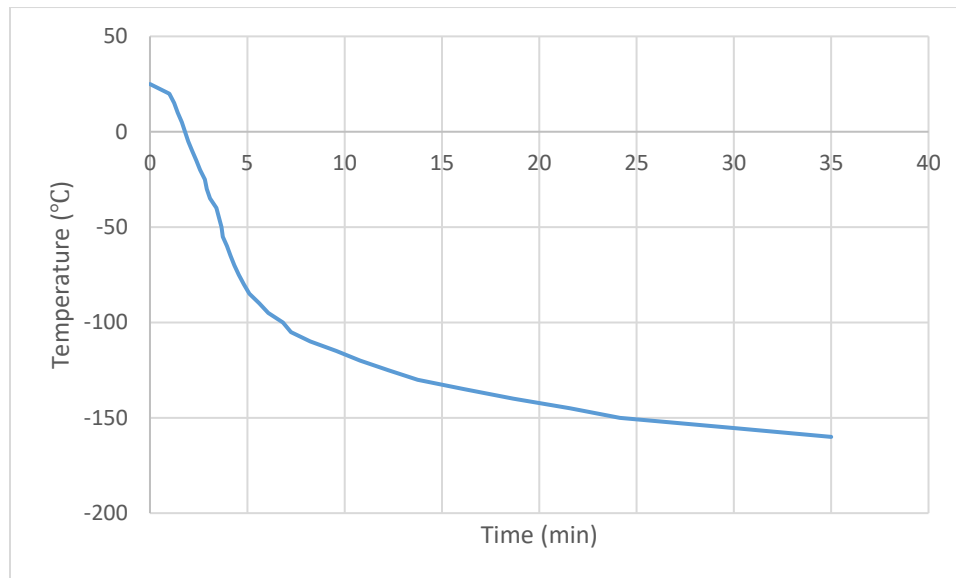


**Figure A.51** Temperature Time Gradient of AA5182-O from  $25^\circ\text{C}$  to  $-160^\circ\text{C}$  in the MTS Tensile Testing Machine Environmental Chamber.

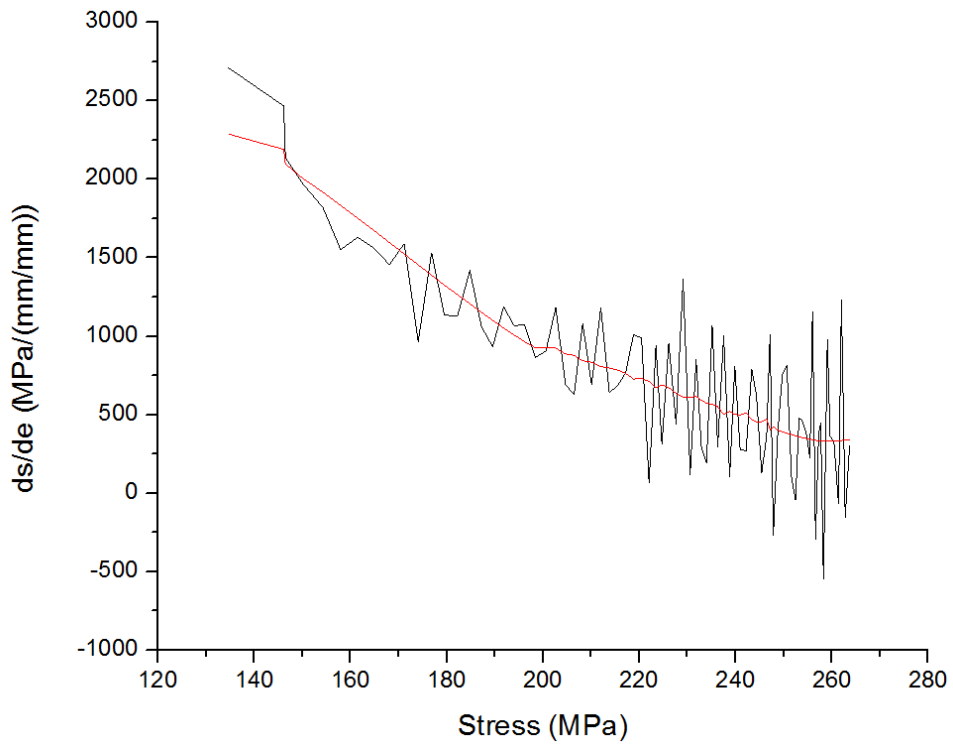
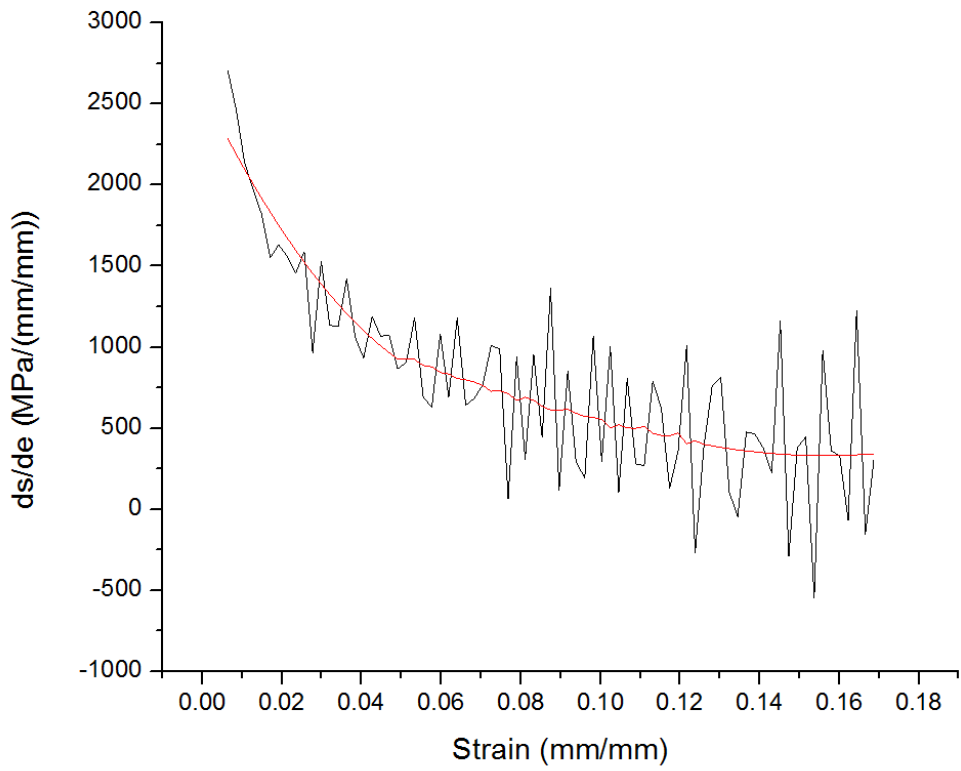


**Figure A.52** Plot of (a)  $ds/de$  as a function of strain and (b)  $ds/de$  as a function of Stress from tensile testing data at 25°C and initial cross-head velocity of 0.084 mm/s

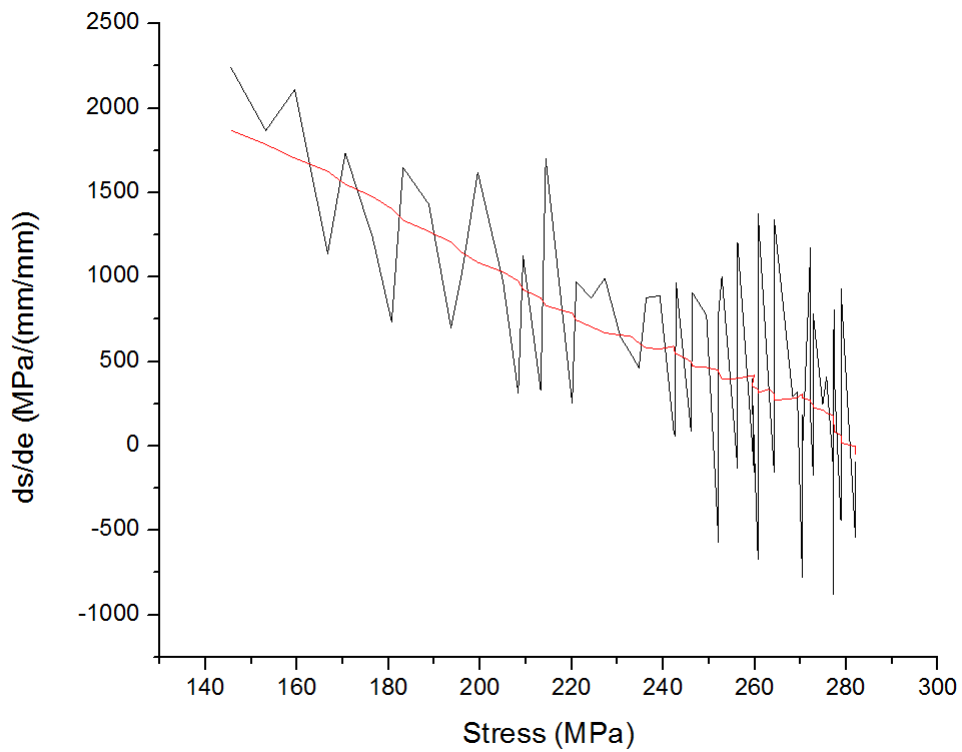
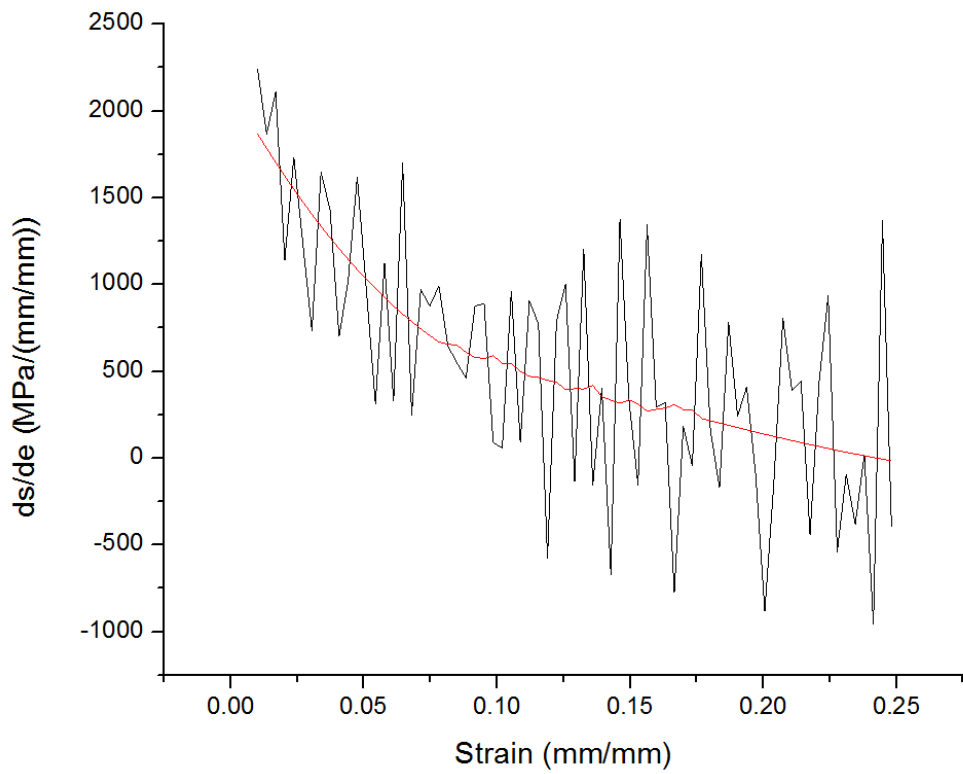


**Figure A.53** Plot of (a)  $ds/de$  as a function of strain and (b)  $ds/de$  as a function of Stress from tensile testing data at  $-40^{\circ}\text{C}$  and initial cross-head velocity of  $0.084\text{ mm/s}$

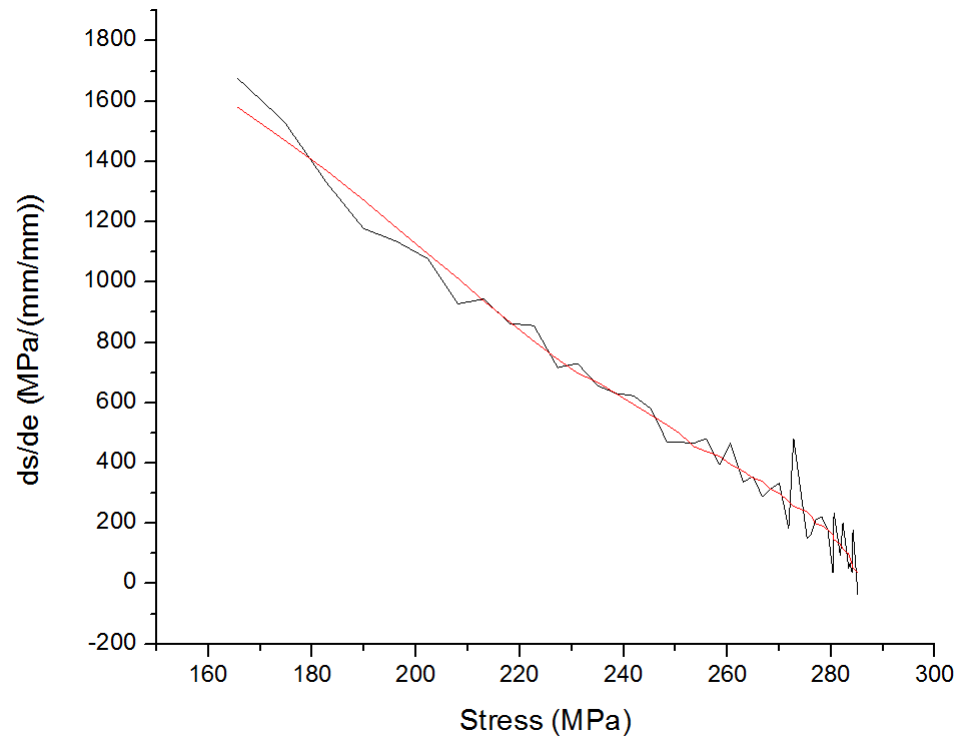
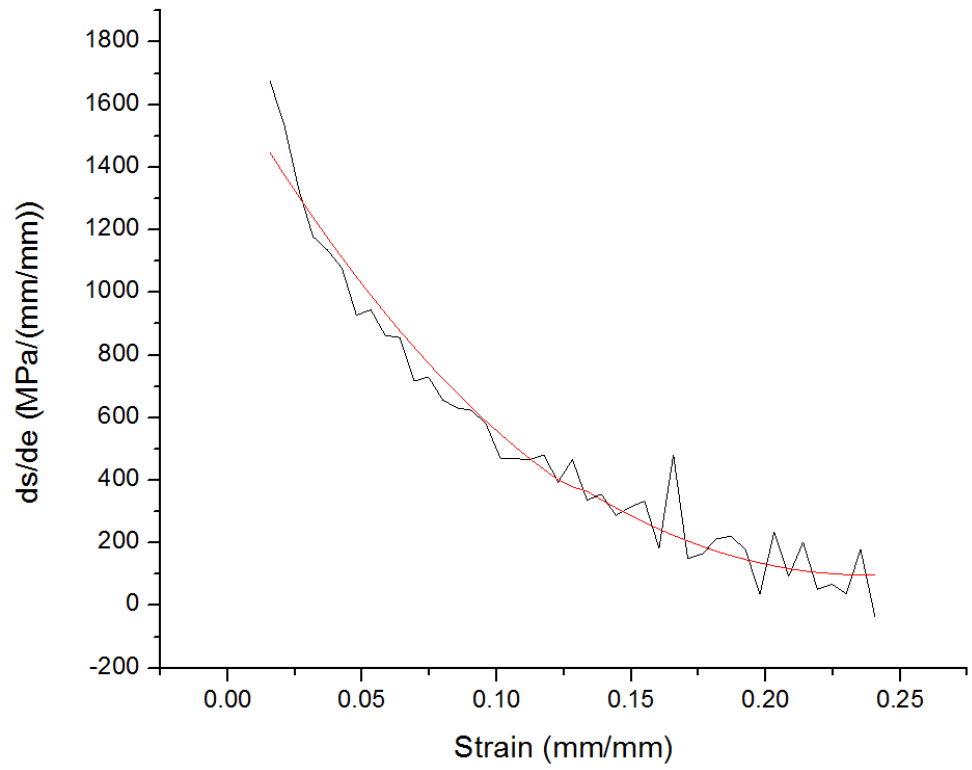


**Figure A.54** Plot of (a)  $ds/de$  as a function of strain and (b)  $ds/de$  as a function of Stress from tensile testing data at  $-80^{\circ}\text{C}$  and initial cross-head velocity of  $0.084\text{ mm/s}$

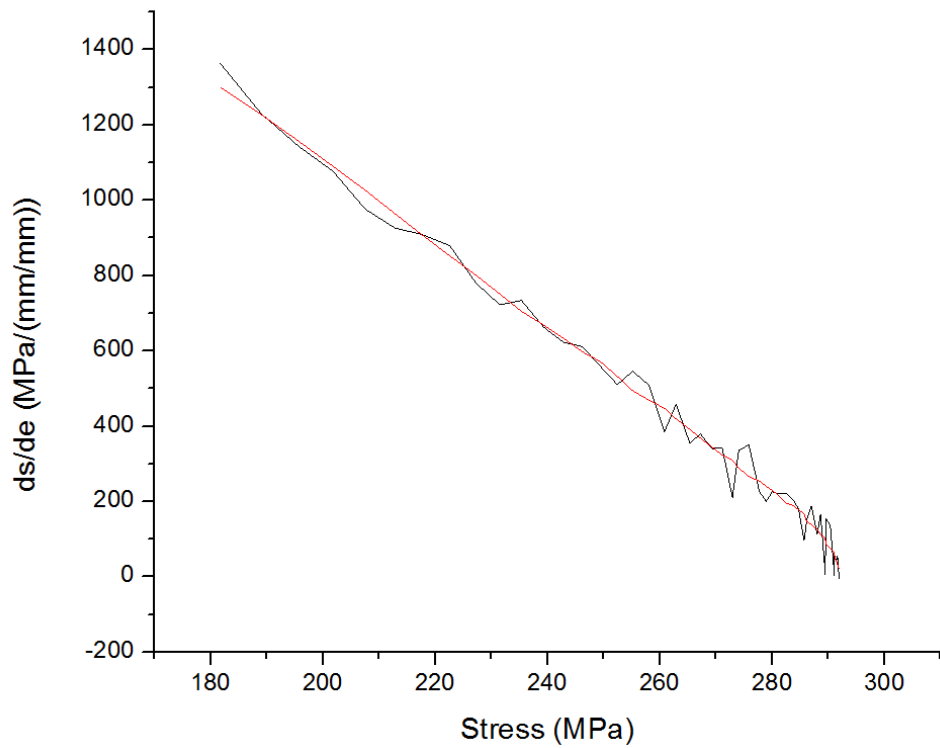
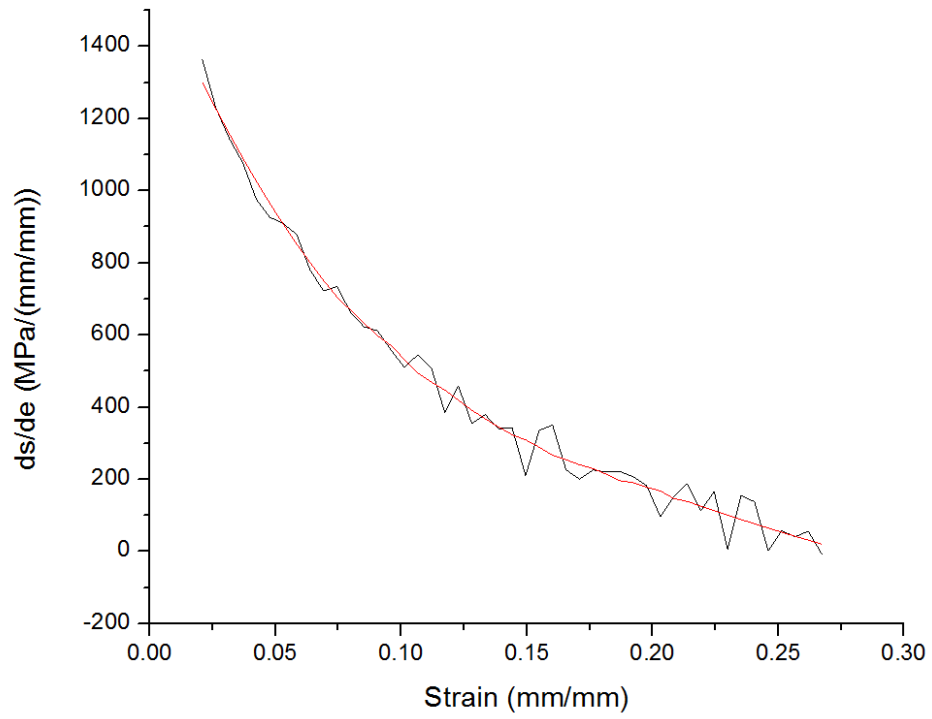


**Figure A.55** Plot of (a)  $ds/de$  as a function of strain and (b)  $ds/de$  as a function of Stress from tensile testing data at  $-120^{\circ}\text{C}$  and initial cross-head velocity of  $0.084\text{ mm/s}$

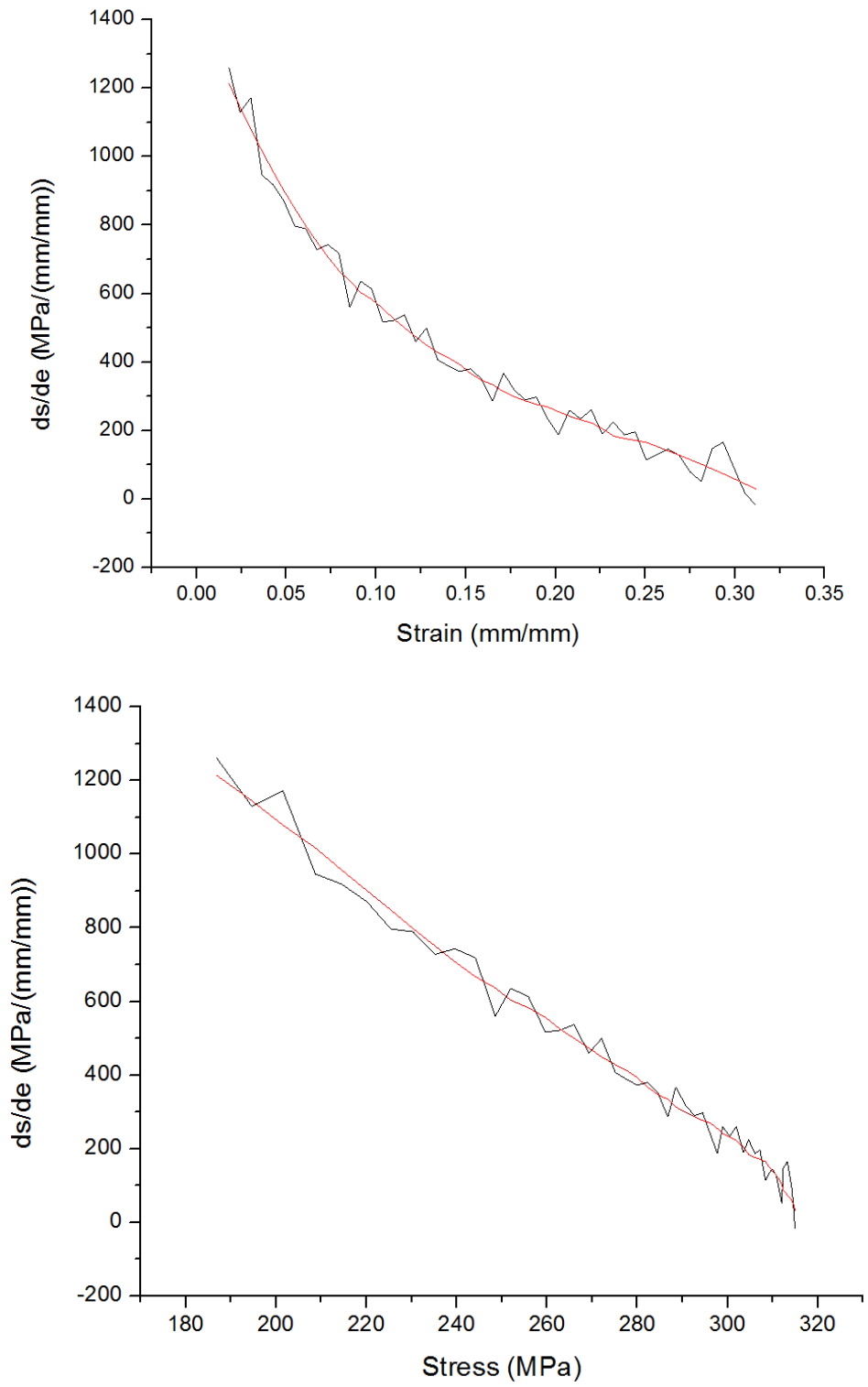


**Figure A.56** Plot of (a)  $ds/de$  as a function of strain and (b)  $ds/de$  as a function of Stress from tensile testing data at  $-160^{\circ}\text{C}$  and initial cross-head velocity of  $0.084\text{ mm/s}$

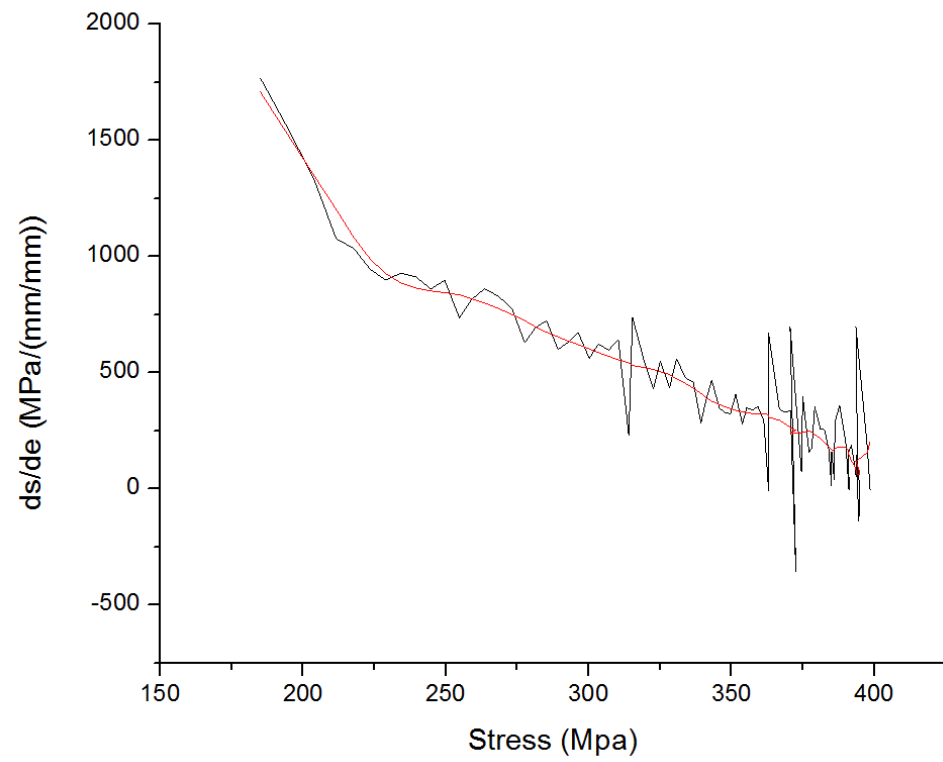
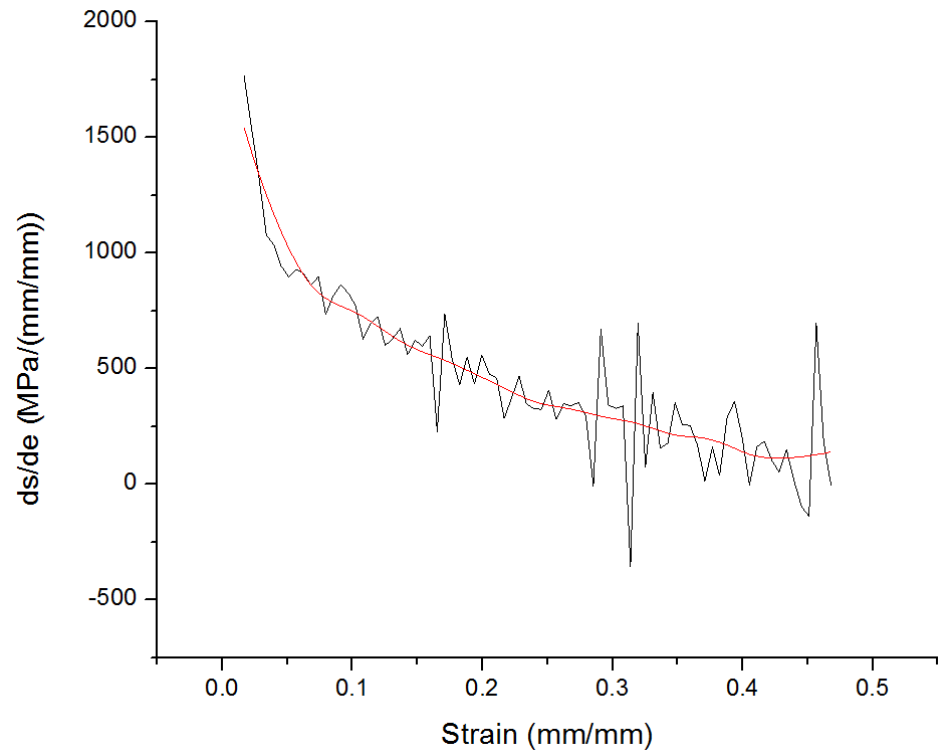


**Figure A.57** Plot of (a)  $ds/de$  as a function of strain and (b)  $ds/de$  as a function of Stress from tensile testing data at  $-196^{\circ}\text{C}$  and initial cross-head velocity of  $0.084\text{ mm/s}$

### A.3.4 Cottrell-Stokes Testing

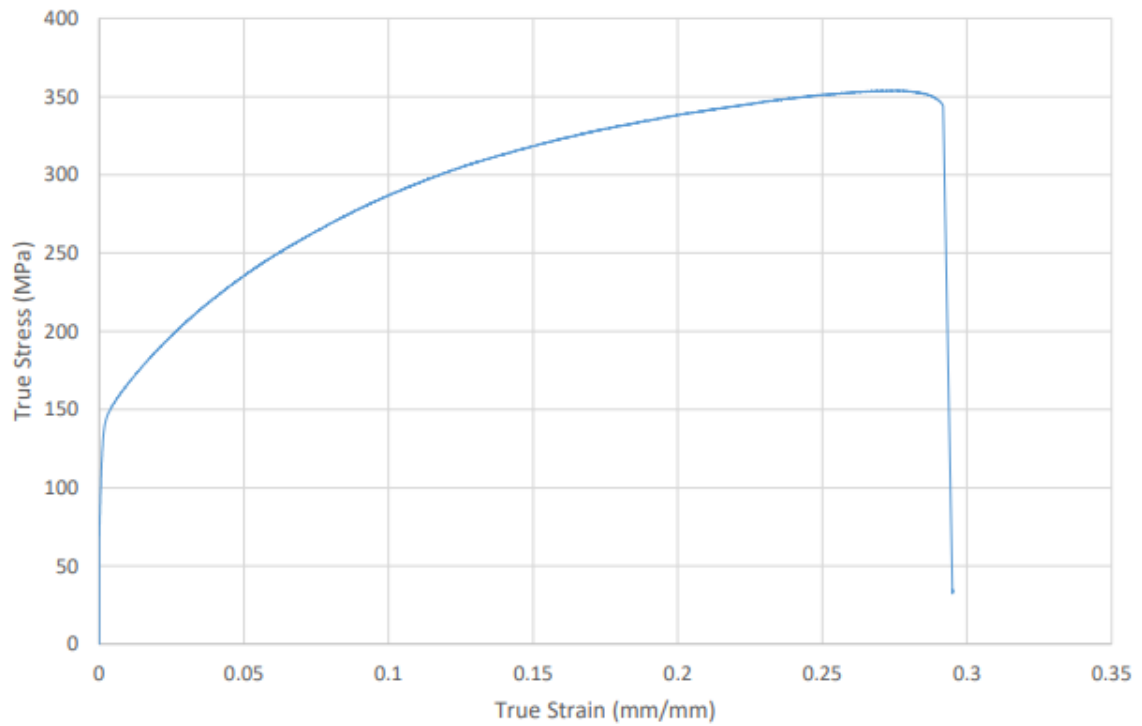


**Figure A.58** True Stress Strain Curve for aluminum alloy AA5182 obtained at 120°C and 0.002 offset of elastic region; respective strain rate  $1.9 \times 10^{-3} \text{ s}^{-1}$

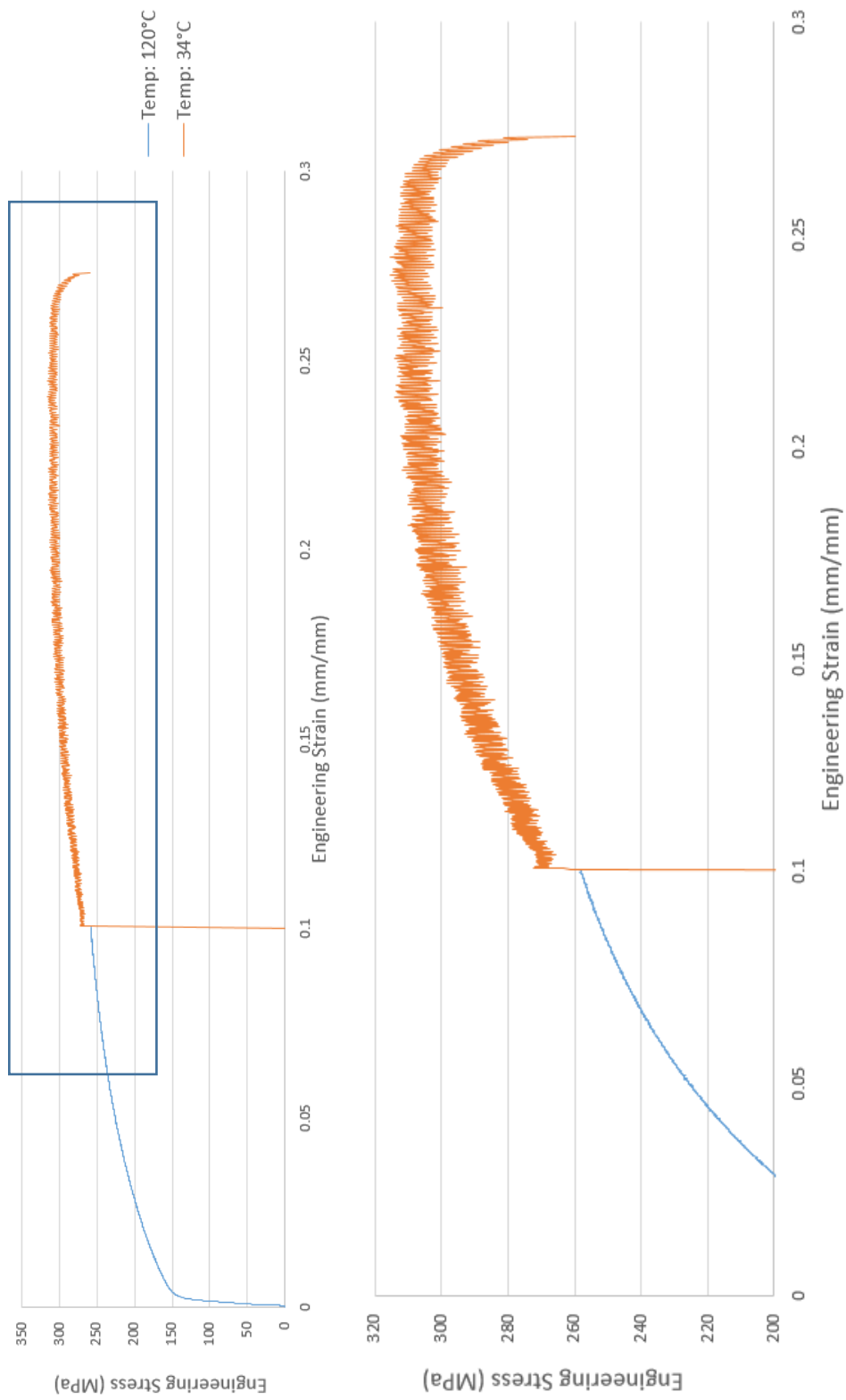


**Figure A.59** True Stress Strain Curve for aluminum alloy AA5182 obtained at 120°C and 0.002 offset of elastic region; respective strain rate  $1.9 \times 10^{-3} \text{ s}^{-1}$

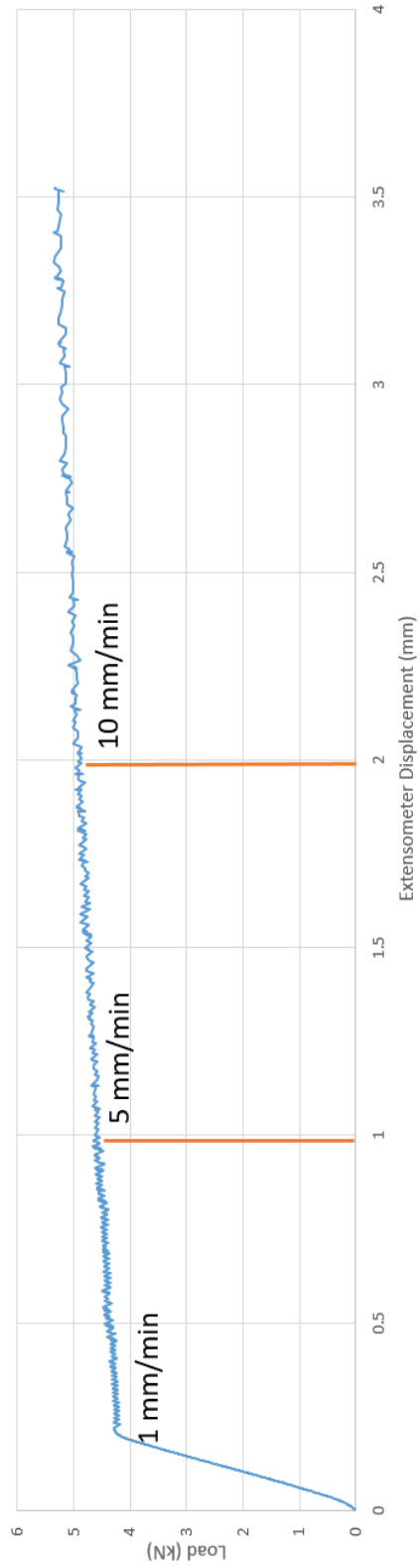


**Figure A.60** True Stress Strain Curve for aluminum alloy AA5182 obtained at 120°C and 0.002 offset of elastic region; respective strain rate  $1.9 \times 10^{-3} \text{ s}^{-1}$

### Jump Test 1 Calculations

$$m = \frac{\ln \frac{L2}{L1}}{\ln \frac{V2}{V1}}$$

$$m = \frac{\ln \frac{4.5838kN}{4.595kN}}{\ln \frac{5mm/min}{1mm/min}}$$

$$m = -1.52 \times 10^{-3}$$

$$m = \frac{\ln \frac{L4}{L3}}{\ln \frac{V2}{V1}}$$

$$m = \frac{\ln \frac{4.9255kN}{4.9333kN}}{\ln \frac{10mm/min}{5mm/min}}$$

$$m = -1.54 \times 10^{-3}$$

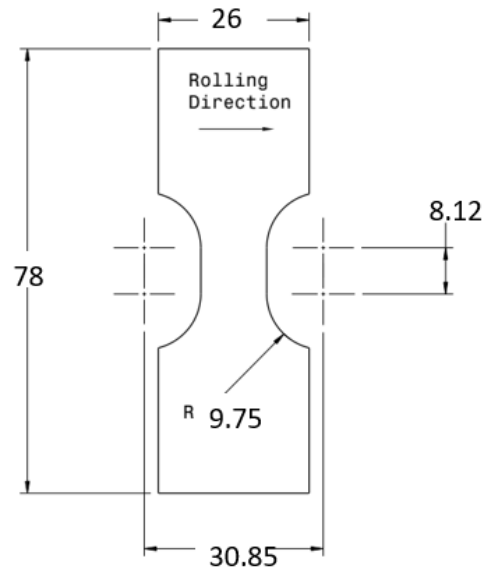
### Jump Test 2 Calculations

$$m = \frac{\ln \frac{L2}{L1}}{\ln \frac{V2}{V1}}$$

$$m = \frac{\ln \frac{0.2541kN}{0.3243kN}}{\ln \frac{100mm/min}{1mm/min}}$$

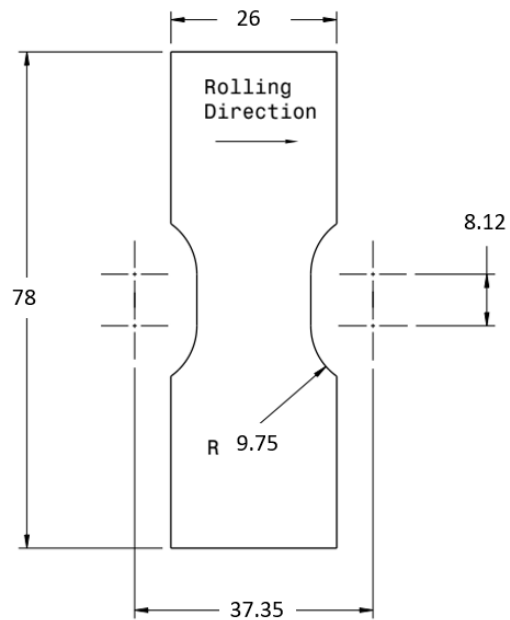
$$m = -0.053$$

## A.4 Formability Testing



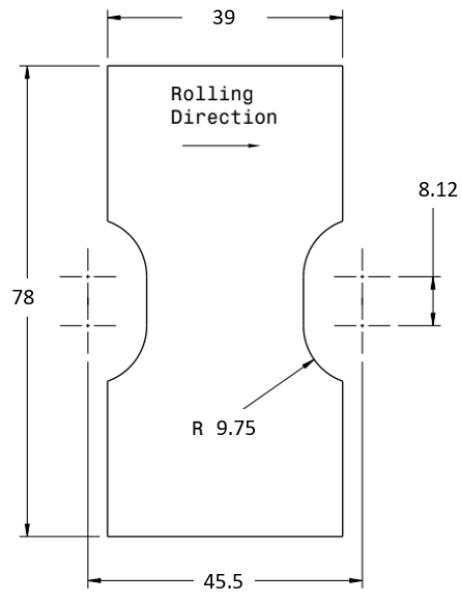
Dimensions in mm

**Figure A.61** Drawing of specimen #1 for sheet metal formability testing



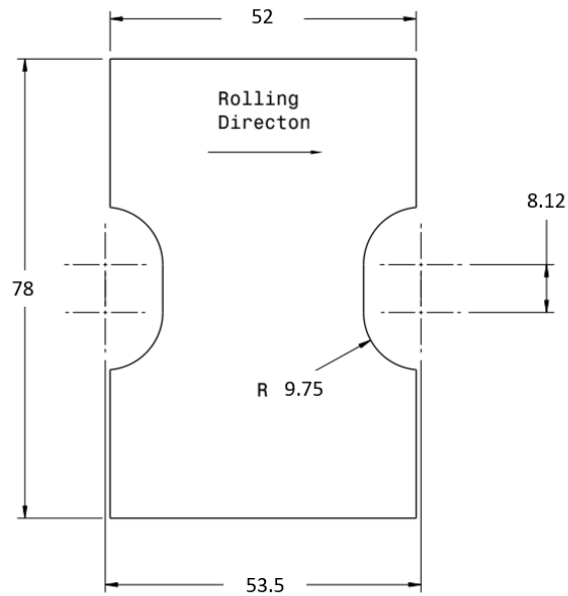
Dimensions in mm

**Figure A.62** Drawing of specimen #2 for sheet metal formability testing



Dimensions in mm

**Figure A.63** Drawing of specimen #3 for sheet metal formability testing



Dimensions in mm

**Figure A.64** Drawing of specimen #4 for sheet metal formability testing

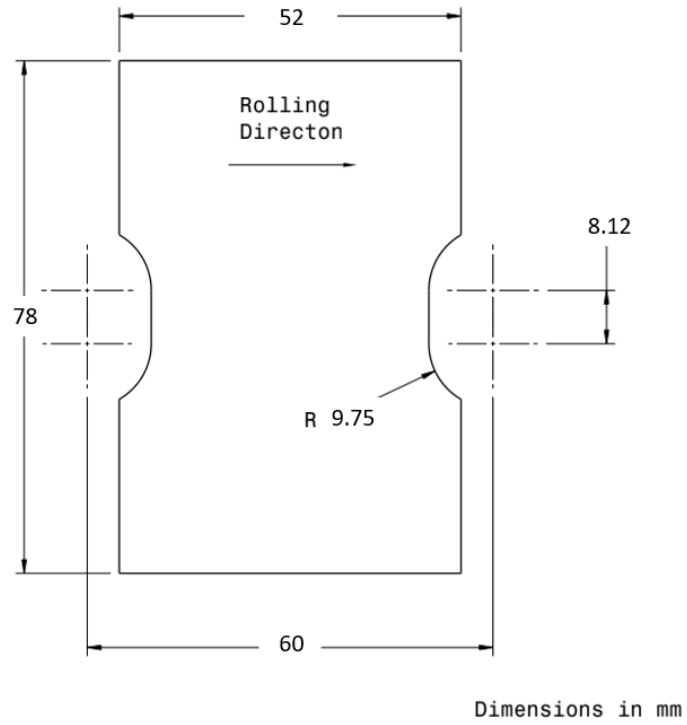


**Figure A.65** Drawing of specimen #5 for sheet metal formability testing

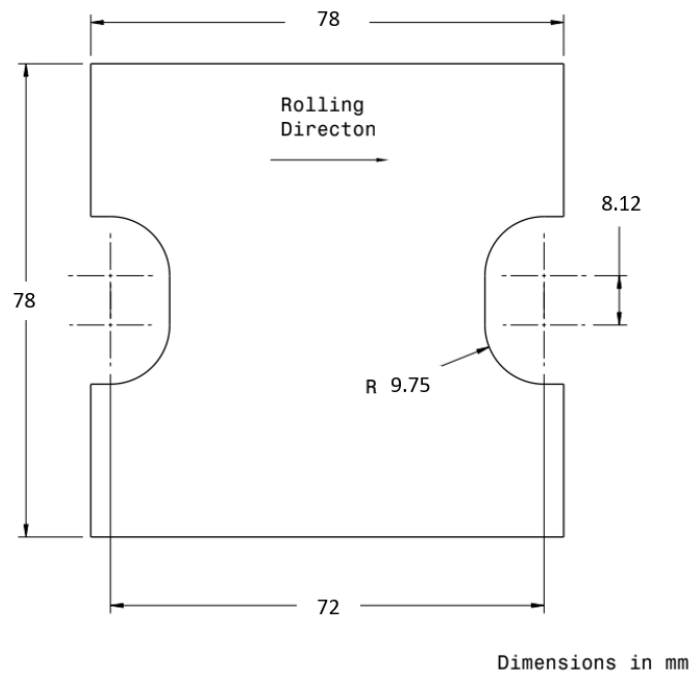


**Figure A.66** Drawing of specimen #6 for sheet metal formability testing

# Vita Auctoris

Taryn Coutts was born in 1996 in Windsor, Ontario. She completed her undergraduate degree in mechanical engineering at the University of Windsor in 2018, graduating with a specialization in materials. She completed her master's degree in materials engineering from the University of Windsor in 2022.